Tunable Photoluminescence and Visible light Photocatalysis by Mesoporous Si Nanowires Array and its Heterostructures

A Thesis Submitted to
Indian Institute of Technology Guwahati
For the Degree of

Doctor of Philosophy

By
Ramesh Ghosh

Department of Physics
Indian Institute of Technology Guwahati
Guwahati-781039, India
August 2016

Dedicated to

... My Beloved ***Grandfather***

Department of Physics
Indian Institute of Technology Guwahati
Guwahati-781039, India

STATEMENT

The work contained in the thesis entitled "***Tunable Photoluminescence and Visible light Photocatalysis by Mesoporous Si Nanowires Array and its Heterostructures***" has been carried out by me at Indian Institute of Technology Guwahati under the supervision of **Prof. P. K. Giri**, Professor, Department of Physics, Indian Institute of Technology Guwahati. This work has not been submitted elsewhere for the award of any degree.

Ramesh Ghosh
Roll No. - **10612110**

Senior Research Fellow
Department of Physics
Indian Institute of Technology Guwahati
Guwahati-781039, India

Prof. P. K. Giri
Professor
Department of Physics
Indian Institute of Technology Guwahati
Guwahati-781039, India
Phone: +91 361 2582703, Fax: +91 361 2690762
Email: giri@iitg.ernet.in

CERTIFICATE

This is to certify that the work contained in the thesis entitled "***Tunable Photoluminescence and Visible light Photocatalysis by Mesoporous Si Nanowires Array and its Heterostructures***" has been carried out by **Mr. Ramesh Ghosh** at Indian Institute of Technology Guwahati under my supervision. This work has not been submitted elsewhere for the award of any degree.

Prof. P. K. Giri
Thesis supervisor

ACKNOWLEDGEMENT

This thesis becomes a reality with the kind support and encouragement from numerous people. Now, it is my pleasure to express my gratitude to those persons for their assistance, support and inspiration.

First of all, I would like to express my sincere gratitude to my thesis supervisor, Prof. P. K. Giri for his inspiring guidance, valuable discussion, kind support, constant encouragement and useful suggestions. I am privileged for getting me the opportunity to work under his supervision. His vast knowledge and strong technical expertise have helped me in getting an excellent background in the semiconductor technology, identifying the opportunities in this field and preparing for the challenges. I am very much thankful for giving me the complete freedom in my work and providing the essential arrangements, laboratory facilities and moral supports throughout my Ph. D. work to achieve the goal.

I would like to thank my Doctoral Committee members, Dr. Ashwini Kumar Sharma, Dr. Subhash Thota, Dr. Dipankar Bandyopadhyay and former member Dr. Dipak Kumar Goswami for their regular review of my work, constructive criticism and valuable suggestions.

I am thankful to our Head of the Department of Physics, other faculty members of Physics, members of the Central Instruments Facilities and Centre for Nanotechnology for providing me a research friendly environment with up-to-date research facilities. I am grateful to Indian Institute of Technology Guwahati for providing the fellowship, good accommodation in this beautiful campus and having pleasant working environment. A special thanks to the scientific/technical officers, Dr. Sidananda Sarma, Indrajit Talukdar, Kaustubh Acharya, Dr. Kula K. Senapati, Chandan Borgohain and Madhurjya Borah for their help and co-operation to complete my work. I am also thankful to Central Workshop, Department of Mechanical Engineering for the fabrication of essential components used in my experimental setup. I am thankful to Centre for Excellence in Nanoelectronics & Theranostic Devices, IIT Guwahati for offering me the opportunity to build up research skills and for financial assistance. I would like to thank specially Prof. Minoru Fujii and Dr. Kenji Imakita of Kobe University for providing the opportunity to use some of the laboratory facilities.

I would like to express my appreciation and thanks to my friends and lab-mates for their help and good company. I should not forget to mention a few of them. I express my sincere thanks to my seniors Dr. Soumen Dhara, Dr. Arindam Pal, Dr. Biswajit Choudhury, Dr. Himanshu Jha, Dr. Batakrushna Santara, and Dr. Ravi Kumar Biroju for their help in research

and their good company. Thanks to my lab mates Jitendra, Obaidulla, Gone, Manjira, Somorjit, Ruma and Joydip for their help and support. I should not forget to mention Kamal, Lario from my LAB and Arindam, Bishu and Anabil from other LAB for their cheerful and enjoyable company and the moral support during my depression.

I am very much thankful to my father and mother for their love, blessing and constant encouragement to pursue higher study. I would like to thank Priya, Soumik and my sister Mousumi for their cheerful support and encouragement. Finally, I wish to express my deep sense of gratitude to my grandfather for his constant support and encouragement for higher studies. I spent my childhood days under his guidance and he was instrumental to build my character, morality and personality. I am dedicating this thesis to my grandfather.

Ramesh Ghosh

IIT Guwahati

CONTENTS

Synopsis IX

List of Publications XIV

List of Abbreviations XVI

Chapter 1: **Introduction** **1**

1.1. Si Nanostructures 2

1.2. Si Nanowires 2

1.3. Growth of Si Nanowires 4

1.3.1. Metal Assisted Chemical Etching 6

1.4. Mesoporous Si Nanowires 7

1.5. Defects in the Si Nanostructures 8

1.5.1. Oxygen Vacancy 9

1.5.2. Non-bridging Oxygen Hole Center 10

1.5.3. H-terminated Si 10

1.6. Si Nanowire Heterostructures 11

1.7. Fabrication of Si Nanowire Heterostructures 12

1.8. Application of Si Nanowire & its Heterostructures 13

1.8.1. Light Emitting Diode 14

1.8.2. Solar Cell 16

1.8.3. Artificial Photosynthesis 19

1.8.4. Thermoelectrics 20

1.8.5. Energy Storage Devices 21

1.8.6. Sensors 24

1.8.7. Environmental Cleaning 25

1.9. Challenges in Fabrication and Applications of Si Nanowires and its Heterostructures 27

1.10. Focus of the Present Thesis 28

1.11. Organization of the Thesis 28

References 29

Chapter 2: **Experimental Techniques 37**

2.1. Fabrication of Si Nanowires and Heterostructures 37

2.1.1. Metal Assisted Chemical Etching Method 37

2.1.1.1. Wafer Cleaning and Substrate Preparation 38

2.1.1.2. Metal Deposition 39

2.1.1.3. Etching in Etchant …….. 39
2.1.2. Rapid Thermal Annealing ……..……..…….……... 41
2.1.3. RF Magnetron Sputtering ……..……..…… 42
2.2. Characterization Techniques ……..……..…….. 43
2.2.1. Morphological and Structural Characterization ….…… 43
2.2.1.1. Field Emission Scanning Electron Microscopy (FESEM) …. 43
2.2.1.2. Transmission Electron Microscopy (TEM) ……..…..…… 46
2.2.1.3. Atomic Force Microscopy (AFM) ……..……...…..… 47
2.2.1.4. X-ray Diffraction (XRD) ……..……..……...… 48
2.2.1.5. X-ray Photoelectron Spectroscopy (XPS) ……..…..... 50
2.2.1.6. Fourier Transform Infrared (FTIR) Spectroscopy ……..… 51
2.2.1.7. Brunnauer-Emmett-Teller (BET) Surface Area Analyzer …. 52
2.2.2. Optical Characterization ……..……...……..… 53
2.2.2.1. UV-Vis-NIR Absorption Spectroscopy ……..…….. 53
2.2.2.2. Diffuse Reflectance Spectroscopy (DRS) ……..……..… 54
2.2.2.3. Micro-Raman Spectroscopy ……..……..…… 56
2.2.2.4. Photoluminescence (PL) Spectroscopy ……..……..….. 57
2.2.2.5. In-house Design and Development of Laser based
PL Measurement Setup ……..……..…….. 58
2.2.2.6. Time-resolved Photoluminescence (TRPL) Spectroscopy … 59
2.2.2.7. Photochemical Reactor ……..……..…… 61
References ……..…… 62

Chapter 3: **Controlled Growth of Mesoporous Si Nanowires Array by Metal Assisted Chemical Etching ….……...…. 65**
3.1. Introduction ……..……...… 65
3.2. Metal Assisted Chemical Etching ……..……..… 66
3.3. Etching Mechanism ……..……..……. 66
3.4. Calculation of Growth Exponents at the Early Stage of Etching ……..……..…. 68
3.5. Si Nanocrystals Decorated Si Nanowires ……..……..…. 72
3.5.1. Surface Porosity Analysis by BET ……..…… 75
3.6. Effect of Etching Parameters on the Morphology & Structure of Si NWs …… 76
3.6.1. Effect of Etching Duration ……..……..…….. 77
3.6.2. Effect of Metal Nanoparticle Species on the MACE Growth …..……. 79
3.6.3. Effect of Etching Concentration ……..…….. 81
3.6.4. Orientation Controlled Growth of Si NWs …… 83
3.6.5. Effect of Resistivity of Si Wafer ……..……...… 84

3.8. Controlling the Diameter of the Si NWs ……. 86
3.9. Structural and Compositional Analysis of Si NWs ……. 87
3.9.1. Energy Dispersive X-ray Analysis ……. 87
3.9.2. X-ray Diffraction Pattern ……. 88
3.9.3. X-ray Photoelectron Spectroscopy ……. 89
3.9.4. Raman Spectroscopy ……. 92
3.9.5. Fourier Transform Infrared Spectroscopy ……. 95
3.10. Conclusion ……. 96
References ……. 96

Chapter 4: **On the Origin of the Broadband Visible and Near Infrared Photoluminescence from Mesoporous Si Nanowires ……. 101**
4.1. Introduction ……. 101
4.2. Sample Preparation for Photoluminescence Studies ……. 102
4.3. Origin of Visible Photoluminescence from Self-Grown Si Nanocrystal Decorated Si Nanowires ……. 102
4.3.1. Quantum Confinement Model ……. 103
4.3.2. Quantitative Analysis of the Photoluminescence Spectra ……. 104
4.4. Contribution of NBOHC Defects to the Photoluminescence ……. 106
4.5. Tunability of the Visible Photoluminescence from Mesoporous Si NWs ……. 107
4.5.1. Etching Duration ……. 108
4.5.2. Etchant Concentration ……. 109
4.5.3. Wafer Resistivity/Doping Concentration ……. 110
4.5.4. Oxide Layer Thickness ……. 111
4.5.5. Nature of Noble Metal during MACE ……. 112
4.5.6. PL Excitation Spectra ……. 114
4.5.7. Laser Excitation Power ……. 115
4.5.8. Laser Exposer Time: Temporal Decay ……. 116
4.5.9. Absorption Spectra of Si NWs ……. 117
4.5. Low Temperature Photoluminescence ……. 118
4.6. Near-Infrared Photoluminescence ……. 120
4.7. Time Resolved Photoluminescence ……. 123
4.8. Illustration of PL Mechanism Using the Energy Band Diagram ……. 125
4.9. Conclusion ……. 126
References ……. 127

Chapter 5: **Quantitative Analysis of the Phonon Confinement Effect in Arbitrarily Shaped Si Nanocrystals Decorated on Si Nanowires and its Correlation with the Photoluminescence Analysis ……..…….. 129**

5.1. Introduction ……..……. 129

5.2. Growth of Si NC Decorated Si NWs ……..……...…… 131

5.3. Morphology ……..……..……. 132

5.3.1. FESEM Analysis ……..……..… 132

5.3.2. TEM Analysis ……..……..… 132

5.4. Raman Spectral Analysis …….. 134

5.4.1. Effect of Lattice Strain ……. 136

5.4.2. Effect of Laser Heating …… 136

5.4.3. Quantitative Analysis of the Raman Spectra ……...…… 138

5.5. Photoluminescence Analysis ……. 141

5.6. Correlation between the Raman and PL Analysis: Calculation of the Size Distribution of Si NCs ……..…….. 143

5.7. Conclusion ……..……...…. 146

References ……..……..……. 147

Chapter 6: **The Visible Light Photocatalytic Performance of the Mesoporous Si Nanowires ……...…… 149**

6.1. Introduction …… 149

6.2. Visible Light Photocatalysis …….. 150

6.2.1. Sample Preparation for Photocatalysis Studies …….. 150

6.2.2. Photocatalysis Setup …….. 150

6.2.3. Photodegradation Procedure …….. 150

6.3. Visible Light Photocatalysis of Methylene Blue (MB) ……. 151

6.4. Effect of Different Growth Parameters on the Photocatalytic Performance …….. 153

6.4.1. Etching Duration …… 153

6.4.2. Etching Solution ……. 154

6.4.3. Etchant Concentration …… 155

6.4.4. Si Wafer Resistivity …… 156

6.4.5. Nature of Noble Metals during MACE Growth ……..…….. 157

6.5. Visible Light Photocatalysis of Methyl Orange (MO) ……..…. 159

6.6. Photocatalytic Rate Constant …….. 159

6.7. Surface Evolution of the Si NWs after Photocatalysis ……... 161

6.8. Recyclability of Si NW Photocatalyst …… 162

6.9. Illustration of Photocatalysis Mechanism using Energy Band Diagram ……..... 163

6.10. Comparison of Photocatalytic Performance of Mesoporous Si NWs & Commercial P25 165
6.11. Correlation between PL Intensity and Photocatalytic Performance of Mesoporous Si NWs 166
6.12. Conclusion 167
References 168

Chapter 7: **Photoluminescence Signature of Resonant Energy Transfer in ZnO Thin Film Coated Mesoporous Si Nanowires Array 169**
7.1. Introduction 169
7.2. Experimental Procedure 171
7.2.1. Growth of Si NCs decorated Si NWs 171
7.2.2. Growth of ZnO Thin Film on Mesoporous Si NWs 171
7.3. Morphology 172
7.3.1. FESEM Imaging 172
7.3.2. TEM Imaging 173
7.4. Structural and Composition Analysis 174
7.4.1. X-Ray Diffraction 174
7.4.2. X-Ray Photoelectron Spectroscopy 175
7.5. Optical Characterization 176
7.5.1 Absorption Study 176
7.5.2. Photoluminescence Study 178
7.5.3. Time Resolved Photoluminescence Study 185
7.6. Illustration of Si NW/ZnO Band Alignment and the FRET Process 188
7.7. Conclusions 190
References 190

Chapter 8: **Metal Nanoparticle Decorated Si Nanowire Heterostructures: Fabrication, Properties and Applications 193**
8.1. Introduction 193
8.2. Fabrication of Metal NP Decorated Si NWs 194
8.2.1. Fabrication of Si NWs 194
8.2.2. Metal NPs Decoration on Si NWs 195
8.3. Morphology and Structure of Ag NP Decorated Si NWs 195
8.3.1. FESEM Analysis 195
8.3.2. XPS Analysis 196
8.4. Optical Properties of Metal NP Decorated Si NWs 197
8.4.1. Reflectance Study 197

8.4.2. Photoluminescence Study …….. 197
8.4.3. Photocatalysis Study …….. 200
8.4.4. Optical Sensing and SERS Detection Using
Mesoporous Si NWs …… 202
8.4.4.1. Fluorescence Detection of Methylene Blue …… 202
8.4.4.2. SERS Detection of Methylene Blue ……. 204
8.5. Conclusion …….. 205
References ……..…….. 205

Chapter 9: **Summary and Outlooks ……... 207**
9.1. Summary ……..…….. 207
9.2. Highlight of the Thesis Contributions ……..…….. 208
9.2.1. Critical Growth Parameters for Morphology Controlled
Growth of Si NC Decorated Si NWs …… 208
9.2.2. Elucidating of the Origin of Visible and NIR Photoluminescence
from the Mesoporous Si Nanowires …….. 209
9.2.3. Quantitative Analysis of the Phonon & Electron Confinement Effect
in the Arbitrary Shaped Si NCs based on Raman and PL Studies …… 209
9.2.4. Efficient Photocatalytic Degradation of Organic Dyes by Mesoporous
Si Nanowires …….. 210
9.2.5. Multifunctional Si NW Heterostructures: Tunable Photoluminescence,
Efficient Photocatalytic Performance and SERS Detection ……. 211
9.3. Future Scope …… 212

Corrigendum

Synopsis:

1. Page x: Para 2, Line 2: Replace “its” by “the”.
2. Page x: Para 2, Line 4: Delete “both”.
3. Page x: Para 2, Line 5: Replace “HSs is” by “HSs form”.
4. Page xi: Para 2, Line 4: Delete “about”.
5. Page xi: Para 2, Line 6: Delete “is presented”.
6. Page xi: Para 3, Line 6: Replace “the arbitrary” “arbitrary”.

Chapter 1:

1. Page 7: Section 1.4., Line 5: Replace “leads” by “lead”.
2. Page 11: Section 1.6., Line 2: Replace “materials is being” by “materials are being”.
3. Page 11: Section 1.6., Line 4: Delete “both”.
4. Page 11: Section 1.6., Line 5: Replace “as well as its” by “and their”.
5. Page 25: Section 1.8.7., Line 1: Replace “NWs is” by “NWs are”.
6. Page 27: Section 1.9., Line 1: Replace “by using MACE” by “using MACE by”.
7. Page 28: Section 1.10., Line 1: Replace “several of challenges” by “several challenges”.

Chapter 2:

1. Page 37: Para1, Line 4: Replace “excitation based” by “excitation-based”.
2. Page 37: Section 2.1.1., Line 1: Replace “solution based” by “solution-based”.

Chapter 3:

1. Page 78: Fig. 3.10: Replace “nm” by “μm” in the Y-axis unit of the Fig. 3.10(a) and (b).
2. Page 79: Section 3.6.2., Line 7: Replace “Au (2 nm) and Ag (10 nm)” by “Au (2 nm), and Ag (10 nm)”.
3. Page 81: Section 3.6.3., Line 1: Replace “etching” by “etchant”.
4. Page 83: Section 3.6.4., Line 12: Replace “underneath atoms” by “atoms underneath”.
5. Page 85: Table 3.2, Column 2 heading: Replace “in μm Si NWs” by “Si NWs in μm”.

Chapter 4:

1. Page 102: Section 4.2., Line 6: Replace “in the PL” by “on the PL”.
2. Page 102: Section 4.3., Line 7: Replace “diameter is Si” by “diameter in Si”.
3. Page 102: Section 4.3., last Line: Replace “over layer” by “over-layer”.
4. Page 105: Para2, Line 2: Replace “the equation 2” by “equation 4.2”.
5. Page 105: Table 4.1, Caption: Replace “Eqn. 2” by “Eqn. 4.2”.
6. Page 105: Line 10 (from bottom): Replace “that of the” by “those of”.
7. Page 109: Section 4.5.2., Line 1: Replace “etching concentration strongly” by “etchant concentration has strong”.

8. Page 109: Section 4.5.2., Line 5: Replace “concentration” by “concentrations”.
9. Page 116: Section 4.5.8. Line 7 (from bottom): Replace “exposer” by “exposure”.

Chapter 5:

1. Page 129: Section 5.1., Line 5: Replace “is well” by “are well”.
2. Page 130: Para 1, Line 19: Replace “board” by “broad”.
3. Page 136: Section 5.4.2., Line 1: Replace “exposer” by “exposure”.
4. Page 145: Line 5: Replace “of very small” by “very small”.
5. Page 146: Section 5.7., Line 2: Replace “the etching” by “etching”.

Chapter 6:

1. Page 150: Section 6.2.2., Line 4: Replace “Fig. 2.18” by “Fig. 2.17”.
2. Page 152: Line 3: Replace “electron deficient” by “electron-deficient”.
3. Page 153: Section 6.5., Line 2: Replace “as grown” by “as-grown”.
4. Page 159: Section 6.5., Line 8: Delete “subsequently”.
5. Page 167: Line 12: Replace “ones need” by “one’s need”.
6. Page 167: Line 13: Replace “increasing the resistivity” by “increasing resistivity”.

Chapter 7:

1. Page 170: Line 12: Replace “low cost” by “low-cost”.
2. Page 177: Line 7: Replace “as well as ZnO coated” by “and ZnO-coated”.
3. Page 177: Line 5 (from bottom): Replace “to that of pure ZnO” by “to the bulk ZnO crystal (~3.3 eV)”.
4. Page 177: Line 3 (from bottom): Replace “defect induced” by “defect-induced”.
5. Page 184: Para 2, Line 12: Replace “FRET mediated” by “FRET-mediated”.
6. Page 187: Line 11: Replace “has” by “have”.
7. Page 188: Section 7.6., Line 3-4: Replace “downward” by “upward”, and “upward” by “downward”.
8. Page 188: Last line: Replace “EF” by “EA”.
9. Page 189: Line 3: Replace “lighter” by “smaller”.

Chapter 8:

1. Page 194: Para 2, Line 4: Replace “coming Ag” by “coming from Ag”.
2. Page 196: Fig. 8.2, Caption: Replace “thecCore” by “the core”.
3. Page 201: Line 1: Replace “an observed the” by “observed”.
4. Page 202: Section 8.4.4., Line 2: Replace “candidate” by “candidates”.

Chapter 9:

1. Page 207: Section 9.1., Line 9: Replace “condiment” by “confinement”.
2. Page 213: Point 6, Line 1: Replace “we are observed” by “we have observed”.

SYNOPSIS

Semiconductor nanowires (NWs) are an important class of one dimensional (1D) material that has been attracting a great deal of interest over the past two decades. Due to their unique electrical, optical, mechanical, thermal, and chemical properties, Si NWs have been explored in diverse range of applications, e.g., nanoelectronics, optoelectronics, thermoelectric, photovoltaics, energy storage, photocatalysis and bio-chemical sensors etc. Interestingly, Si NWs-based nanodevices are fully compatible with the current Si-based technology, and already a number of nanodevices based on Si NWs as building blocks have been demonstrated. However, large scale fabrication and their integration into robust and functional devices are still challenging to the research community.

Over the past decades, several approaches have developed for the synthesis of Si NWs, such as vapor-liquid-solid growth, laser ablation, solution phase synthesis, molecular beam epitaxy, template assisted growth, oxide assisted growth, RF magnetron sputtering, thermal evaporation etc. However, these growth processes generally need a high temperature, high vacuum, templates and sophisticated equipment, or hazardous Si precursors in some cases, which make them time consuming and expensive. A relatively simple yet rapid method, i.e., metal-assisted chemical etching (MACE) has been developed recently and it has emerged as a powerful tool to grow single crystalline Si NWs. First, MACE is a low cost method for fabricating vertical Si NWs with the ability to control the cross section, shape, diameter, length, orientation, uniformity, doping type and doping level of the NWs. Second, the vertical Si NWs grown by MACE have fascinating physical and chemical characteristics that have found applications in wide areas of energy and environment, such as solar cell, Li-ion battery, photochemical reactor and sensors etc.

Though Si is the material of choice for electronics industry, it has major limitations for optoelectronic and photonics applications due to its indirect bandgap. However, low-dimensional Si nanostructures can absorb and emit visible light as a result of the quantum-confinement effect and the Si NWs have a remarkable optical antireflection ability. The absorption coefficient is large for the array of Si NWs because of the multiple reflection induced light trapping. Si NW based solar cells have been explored with reduced optical loss, enhanced optical absorption, and improved carrier separation for high performance and low cost designs. MACE grown Si NWs exhibit high absorption, extremely low reflection and tunable photoluminescence (PL) in the entire visible to near infrared (NIR) range. Some

studies suggest that excitons generated within the nanoporous Si NWs are energetic enough to drive the photoelectrochemical reactions under visible light illumination on Si NWs. Si NWs exhibit efficient and stable visible light photocatalysis without and with the decoration of plasmonic metal nanoparticles (NPs), e.g, Ag, Au NPs. These results open up possibility of using Si NWs array for organic waste treatment and hydrogen production by photocatalytic water splitting. However, several issues need to be addressed for commercial applications of the Si NWs grown by MCAE process. For example, reproducibility of morphology and surface oxidation of the Si NWs grown by MACE are among the major concerns for device fabrication.

Semiconductor heterostructures (HSs) fabricated on 1D Si NWs template have been found to be attractive for its additional structural complexity and functionality arising from the junction of different materials. Several reports have been published on Si NWs based HSs and both organic/inorganic materials as well as its different combinations are used as the HS material. Recent investigations have revealed that Si NW HSs is a powerful approach to improve the performance of Si NWs based solar cells, sensors and photochemical reactors, light emitting diodes (LEDs) etc. Although the HSs are superior for modulation of the properties, selection of right material, control of external layer and the formation of high quality interface between the external material and NW are still challenging.

This thesis presents a systematic study on the growth mechanism, orientation controlled growth and tunable photophysical and photochemical properties of mesoporous Si NWs and its heterostructures for light emission and environmental cleaning applications. These studies are very significant and timely to address the environmental and energy challenges currently being faced by the humanity. The complete thesis work has been organized into nine chapters as summarized below:

Chapter 1 presents a brief introduction to the robust developments in the 1D Si NWs including growth strategies, important properties and their promising applications ranging from field effect transistors (FET), LED, solar cells, sensors, and energy storage to photochemical reactor. In addition, fundamental issues related to the growth mechanism and origin of superior properties of the Si NWs is discussed. A brief discussion on the important features of Si NWs HSs and their potential technological applications in the above field are addressed in this chapter. The problems and challenges of utilizing the Si NWs as well as its

HSs in the device applications and the key parameters to improve the devices performances are discussed and the motivation of the present work is presented at the end of the chapter.

Chapter 2 provides a brief description of the experimental techniques used for the present work along with their working principles. Brief account of the experimental procedures for the fabrication of the different kinds of Si NWs and NW heterostructures with other materials are discussed. We also briefly discuss about various characterization techniques used in the present work including the in-house developed photoluminescence measurement system using external laser excitation source is presented. The methodology adopted and the software used to analyze the raw data from various microscopic and spectroscopic techniques are also discussed.

Chapter 3 presents results on the early stages of growth and growth mechanism of Si NWs during MACE process using a novel scaling approach. One-step and two-step MACE of Si wafer are used for the fabrication of arrays of Si NWs. AFM, FESEM and TEM including HRTEM studies revealed the detail growth kinetics of MACE grown Si NWs. The high resolution imaging and its analysis confirms that the surface of the Si NWs is covered with ultra-small size Si nanocrystals (NCs) of the arbitrary shape. The length, orientation, diameter and porosity of the Si NWs are tuned by controlling the growth parameters, such as, etching duration, wafer orientation, wafer type and resistivity, shape and size of pre-deposited metal and relative etchant concentration. Orientation controlled growth of Si NWs has also been demonstrated in this work. This work provides valuable insights on the controlled growth of Si NWs that is crucial for exploring its novel applications.

Chapter 4 presents the origin of the broad band visible and NIR PL from the as-grown Si NCs decorated Si NWs samples. The critical role of quantum confinement (QC) of carriers in Si NCs and the contribution of intrinsic defects in Si NW surface in the extended visible absorption, visible-NIR PL from the Si NWs grown for both one-step and two-step MACE process have been presented and analyzed in details. In particular, monitoring the time evolution of the visible and NIR PL emissions at low temperature, under high vacuum and oxygen environment (in-situ) allowed us to distinguish and unambiguously identify the sources of various PL peaks. The identification of band gap tuning of Si NCs and the defect engineering in Si-SiO_x interface is an important milestone in realizing the improved visible light photocatalysis, LED and photovoltaic applications of the Si NWs/NCs system.

Chapter 5 presents a quantitative analysis of the phonon confinement effect in arbitrary shaped Si NCs decorated on Si NWs and its correlation with the PL spectrum. The size distributions of Si NCs are estimated in terms of the mean diameter and skewness from the Raman spectra using simulation and it is compared with the size distribution obtained from the PL and HRTEM analyses. Raman and PL results are quantitatively analyzed using the phonon and electron confinement models, respectively, and the correlation between two was shown to be fairly good. Such a correlation between Raman and PL spectra allows spectroscopic evaluation of the accurate size distribution of the Si NCs on the surface of the Si NWs, even for arbitrary shaped Si NCs. These results are useful for design of high performance optoelectronic devices based on the Si NWs/NCs.

Chapter 6 presents the results of the visible light photocatalysis by Si NCs decorated Si NWs. Besides the tunable PL emission, the MACE grown Si NWs show excellent visible light photocatalysis for the degradation of organic dyes (Methylene blue and Methyl orange) and the photocatalytic effect is quite stable up to 5 cycles of catalysis. It is shown that Si-H bonds present on the surface of the Si NWs/NCs actually facilitate the photocatalytic activity by the efficient separation of photogenerated e-h pairs. The presence of Schottky junction between the Si NW and undesolved metal NP, and the strong visible light absorption are partly responsible for the high photocatalysis efficiency. The effect of Si NW length, orientation, resistivity and the relative etchant concentration on the photocatalysis properties are discussed systematically. We find a clear correlation between PL and photocatalysis efficiencies for each set of Si NWs/NCs. This work opens up the possibility of using Si NWs in organic waste treatment and hydrogen production by photocatalytic water splitting.

In Chapter 7, PL signature of resonant energy transfer in ZnO coated Si NWs/NCs array is presented. Here we describe the fabrication of Si NW/ZnO film core-shell HSs and their optoelectronic properties. We have analyzed the UV-Vis-NIR absorption and UV-visible-NIR PL emission from arbitrary shaped Si NCs decorated on the Si NWs before and after coating of ZnO thin film on it. The red shift and reduced intensity of the visible PL from the Si NC/ZnO HSs are explained on the basis of Forster resonant energy transfer from ZnO layer to Si NCs. This work is important for efficient solar energy harvesting across the entire spectrum of visible-NIR wavelengths based on the concept of hybrid core shell HS and it also sheds light on the development of Si-based light emitting devices using HS of oxide semiconductors, such as ZnO.

Chapter 8 presents the results of fabrication, properties and applications of metal NP decorated Si NWs. Since HSs provide additional structural complexity and functionality, the properties of Si NWs have been tuned by incorporating suitable external materials according to the requirements. The PL spectra of the Si NWs become broad and extended over the entire visible region after Ag NPs decoration. The photocatalytic efficiency of the Si NWs are enhanced with the decoration of noble metal (Ag, Au, Au-Pd) NPs on the Si NWs. Next, the metal NPs decorated Si NWs exhibited high surface enhanced Raman scattering (SERS) activity and enhanced PL intensity for the detection of ultralow concentration of methylene blue. The overall absorbance of the HS system is enhanced after Ag NPs decoration, which strongly influenced the PL and the photocatalytic performance of the Si NW HSs. This opens up the possibility of efficient use of metal NPs decorated Si NW HSs for energy and environmental applications.

Chapter 9 presents the summary and highlights of the contributions of the present thesis. In addition, open questions and future directions of research in the related area are presented at the end.

LIST OF PUBLICATIONS:

A. In Peer-Reviewed Journals:

1. Ramesh Ghosh, P. K. Giri, Kenji Imakita and Minoru Fujii, "Origin of Visible and Near Infrared Photoluminescence from Chemically Etched Si Nanowires Decorated with Arbitrary Shaped Si Nanocrystals" ***Nanotechnology***, 25, 045703 (2014)
2. Ramesh Ghosh, P. K. Giri, Kenji Imakita and Minoru Fujii, "Photoluminescence signature of resonant energy transfer in ZnO coated Si nanocrystals decorated on vertical Si nanowires array" ***J. Alloys Compd.***, 638, 419 (2015)
3. Ramesh Ghosh, Arindam Pal and P. K. Giri, "Quantitative analysis of the phonon confinement effect in arbitrarily shaped Si nanocrystals decorated on Si nanowires and its correlation with the photoluminescence spectrum" ***J. Raman Spec.***, 46, 624 (2015).
4. Arindam Pal, Ramesh Ghosh and P. K. Giri, "Early Stages of Growth of Si NWs by Metal Assisted Chemical Etching: A Scaling Study" ***Appl. Phys. Lett.***, 107, 072104 (2015)
5. Ramesh Ghosh, Kenji Imakita, Minoru Fujii and P. K. Giri, "Effect of Ag/Au Bilayer Assisted Etching on the Strongly Enhanced Photoluminescence and Efficient Visible Light Photocatalysis from Si Nanocrystal Decorated Si Nanowires Array" ***Phys. Chem. Chem. Phys.***, 18, 7715 (2016)
6. Ramesh Ghosh and P. K. Giri, "Silicon Nanowire HSs: Growth Strategies, Novel Properties and Emerging Applications" ***Sci. Adv. Today.***, 2, 25230 (2016). *Invited Review Article.*
7. Ramesh Ghosh and P. K. Giri, "Efficient Visible Light Photocatalysis and Tunable Photoluminescence from Orientation Controlled Mesoporous Si Nanowires" ***RSC Adv.***, 6, 35365 (2016).
8. Ramesh Ghosh and P. K. Giri, "Effect of Rapid Thermal Annealing on the Photoluminescence from Si Nanocrystal Decorated Si Nanowires Array Grown by a Metal Assisted Chemical Etching Method" ***Adv. Sci. Lett.***, 22, 71 (2016)
9. Kamal Kr Paul, Ramesh Ghosh and P K Giri, "Mechanism of strong visible light photocatalysis by Ag_2O-nanoparticledecorated monoclinic TiO_2(B) porous nanorods" ***Nanotechnology***, 27, 315703 (2016)

A. Manuscripts Under Review:

1. Ramesh Ghosh and P. K. Giri, "Silicon Nanowire Heterostructures for Advanced Energy and Environmental Applications: A Review" ***Nanotechnology***, *Invited Review Article* (Under Review).

C. Conference Papers Presented:

1. Ramesh Ghosh and P. K. Giri, *'Optimized Growth of Dense Array of Silicon Nanowires at Room Temperature By Chemical Etching and its Characterization*', 4th International Conference on Advanced Nano Materials (**ANM 2012**), *IIT Madras, 17-19 October, 2012*
2. Ramesh Ghosh and P. K. Giri, *'Understanding the Dual Role of Silver in the Fabrication of Silicon Nanowire Arrays by Metal Assisted Chemical Etching Process and its Characterizations*',

6th India Singapore Joint Physics Symposium on Physics and Advanced Materials (**ISJPS 2013)**, *IIT Kharagpur, 25-27 February, 2013*

3. Ramesh Ghosh and P. K. Giri, *'Size dependent visible photoluminescence from chemically etched Si nanowires decorated with arbitrary shaped Si nanocrystals*', International Conference on Nanoscience and Technology (**ICONSAT 2014)**, *INST Chandigarh, 2-5 March, 2014*

4. Ramesh Ghosh and P. K. Giri, *''Photoluminescence Modification by Resonant Energy Transfer in ZnO Coated Si Nanocrystals Decorated on Vertical Si Nanowires Array*', Condensed Matter Days (**CMDAYS 2014)**, *CU Kolkata, 25-27th August, 2014*

5. Ramesh Ghosh and P. K. Giri, *'Effect of Rapid Thermal Annealing and Laser Heating on the Photoluminescence Properties of Si Nanocrystal Decorated Si Nanowires Grown by Metal Assisted Chemical Etching Method*', Emerging Materials : Characterization and Applications (**EMCA 2014)**, *CGCRI Kolkata, 4-6th December, 2014*

6. Ramesh Ghosh, Arindam Pal and P. K. Giri, *'Raman Study of Laser Induced Heating Effects in Si Nanocrystals Decorated on Vertical Si Nanowire Array*', International Conference on Nanotechnology (**ICNT 2015)**, *HIT Haldia, 19-22nd February, 2015*

7. Ramesh Ghosh and P. K. Giri, *'Photocatalytic Nature of Si Nanowires Grown by Metal Assisted Chemical Etching Method*', 6th International Conference on Advanced Nano Materials **(ANM 2015)**, *Aveiro, Portugal, 20-22 July, 2015*

8. Ramesh Ghosh and P. K. Giri, *'Electron Microscopy and Spectroscopic Studies of Arbitrary Shaped Si Nanocrystals Decorated on Vertical Si Nanowires Array*, Microscopy Conference (**MC 2015)**, *Göttingen, Germany, 6-11 September, 2015*

9. Ramesh Ghosh and P. K. Giri, *'Electron Microscopy and Spectroscopic Studies of Arbitrary Shaped Si Nanocrystals Decorated on Vertical Si Nanowires Array*" National Workshop on Advanced Probing techniques in TEM (**APTTEM-2016**), Guwahati, India, Feb 15-16, 2016. ***(Best Poster Award)*.**

D. Workshops Attended:

1. Indo-US Workshop on *'Frontiers of Excellence in Photovoltaic Science and Technologies', IIT Bombay, 15-17 January ,2012*
2. *INUP Familiarization Workshop on 'Nanofabrication Technologies', IIT Guwahati, 28-29 September, 2012*
3. *INUP Hands – on Training on Nanofabrication Technologies, IISc Bangalore, 18-28 June, 2013*
4. *National Workshop on "MEMS/NEMS and Theranostic Devices" (NWNTD), IIT Guwahati, 16-17 March, 2015*
5. *National Workshop on "Advanced Probing Techniques", IIT Guwahati, 15-16 February, 2016*
6. *2nd National Workshop on "MEMS/NEMS and Theranostic Devices" (NWNTD), IIT Guwahati, 21-22 March, 2016*

LIST OF ABBREVIATIONS

Abbreviation	*Description*
1D	One dimensional
DRS	Diffuse Reflectance Spectroscopy
EDX	Energy Dispersive X-ray Analysis
ESR	Electron Spin Resonance
FESEM	Field Emission Scanning Electron Microscopy
FTIR	Fourier Transform Infrared Spectroscopy
HRTEM	High Resolution Transmission Electron Microscopy
NBOHC	Nonbridging Oxygen Hole Center
NC	Nanocrystal
NIR	Near Infrared
NP	Nanoparticle
NR	Nanorod
NS	Nanostructures
NT	Nanotube
NW	Nanowire
O_v	Oxygen vacancy
O_i	Oxygen interstitial
PL	Photoluminescence
QC	Quantum Confinement
SAED	Selected Area Electron Diffraction
SERS	Surface Enhanced Raman Scattering
TEM	Transmission Electron Microscopy
TRPL	Time Resolved Photoluminescence
UV-visible-NIR	Ultraviolet visible Near Infrared
XPS	X-ray Photoelectron Spectroscopy
XRD	X-ray Diffraction

Chapter 1

Introduction

The enormous development in nanoscience and nanotechnology has been made possible with the development of new nanomaterials with extraordinary properties, which are entirely different from the bulk counterpart. Nanostructured materials are modulated over nanometer range at different dimensions and can be categorized into 0D, 1D, 2D and 3D structures. From 0D to 3D structures, a variety of nanomaterials including metals, both inorganic and organic semiconductors have been extensively studied and making pathways into the industry and everyday life. The interest in nanostructures stems from the fact that at the nanoscale dimension, the properties of the materials change and start to exhibit size and shape dependent features. From the scientific point of view, high aspect ratio and quantum confinement (QC) effect are the two unique features of nanostructured materials that modify the characteristic properties, which include structural chemical, electrical, optical and magnetic properties. By incorporating additional complexities and functionalities through the heterostructure (HS) approach, scientists are able to modify/improve the selective properties of a single nanomaterial according to the requirements. These unique and enhanced properties of the nanostructures and nano-HSs open up huge opportunities for a variety of applications in technological and industrial field, such as photovoltaics, artificial photosynthesis, sensors, environmental cleaning, and micro to nanoelectronic circuit and devices etc. From the technological point of view, a detailed understanding of the effective synthesis strategies of the nanostructures and their HSs how its properties depend on size, shape, surface and interface morphology and structure is of fundamental interest. In this chapter, we briefly present various techniques for the growth of high quality Si nanowires (NWs) and the fundamental issues related to growth mechanism, understanding of defects formation and the useful photophysical properties of the Si NWs. Fabrication methodologies of various types of Si NW based HSs and their recent advancements in energy and environmental applications such as LEDs, lasers, solar energy conversion devices, Li-ion batteries, photochemical reactors and sensors has been discussed briefly along with addressing the problems and challenges in the field. The motivation and the focus of the present thesis with its major contributions are described at the end of the chapter.

1.1. Si Nanostructures

Over the past decades, significant amounts of research have been devoted to the semiconductor nanostructures for their fascinating and exciting properties and several daily life applications of these nanostructures. Si, Ge, ZnO, TiO_2, GaAs, CdS, CdSe, GaN etc. are the most studied semiconductors in nanoscale dimensions and have been extensively explored as potential building blocks for nanoscale electronics, optoelectronics, chemical/bio/optical sensors/detectors, energy harvesting/conversion and environmental purification owing to their size related interesting physical properties. Among the important class of semiconductors, Si is currently the most dominant functional material for commercial electronic applications due to the following benefits: (1) the most abundant semiconductor on Earth; (2) high stability and non-toxic nature; (3) high carrier mobility; (4) well-established fabrication technique; and (5) flexibility to create HSs with other nanostructured materials. Si has a face-centered diamond cubic structure with lattice constant 5.431 Å and belongs to the space group of Fd3m. The well-established and the cubic structure of crystalline Si has a lot of advantages to understand the crystal structure of nanostructured Si. In case of nanostructured Si, with the size reduction, the aspect ratio leads to a larger contact area, decrease of surface free energy and hence a number of physical properties become noticeably pronounced in comparison with those of macroscopic systems. The high surface area brought about by the decreased size is beneficial to many Si nanoscale-based devices, as it facilitates the reaction/interaction between the devices and the interacting media, which mainly occurs on the surface or at the interface. The properties also vary with shapes and crystal structures of the Si nanomaterials and play important roles for the device performances. For example, bulk Si does not emit light upon excitations, but nanostructured Si can emit visible-NIR light depending upon the shape, size and presence of defects in the crystal structures. Thus, low-dimensional Si nanostructures such as, Si nanoparticles (NPs), NWs, nonorods (NRs), nanotips (NTs) have been extensively studied as nanoscale building blocks for high-performance electronic and photonic devices in the light of their attractive properties that are different from those of bulk Si.

1.2. Si Nanowires

During the past decades, 1D Si nanostructures, including NWs, NRs, nanotubes, nanofibers (NFs) and nanobelts, have been attracting a great deal of attention in both basic scientific research and potential technological applications due to their fascinating physical and chemical

characteristics.[1-11] Despite indirect bandgap nature of bulk Si, 1D Si nanostructures show the quasi-direct nature and show visible-NIR emission due to quantum confinement effect. The

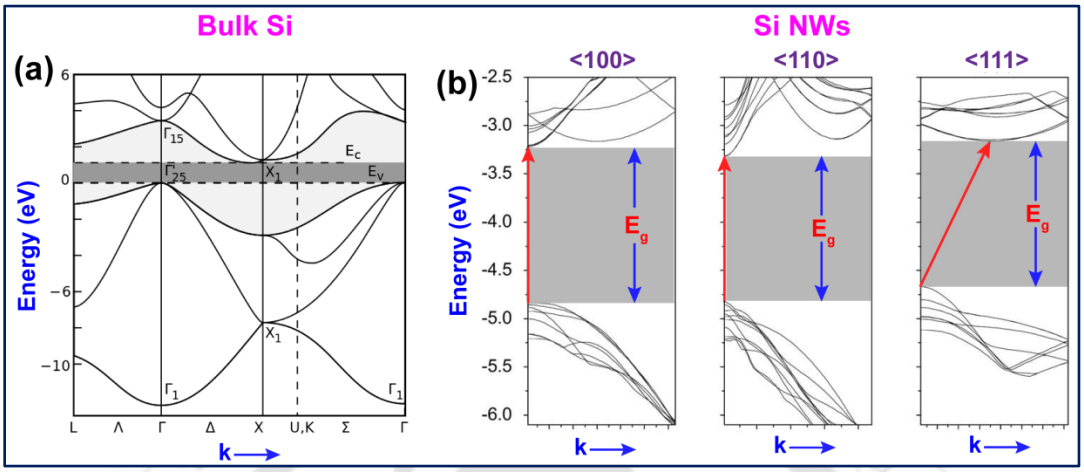

Fig. 1.1. (a) Band structure for bulk Si. Adopted from Ref. [12] (b) The band structures of the <100>, <110>, and <111> oriented Si NWs. The band structure is calculated using the primitive repeating unit for each Si NW. The mean diameters of these Si NWs are 3.06, 2.77, and 2.98 nm, respectively. The shaded portions indicate the band gap in each case. Adopted from Ref. [13]

energy band diagram of bulk Si is shown in Fig. 1.1(a). Ng et al. have theoretically studied the electronic band structure of Si NWs with different orientation, as shown in Fig. 1.1(b). Confinement effect by means of optical confinement of electrons and phonon is one of the major aspects in 1D Si nanostructures when the size of at least one dimension of the material is confined within the excitonic Bohr radius of Si. The effects of confinement in Si NWs are observed in measurements of scattering, transmission, absorption, emission and surface plasmons in case of electromagnetic interaction. In addition to confinement effect in size, the high aspect ratio of 1D Si nanostructures influences its properties related to surface area. 1D nanostructures have direct path for electron transport which helps in the reduction of electron recombination and hence enhance the carrier collections and fast information processing. The abrupt change in conductivity (ballistic conductance) for 1D pathway has strong effect in transport properties of the Si NWs.

Thus, 1D Si nanostructures, especially Si NWs are extensively studied due to the ease of synthesis, fascinating properties and application in wide range of areas such as, high-performance light emitting diodes (LEDs), cost-efficient and highly efficient solar cell, high-capacity and long life Li-ion battery, artificial photosynthesis, ultrahigh sensitive chemical & bio

sensors, low-cost thermoelectric devices, photodetectors and environmental cleaning by pollutant reduction etc.[1-11, 14, 15]

1.3. Growth of Si Nanowires

Over the past decades, Si NWs have been fabricated by several groups worldwide using various methods, such as chemical vapor deposition (CVD), pulsed laser deposition (PLD), thermal evaporation, template assisted growth, molecular beam epitaxy (MBE), reactive ion etching (RIE), and metal assisted chemical etching (MACE) etc.[10, 16-30] The fabrication methods of the Si NWs have strong effects on the properties of Si NWs from the application point of view. The production of large area, highly oriented array of Si NWs structures with controlled properties is extremely important for device applications and improvement in device performances. Over the past decade, concerted efforts have been devoted on the fabrication of Si NWs according to the requirement for dedicated application.[10, 14-29] The reported methods for the fabrication of Si NWs are classified into two main approaches: bottom-up and top-down. The bottom-up approach,

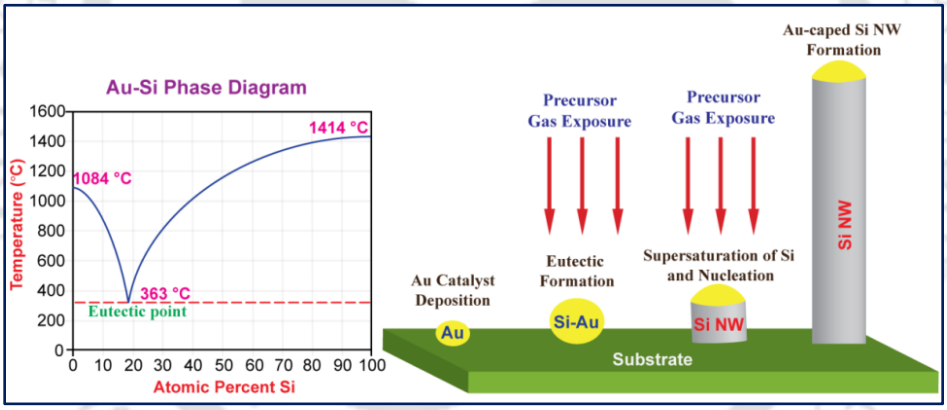

Fig. 1.2. The Au-Si phase diagram and the steps (schematic) of CVD growth of Si NWs using Au catalyst.

which is the oldest method for Si NWs fabrication, is a gathering process constructed by Si atoms in a sequence to form Si NWs. Out of several bottom-up approaches, CVD via vapor-liquid-solid (VLS) process, MBE, PLD and thermal evaporation are commonly used. The top-down approach is the selective reduction of bulk Si wafer by RIE and MACE to form Si NWs. Out of several traditional approaches, CVD and MACE methods are the widely explored and largely usable methods for their versatility about controllability, repeatability, quality, low cost and mass production. Several review articles have been published describing the synthesis of Si NWs.[1, 4-6, 10, 11, 16, 31-37] Among the bottom-up fabrication methods, the CVD approach offers the

concrete capability of fabricating Si NWs with controlled diameter, density, length, position and doping characteristics, for device applications and due to this CVD is extensively used worldwide.[3, 7, 8, 11, 24, 30, 38, 39] Fig. 1.2 shows the Au-Si phase diagram (schematic) and the steps (schematic) of CVD process for the growth of Si NWs using Au catalyst. CVD growth of Si NWs requires a suitable noble metal (Au, Al, Cu, Fe etc.), which serves as catalyst and a gaseous Si precursor such as silane (SiH_4), Si tetrachloride ($SiCl_4$) etc. which are often difficult to handle. The metal catalysts remain unaltered during the NW growth and the presence of metallic contaminations adversely affects the properties of intrinsic Si NWs and eventually it deteriorates the device performances. However, Due to the process compatibility, the CVD grown Si NWs are desirable for complementary metal oxide semiconductors (CMOSs) applications.[5, 7] PLD is another successful method for fabrication of controlled Si NWs. However, the need of high-energy, focused pulse lasers with high cost prevents this method from having wide application.[6, 23, 40, 41] Thermal evaporation technique is a cost effective and easy fabrication technique to produce a large area, high-purity and ultra-long (of the order of mm) Si NWs.[9, 11, 28, 42-46] SiO powder is mainly used as the Si precursor and this process is often referred as oxide assisted growth (OAG). This process often leads to growth of Si NWs with thick SiO_x layer on it. MBE is also a well-established method for growing high quality Si NWs.[18, 22, 47-50] The growth mechanism of Si NWs in MBE process is very similar to a typical CVD process. Since the process requires ultra-high vacuum and slow growth rate as compared to the other bottom up approaches, MBE is undesirable for the growth of high quality long Si NWs. Further, due to the cost issue, MBE is less commonly used worldwide. In contrast to bottom-up approaches, top-down processes are also well known for the fabrication of ordered arrays of Si NWs of controlled size, density, and tunable properties. Among the various top-down approaches, RIE is generally a highly anisotropic process, which is actually the dry etching of Si or SiO_2 by halogen radicals, mainly fluorine-based compound materials for the growth of Si NWs.[10, 16, 19, 20, 51-54] These fluorine radicals from the plasma reach the Si surface and form volatile SiF_x, and therefore impede chemical etching.[20, 52, 53] The anisotropic etch profile, use for high quality mask by expensive lithography, use of toxic and corrosive gases and the need for specialized and expensive equipment prevent RIE to widespread use for the fabrication of Si NWs. Solution based MACE of Si fulfills the drawbacks of RIE and has several advantage over any other

established method for the fabrication of large area, well aligned and rapid production of high quality Si NWs.

1.3.1. Metal Assisted Chemical Etching

The solution based metal assisted chemical etching (MACE) has emerged as a promising and significant tool for the rapid production of large area, aligned and well controlled Si NWs and it has become the most common method for the production of high quality Si NWs.[26, 27, 35, 36, 55-57] The term "metal assisted chemical etching", was first introduced by D. Malinovska et al. in 1997.[58] The idea was to obtain porous Si by etching Al covered Si substrate in a solution containing HF, HNO_3 and DI water. The arrived at the conclusion due to the Al film, there is a dramatic increase in the rate of pore formation on Si wafer. Following this study, Li and Bohn worked on this method in 2000 using various noble metals like Au and Pd instead of Al and examined how these metals reacted with HF, H_2O_2 and ethanol solution.[26] They obtained rather sharper and straight pores within the Si substrate. In 2002, Peng et al. widely investigated the MACE using HF/$AgNO_3$ solution, where Ag coating and Si etching simultaneously took place yielding a NW-like structure.[27] After 2000, MACE became the most powerful tool for the rapid fabrication of large area, vertical, ordered, and single crystalline Si NW arrays due to its ease and low cost of production. The mechanism of one-step MACE process (simultaneous metal deposition and etching of Si) and the two-step MACE (pre-deposited metal on Si wafer) has been explained by different groups, though it is still under doubt.[26, 27, 35, 36, 55-57] The microscopic mechanism for the MACE is mainly based on the noble metal-induced local oxidation and anisotropic dissolution of Si substrates in aqueous oxidizing HF acid solution. The selective etching of Si substrate in preferential direction leads to the growth of vertical and aligned Si NWs. Note that MACE requires a galvanic displacement of noble metal NPs as a catalyst on the surface of the crystalline Si substrate and Ag, Au, Pt, Pd, Cu, Ag/Au and Au/Pd alloy have been demonstrated to be effective catalysts for MACE of Si.[29, 36] Various oxidative agents have been mixed with HF to etch noble metal-loaded Si substrates, including $AgNO_3$, $KAuCl_4$, $HAuCl_4$, H_2PtCl_6, $Fe(NO_3)_3$, H_2O_2, $Na_2S_2O_8$, $KMnO_4$, $K_2Cr_2O_7$ etc.[36] Fig. 1.3(a) shows the etching steps of Ag assisted chemical etching of Si, while Fig. 1.3(b) shows the image of arrays of vertical Si NWs grown by MACE of Si.[59] However, the shape and size, length, diameter, density, crystallinity and the properties of the Si NWs strongly depends the (a) nature of the noble metal, (b) shape and size of the noble metal and the intermediate distance between them, (c) the etching

solution and its concentration, (d) the doping type, resistivity and the orientation of the Si wafer, (e), temperature and (f) etching duration.[26, 27, 29, 35, 36, 56, 59-61] Without the protective layer or masking, MACE is anisotropic and the nanostructures formed in such cases are also highly nonuniform. In the literature, self-assembling polymers and lithography are used for patterning

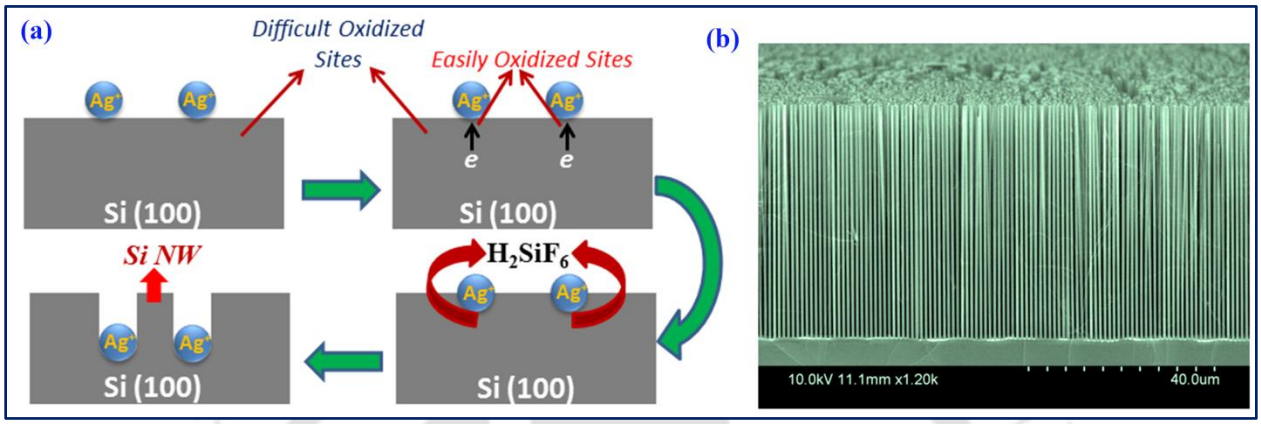

Fig. 1.3. (a) A schematic of the process of Si NW formation by the Ag assisted chemical etching of Si wafer. (b) A cross-sectional FESEM image of an array of vertical Si NWs grown by MACE. Adopted from Ref. [59]

the noble metal on Si wafer to control the diameter of the Si NWs and the spacing between them.[56, 57, 60, 62, 63] Several review articles have been published explaining the controlled synthesis, excellent properties and the device application of MACE grown Si NWs.[1, 5, 10, 32-36, 59] Easy fabrication process, compatibility to create HS with other organic and inorganic material, significant device performances and cost electivity are the major advantage of MACE for the growth of large area, ordered and uniform Si NWs.

1.4. Mesoporous Si Nanowires

Si quantum dots (QDs) and porous Si are well-known for their ability to exhibit excellent photophysical and photochemical properties due to strong QC effects and surface defects. Recent reports on single crystalline porous Si NWs grown by MACE have combined these two features together and form both electrically and optically active Si nanostructures. The MACE grown Si NWs are indeed porous due to the sidewall etching during the NW formation. This could lead to the decoration of arbitrary shaped Si NCs on the surface of the Si NWs due to the pores. The formation mechanism of Si NCs due to the small pores on Si NWs has been discussed by Hochbaum et al.[64] and Yongquan et al.[35] Usually, crystal defects and impurities such as dopants at the Si surface are thought to serve as nucleation sites for the pore formation. As a result, low resistivity wafers show higher porosity.[35] During MACE of Si wafers, metal ions can quickly

react with Si and extract electrons from metal/Si surface and become metallic dendrites. Since the metal ion formation process is continuous, all the ions may not turn into metallic dendrites during vertical etching of Si surface. The extra ions can nucleate near the nucleation sites on the sidewalls of the Si NWs by collecting electrons and etch in the lateral direction of the Si NWs, leading to the formation of Si NCs on Si NW surfaces. The size of the Si NCs are smaller or comparable to the excitonic Bohr diameter of Si (~9.8 nm), which may help to enhance the optoelectronic properties of the Si NWs arrays.[35, 55] From the application point of view, the combined effect of QDs as well as NWs in Si NC decorated Si NWs grown by MACE offer certain advantage over the Si NWs grown by other conventional methods such as, CVD.

1.5. Defects in the Si Nanostructure

The types, concentration and spatial distribution of intrinsic/extrinsic defects in Si have enormous influence on the performance of Si based photonics, electronics, bio-chemical and gas sensing, photochemistry, environmental cleaning etc. In particular, recent studies have revealed that physical and chemical properties of Si, such as light absorption, photocatalytic activity, sensing properties, electrical conductivity etc. can be modulated by the defect/disorder. Therefore detailed understanding of defects has significant importance for the utilization of Si nanostructures into real life applications. Any form of deviation from perfect crystal can be treated as a defect. In a crystal of Si, one often finds point defects (misplaced lattice atoms/ions, vacancies, foreign atoms/ions) and/or extended defects, such as dislocations. The presence of defects will affect the band structure of the materials and as a result, the Si nanostructures can emit different colors of light. Point defects are further classified into native defects and external impurity defects (dopants) which can be found either on the lattice (substitutional site) or at the interstitial positions. Dislocations are the kind of defects that are extra line of atoms inserted or removed in/from the crystal, which does not extend throughout the crystal. In bulk Si, the point defects are located in the volume of the material but in case of Si nanostructure it is dominated by the traps located at the surface/interface, due to high aspect ratio. These traps are formed by the adsorption, dangling bonds, and the internal stresses (induced by misfit). Si has a tendency to form oxide by bonding with oxygen and Si nanostructures are not any exception. Therefore, the understanding of defects present in the Si/SiO_2 interface play a very crucial role in understanding the properties of Si nanostructures embedded in SiO_2 matrix and their improvement strategies. In particular, oxygen vacancy (V_O) and non-bridging oxygen hole center (NBOHC) are two

important kinds of defects that are often encountered in nanostructured Si. The manufacturing process of Si nanostructures can also induce defects or impurities in the interface. For example, the surface of the MACE grown Si NWs are terminated by hydrogen atoms.

1.5.1. Oxygen Vacancy

The basic structural unit of SiO_2 is the SiO_4 regular tetrahedron with four oxygen atoms, located at each apex and a single Si atom is located at the center of the tetrahedron. The schematic of a pure SiO_2 structure is shown in Fig. 1.4(a). The best known V_O defect in SiO_2 is the paramagnetic E´-center. From studies of the hyperfine structure in the electron paramagnetic resonance (EPR) spectrum, it is known that E´-center can include an unpaired electron in a dangling tetrahedral (sp^3) orbital of a single Si atom which is bonded to only three O atoms. This generic E´-center is shown in Fig. 1.4(b), which is often denoted by ≡Si●, where the three parallel lines represent three separate O bonds to one Si atom and the dot denotes the unpaired electron. Another V_O defect center is diamagnetic and it is indicated generally as ≡Si−Si≡. It is

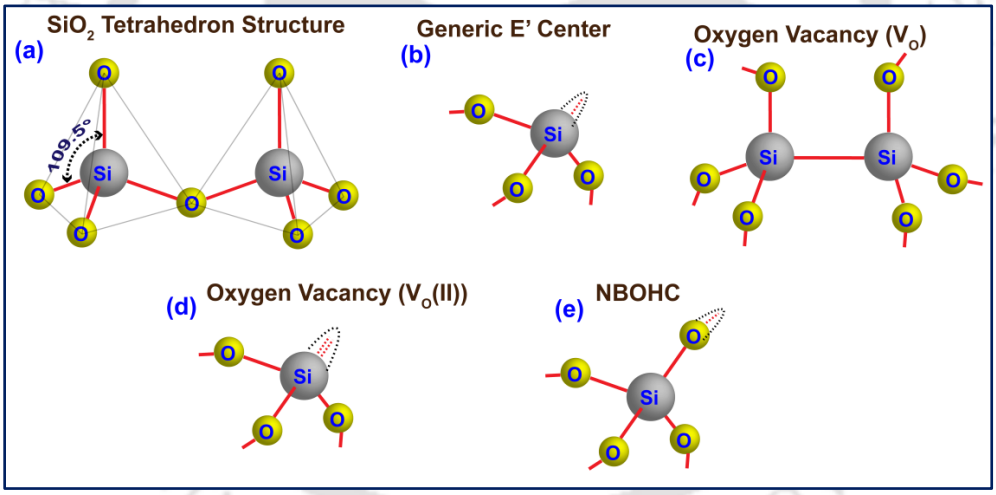

Fig. 1.4. The schematic of (a) pure SiO_2 structure, (b) generic E´ center, (c) neutral V_O, (d) twofold coordinated Si (V_O(II)) and (e) NBOHC defects.

related to neutral oxygen vacancy, which can be directly investigated by PL or cathodoluminescence (CL) spectroscopy. Here, two Si atoms could relax and make a Si-Si bonding as shown in Fig. 1.4(c) The twofold coordinated Si denoted as V_O(II) is also seen in the Si-SiO_2 interface (Fig. 1.4(d)). Here, a single Si atom is bonded to only two O atoms and it is indicated as =Si●●. The V_O defects have strong effect in the optical properties of the nanostructured Si by means of PL and absorption.

1.5.2. Non-bridging Oxygen Hole Center

This defect center can be visualized as the oxygen part of a broken bond as shown in the Fig. 1.4(e) and indicated as ≡Si-O*, where ‘‘*’’ represents an unpaired hole. Out of the earlier discussed defect characteristics, the most unique impression of this center one is the 1.9 eV luminescent bands in the red region of the visible light spectra. There is an asymmetric absorption band at 1.97 eV, FWHM=0.17 eV associated with this NBOHC defect centers. NBOHC defect forms due to the oxygen dangling bonds which are created by the rupturing of the strained Si-O bonds in Si/SiO_2 interface. NBOHC also arises when hydrogen atoms are removed from OH groups present in the Si/SiO_2 structure. Note that the fabrication process of Si nanostructures can induce defects at the interface. In case of MACE of Si, Si atoms beneath the noble metal oxidize by the oxidant and it is dissolved by HF. In this continuous process, Si NWs are formed. However, the formation rate of Si oxide and its dissolution are not same in every case. As a result, MACE grown Si NWs possess different kinds of oxygen related defects specially the NBOHC defects in the Si/SiO_2 interface, which is confirmed by different groups using PL and XPS analysis.

1.5.3. H-terminated Si

The additional foreign atoms attached with Si structure are also a kind of defect. It is well known that hydrogen is present on Si NWs grown by HF based MACE process. It is found that the H-bonding in Si is often associated with the morphology and orientation of the Si. The investigation

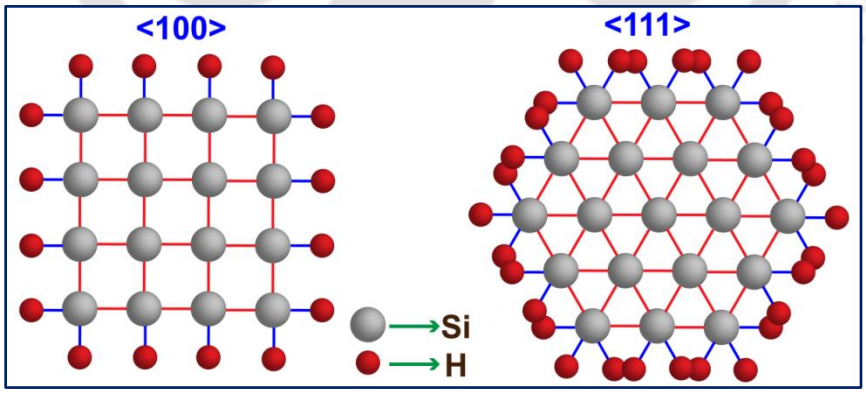

Fig. 1.5. A schematic of the cross sections of the <100> and <111> H-Si NWs. Adopted from Ref. [13]

of the PL, photocatalysis and electrical properties of this H-Si nanostructures show an important role of H-bonds in these processes. Usually, crystalline planes for the direction (100) are covered

with dimer monohydrides (H-Si-Si-H) or dihydrides (SiH_2), for direction (111) are covered with isolated Si-H species. Fig. 1.5 shows the structures of H-Si NWs oriented in <100> and <111> direction. As mentioned before, in case of MACE, the Si NWs are formed by the dissolution of SiO_2 by HF. The presence of excess HF leads to the formation of H-Si NWs. The H-Si NWs can show excellent photocatalytic activity as compared to the bare Si NWs.[15, 65, 66] The terminated hydrogen in Si NWs are electron-deficient and may serve as an electron sink and hence accelerate the separation of photoinduced e-h pairs, which promotes the photocatalytic activity of the Si NWs/NCs.

1.6. Si Nanowire Heterostructures

After the award of Nobel Prize in Physics in 2000 for the discovery of "The double HS: concept and its application in physics, electronics and technology", HSs of different materials are being intensely investigated to exploit the functional properties arising from the junction of different materials.[67] Several reports have been published on Si NW based HSs and both organic/inorganic materials of their different combinations are used as the HS material.[62, 68-120] The Si NW HSs are classified into four different groups: (a) core-shell (radial) HSs, (b) axial HSs, (c) NPs decorated HSs, (d) branched/hierarchical HSs and (e) functionalized HSs.[62, 68-120] Fig. 1.6 shows a schematic diagram of different kinds of Si NWs based HSs. The key parameters of the

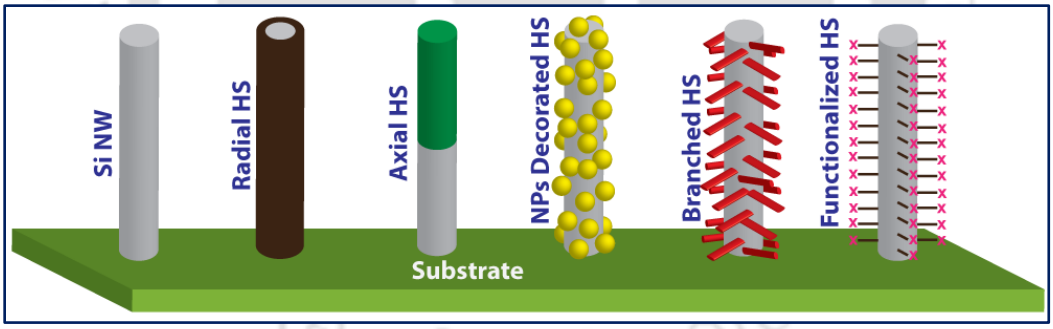

Fig. 1.6. Schematic diagram of different types of heterostructures of Si NWs.

performance index of the bare Si NWs based nano-devices are not up to the level for commercialization. Therefore, together with effective synthesis strategies, significant improvements are required in the design and fabrication of Si NWs to meet future demands for applications in variety of fields. Thus, modification of the surface of the Si NWs by using hybrid structures or HS (HS) approach could enable superior/efficient performance of the nanoscale devices. In particular, much works have been devoted to the fabrication of compound

semiconductor (e.g., group II-VI, III-V etc.) HSs that finds wide spread application in optoelectronics, photonics, sensors. Similarly, the Si NW HSs also find applications in several nanoelectronic and optoelectronic devices, e.g., LED, solar cells, sensor and photochemical reactors etc. These HS devices often show efficient and improved performances in comparison to the bare Si NWs counterpart.

1.7. Fabrication of Si Nanowire Heterostructures

In the past few years, several methodologies have been developed for the fabrication of high quality NW HSs with suitable external materials. In most of the cases, ex-situ processes have been used for the fabrication of the Si NWs HS on preformed Si NWs. Several studies have been devoted for the fabrication of Si NW HSs with inorganic materials, such as SiO_x[23], ZnO[112-115, 121], Al_2O_3[122], TiO_2[110, 116-118], Fe_2O_3[119], SiN_x[123], CdS[106, 124, 125], CdSe[120], SiC[126], ZnS[103], InP[125], Ge[104, 105, 127], etc. and organic materials, such as PDEF[109], P3HT[108], PEDOT:PSS[107, 128], TAPC[107], TMAH[129], different form of carbon[75, 130-136] (graphene, graphite, reduced grapheme oxide (RGO), carbon nanotube (CNT) etc.) etc. Different techniques, such as ALD, CVD, solution synthesis, and sputtering etc. have been used for the synthesis of different forms of Si NWs HSs.[23, 75, 107-110, 112-123, 128-135]

The simplest and the most fundamental form of NW HSs is the coaxial core-shell radial HSs. Core-shell and core-multishell HSs are generally formed by ex-situ deposition of different inorganic/organic semiconductor and metals as an overlayer on the Si NW core. ZnO is one of the widely used semiconductors to form Si NW/ZnO core-shell HS for photodiode, photoresponse, LED and photovoltaic application.[112-114, 121, 137] Sun et al. have fabricated Si NW/ZnO core-shell HS by coating ZnO using MOCVD method.[111] Si NW/TiO_2 radial HS arrays have been prepared by depositing a TiO_2 layer on Si NW arrays by CVD method by H. Liu et al. have fabricated Si NW/Ge core shell HS as a Li-ion battery anode.[127] Multilayer core-shell structures based on Si NW core have also been studied extensively in case of multijunction solar cell, photocatalysts and LEDs.[89, 103, 105, 106, 138] Katiyar et al. have grown Si NW/ZnS/AZO radial HS by PLD of ZnS and Al doped ZnO (AZO) on MACE grown Si NWs.[103]

Based on Si NWs, both straight and kinked axial HS with different materials have been studied. Si/Ge axial HS have been grown by different groups.[71-74, 139, 140] In most cases Si/Ge axial HS are formed by VLS method using noble metal catalyst. GaP-Si, GaP-Si-GaP and GaP-Si-GaP-GaAs-GaP-Si (hybrid Si/GaAs) nanowires have been grown via VLS mechanism.[70] Kim

et al. fabricated wafer-scale Si NWs/graphene HS for molecular sensing. Single layer graphene has been fabricated by CVD and then transferred on vertically aligned and high-density Si NWs grown by MACE.[75]

Several 3D branched Si NWs based HSs systems have been studied including oxide semiconductors, such as Si/ZnO[89, 97-99, 141], Si/TiO_2[88, 91-93], Si/SiO_2[96]; IV-IV semiconductors such as Si/Ge[94]; III-V semiconductors, such as Si/InP[94], Si/GaN[95] Si/GaAs[94], Si/GaP[94], Si/InGaN[90]; II-VI semiconductors, such as Si/CdS[94], metals like Si/Au[142], metallic silicide and alloys such as, Si/Au[94], Si/Co[143] etc. In most of the cases, sequential catalyst-assisted growth technique is used for the fabrication of branched HSs. The process contains three steps: standard Si NWs growth as the backbone, followed by the deposition of metal catalyst onto the NWs, and finally VLS or SLS growth of the branched NWs onto the Si NWs backbones.

Different metal NPs decorated Si NWs HS systems have been reported due to their SPR modified optoelectronic properties, excellent photocatalytic activity under visible light illumination and outstanding SERS detection. In most of the cases, the metal NPs were loaded on Si NWs surface by electroless deposition technique using chemical solution. A variety of metal NPs such as Ag, Au, Pt, Pd, Cu, Co have been decorated on Si NWs by dipping the Si NWs into a solution containing HF and $AgNO_3$, $HAuCl_4$, H_2PtCl_6, $PdAc_2$, $Cu(NO_3)_2$, $Co(NO_3)_2$, respectively.[81] A mixture of HF and $AgNO_3$, $AuCl_3$, $PtCl_2$, $PdCl_2$, $RhCl_3$, $CuCl_2$ have been used to decorate Ag[15], Au[15, 86], Pt[15], Pd[15, 86], Rh[15], Cu[65] NPs on Si NWs for the photocatalytic application. Thermal evaporation techniques also used to decorate the metal NPs on the Si NWs.[84] However, bimetal NPs such as Au-Pd, Pd-Ni decorated Si NWs system showed superior properties than the single metal NPs decoration.

The functionalized Si NWs can be treated as a HS and has huge impact in Si NWs based sensors, photocatalysis and photovoltaic devices.[15, 65, 66, 144] The surface modification and functionalization has been done mainly by chemical process. Yuan et al. has tuned the electrical properties of Si NWs by creating H-terminated Si NWs.[145] H-Si NWs has been prepared by dipping the Si NWs into HF solution and these H-Si NWs show excellent photocatalytic activity as compared to the bare Si NWs.[15, 65, 66, 144]

1.8. Application of Si Nanowire & its Heterostructures

Due to the unique structural, electrical, optical, and thermal properties, Si NWs have attracted enormous interest as a promising nanoscale material for advanced energy and

environment applications. Si NW HSs provide additional structural complexity and functionality and by choosing suitable external materials for the HSs, one can modify the functionality of Si NWs according to the requirements in various applications. Based on the improved optoelectronic properties of the Si NW HS, possibilities for the efficient applications of Si NW HS based devices are being investigated extensively and various model devices have been fabricated to investigate the superiority of the Si NWs as well as its HSs over the bare Si and other semiconductor based devices. Some of these are discussed below:

1.8.1. Light Emitting Diode

Bulk Si has an indirect band gap, which is an inherent obstacle for potential applications to light-emitting devices. On the other hand, Si NWs can emit light at room temperature with tunable wavelength depending on size, doping and surface conditions.[146-154] Various mechanisms, including QC effect and surface state or defects have been proposed for the light emission and the debate still continues.[146-154] It may be noted that aligned Si NWs exhibit excellent antireflection properties over a broad range of wavelength, which implies higher absorption and excitation of carriers, finally leading to enhanced radiative recombination in the form of

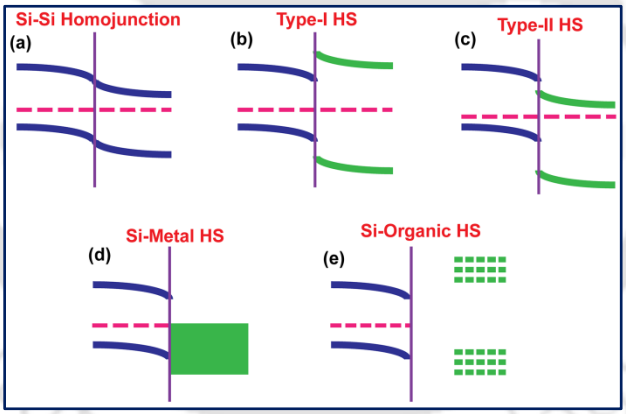

Fig. 1.7. (a-e) The band alignment of Si NW HSs at the interface depending upon nature of the HS materials.

enhanced PL.[138] The light emitting properties of the Si NWs can be enhanced with tunable color by creating HS with suitable material with appropriate arrangement.[103, 155-158] However, most studies to date have dealt mainly with fundamental understanding of light emission of Si NWs and its HSs, rather than to real-world applications for light emitting devices. The MACE grown Si NWs are usually decorated with arbitrary shaped quantum sized Si NCs and covered by a native oxide layer. As a result, the Si NWs show broad visible-NIR PL due to the QC effect in Si

NCs and the presence of the surface states and defects i.e. non-bridging oxygen hole center (NBOHC) and oxygen vacancy (V_O).[148, 151, 153, 154] Phonon assisted radiative recombination has also been proposed as a powerful mechanism of NIR PL in core-shell Si/SiO_x HS.[149, 150] In recent years, Si NW based hybrid LEDs promise improvement in the PL and electroluminescence (EL), compared to the bare Si NW LED and even for other hybrid LED.[103, 155-158] The band alignment of Si NWs HSs can be modified at the interface depending upon nature of the HS materials (as shown in Fig. 1.7). A variety of materials including semiconductors, metals and dielectrics have been tested for the enhancement and tuning of PL and EL properties of Si NWs and other kind of Si nanostructures.[103, 111, 118, 155-157, 159] PL and EL properties of Si NW/ZnO HSs have been studied extensively in the last decade.[111, 155-157, 159] In most of the cases, n-type ZnO is deposited on p-type Si NWs/NRs to form core-shell structure or NCs decorated p-n junction hybrid LED.

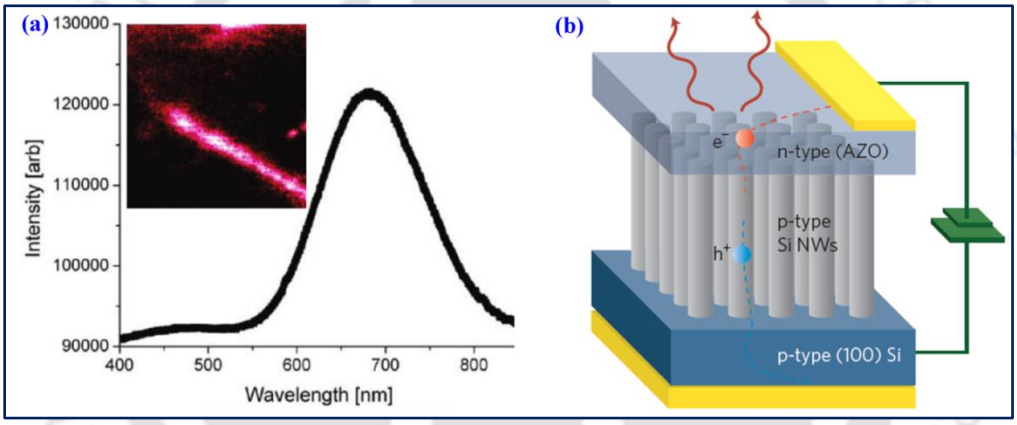

Fig. 1.8. (a) PL spectrum of MACE grown Si NWs. Inset: confocal PL image from a single mesoporous Si NW on a TEM grid. Adopted from Ref. [64] (b) A schematic of an LED device using p-type Si NWs with a transparent n-type Al-doped ZnO (AZO) top electrode. Adopted from Ref. [160]

The increased surface area resulting from the enhanced structural aspect ratio and the antireflective characteristics inherent to the NWs structure were believed to be responsible for the orders of magnitude enhancement in emission intensity in most of the cases.[157]

Solid-state white light sources are in great demand for future day-to-day lighting applications. Si NWs based broadband white LEDs have been successfully demonstrated.[103, 111, 155, 158] Si/ZnO HS NWs have been demonstrated as a potential light source for future solid-state white LED devices.[155, 159] Sun et al. have grown Si NW/ZnO core-shell and ZnO QDs coated Si NWs by CVD and showed that in presence of ZnO the PL spectra of the HS covered the entire visible region (400-800 nm), which is important for the fabrication of white light LED.[111] Fig.

1.8(a) shows the PL spectrum of MACE grown Si NWs with the confocal PL image from a single mesoporous Si NW on a TEM grid as an inset.[64] Schematic of an LED device using p-type MACE grown Si NWs with a transparent n-type Al-doped ZnO (AZO) top electrode is shown in Fig. 1.8(b).[160] The PL and EL properties of other systems such as Si NW/TiO_2[118], Si NW/ZnS[103], Si NWs/CNT[136] etc. were also studied. In recent years, researchers have paid considerable attention in fabricating Si NWs based LED HSs with different plasmonic materials, group IV, II-VI and III-V semiconductors, organic semiconductors etc.

1.8.2. Solar Cell

With the exhaustion of limited fossil fuel, ever rising demands of energy have encouraged scientists to develop cost effective and environment friendly renewable energy sources. Solar cells, which directly convert solar energy into electricity, offer most acceptable and stable solution to the challenge of meeting the growing global energy demand. Among current solar cell technologies, Si NW based solar cells are the most popular, dominating the market over 80% due to its high efficiency, long-term stability, abundant material resources, and well-established fabrication techniques. To meet the key issues related to the Si NW based photovoltaics i.e. photon absorption, exciton transport, exciton dissociation/charge separation, and charge collection, Si NWs with surface modification and HS formation have dwawn considerable attention of the researchers. Fig. 1.9(a) shows the photograph of a commercial c-Si solar cell (left), a planar polished Si wafer (middle) and a wafer-scale Si NW array prepared by MACE (right).[34] Table 1.1 summarizes the recent progress in the performance of the Si NWs based solar cells describing the efficiency of the respective solar cells. Due to the superior photovoltaic properties of MACE grown Si NWs over the NWs grown by any other conventional method[161], researchers have focused their attention extensively in choosing appropriate material to form HS with MACE grown Si NWs in order to improve the photovoltaic properties. However, there are three types of Si NWs HS solar cells: (a) p-n homojunction[100-102, 162, 163], (b) Schottky junction[78, 130, 131, 164] and (c) p-n heterojunctions[62, 107-109, 123, 138, 141, 165, 166].

The photovoltaic properties of the Si NW based radial and axial p-n homojunction were studied by different groups to overcome the drawbacks of Si bulk or thin film based solar cells. Among several growth strategies, MACE grown bare Si NWs show the highest power conversion efficiency (PCE = 9.3%) due to the ultra-low reflectivity over the entire range of wavelength because of the multiple reflections on the inner surface of the vertical Si NWs array

and a broad range of size distribution of the Si NCs on the surface.[162] The importance of good electrical contact, formation of surface and interface by crating functionalities to reduce the

Table 1.1: *Summary of the reported Si NW HSs based solar cells including the HS components, fill factor (FF) and the photo conversion efficiency (PCE) of the respective solar cells arranged in the order of ascending PCE.*

NW HS Components	Si NW Growth Process	FF (%)	PCE (%)	References
n-Si NW/p-Si	RIE	60.7	5.3	[102]
Si NW/Si	CVD	65.4	7.9	[100]
Si NW/graphene	MACE	66.0	7.7	[131]
Si NW/Pt NPs		61.0	8.1	[78]
Si NW/Carbon Q-dot		59.3	9.1	[62]
Si NW/P3HT		54.0	9.2	[108]
Si NW/Si		65.1	9.3	[162]
Si NW/P3HT/graphene		55.2	10.3	[130]
Si NW/ZnO NRs		67.7	10.5	[141]
Si NW/Carbon/Pt		55.5	10.9	[164]
Si NW/PEDOT:PSS		64.2	11.6	[107]
Si NW/Alq3/PEDOT:PSS		68.2	11.9	[167]
a-Si:H/a-Si:H/c-Si NW/a-Si:H/a-Si:H		81.0	12.4	[168]
Si NW/OXD-7/PEDOT:PSS		69.9	12.9	[167]
Si NW/TAPC/PEDOT:PSS		67.1	13.1	[107]
Si NWs/CNT		76.0	15.1	[169]
Si NW/SiN_x		79.2	17.8	[123]
Si NW/Al_2O_3/TiO_2/FGA		79.9	18.5	[138]
Si NW/Al_2O_3		78.7	22.1	[122]

carrier recombination for improving the performance of Si NW-based solar cell was eventually realized. By using a-SiN:H for passivating Si NWs surface, Kim et al. have shown that PCE of the solar cell improved significantly from 7.2% to 11.0% due to the increased light absorption and improved charge-carrier collections.[170] Surface/interface recombination and high series resistance are the issues for the low efficiencies. Very recently, Lin et al. have demonstrated high performance Si NW-based solar cell through surface passivation by using the SiO_2 and SiN_x and the PCE was 17.75%.[123] Feng et al. combined ZnO NRs branches with Si NWs for the

enchantment of the solar cells performance.[141] FF increases from 56.3% to 67.7% and the efficiency improves from 9.2% to 10.8%, respectively. The efficient carriers' collection and enhanced photon absorption caused by ZnO NRs are mainly responsible for the same.[141] Al_2O_3 is commonly used to suppress the Auger and surface recombination significantly via the field effect passivation. More recently, Wang et al. fabricated solar cells composed of Si NWs arrays and an

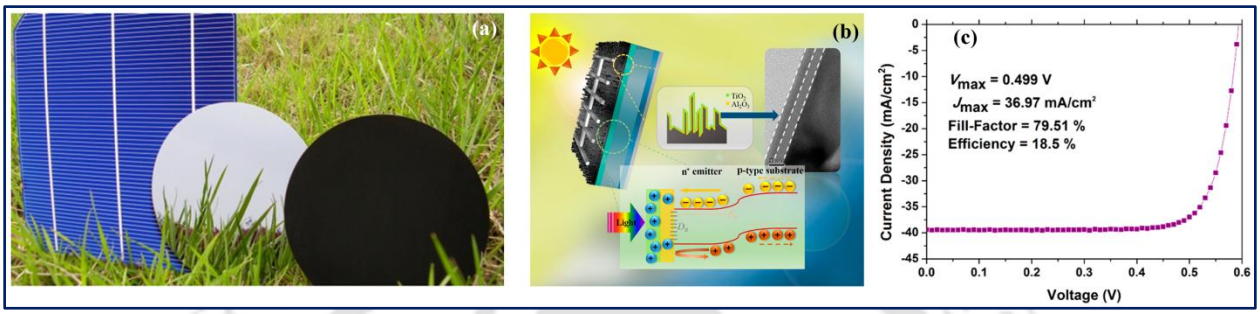

Fig. 1.9. (a) The photograph of a commercial c-Si solar panel (left), a planar polished Si wafer (middle) and a wafer-scale Si NW array prepared by MACE (right). Adopted from Ref. [34] (b) The schematic diagram of a Si NW/Al_2O_3/TiO_2 HS solar cell with the n^+-emitter/p-base structure, along with the band diagram. (c) Illuminated I−V characteristics of the respective solar cell. Adopted from Ref. [138]

Al_2O_3/TiO_2 dual-layer passivation stack on the n^+ emitter.[138] The Si NW/Al_2O_3/TiO_2 HS solar cell showed 11% increased short-circuit current density and 18.5% efficiency after performing forming gas annealing (FGA).[138] Fig. 1.9(b) shows the schematic diagram of the Si NW/Al_2O_3/TiO_2 HS solar cell with the n^+-emitter/p-base structure, along with a band diagram. The Al_2O_3/TiO_2 dual-layer passivation stack causes enormous decrease in the total reflectance, with the reflectance ranging from 1.5 to 2.5% between 400 and 700 nm. This enhanced reduction in the total reflectance could be attributed to the refractive index gradient caused by the insertion of a low refractive index layer between Si NWs and air. The illuminated I−V curve of the solar cell is shown in Fig. 1.9(c) mentioning the J_{SC}, V_{OC}, and PCE. The enhanced efficiency (18.5%) can be attributed to the increased J_{SC}, which is caused by the decreased surface recombination rate, and the increased light absorption, which is due to the reduced total reflectance.[138] The decreased surface recombination rate and total reflectance of the cells with surface passivation layer are responsible for the increases in EQE.[138] H. Savin et al. fabricated greater than 22% efficient solar cell by conformal ALD coated Al_2O_3 on Si NWs with a surface area of 9.0 cm^2.[122]

Recently, immense effort has been made for realizing efficient Si NWs-based organic HS solar cells to reduce cost by adopting low-temperature, scalable, and soluble processing of conjugated polymers, such as P3HT, poly(3,4-ethylene dioxythiophene):poly-(styrenesulfonate)

(PEDOT:PSS), 1,1-bis[(di-4-tolylamino) phenyl]cyclohexane (TAPC), p-poly(9,9-diethylfluorene) (PDEF), Tris(8-hydroxyquinolinato) Aluminium (Alq3) and 1,3-bis(2-(4-tert-butylphenyl)-1,3,4-oxadiazol-5-yl) benzene (OXD-7) etc.[107-109, 166] However, the maximum PCE obtained till date are 5.9%, 9.2%, 9.7% using PDEF[109], P3HT[108], PEDOT:PSS[166] as the conjugated polymer, respectively. Though the PCEs are not high enough, it could be improved by surface passivation, nature and size of the top and bottom contact and the dimension of the Si NWs. Photovoltaic properties of Si NWs in low cost liquid-state junction photoelectrochemical (PEC) solar cell have also emerged but the efficiency till date is not considerable for practical application.[78, 88, 164]

1.8.3. Artificial Photosynthesis

The direct conversion of sunlight into energy stored in chemical bonds is termed as artificial photosynthesis. Solar energy to chemical fuel is referred as artificial photosynthesis which mimics the natural photosynthesis in plant. Typically solar light driven water splitting to produce H_2 and O_2 and reduction of CO_2 for the production of hydrocarbon and other carbon based organic fuels are involved in this process. Unlike photovoltaics, which aim to maximize power output, producing fuels from sunlight in PEC cell requires a minimum voltage output that is imposed by the chemical reaction involved. Additionally, electrochemical overpotential need to be overcome to facilitate a high reaction rate.[171] Under the "Z-scheme" approach, NWs array electrodes can provide a reduced overpotential for solar to fuel conversion. It also provides the necessary photocurrent flux for practical applications, while maintaining a desirable voltage output.[172] TiO_2 is the most used electrode in PEC cell for artificial photosynthesis. Bare Si NWs[66] and its HSs with different semiconductors such as TiO_2[88, 92, 110], ZnO[99], InGaN[90], Fe_2O_3[119], SnO_2/Fe_2O_3[173], MoS_2[174], TiO_2/MoS_2[174], $TiO_2/ZnIn_2S_4$[175], Pt[176] have shown efficient PEC water splitting for the production of clean H_2 fuel on a large-scale via splitting water into O_2 and H_2 under sunlight. P-type Si NWs were used as the photocathode, n-type TiO_2 nanotube films were used as the photoanode and saturated aqueous $NaHCO_3$ solution was used as electrolyte in a PEC cell for the reduction of CO_2.[177] C3-C4 hydrocarbons, methane, ethylene, CO, O_2 and H_2 were formed. Si-H NWs photocathodes and Mn-based carbonyl bipyridyl complexes as homogeneous molecular catalyst were used for the reduction of CO_2 to CO in hydroorganic medium.[178] Liu et al. have used Si NWs for the CO_2 photofixation with ketone-based substrates.[179] The reactions in the PEC cell produce organic targets that can be readily used

to synthesize NSAIDs (nicotinamide adenine dinucleotide phosphate), such as ibuprofen and naproxen and ATP (adenosine-5'-tiphosphate).[179] Although a lot of research is going on worldwide for PEC process, effort should focus on the Si NW HSs based effective

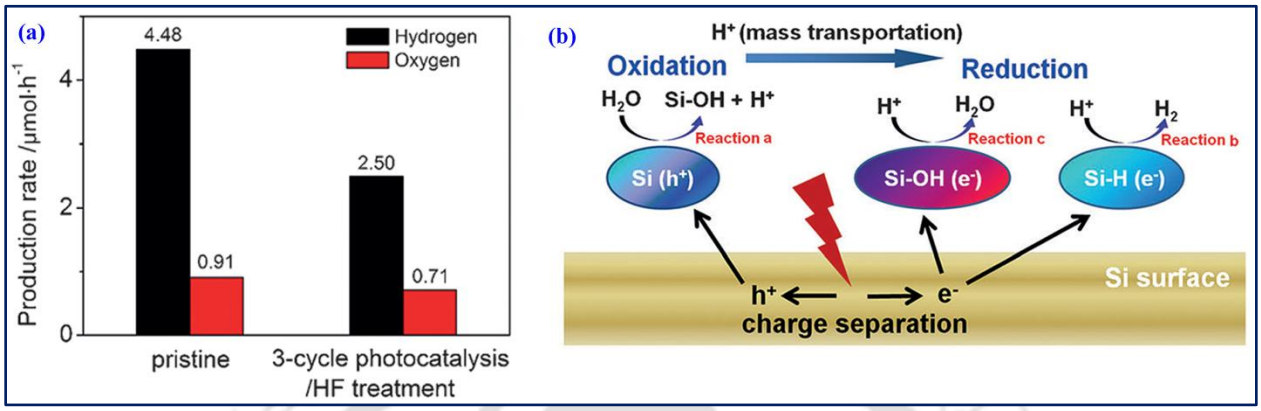

Fig. 1.10. (a) Photocatalytic H_2 and O_2 production rate from pure water under full-spectrum irradiation for 4 h, using the H-Si NWs and after three-cycle photocatalysis (HF treated). (b) A schematic of the overall reaction mechanisms those are mainly responsible for photocatalytic H_2 production on Si surface. Adopted from Ref. [66]

photoelectrodes that offer enhanced photocurrent and photoresponse, reduced turn-on potential, increased solar to fuel conversion efficiency, improved stability, and most importantly property tunability.

Since the PEC process requires a conducting substrate and bias voltage, direct photocatalysis is a simpler and less expensive approach for H_2 production, fuel generation and environmental cleaning, despite its lower efficiency of charge separation as compared to the PEC process. So, Si NW based HSs are attracting much attention in direct photocatalytic application as compared to the PEC. Liu et al. have produced H_2 and O_2 through simple pure water-splitting by Si NWs grown by MACE under light illumination.[66] Fig. 1.10(a) shows the photocatalytic H_2 and O_2 production rate from pure water under full-spectrum irradiation for 4 h, using the H-Si NWs and after three-cycle photocatalysis (HF treated). Instead, the production of H_2 occurs through the cleavage of Si-H bonds and the formation of Si-OH bonds and the overall reaction mechanism is shown in Fig. 1.1(b). From the apparent quantum efficiency (AQE) measurements, solar to chemical conversion efficiency of Si NWs was found comparable to those of many other visible light photocatalysts.[66]

1.8.4. Thermoelectrics

Approximately 90% of the world's power is generated from the thermal plant that uses fossil fuel combustion as a heat source. The power conversion efficiency is typically 30-40% and the rest of

the 60-70% thermal energy is lost to the environment.[180] Immense efforts have been devoted to recover waste heat generated from various heating systems to useful energy source by the thermoelectric modules. However, widespread use of thermoelectricity as an alternative energy source has been hindered by the low figure of merit ($ZT = S^2\sigma/\kappa$) of materials due to the correlation between the thermal conductivity (κ), Seebeck coefficient (S=dV/dT) and electrical conductivity (σ). MACE grown Si NWs are currently attracting great interest as a promising alternative to commercial thermoelectric materials such as bulk Bi_2Te_3 due to the increased ZT because of the value of κ of the rough Si NWs is significantly reduced by enhanced phonon scattering at NWs interfaces without affecting the σ.[180] Hochbaum et al. have found that the MACE grown Si NWs were much rougher than those grown by VLS method, which resulted in 5-8 fold reduction in κ and enhanced ZT was observed for MACE grown Si NWs. Interestingly, the value of ZT of the Si NWs (~0.6) was two orders of magnitude higher than that of bulk Si due to the significantly reduced κ.[180] For improving ZT, alternate attempts were taken to increase the value of σ by functionalization of Si NWs surfaces chemically, without altering the value of κ. Li et al. used NH_3 for the modulation of σ and shown that the value of σ greatly increased after NH_3 adsorption on the surface of the Si NWs.[181] The enhancement of the electrical conduction was interpreted in terms of electron trap filling of the native oxide via NH_3 adsorption.[181] Lee et al. have reported a large improvement in ZT values, experimentally ZT=0.46 at 450K and computationally ZT=2.2 at 800K, from Si-Ge NW HSs.[182] The ZT improvement was attributed to a remarkable reductions in κ, which were thought to arise from the effective scattering of a broad range of phonons by alloying Si with Ge as well as by limiting phonon transport within the NW diameters.[182] Recently, Yang et al. have theoretically shown that a system of Si NW core with a thin layer of Si-Ge alloy provides the improved thermoelectric ZT.[183] Si NWs and its HSs are still less efficient than the current most efficient thermoelectric materials and researchers are optimistic for the improvement of ZT up to the commercial level at room temperature by further optimizing the size, morphology, surface and interface of Si NWs and its HSs.

1.8.5. Energy Storage Devices

The depletion of finite fossil fuel and cost effective renewable energy sources have encouraged scientists to develop new energy storage and conversion technologies for the ever rising demands of energy.[133, 184-186] Among various energy storage technologies, rechargeable Li-ion battery (LIB) has been received considerable attention owing to their marvelous potential for energy

storage applications, such as portable electronics and electric-powered transportations due to their relatively high energy density, good cycle life, and good power performance. For commercial batteries, graphite is the most reliable material used as LiC_6 anode but the capacity is not considerable. However, despite its mechanical instability upon alloying with Li, nanostructured Si, mainly Si NWs, remains a very interesting material for LIB anodes because of several reasons: (a) Si provides the highest known specific capacity for room temperature electrochemical lithiation (3800 mAh/g), one order of magnitude larger than that of graphite; (b) Si has low delithiation potential, around 0.4 V against Li/Li^+, so that high battery voltages can still be reached with the different oxide and other types of cathodes; (c) Si NWs can be directly

Table 1.2: *The Si NW HSs anodes and their LIB performances*

System	Capacity in 1st cycle (mAh/g)	Cycles, n	Capacity after n-th cycles (mAh/g)	Reference
Si NW/a-Si	1060	100	901	[187]
Si NW/Carbon	~2500	100	~2000	[188]
	~1200		~1200	
Si NW/RGO	3350	20	3350	[189]
Si NW/Graphitic	2100	45	1040	[134]
Si NW/Graphene	3924	200	2400	[190]
Si NW/MWCNT	4250	50	1350	[191]
Si NW/Cu	2967	30	2138	[192]
Si NW/Sn	3192	100	1874	[193]
Si NW/Al	3347	100	1300	[194]
Si NW/Mg	3209	100	~980	[195]
Si NW/Au	3362	100	~2000	[196]
Si NW/TiO_2	3000	100	1600	[197]
Si NW/TiN	2915	100	1566	[198]
NiSi NW/a-Si/Al_2O_3	3000	90	3000	[199]
Si NW/PEDOT	3850	100	2510	[185]

connected to the current collector without additional binders or conducting additives; (d) Si NWs can prevent fragmentation and offer rapid charge transport and hence charge/discharge rates due to direct 1D electronic pathways and high aspect ratio.[133, 184] Table 1.2 shows the Si NWs and its HSs based LIB and their performances. A variety of carbon based materials, such as carbon, graphite, graphene, CNT, RGO etc. have been used to improve the cycling rate, cycling stability, durability and the coulombic efficiencies of the Si NWs based LIB.[134, 135, 188-191, 200, 201] Different

metal NPs such as Cu[192], Mg[195], AL[194], Sn[193], Au[196] NPs coated on the Si NWs and these metal NPs decorated Si NWs anodes in LIB exhibit high capacity, excellent coulombic efficiency, increased cycle rate and enhanced capacity retention after much larger cycles. Coatings consisting of conducting polymers, such as PEDOT, have also been used to improve the cycling properties of Si NWs.[185]

However, electrode cracking and pulverization problems related to phase transformations and huge volume expansions (320%) for repeated Li insertion/extraction results the degradation

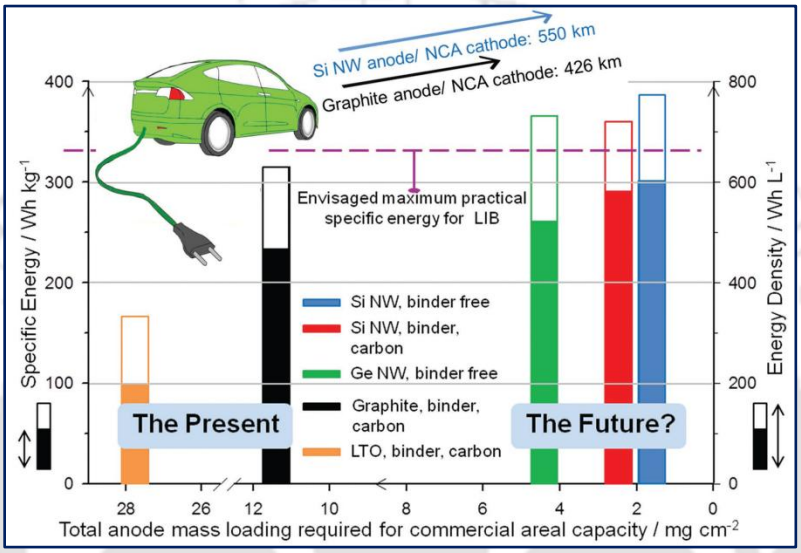

Fig. 1.11. Estimated specific energy and energy density values evaluated for LIBs containing Si NWs and other anode materials. The values are plotted against the anode mass (active material plus conductive carbon (CC) and binder if applicable) required to achieve a commercially relevant loading of 4 mA h cm^{-2} with the constant cathode $LiNiCoAlO_2$ (NCA), which delivers a capacity of 200 mAh/g. Adopted from Ref. [202]

of the Si based anode, which is the main difficulty for the commercialization of Si NWs based LIB, although an intense research is going on worldwide. Fig. 1.11 illustrates the significant improvements in performance of Si NWs based LIB that are achievable in comparison to conventional systems.[202]

Supercapacitors with high power density, fast charge/discharge kinetics and long cycle life are also an attractive energy storage device for various applications, such as portable electronics and electric-powered transportations. The last few years have witnessed a few reports on the use of Si NW as electrode materials for supercapacitors due to their fascinating capacitive properties. Low energy density, poor stability and production cost are the main issues for the utilization of supercapacitor as compared to the other energy storage devices.

1.8.6. Sensors

Si NWs have excellent charge transport properties, environment friendly and are demonstrated as excellent candidate for sensing of chemical and biological molecules. Individual Si NWs as well as its HSs can act as a charge accumulation and depletion site, inducing large change in the electrical properties by chemical or biological species. Among various bio-chemical sensing techniques Si NWs based FET was first introduced in 2001 by Cui et al. and since then it has attracted much attention in the semiconductor industry.[203] Si NWs FETs modified with calmodulin were used to detect the calcium ions (Ca^{2+}), which are important for activating biological processes such as muscle contraction, protein secretion, cell death, and development.[203] Si NWs coated with self-assembled monolayers of APTES, which were further functionalized with $-CH_3$, $-C_6H_5$, $-COOH$, and $-COOCH_3$ have been used for the detection of various volatile organic compounds (VOCs).[204] Fig. 1.12 shows the schematic illustration of the steps involved in the Si NWs based sensor fabrication for the selective detection of VOCs that are linked with gastric cancer conditions in exhaled breath.[205] Si NWs are also used for the detection of Na^+ via pH response.[206] Optical based surface enhanced Raman scattering (SERS) by metal NPs decorated Si NW HS is another way of sensing chemical and biological molecules with surface-seeking group since only molecules on or near the metal surface experience the large near-field enhancements upon resonant plasmon excitation. Si NWs coated with metal NPs, mainly Ag, Au, Pd, Cu, and Pt have been used as SERS effective substrates for sensing a variety of inorganic and organic molecules, such as: 4-methylbenzenethiol[82], crystal violet[28, 207, 208] (CV), RhB[209], R6G[14, 28, 142, 207, 208], MO[207], nicotine[28], carbaryl[208], calcium dipicolinate[210] (CaDPA), p-aminothiophenol[207] (PATP), 4-aminothiophenol[211] etc.

Modified with different organic biomolecule, Si NWs based FET sensors were used for the label-free, highly accurate, and real-time detection of nucleic acids, proteins, protein-DNA interactions, small molecule-protein interactions, cells, virus etc. and diagnosis of different kinds of disease such as dengue, cancer etc.[212-215] Metal NPs decorated SERS effective Si NW HSs are used for sensing a variety of bio-molecules such as: DNA[28, 216], immune[217] and bacteria[208, 210] (E. coli, Bacillus anthraces etc.) etc. Si NWs are also used to detect bio molecules such as proteins and DNA using florescence detection.[218, 219] Su et al. recently developed novel Au NP decorated Si NW-based molecular beacons for high-sensitivity multiplex DNA detection,[218] while Han et al. used APTES modified Si NWs for fluorescence detection of protein immunosensor.[219]

During the last decade, industrial development and rapid consumption of fuel cell casus environmental pollution. The sensitive and selective detection of toxic and harmful gases have taken enormous attention for making the environment safe. Si NWs have been exploited in gas

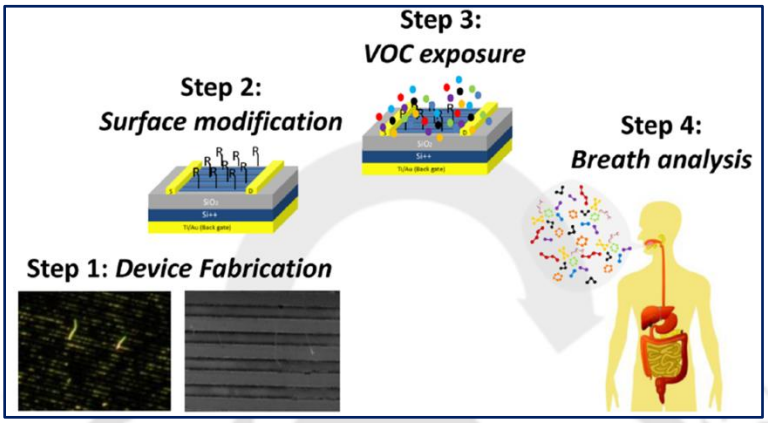

Fig. 1.12. Schematics demonstrating the Si NWs FET based sensor: fabrication of Si NW FETs (step 1); modification of the Si NWs with molecular layers (step 2); exposure of the molecularly modified Si NW FETs to VOCs that are linked with gastric cancer conditions, and for comparison, to VOCs that serve as confounding environmental factors (step 3); and exposure of the molecularly modified Si NW FETs to real breath samples collected from volunteers who have gastric cancer or from volunteers with control (healthy) conditions (step 4).[205]

sensing applications for the detection of different hazardous and nonhazardous gases. Compared to the conventional sensors based on flat Si films, the NWs gas sensors exhibit many impressive characteristics, such as ultra-high sensitivity, fast response time, higher selectivity, less power consumption and better stability. Due to the small gap in between the NWs arrays with high aspect ratio, a few gas molecules are sufficient to change the electrical properties of the sensing elements. This allows the detection of a very low concentration of gas within several seconds. H_2[75, 220, 221], H_2S[220], NH_3[220, 222], CO[220], O_2[75, 220, 221], NO[220], NO_2[220, 223], humidity[224], TNT[225], acetic acid[222], different VOCs (Hexane, Octane, Decane, Hexanol, Ethanol, Octanol, Decanol)[204], volatile linkers used as medicine[205] etc. have been successfully detected with high accuracy and sensitivity by the Si NWs functionalized with different materials. Sensitivity/selectivity of the target material, the speed of response and stability of the sensor device are the important issues in the field of sensor development in general.

1.8.7. Environmental Cleaning

Si NWs are an ecofriendly, photostable, inexpensive and nontoxic material and is able to utilize near UV, visible and NIR light for the degradation of organic pollutants.[65, 66, 86, 226] Si NWs functionalized with –H has shown excellent photocatalysis for the photodegradation of organic

pollutants.[15, 65] High aspect ratio, Si NCs decorated Si NWs with Si-H terminated surface grown by MACE have shown excellent photocatalytic activity under visible light illumination.[15, 65] H-Si NWs has shown strong reducing capacity for the reduction of azo dyes and MTT (3-(4,5-dimethyl-2-thiazol)-2,5-diphenyl-2H-tetrazolium bromide). In presence of coenzyme, reducing capacity of H-Si NWs was enhanced.[227] H-Si NWs are also very efficient for the discoloration of various remazol azo dyes including Red F3B, Brilliant Orange 3R, Golden RNL 150%, and Brilliant Purple 5R in aqueous solution. H-Si NWs were also found to have catalytic activities similar to those of biological enzymes catalase and peroxidase and can be used for the oxidation of ligand precursor ophenylenediamine (OPD).[228] These results suggest that these H-Si NWs can be used as enzyme-mimics in biotechnology. To overcome the drawbacks of Si NW based devices for environmental cleaning, many strategies have been developed in the past few decades and the most widely used one is to develop photocatalytic heterojunctions by incorporating semiconductors, metals and other functionalities. [15, 65, 86, 226-230] Metal NPs decorated Si NW HSs are studied extensively for the photodegradation of organic pollutants, such as MB, methyl red (MR), methyl orange (MO), phenol, rhodamine 6G (R6G), benzyl alcohol, rhodamine B (RhB) etc. The main advantages of using noble metals with Si NWs as photocatalyst are: (i) the high work function of noble metals (Pt, Pd, Au, Ag, etc.) facilitates the electron transfer from Si NWs

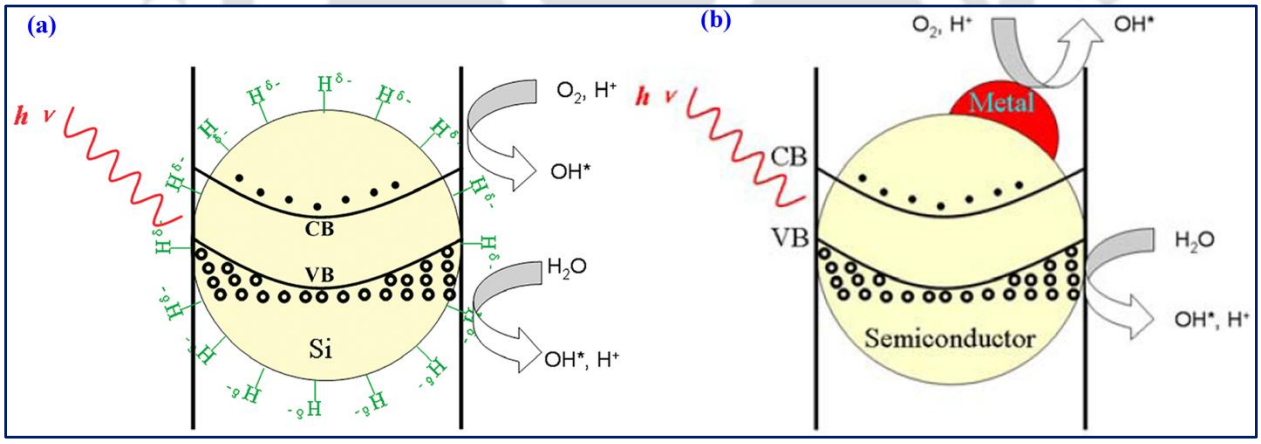

Fig. 1.13. Schematic of the e-h pair generation in (a) H-Si NW and (b) metal-semiconductor photocatalyst. The mechanisms involved: (left) The incident ray promotes the formation of the electron and hole; (middle) the electron transfer to hydrogen atom on the surface; (right) hole is used in the formation of the OH* groups promoting oxidizing processes. Adopted from Ref. [15]

to noble metal in the Schottky junction, which significantly reduces the recombination of photogenerated e-h pairs; (ii) higher absorption due to the SPR effect of noble metals. Fig. 1.13(a, b) shows the schematic of the e-h generation in H-Si NW and metal-semiconductor

photocatalyst under light illumination.[15] Liao et al. showed that Au-Pd and Pd-Ni bimetal decorated Si NWs show higher photocatalytic degradation rate as compared to the bare Si NWs or the single metal decorated Si NWs.[226] Duan et al. have introduced an inert conductive polymer PEDOT in between Ag NPs and Si NWs and found that Si NWs/PEDOT/Ag NPs show ~92% photodegradation of RhB, while H-Si NWs show only ~51% in 180 min.[231] In the same time SiNWs/PEDOT/Ag NPs show excellent stability as compared to the H-Si NWs. Si NWs HSs with different semiconductor materials, such as ZnO, TiO_2, CdSe, are also extensively studied for the degradation of environmental pollutants.[229, 230, 232]

1.9. Challenges in Fabrication and Applications of Si Nanowires and its Heterostructures

After the successful synthesis of Si NWs by using MACE by Li and Bohn,[26] extensive research has been carried for the controlled growth of aligned Si NWs by tuning various growth parameters those affect the Si nanostructure formation and resultant morphology.[27, 35, 36, 55-57] However, controlled growth of well aligned, vertical Si NWs by MACE without using expensive lithography is a great challenge. Furthermore, the exact growth mechanism of Si NWs decorated with Si NCs on its surface is still unclear and it is debated in the literature. Understanding the formation mechanism and tuning the optical properties of Si nanostructures by morphology control and the manipulation of defects remain a considerable challenge for exploiting their applications in various fields. The morphology and the defects in the Si nanostructures determine the optical properties of the Si nanostructure. Optical spectroscopic techniques are desirable for non-destructive evaluation of new structure & properties of Si NWs. A systematic correlation between different optical techniques remains a challenge in the field. There has been a lot of debate on the origin of visible PL from Si NWs grown by MACE. In addition, there are plenty of challenging issues to improve the performance of the Si NWs based optoelectronic devices. In order to improve the Si NW's photophysical properties and achieve synergistic effects, one of the well accepted strategy is the HS approach. The choice of suitable material for the HS and the fabrication of high quality Si NWs based HSs for better control in dimensions, compositions, structures, interfaces and uniformity have enormous attention in the areas of nanotechnology. Although, Si NWs and its different HSs are already exploited in several applications, still there are several problems and challenges in the real life devices, such as (a) optimization of power consumption, (b) energy utilization efficiency, (c) device stability, (d) flexibility, (e) device performance, (f) cost reduction etc. In this thesis, we fabricate Si NWs with high structural

quality by a simple, robust and low cost technique and study their morphology, structure and photophysical properties for different application related to energy and environment.

1.10. Focus of the Present Thesis

Despite of considerable success, there are several challenges for the fabrication of high quality Si NWs and its different HSs with reproducible properties for their applications in various areas of nanotechnology. In the present thesis, we have made attempts for controlled fabrication and tuning the properties of the Si NWs by forming HS with different materials. The main focus of the present thesis is as follows:

- Fabrication of large area, well aligned and controlled Si NWs of high crystalline quality by a cost effective MACE process. We attempt to understand the growth mechanism of Si NWs during the early stages of MACE process using a scaling approach, for the first time.
- Study the effect of growth parameters on the morphology and photophysical properties of Si NWs.
- The advantage of Au/Ag bilayer over conventional single layer Ag or Au assisted MACE of Si for the improved morphology and optical properties of the Si NWs.
- Quantitative analysis of the tunable visible PL of the Si NCs decorated Si NWs on the basis of quantum confinement effect and NBOHC defects.
- A correlation between the PL and Raman analysis of the Si NCs decorated Si NWs.
- A correlation between the PL and Photocatalysis of the Si NCs decorated Si NWs.
- Fabrication of high quality Si NWs based HSs with semiconducting material ZnO and different noble metal NPs, such as Ag, Au, Au/Pd to improve the photophysical properties of Si NWs.
- Application of Si NWs and its HSs in broadband light emission, organic pollutant degradation by photocatalysis and SERS detection.

1.11. Organization of the Thesis

This thesis presents a systematic study on the growth mechanism, orientation controlled growth and tunable photophysical and photochemical properties of mesoporous Si NWs and its HSs for light emission and environmental cleaning applications. The complete thesis work has been organized into nine chapters. The present chapter i.e., **Chapter 1** presented a brief summary of

the latest developments in 1D Si NWs, including growth strategies, important properties and their promising applications ranging from LED, solar cells, sensors, and energy storage to photochemical reactor. **Chapter 2** provides a brief description of the experimental techniques used for the present work along with the working principles of some characterization tools. **Chapter 3** presents results on the early stages of growth and growth mechanism of Si NWs using MACE process through a scaling approach. The controlled fabrication of Si NWs by tuning the growth parameters is described elaborately in this chapter. The origin of the broad band visible-NIR PL from the as-grown Si NWs decorated with Si NCs of arbitrary shape is discussed in **Chapter 4. Chapter 5** presents a quantitative analysis of the phonon confinement effect in arbitrary shaped Si NCs decorated on Si NWs and its correlation with the PL analysis. Visible light photocatalysis by mesoporous is described in **Chapter 6.** In **Chapter 7,** PL signature of resonant energy transfer in ZnO coated Si NWs/NCs array is presented. **Chapter 8** presents the results of fabrication, properties and applications of metal NPs decorated Si NWs. The highlights of the major contributions of the thesis, important conclusions of the present work and scope for future studies on Si NWs and its HSs are discussed in the last chapter i.e. **Chapter 9.**

References

1. Otto, M.; Algasinger, M.; Branz, H.; Gesemann, B.; Gimpel, T.; Füchsel, K.; Käsebier, T.; Kontermann, S.; Koynov, S.; Li, X.; Naumann, V.; Oh, J.; Sprafke, A. N.; Ziegler, J.; Zilk, M.; Wehrspohn, R. B. *Adv. Optical Mater.,* **2015,** 3, 147.
2. Chen, C. C.; Yeh, C. C.; Chen, C. H.; Yu, M. Y.; Liu, H. L.; Wu, J. J.; Chen, K. H.; Chen, L. C.; Peng, J. Y.; Chen, Y. F. *J. Am. Chem. Soc.,* **2001,** 123, 2791.
3. Wu, Y.; Yang, P. *Chem. Mater.,* **2000,** 12, 605.
4. Schmidt, V.; Wittemann, J. V.; Gösele, U. *Chem. Rev.,* **2010,** 110, 361.
5. Peng, K.-Q.; Lee, S.-T. *Adv. Mater.,* **2011,** 23, 198.
6. Shao, M.; Ma, D. D. D.; Lee, S.-T. *Eur. J. Inorg. Chem.,* **2010,** 2010, 4264.
7. Peng, K.-Q.; Wang, X.; Li, L.; Hu, Y.; Lee, S.-T. *Nano Today,* **2013,** 8, 75.
8. Dhara, S.; Giri, P. K. *Rev. Nanosci. Nanotechnol. ,* **2013,** 2, 147.
9. Niu, J.; Sha, J.; Yang, D. *Physica E Low Dimens. Syst. Nanostruct.,* **2004,** 23, 131.
10. Liu, X.; Coxon, P. R.; Peters, M.; Hoex, B.; Cole, J. M.; Fray, D. J. *Energy Environ. Sci.,* **2014,** 7, 3223.
11. Schmidt, V.; Wittemann, J. V.; Senz, S.; Gösele, U. *Adv . Mater.,* **2009,** 21, 2681.
12. Chelikowsky, J. R.; Cohen, M. L. *Phys. Rev. B,* **1976,** 14, 556.
13. Ng, M.-F.; Zhou, L.; Yang, S.-W.; Sim, L. Y.; Tan, V. B. C.; Wu, P. *Phys. Rev. B,* **2007,** 76, 155435.
14. Galopin, E.; Barbillat, J.; Coffinier, Y.; Szunerits, S.; Patriarche, G.; Boukherroub, R. *ACS Appl. Mater. Interfaces,* **2009,** 1, 1396.
15. Shao, M.; Cheng, L.; Zhang, X.; Ma, D. D. D.; Lee, S. T. *J. Am. Chem. Soc.,* **2009,** 131, 17738.

16. Dussart, R.; Tillocher, T.; Lefaucheux, P.; Boufnichel, M. *J. Phys. D: Appl. Phys.,* **2014,** 47, 123001.
17. Eisenhawer, B.; Zhang, D.; Clavel, R.; Berger, A.; Michler, J.; Christiansen, S. *Nanotechnology,* **2011,** 22, 075706.
18. Schubert, L.; Werner, P.; Zakharov, N. D.; Gerth, G.; Kolb, F. M.; Long, L.; Gösele, U.; Tan, T. Y. *Appl. Phys. Lett.,* **2004,** 84, 4968.
19. Schwartz, G. C.; Schaible, P. M. *J. Vac. Sci. Technol.,* **1979,** 16, 410.
20. Choi, D.-G.; Yu, H. K.; Jang, S. G.; Yang, S.-M. *J. Am. Chem. Soc.,* **2004,** 126, 7019.
21. Gu, Q.; Dang, H.; Cao, J.; Zhao, J.; Fan, S. *Appl . Phys. Lett.,* **2000,** 76, 3020.
22. Das Kanungo, P.; Zakharov, N.; Bauer, J.; Breitenstein, O.; Werner, P.; Goesele, U. *Appl. Phys. Lett.,* **2008,** 92, 263107.
23. Morales, A. M.; Lieber, C. M. *Science,* **1998,** 279, 208.
24. Wu, Y.; Yang, P. *J. Am. Chem. Soc.,* **2001,** 123, 3165.
25. Wen, C. Y.; Reuter, M. C.; Tersoff, J.; Stach, E. A.; Ross, F. M. *Nano Lett.,* **2010,** 10, 514.
26. Li, X.; Bohn, P. W. *Appl. Phys. Lett.,* **2000,** 77, 2572.
27. Peng, K. Q.; Yan, Y. J.; Gao, S. P.; Zhu, J. *Adv. Mater.,* **2002,** 14, 1164.
28. Shao, M.-W.; Zhang, M.-L.; Wong, N.-B.; Ma, D. D.-d.; Wang, H.; Chen, W.; Lee, S.-T. *Appl. Phys. Lett.,* **2008,** 93, 233118.
29. Kim, J.; Han, H.; Kim, Y. H.; Choi, S. H.; Kim, J. C.; Lee, W. *ACS Nano,* **2011,** 5, 3222.
30. Kayes, B. M.; Filler, M. A.; Putnam, M. C.; Kelzenberg, M. D.; Lewis, N. S.; Atwater, H. A. *Appl. Phys. Lett.,* **2007,** 91, 103110.
31. Bandaru, P. R.; Pichanusakorn, P. *Semicond. Sci. Tech.,* **2010,** 25, 024003.
32. Hasan, M.; Huq, M. F.; Mahmood, Z. H. *SpringerPlus,* **2013,** 2, 151.
33. Han, H.; Huang, Z.; Lee, W. *Nano Today,* **2014,** 9, 271.
34. Song, T.; Lee, S.-T.; Sun, B. *Nano Energy,* **2012,** 1, 654.
35. Qu, Y.; Zhoua, H.; Duan, X. *Nanoscale,* **2011,** 3, 4060.
36. Huang, Z.; Geyer, N.; Werner, P.; de Boor, J.; Gosele, U. *Adv. Mater.,* **2011,** 23, 285.
37. Ramanujam, J.; Shiri, D.; Verma, A. *Mater. Exp.,* **2011,** 1, 105.
38. Wei, Y.; Wu, W.; Guo, R.; Yuan, D.; Das, S.; Wang, Z. L. *Nano Lett.,* **2010,** 10, 3414.
39. Cui, Y.; Lauhon, L. J.; Gudiksen, M. S.; Wang, J.; Lieber, C. M. *Appl. Phys. Lett.,* **2001,** 78, 2214.
40. Wang, N.; Zhang, Y. F.; Tang, Y. H.; Lee, C. S.; Lee, S. T. *Appl. Phys. Lett.,* **1998,** 73, 3902.
41. Zhang, Y. F.; Tang, Y. H.; Peng, H. Y.; Wang, N.; Lee, C. S.; Bello, I.; Lee, S. T. *Appl. Phys. Lett.,* **1999,** 75, 1842.
42. Pan, Z. W.; Dai, Z. R.; Xu, L.; Lee, S. T.; Wang, Z. L. *J. Phys. Chem. B,* **2001,** 105, 2507.
43. Pan, H.; Lim, S.; Poh, C.; Sun, H.; Wu, X.; Feng, Y.; Lin, J. *Nanotechnology,* **2005,** 16, 417.
44. Shao, M.; Cheng, L.; Zhang, M.; Ma, D. D. D.; Zapien, J. A.; Lee, S.-T.; Zhang, X. *Appl. Phys. Lett.,* **2009,** 95, 143110.
45. Lim, K. W.; Lee, J.-I.; Yang, J.; Kim, Y.-K.; Jeong, H. Y.; Park, S.; Shin, H. S. *ACS Appl. Mater. Interfaces,* **2014,** 6, 6340.
46. Shi, W. S.; Peng, H. Y.; Zheng, Y. F.; Wang, N.; Shang, N. G.; Pan, Z. W.; Lee, C. S.; Lee, S. T. *Adv. Mater.,* **2000,** 12, 1343.
47. Liu, J. L.; Cai, S. J.; Jin, G. L.; Thomas, S. G.; Wang, K. L. *J. Cryst. Growth,* **1999,** 200, 106.
48. Zakharov, N.; Werner, P.; Sokolov, L.; Gösele, U. *Physica E Low Dimens. Syst. Nanostruct.,* **2007,** 37, 148.
49. Bauer, J.; Fleischer, F.; Breitenstein, O.; Schubert, L.; Werner, P.; Gösele, U.; Zacharias, M. *Appl. Phys. Lett.,* **2007,** 90, 012105.
50. Fuhrmann, B.; Leipner, H. S.; Höche, H.-R.; Schubert, L.; Werner, P.; Gösele, U. *Nano Lett.,* **2005,** 5, 2524.
51. Jeng, S. J.; Oehrlein, G. S. *Appl. Phys. Lett.,* **1987,** 50, 1912.

52. Jansen, H.; Boer, M. d.; Legtenberg, R.; Elwenspoek, M. *J. Micromech. Microeng.,* **1995,** 5, 115.
53. Hsu, C.-M.; Connor, S. T.; Tang, M. X.; Cui, Y. *Appl. Phys. Lett.,* **2008,** 93, 133109.
54. Fu, Y. Q.; Colli, A.; Fasoli, A.; Luo, J. K.; Flewitt, A. J.; Ferrari, A. C.; Milne, W. I. *J. Vac. Sci. Technol. B,* **2009,** 27, 1520.
55. Bachtouli, N.; Aouida, S.; Bessais, B. *Microporous Mesoporous Mater.,* **2014,** 187, 82.
56. Peng, K.; Zhang, M.; Lu, A.; Wong, N.-B.; Zhang, R.; Lee, S.-T. *Appl. Phys. Lett.,* **2007,** 90, 163123.
57. Hildreth, O. J.; Lin, W.; Wong, C. P. *ACS Nano,* **2009,** 3, 4033.
58. Dimova Malinovska, D.; Sendova Vassileva, M.; Tzenov, N.; Kamenova, M. *Thin Solid Films,* **1997,** 297, 9.
59. Li, X. *Curr. Opin. Solid State Mater. Sci.,* **2012,** 16, 71.
60. Chen, C.-Y.; Liu, Y.-R. *Phys. Chem. Chem. Phys.,* **2014,** 16, 26711.
61. Kim, S. M.; Khang, D. Y. *Small,* **2014,** 10, 3761.
62. Xie, C.; Nie, B.; Zeng, L.; Liang, F.-X.; Wang, M.-Z.; Luo, L.; Feng, M.; Yu, Y.; Wu, C.-Y.; Wu, Y.; Yu, S.-H. *ACS Nano,* **2014,** 8, 4015.
63. Chern, W.; Hsu, K.; Chun, I. S.; Azeredo, B. P. d.; Ahmed, N.; Kim, K. H.; Zuo, J.-m.; Fang, N.; Ferreira, P.; Li, X. *Nano Lett.,* **2010,** 10, 1582.
64. Hochbaum, A. I.; Gargas, D.; Hwang, Y. J.; Yang, P. *Nano Lett.,* **2009,** 9, 3550.
65. Megouda, N.; Cofininier, Y.; Szunerits, S.; Hadjersi, T.; ElKechai, O.; Boukherroub, R. *Chem. Comm.,* **2011,** 47, 991.
66. Liu, D.; Li, L.; Gao, Y.; Wang, C.; Jiang, J.; Xiong, Y. *Angew. Chem. Int. Ed. ,* **2015,** 54, 2980.
67. Alferov, Z. I. *Rev. Mod. Phys.,* **2001,** 73, 767.
68. Chao, Z.; Zhi, X.; Wei, T.; Dai-Ming, T.; Xi, W.; Yoshio, B.; Naoki, F.; Dmitri, G. *Nanotechnology,* **2015,** 26, 154001.
69. Liu, H.; She, G.; Huang, X.; Qi, X.; Mu, L.; Meng, X.; Shi, W. *J. Phys. Chem. C,* **2013,** 117, 2377.
70. Hocevar, M.; Immink, G.; Verheijen, M.; Akopian, N.; Zwiller, V.; Kouwenhoven, L.; Bakkers, E. *Nature Comm.,* **2012,** 3, 1266.
71. Mullane, E.; Geaney, H.; Ryan, K. M. *Phys. Chem. Chem. Phys.,* **2015,** 17, 6919.
72. Amato, M.; Palummo, M.; Rurali, R.; Ossicini, S. *Chemical Rev.,* **2014,** 114, 1371.
73. Geaney, H.; Mullane, E.; Ramasse, Q. M.; Ryan, K. M. *Nano Lett.,* **2013,** 13, 1675.
74. Chen, L.; Fung, W. Y.; Lu, W. *Nano Lett.,* **2013,** 13, 5521.
75. Kim, J.; Oh, S. D.; Kim, J. H.; Shin, D. H.; Kim, S.; Choi, S.-H. *Sci. Rep.,* **2014,** 4, 5384.
76. Zhang, Y. F.; You, L. P.; Shan, X. D.; Wei, X. L.; Huo, H. B.; Xu, W. J.; Dai, L. *J. Phys. Chem. C,* **2007,** 111, 14343.
77. Hu, J.; Chen, Z.; Sun, Y.; Jiang, H.; Wang, N.; Zou, R. *J. Mater. Chem.,* **2009,** 19, 7011.
78. Peng, K.-Q.; Wang, X.; Wu, X.-L.; Lee, S.-T. *Nano Lett.,* **2009,** 9, 3704.
79. Song, Z.; Chang, H.; Zhu, W.; Xu, C.; Feng, X. *Sci. Rep.,* **2015,** 5, 7792.
80. Mulazimoglu, E.; Nogay, G.; Turan, R.; Emrah Unalan, H. *Appl. Phys. Lett. ,* **2013,** 103, 143124.
81. Fang, C.; Agarwal, A.; Widjaja, E.; Garland, M. V.; Wong, S. M.; Linn, L.; Khalid, N. M.; Salim, S. M.; Balasubramanian, N. *Chem. Mater.,* **2009,** 21, 3542.
82. Yang, J.; Li, J. B.; Gong, Q. H.; Teng, J. H.; Hong, M. H. *Nanotechnology,* **2014,** 25, 465707.
83. Alava, M.; Dubé, M.; Rost, M. *Adv. Phys.,* **2004,** 53, 83-175.
84. Convertino, A.; Cuscunà, M.; Martelli, F.; Manera, M. G.; Rella, R. *J. Phys. Chem. C,* **2014,** 118, 685.
85. Wang, Y.; Liu, Y. P.; Liang, H. L.; Mei, Z. X.; Du, X. L. *Phys. Chem. Chem. Phys.,* **2013,** 15, 2345.
86. Brahiti, N.; Hadjersi, T.; Menari, H.; Amirouche, S.; El Kechai, O. *Mater. Res. Bul.,* **2015,** 62, 30.
87. Sudhagar, P.; Song, T.; Lee, D. H.; Mora-Seró, I.; Bisquert, J.; Laudenslager, M.; Sigmund, W. M.; Park, W. I.; Paik, U.; Kang, Y. S. *J. Phys. Chem. Lett.,* **2011,** 2, 1984.
88. Shi, J.; Hara, Y.; Sun, C.; Anderson, M. A.; Wang, X. *Nano Lett.,* **2011,** 11, 3413.

89. Kargar, A.; Sun, K.; Jing, Y.; Choi, C.; Jeong, H.; Jung, G. Y.; Jin, S.; Wang, D. *ACS Nano,* **2013,** 7, 9407.
90. Hwang, Y. J.; Wu, C. H.; Hahn, C.; Jeong, H. E.; Yang, P. *Nano Lett.,* **2012,** 12, 1678.
91. Liu, C.; Tang, J.; Chen, H. M.; Liu, B.; Yang, P. *Nano Lett.,* **2013,** 13, 2989.
92. Shi, J.; Wang, X. *Energy Environ. Sci.,* **2012,** 5, 7918.
93. Noh, S. Y.; Sun, K.; Choi, C.; Niu, M.; Yang, M.; Xu, K.; Jin, S.; Wang, D. *Nano Energy,* **2013,** 2, 351.
94. Jianga, X.; Tiana, B.; Xianga, J.; Qiana, F.; Zhenga, G.; Wang, H.; Maia, L.; Liebera, C. M. *PNAS,* **2011,** 108, 12212.
95. Wang, D.; Qian, F.; Yang, C.; Zhong, Z.; Lieber, C. M. *Nano Lett.,* **2004,** 4, 871.
96. Hu, J.; Bando, Y.; Zhan, J.; Yuan, X.; Sekiguchi, T.; Golberg, D. *Adv. Mater.,* **2005,** 17, 971.
97. Lv, S.; Li, Z.; Chen, C.; Liao, J.; Wang, G.; Li, M.; Miao, W. *ACS Appl. Mater. Interfaces,* **2015,** 7, 13564.
98. Chong, S. K.; Lim, E. L.; Yap, C. C.; Chiu, W. S.; Dee, C. F.; Rahman, S. A. *Sci. Adv. Mate.,* **2014,** 6, 782.
99. Kargar, A.; Sun, K.; Kim, S. J.; Lu, D.; Jing, Y.; Liu, Z.; Pan, X.; Wang, D. *Phys. Status Solidi A,* **2013,** 210, 2561.
100. Putnam, M. C.; Boettcher, S. W.; Kelzenberg, M. D.; Turner-Evans, D. B.; Spurgeon, J. M.; Warren, E. L.; Briggs, R. M.; Lewis, N. S.; Atwater, H. A. *Energy Environ. Sci.,* **2010,** 3, 1037.
101. Tian, B.; Zheng, X.; Kempa, T. J.; Fang, Y.; Yu, N.; Yu, G.; Huang, J.; Lieber, C. M. *Nature,* **2007,** 449, 885.
102. Garnett, E.; Yang, P. *Nano Lett.,* **2010,** 10, 1082.
103. Katiyar, A. K.; Sinha, A. K.; Manna, S.; Ray, S. K. *ACS Appl. Mater. Int.,* **2014,** 6, 15007.
104. Pan, L.; Lew, K.-K.; Redwing, J. M.; Dickey, E. C. *Nano Lett.,* **2005,** 5, 1081.
105. Ben-Ishai, M.; Patolsky, F. *Adv. Mater.,* **2010,** 22, 902.
106. Manna, S.; Das, S.; Mondal, S. P.; Singha, R.; Ray, S. K. *J. Phys. Chem. C,* **2012,** 116, 7126.
107. Yu, P.; Tsai, C.-Y.; Chang, J.-K.; Lai, C.-C.; Chen, P.-H.; Lai, Y.-C.; Tsai, P.-T.; Li, M.-C.; Pan, H.-T.; Huang, Y.-Y.; Wu, C.-I.; Chueh, Y.-L.; Chen, S.-W.; Du, C.-H.; Horng, S.-F.; Meng, H.-F. *ACS Nano,* **2013,** 7, 10780.
108. Zhang, F.; Han, X.; Lee, S.-t.; Sun, B. *J. Mater. Chem.,* **2012,** 22, 5362.
109. Cheng, Y.; Fang, G.; Li, C.; Yuan, L.; Ai, L.; Chen, B.; Zhao, X.; Chen, Z.; Bai, W.; Zhan, C. *J. Appl. Phys.,* **2007,** 102, 083516.
110. Hwang, Y. J.; Boukai, A.; Yang, P. *Nano Lett.,* **2009,** 9, 410.
111. Sun, L.; He, H.; Liu, C.; Lu, Y.; Ye, Z. *CrystEngComm,* **2011,** 13, 2439.
112. Zhou, H.; Fang, G.; Yuan, L.; Wang, C.; Yang, X.; Huang, H.; Zhou, C.; Zhao, X. *Appl. Phys. Lett.,* **2009,** 94, 013503.
113. Kang, H.; Park, J.; Choi, T.; Jung, H.; Lee, K. H.; Im, S.; Kim, H. *Appl. Phys. Lett.,* **2012,** 100, 041117.
114. Um, H.-D.; Moiz, S. A.; Park, K.-T.; Jung, J.-Y.; Jee, S.-W.; Ahn, C. H.; Kim, D. C.; Cho, H. K.; Kim, D.-W.; Lee, J.-H. *Appl. Phys. Lett.,* **2011,** 98, 033102.
115. Kale, V. S.; Prabhakar, R. R.; Pramana, S. S.; Rao, M.; Sow, C.-H.; Jinesh, K. B.; Mhaisalkar, S. G. *Phys. Chem. Chem. Phys.,* **2012,** 14, 4614.
116. Yu, H.; Chen, S.; Quan, X.; Zhao, H.; Zhang, Y. *Appl. Catal. B: Environ.,* **2009,** 90, 242.
117. Yu, H.; Li, X.; Quan, X.; Chen, S.; Zhang, Y. *Environ. Sci. Technol.,* **2009,** 43, 7849.
118. Yenchalwar, S. G.; Azhagan, V. K.; Shelke, M. V. *Phys. Chem. Chem. Phys.,* **2014,** 16, 17786.
119. Mayer, M. T.; Du, C.; Wang, D. *J. Am. Chem. Soc.,* **2012,** 134, 12406.
120. Li, Q.; Wang, C. *J. Am. Chem. Soc.,* **2003,** 125, 9892.
121. Adachi, M. M.; Anantram, M. P.; Karim, K. S. *Sci. Rep.,* **2013,** 3, 1546.
122. Savin, H.; Repo, P.; von Gastrow, G.; Ortega, P.; Calle, E.; Garín, M.; Alcubilla, R. *Nature nanotechnology,* **2015,** 10, 624.

123. Lin, X. X.; Zeng, Y.; Zhong, S. H.; Huang, Z. G.; Qian, H. Q.; Ling, J.; Zhu, J. B.; Shen, W. Z. *Nanotechnology,* **2015,** 26, 125401.
124. Katiyar, A. K.; Mukherjee, S.; Zeeshan, M.; Ray, S. K.; Raychaudhuri, A. K. *ACS Appl. Mater. Int.,* **2015,** 7, 23445.
125. Mankin, M. N.; Day, R. W.; Gao, R.; No, Y.-S.; Kim, S.-K.; McClelland, A. A.; Bell, D. C.; Park, H.-G.; Lieber, C. M. *Nano Lett.,* **2015,** 15, 4776.
126. Zhou, X. T.; Zhang, R. Q.; Peng, H. Y.; Shang, N. G.; Wang, N.; Bello, I.; Lee, C. S.; Lee, S. T. *Chem. Phys. Lett.,* **2000,** 332, 215.
127. Liu, Y.; Vishniakou, S.; Yoo, J.; Dayeh, S. A. *Sci. Rep.,* **2015,** 5, 18482.
128. Subramani, T.; Syu, H.-J.; Liu, C.-T.; Hsueh, C.-C.; Yang, S.-T.; Lin, C.-F. *ACS Appl. Mater. Interfaces,* **2016,** 8, 2406.
129. Wang, F.; Jiang, Y.; Li, T.; Zhao, Y.; Zhang, X. *J. Mater. Chem. A,* **2015,** 3, 22902.
130. Zhang, X.; Xie, C.; Jie, J.; Zhang, X.; Wu, Y.; Zhang, W. *J. Mater. Chem. A,* **2013,** 1, 6593.
131. Lin, Y.; Li, X.; Xie, D.; Feng, T.; Chen, Y.; Song, R.; Tian, H.; Ren, T.; Zhong, M.; Wang, K.; Zhu, H. *Energy Environ. Sci.,* **2013,** 6, 108.
132. Xie, C.; Lv, P.; Nie, B.; Jie, J.; Zhang, X.; Wang, Z.; Jiang, P.; Hu, Z.; Luo, L.; Zhu, Z.; Wang, L.; Wu, C. *Appl . Phys. Lett.,* **2011,** 99, 133113.
133. Zamfir, M. R.; Nguyen, H. T.; Moyen, E.; Lee, Y. H.; Pribat, D. *J. Mater. Chem. A,* **2013,** 1, 9566.
134. Cho, Y. J.; Kim, H. S.; Im, H.; Myung, Y.; Jung, G. B.; Lee, C. W.; Park, J.; Park, M.-H.; Cho, J.; Kang, H. S. *J. Phys. Chem. C,* **2011,** 115, 9451.
135. Wang, B.; Li, X.; Zhang, X.; Luo, B.; Jin, M.; Liang, M.; Dayeh, S. A.; Picraux, S. T.; Zhi, L. *ACS Nano,* **2013,** 7, 1437.
136. Lo Faro, M. J.; D'Andrea, C.; Messina, E.; Fazio, B.; Musumeci, P.; Reitano, R.; Franzò, G.; Gucciardi, P. G.; Vasi, C.; Priolo, F.; Iacona, F.; Irrera, A. *Sci. Rep.,* **2015,** 5, 16753.
137. Ghosh, R.; Giri, P. K.; Imakita, K.; Fujii, M. *J. Alloy Compd.,* **2015,** 638, 419.
138. Wang, W.-C.; Tsai, M.-C.; Yang, J.; Hsu, C.; Chen, M.-J. *ACS Appl. Mater. Int.,* **2015,** 7, 10228.
139. Chou, Y.-C.; Wen, C.-Y.; Reuter, M. C.; Su, D.; Stach, E. A.; Ross, F. M. *ACS Nano,* **2012,** 6, 6407.
140. Flynn, G.; Ramasse, Q. M.; Ryan, K. M. *Nano Lett.,* **2016,** 16, 374.
141. Feng, Z.; Jia, R.; Dou, B.; Li, H.; Jin, Z.; Liu, X.; Li, F.; Zhang, W.; Wu, C. *Appl . Phys. Lett.,* **2015,** 106, 053118.
142. Huang, Y.; Ferhan, A. R.; Cho, S.-J.; Lee, H.; Kim, D.-H. *ACS Appl. Mater. Int.,* **2015,** 7, 17582.
143. Zhao, L.; Liao, K.; Pynenburg, M.; Wong, L.; Heinig, N.; Thomas, J. P.; Leung, K. T. *ACS Appl. Mater. Int.,* **2013,** 5, 2410.
144. Ghosh, R.; Imakita, K.; Fujii, M.; Giri, P. K. *Phys. Chem. Chem. Phys.,* **2016,** 18, 7715.
145. Yuan, G. D.; Zhou, Y. B.; Guo, C. S.; Zhang, W. J.; Tang, Y. B.; Li, Y. Q.; Chen, Z. H.; He, Z. B.; Zhang, X. J.; Wang, P. F.; Bello, I.; Zhang, R. Q.; Lee, C. S.; Lee, S. T. *ACS Nano,* **2010,** 4, 3045.
146. Canham, L. T. *Appl. Phys. Lett.,* **1990,** 57, 1046.
147. Guichard, A. R.; Kekatpure, R. D.; Brongersma, M. L.; Kamins, T. I. *Phys. Rev. B,* **2008,** 78, 235422.
148. Suzuki, T.; Skuja, L.; Kajihara, K.; Hirano, M.; Kamiya, T.; Hosono, H. *Phys. Rev. Lett.,* **2003,** 90, 186404.
149. Demichel, O.; Calvo, V.; Noé, P.; Salem, B.; Fazzini, P. F.; Pauc, N.; Oehler, F.; Gentile, P.; Magnea, N. *Phys. Rev. B,* **2011,** 83, 245443.
150. Demichel, O.; Calvo, V.; Besson, A.; Noe, P.; Salem, B.; Pauc, N.; Oehler, F.; Gentile, P.; Magnea, N. *Nano Lett.,* **2010,** 10, 2323.
151. Walavalkar, S. S.; Hofmann, C. E.; Homyk, A. P.; Henry, M. D.; Atwater, H. A.; Scherer, A. *Nano Lett.,* **2010,** 10, 4423.
152. Valenta, J.; Bruhn, B.; Linnros, J. *Nano Lett.,* **2011,** 11, 3003.
153. Skuja, L.; Suzuki, T.; Tanimura, K. *Phys. Rev. B,* **1995,** 52, 15208.

154. Tsybeskov, L.; Vandyshev, J. V.; Fauchet, P. M. *Phys. Rev. B,* **1994,** 49, 7821.
155. Chan, Y. F.; Su, W.; Zhang, C. X.; Wu, Z. L.; Tang, Y.; Sun, X. Q.; Xu, H. J. *OPTICS EXPRESS,* **2012,** 20, 24280.
156. Tan, S. T.; Sun, X. W.; Zhao, J. L.; Iwan, S.; Cen, Z. H.; Chen, T. P.; Ye, J. D.; Lo, G. Q.; Kwong, D. L.; Teo, K. L. *Appl. Phys. Lett.,* **2008,** 93, 013506.
157. Yuan-Ming, C.; Sheng-Rui, J.; Hsin-Yi, L.; Chih-Ming, L.; Jenh-Yih, J. *Nanotechnology,* **2010,** 21, 385705.
158. Moon, K.-J.; Lee, T. I.; Lee, W.; Myoung, J.-M. *Nanoscale,* **2014,** 6, 3611.
159. Hsieh, Y.-P.; Chen, H.-Y.; Lin, M.-Z.; Shiu, S.-C.; Hofmann, M.; Chern, M.-Y.; Jia, X.; Yang, Y.-J.; Chang, H.-J.; Huang, H.-M.; Tseng, S.-C.; Chen, L.-C.; Chen, K.-H.; Lin, C.-F.; Liang, C.-T.; Chen, Y.-F. *Nano Lett.,* **2009,** 9, 1839.
160. Irrera, A.; Artoni, P.; Iacona, F.; Pecora, E. F.; Franz`o, G.; Galli, M.; Fazio, B.; Boninelli, S.; Priolo, F. *Nanotechnology,* **2012,** 23.
161. Yuan, G.; Aruda, K.; Zhou, S.; Levine, A.; Xie, J.; Wang, D. *Angew. Chem. Int. Ed.,* **2011,** 50, 2334.
162. Peng, K.; Xu, Y.; Wu, Y.; Yan, Y.; Lee, S.-T.; Zhu, J. *Small,* **2005,** 1, 1062.
163. Kim, D. R.; Lee, C. H.; Zheng, X. *Nano Lett.,* **2010,** 10, 1050.
164. Wang, X.; Peng, K.-Q.; Pan, X.-J.; Chen, X.; Yang, Y.; Li, L.; Meng, X.-M.; Zhang, W.-J.; Lee, S.-T. *Angew. Chem. Int. Ed.,* **2011,** 50, 9861.
165. Song, T.; Zhang, F.; Lei, X.; Xu, Y.; Lee, S.; Sun, B. *Nanoscale,* **2012,** 4, 1336.
166. Shen, X.; Sun, B.; Liu, D.; Lee, S.-T. *J. Am. Chem. Soc.,* **2011,** 133, 19408.
167. Lai, Y.-C.; Chang, Y.-F.; Tsai, P.-T.; Chang, J.-k.; Tseng, W.-H.; Lin, Y.-C.; Hsiao, C.-Y.; Zan, H.-W.; Wu, C.-I.; Chi, G.-C.; Meng, H.-F.; Yu, P. *Opt. Exp.,* **2016,** 24, A414.
168. Togonal, A. S.; Foldyna, M.; Chen, W.; Wang, J. X.; Neplokh, V.; Tchernycheva, M.; Nassar, J.; Roca i Cabarrocas, P.; Rusli. *J. Phys. Chem. C,* **2016,** 120, 2962.
169. Petterson, M. K.; Lemaitre, M. G.; Shen, Y.; Wadhwa, P.; Hou, J.; Vasilyeva, S. V.; Kravchenko, I. I.; Rinzler, A. G. *ACS Appl. Mater. Int.,* **2015,** 7, 21182.
170. Kim, D. R.; Lee, C. H.; Rao, P. M.; Cho, I. S.; Zheng, X. *Nano Lett.,* **2011,** 11, 2704.
171. Dasgupta, N. P.; Sun, J.; Liu, C.; Brittman, S.; Andrews, S. C.; Lim, J.; Gao, H.; Yan, R.; Yang, P. *Adv. Mater.,* **2014,** 26, 2137.
172. Liu, C.; Dasgupta, N. P.; Yang, P. *Chem. Mater.,* **2014,** 26, 415.
173. Kargar, A.; Kim, S. J.; Allameh, P.; Choi, C.; Park, N.; Jeong, H.; Pak, Y.; Jung, G. Y.; Pan, X.; Wang, D.; Jin, S. *Adv. Func. Mater.,* **2015,** 25, 2609.
174. Zhang, L.; Liu, C.; Wong, A. B.; Resasco, J.; Yang, P. *Nano Res.,* **2015,** 8, 281.
175. Liu, Q.; Wu, F.; Cao, F.; Chen, L.; Xie, X.; Wang, W.; Tian, W.; Li, L. *Nano Res.,* **2015,** 8, 1.
176. Boettcher, S. W.; Warren, E. L.; Putnam, M. C.; Santori, E. A.; Turner-Evans, D.; Kelzenberg, M. D.; Walter, M. G.; McKone, J. R.; Brunschwig, B. S.; Atwater, H. A.; Lewis, N. S. *J. Am. Chem. Soc.,* **2011,** 133, 1216.
177. LaTempa, T. J.; Rani, S.; Bao, N.; Grimes, C. A. *Nanoscale,* **2012,** 4, 2245.
178. Torralba-Peñalver, E.; Luo, Y.; Compain, J.-D.; Chardon-Noblat, S.; Fabre, B. *ACS Catalysis,* **2015,** 5, 6138.
179. Liu, R.; Yuan, G.; Joe, C. L.; Lightburn, T. E.; Tan, K. L.; Wang, D. *Angew. Chem. Int. Ed.,* **2012,** 51, 6709.
180. Hochbaum, A. I.; Chen, R.; Delgado, R. D.; Liang, W.; Garnett, E. C.; Najarian, M.; Majumdar, A.; Yang, P. *Nature,* **2008,** 451, 163.
181. Li, C.; Krali, E.; Fobelets, K.; Cheng, B.; Wang, Q. *Appl. Phys. Lett. ,* **2012,** 101, 222101.
182. Lee, E. K.; Yin, L.; Lee, Y.; Lee, J. W.; Lee, S. J.; Lee, J.; Cha, S. N.; Whang, D.; Hwang, G. S.; Hippalgaonkar, K.; Majumdar, A.; Yu, C.; Choi, B. L.; Kim, J. M.; Kim, K. *Nano Lett.,* **2012,** 12, 2918.
183. Yang, K.; Cantarero, A.; Rubio, A.; D'Agosta, R. *Nano Res.,* **2015,** 8, 2611.

184. McSweeney, W.; Geaney, H.; O'Dwyer, C. *Nano Res.,* **2015,** 8, 1395.
185. Yao, Y.; Liu, N.; McDowell, M. T.; Pasta, M.; Cui, Y. *Energy Environ. Sci.,* **2012,** 5, 7927.
186. Liang, B.; Liu, Y.; Xu, Y. *J. Power Sources,* **2014,** 267, 469.
187. Cui, L.-F.; Ruffo, R.; Chan, C. K.; Peng, H.; Cui, Y. *Nano Lett.,* **2009,** 9, 491.
188. Bogart, T. D.; Oka, D.; Lu, X.; Gu, M.; Wang, C.; Korgel, B. A. *ACS Nano,* **2014,** 8, 915.
189. Wang, B.; Li, X.; Luo, B.; Jia, Y.; Zhi, L. *Nanoscale,* **2013,** 5, 1470.
190. Xia, F.; Kwon, S.; Lee, W. W.; Liu, Z.; Kim, S.; Song, T.; Choi, K. J.; Paik, U.; Park, W. I. *Nano Lett.,* **2015,** 15, 6658.
191. Chan, C. K.; Patel, R. N.; O'Connell, M. J.; Korgel, B. A.; Cui, Y. *ACS Nano,* **2010,** 4, 1443.
192. Chen, H.; Xiao, Y.; Wang, L.; Yang, Y. *J. Power Sources,* **2011,** 196, 6657.
193. Kohandehghan, A.; Cui, K.; Kupsta, M.; Memarzadeh, E.; Kalisvaart, P.; Mitlin, D. *J. Mate. Chem. A,* **2014,** 2, 11261.
194. Memarzadeh, E. L.; Kalisvaart, W. P.; Kohandehghan, A.; Zahiri, B.; Holt, C. M. B.; Mitlin, D. *J. Mate. Chem.,* **2012,** 22, 6655.
195. Kohandehghan, A.; Kalisvaart, P.; Kupsta, M.; Zahiri, B.; Amirkhiz, B. S.; Li, Z.; Memarzadeh, E. L.; Bendersky, L. A.; Mitlin, D. *J. Mate. Chem. A,* **2013,** 1, 1600.
196. Chockla, A. M.; Bogart, T. D.; Hessel, C. M.; Klavetter, K. C.; Mullins, C. B.; Korgel, B. A. *J. Phys. Chem. C,* **2012,** 116, 18079.
197. Memarzadeh Lotfabad, E.; Kalisvaart, P.; Cui, K.; Kohandehghan, A.; Kupsta, M.; Olsen, B.; Mitlin, D. *Phys. Chem. Chem. Phys.,* **2013,** 15, 13646.
198. Kohandehghan, A.; Kalisvaart, P.; Cui, K.; Kupsta, M.; Memarzadeh, E.; Mitlin, D. *J. Mate. Chem. A,* **2013,** 1, 12850.
199. Nguyen, H. T.; Zamfir, M. R.; Duong, L. D.; Lee, Y. H.; Bondavalli, P.; Pribat, D. *J. Mater. Chem. ,* **2012,** 22, 24618.
200. Wang, J.; Meng, X.; Fan, X.; Zhang, W.; Zhang, H.; Wang, C. *ACS Nano,* **2015,** 9, 6576.
201. Wang, X.-L.; Han, W.-Q. *ACS Appl. Mater. Int.,* **2010,** 2, 3709.
202. Kennedy, T.; Brandon, M.; Ryan, K. M. *Adv . Mater. doi:10.1002/adma.201503978,* **2016**.
203. Cui, Y.; Wei, Q.; Park, H.; Lieber, C. *Science,* **2001,** 293, 1289.
204. Wang, B.; Haick, H. *ACS Appl. Mater. Int.,* **2013,** 5, 2289.
205. Shehada, N.; Brönstrup, G.; Funka, K.; Christiansen, S.; Leja, M.; Haick, H. *Nano Lett.,* **2015,** 15, 1288.
206. Wipf, M.; Stoop, R. L.; Tarasov, A.; Bedner, K.; Fu, W.; Wright, I. A.; Martin, C. J.; Constable, E. C.; Calame, M.; Schönenberger, C. *ACS Nano,* **2013,** 7, 5978.
207. Zhang, C. X.; Liu, L.; Yin, H. J.; Fang, H.; Zhao, Y. M.; Bi, C. J.; Xu, H. J. *Appl. Phys. Lett.,* **2014,** 105, 011905.
208. Han, X.; Wang, H.; Ou, X.; Zhang, X. *J. Mater. Chem.,* **2012,** 22, 14127.
209. Yang, X.; Zhong, H.; Zhu, Y.; Shen, J.; Li, C. *Dalton Trans.,* **2013,** 42, 14324.
210. Zhang, B.; Wang, H.; Lu, L.; Ai, K.; Zhang, G.; Cheng, X. *Adv. Func. Mater.,* **2008,** 18, 2348.
211. Huang, J.-A.; Zhao, Y.-Q.; Zhang, X.-J.; He, L.-F.; Wong, T.-L.; Chui, Y.-S.; Zhang, W.-J.; Lee, S.-T. *Nano Lett.,* **2013,** 13, 5039.
212. Zhang, G.-J.; Ning, Y. *Anal. Chim. Acta,* **2012,** 749, 1.
213. Chen, K.-I.; Li, B.-R.; Chen, Y.-T. *Nano Today,* **2011,** 6, 131.
214. Nuzaihan M.N, M.; Hashim, U.; Md Arshad, M. K.; Kasjoo, S. R.; Rahman, S. F. A.; Ruslinda, A. R.; Fathil, M. F. M.; Adzhri, R.; Shahimin, M. M. *Biosens. Bioelectron.,* 83, 106.
215. Adam, T.; Hashim, U. *Biosens. Bioelectron.,* **2015,** 67, 656.
216. Xu, T.-T.; Huang, J.-A.; He, L.-F.; He, Y.; Su, S.; Lee, S.-T. *Appl . Phys. Lett.,* **2011,** 99, 153116.
217. Zhang, M.-L.; Yi, C.-Q.; Fan, X.; Peng, K.-Q.; Wong, N.-B.; Yang, M.-S.; Zhang, R.-Q.; Lee, S.-T. *Appl. Phys. Lett.,* **2008,** 92, 043116.

218. Su, S.; Wei, X.; Zhong, Y.; Guo, Y.; Su, Y.; Huang, Q.; Lee, S.-T.; Fan, C.; He, Y. *ACS Nano,* **2012,** 6, 2582.
219. Han, S. W.; Lee, S.; Hong, J.; Jang, E.; Lee, T.; Koh, W.-G. *Biosensors and Bioelectronics,* **2013,** 45, 129.
220. Han, J.-W.; Rim, T.; Baek, C.-K.; Meyyappan, M. *ACS Appl. Mater. Int.,* **2015,** 7, 21263.
221. Noh, J.-S.; Kim, H.; Kim, B. S.; Lee, E.; Cho, H. H.; Lee, W. *J. Mate. Chem.,* **2011,** 21, 15935.
222. McAlpine, M. C.; Agnew, H. D.; Rohde, R. D.; Blanco, M.; Ahmad, H.; Stuparu, A. D.; Goddard, W. A.; Heath, J. R. *J. Am. Chem. Soc.,* **2008,** 130, 9583.
223. Liao, J.; Li, Z.; Wang, G.; Chen, C.; Lv, S.; Li, M. *Phys. Chem. Chem. Phys.,* **2016,** 18, 4835.
224. Chen, X.; Zhang, J.; Wang, Z.; Yan, Q.; Hui, S. *Sensor. Actuat. B: Chem.,* **2011,** 156, 631.
225. Engel, Y.; Elnathan, R.; Pevzner, A.; Davidi, G.; Flaxer, E.; Patolsky, F. *Angew. Chem. Int. Ed.,* **2010,** 49, 6830.
226. Liao, F.; Wang, T.; Shao, M. *J. Mater. Sci: Mater. Electron.,* **2015,** 26, 4722.
227. Wang, H.; Jiang, W.; Yuan, L.; Wang, L.; Chen, H. *ACS Appl. Mater. Int.,* **2013,** 5, 1800.
228. Wang, H.; Jiang, W.; Wang, Y.; Liu, X.; Yao, J.; Yuan, L.; Wu, Z.; Li, D.; Song, B.; Chen, H. *Langmuir : the ACS journal of surfaces and colloids,* **2013,** 29, 3.
229. Song, H. S.; Zhang, W. J.; Cheng, C.; Tang, Y. B.; Luo, L. B.; Chen, X.; Luan, C. Y.; Meng, X. M.; Zapien, J. A.; Wang, N.; Lee, C. S.; Bello, I.; Lee, S. T. *Cryst. Growth Des.,* **2011,** 11, 147.
230. Chia-Yun, C.; Arh-Hwang, C. *J. Phys. D: Appl. Phys.,* **2012,** 45, 365304.
231. Duan, C.; Wang, H.; Zhang, B.; Li, F.; Ou, X.; Zhang, X. *Chem. Comm.,* **2015,** 51, 3383.
232. Chen, Y.-H.; Li, W.-S.; Liu, C.-Y.; Wang, C.-Y.; Chang, Y.-C.; Chen, L.-J. *J. Mater. Chem. C,* **2013,** 1, 1345.

Chapter 2

Experimental Techniques

In this chapter, the details of the fabrication method of Si NWs by metal assisted chemical etching are presented followed by the fabrication of NW heterostructure. For the characterization of the as-grown and processed samples, several standard analytical and spectroscopic tools are used, which are presented in briefly. The in-house development of laser excitation-based photoluminescence measurement setup is described elaborately. The methodology adopted to analyze the data from various spectroscopic tools is also presented at the end.

2.1. Fabrication of Si Nanowires and Heterostructures

From the application point of view, the method of fabrication of the Si NWs strongly influences the properties of Si NWs. The production of large area, highly oriented array of Si NWs structures with controlled properties is extremely important for device applications and improvement in device performances. Over the past decades, Si NWs have been fabricated by several groups worldwide using various bottom-up methods, such as chemical vapor deposition (CVD), pulsed laser deposition (PLD), thermal evaporation, template assisted growth, molecular beam epitaxy (MBE) etc. and top-down approaches, such as reactive ion etching (RIE), and metal assisted chemical etching (MACE) etc.[1-16] Out of several traditional top-down and bottom-up approaches, MACE method is widely explored for their versatility about controllability, quality, low cost and mass production of Si NWs. Several review articles have been published describing the synthesis of Si NWs.[1, 2, 17-28] Easy fabrication process, significant by improved device performance and cost effectiveness are the major advantages of MACE for the growth of large area, ordered and uniform Si NWs.

2.1.1. Metal Assisted Chemical Etching Method

The solution-based MACE has emerged as a promising and significant tool for large area, vertical, ordered, and single crystalline Si NW arrays due to its ease and low cost of production.[12, 13, 22, 24, 29-32] The microscopic mechanism for the MACE is mainly based on noble metal-induced local oxidation and anisotropic dissolution of Si substrates in aqueous oxidizing HF acid solution. The MACE process is divided into two subgroup; (a) one-step etching

(simultaneous metal deposition and etching of Si) and two-step etching of Si (pre-deposited metal on Si wafer). The mechanism of etching is same in both the cases, although the mechanism of MACE is still under debate.[12, 13, 22, 24, 29-31] The selective etching of Si substrate in preferential direction leads to the growth of vertical and aligned Si NWs. Note that MACE requires a galvanic displacement of noble metal NPs as a catalyst on the surface of the crystalline Si substrate and Ag, Au, Ag/Au and Au/Pd alloy have been demonstrated to be effective catalysts for MACE of Si for the present study.[32-36] Various oxidative agents have been mixed with HF to etch noble metal-loaded Si substrates, including $AgNO_3$ and H_2O_2.[32-36] Fig. 2.1(a) shows a digital photograph of Teflon beaker and Teflon tweezer, and (b) shows a schematic diagram of two-step etching process in a Teflon beaker.

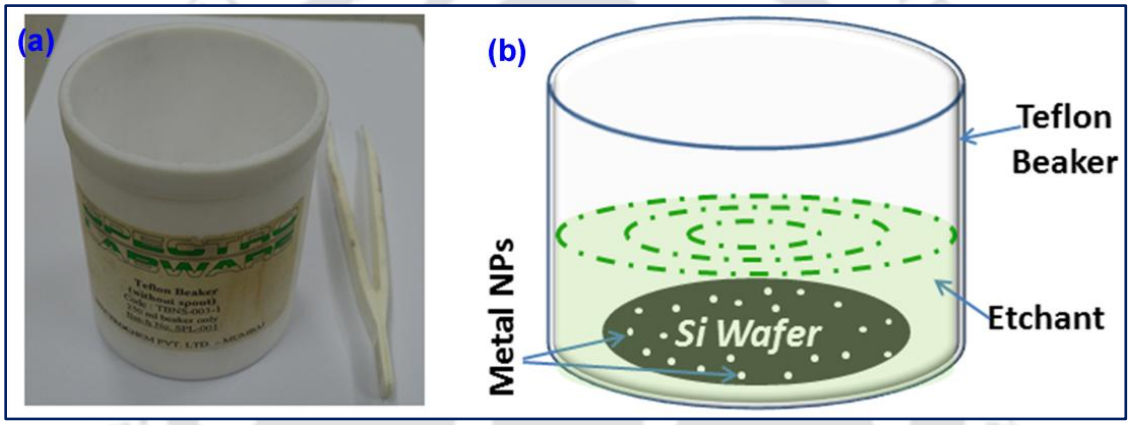

Fig. 2.1. (a) A digital photograph of Teflon beaker and Teflon tweezer. (b) A schematic diagram of two-step etching process in Teflon beaker.

2.1.1.1. *Wafer Cleaning and Substrate Preparation*

Prior to etching, Si wafers are cleaned to remove dust and contaminations on itshe surface. For cleaning the Si wafers, we have followed the standard RCA process. Firstly, the Si wafers were cleaned by rinsing in acetone followed by ethanol for 5 min in each step. The wafers were cleaned in piranha solution (a 5:1 mixture of H_2SO_4 and H_2O_2) for 10 min to remove the metallic and alkaline contamination as well as for the reduction of organic residues on the wafer surface. Native oxide layer (SiO_2) was removed by immersing the wafers in 10% hydrofluoric acid (HF) for a few minutes. The samples were rinsed in de-ionized (DI) water after each step. Finally the cleaned wafers were dried by a blow of Ar gas.

2.1.1.2. *Metal Deposition*

For the deposition of thin layer of Ag nanoparticles (NPs), the Si substrates were dipped into a solution containing 0.015 M $AgNO_3$ plus 5.55 M HF for 2, 4, 6 and 8 sec. The beaker contained 5 mL HF (48%), 64 mg $AgNO_3$ and 20 mL DI water.

In case of Au NPs, an ultrathin Au layer was deposited on Si wafer by a mini sputtering system (C7620, Polaron, UK) with fixed bias of 1 kV. The Au sputtering was carried out in vacuum at a current of 5 mA for 30, 60 and 120 sec. Corresponding thickness are ~10, ~20 and ~40 nm, respectively.

2.1.1.3. *Etching in Etchant*

In case of one-step MACE process, the cleaned wafers are dipped into a solution in the Teflon beaker containing HF + $AgNO_3$. Several reports have been published explaining the possible mechanism of Si nanostructure formation by one-step MACE.[24, 29, 37-40] Out of these models, microscopic electrochemical cell model is considered very important, where Ag-NPs acts as the cathode and Si beneath the Ag NP acts as the anode. In this self-assembled Ag induced selective etching process, continuous galvanic displacement of Si by Ag^+ via $Ag^+ \rightarrow Ag$ reduction occurs on the Si surface.[29, 34, 37, 39, 40] It results in a large density of local nano electrochemical cells being formed on the Si surface. The self-assembled reactions taking place during the etching process is described as:

In the Solution

$$AgNO_3 \rightarrow Ag^+ + NO_3^- \quad \text{..... (2.1a)}$$

At the cathode

$$4Ag^+ \rightarrow 4Ag + 4h^+ \quad \text{..... (2.1b)}$$

At the anode

$$Si + 2H_2O + 4h \rightarrow SiO_2 + 4H^+ \quad \text{..... (2.1c)}$$

$$SiO_2 + 6HF \rightarrow H_2SiF_6 + 2H_2O \quad \text{..... (2.1d)}$$

The complete reaction

$$Si + 4Ag^+ + 6HF \rightarrow 4Ag + H_2SiF_6 + 2H_2\uparrow \quad \text{..... (2.1e)}$$

In the cathode, the reduction of Ag^+ ions produces metallic Ag droplets. It is considered that holes are injected into Si following the capture of electrons by Ag^+ ions, since Ag is more electronegative than the Si and hence providing an easy injection path for the hole. Consequently, in the anodic reaction, oxidization of the atoms of Si surface takes place by the

release of electrons. The oxidized Si is chemically dissolved in HF etchants (in the form of H_2SiF_6), allowing the newly exposed Si to come in contact with the Ag catalysts, which is further etched in the next cycle of the continuous process. As discussed above, the charge exchange and

Table 2.1: *Details of the growth parameters of Si NWs and the corresponding sample codes.*

Si Wafer Specification	Etching Type	Noble Metal Used	Metal Deposition Process	Etching Duration	Etching Solution	Sample Code
P-type, Si(100), 1-10 Ω-cm	One-step	Ag	--	60 min	0.015M $AgNO_3$ & 5.55M HF	P
	Two-step		Chemical	60 min		Q
P-type, Si(100), 1-10 Ω-cm	Two-step	Ag	Chemical	15 min	4.6M HF & 1.422M H_2O_2	R
	Two-step	Ag	Chemical	20 min		R1
P-type, Si(100), 0.01 Ω-cm	Two-step	Ag	Chemical	20 min	H_2O_2 : HF:: 2:2	S1HF2
					H_2O_2 : HF:: 2:3	S1HF3
					H_2O_2 : HF:: 2:4	S1HF4
					H_2O_2 : HF:: 2:5	S1HF5
					H_2O_2 : HF:: 2:6	S1HF6
					H_2O_2 : HF:: 2:7	S1HF7
					H_2O_2 : HF:: 2:8	S1HF8
P-type, Si(111), 0.001 Ω-cm	Two-step	Ag	Chemical	20 min	H_2O_2 : HF:: 2:2	S2HF2
					H_2O_2 : HF:: 2:3	S2HF3
					H_2O_2 : HF:: 2:4	S2HF4
					H_2O_2 : HF:: 2:5	S2HF5
					H_2O_2 : HF:: 2:6	S2HF6
					H_2O_2 : HF:: 2:7	S2HF7
					H_2O_2 : HF:: 2:8	S2HF8
P-type, Si(100), 1-10 Ω-cm	Two-step	Ag	Thermal Evaporation	5 min	H_2O_2 : HF:: 1:4	AgSi
		Au				AuSi
		Ag/Au				AgAuSi

transport between the anode (Si) and the cathode sites (Ag particles) would be more favorable at the Ag/Si interface as compared to the regions devoid of Ag particles (examples: pore walls and Si regions not covered by Ag). Consequently, oxidation and dissolution of Si occur at the bottom of the pore to the location where Ag particles reside and sink as the process proceeds with time, rather than at the pore walls. A schematic diagram of this growth process is shown in Fig. 1.3(a), *Chapter 1*. In fact, the Ag particles tend to move along the direction in which the substrate Si is oriented intrinsically.[39, 41] In a continuous process, it leads to straight vertical pores on the Si surface resulting in vertical Si NW arrays. On the other hand, the unreacted Ag nanoclusters agglomerate on top of Si surface to form the dendritic structures, resulting in a noncompact Ag layer. The Ag dendrites are easily removed by HNO_3 etching and an array of vertical Si NWs is thus formed by single a step MACE.

In case of two-step MACE, the Si wafers with pre-deposited metal NPs are dipped into HF/H_2O_2 solution. The metal NPs become metal ions very easily due to the presence of H_2O_2

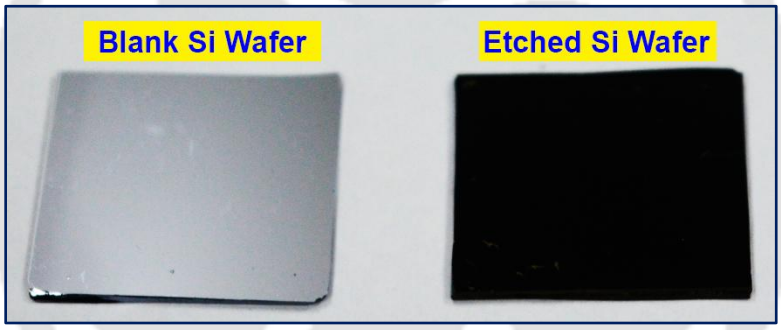

Fig. 2.2. Digital photographs of Si wafer before and after MACE process.

and then the rest of the reaction is same as it is in one-step MACE. The main advantage of two-step MACE over one-step MACE is its control over the diameter of the Si NWs and the inter-NWs spacing. However, after Si NWs formation the color of the etched Si becomes very dark as shown in Fig. 2.2. The details of the sample codes and the growth parameters including the type of the Si wafers used for MACE, etching condition and the type of noble metal used with their deposition process are presented in Table 2.1.

2.1.2. Rapid Thermal Annealing

Conventional furnace annealing (CFA) and rapid thermal annealing (RTA) are often used for improving the material properties, processing of substrate, sample and surface modification. RTA provides certain advantages over CFA. Relatively long thermal cycles of CFA may cause

certain impurities to activate and they may be diffused into the material under investigation which is highly undesirable. On the other hand, RTA provides much reduced thermal cycles in the order of a few minutes rather than hours in case of CFA. Therefore, RTA can provide a better structural quality with a less time consuming process. We have used the RTA (Mila 3000P, ULVAC, Japan) to form metal NPs droplets on Si wafer from the vacuum deposited metal film on Si wafer. Fig. 2.2 shows the digital photograph of the compact table-top mini lamp RTA system. The system is build up around a gold reflector infrared lamp furnace and contains a high precision programmable temperature controller. The system can perform maximum temperature up to 1200℃ and a maximum heating rate of 50℃/sec. This system also has option for annealing in vacuum and different gas environment. We have performed RTA under vacuum and different gas environment for the surface modification of Si NWs.

Fig. 2.2. A digital photograph of the RTA system (Mila 3000P, ULVAC, Japan).

2.1.3. RF Magnetron Sputtering

Magnetron sputtering is a very useful technique for the preparation of high quality crystalline thin films of any kind of materials. We used this technique for the fabrication of good quality ZnO film on Si NWs to form Si NW/ZnO core/shell heterostructure. The photograph of the magnetron sputtering system is shown in Fig. 2.4.The magnetron sputtering system consists of a high vacuum chamber (HHV, India), magnetron head (Angstrom Science, USA) along with the holder of the target material, 13.56 MHz radio frequency (RF) source (Comdel, USA) and a substrate heater assembly (Hind Hivac, India). The magnetron sputtering is the process of ejection of atoms by ionic bombardment under the magnetic field and RF source. Here crossed electric and magnetic field lines are created by alternate arrangement of permanent magnet pole assembly and RF source. Magnetic field lines form a closed path on the target (material to be

deposited) surface, which confines more and more electrons on the surface causing ionization. The ions are accelerated towards the target and it ejects surface atoms from the target. Then these atoms move towards the substrate by electric field and then condensed on the substrate surface resulting in a thin film. Our RF magnetron sputtering operated with a power of 50-200 W.

Fig. 2.4. A Photograph of the magnetron sputtering system (Hind Hivac, Bangalore).

2.2. Characterization Techniques

Several experimental tools are used to study the characteristic properties of the different samples. Morphological and structural characterizations were performed by the field emission scanning electron microscopy (FESEM), transmission electron microscopy (TEM), high resolution TEM (HRTEM), atomic force microscopy (AFM), X-ray diffraction (XRD) techniques, X-ray photoelectron spectroscopy (XPS), and Fourier transform infrared (FTIR) spectroscopy. These studies help us to understand the surface morphologies, crystal structure, crystalline quality, presence of impurities in the structure etc. For optical characterizations, we used micro-Raman, UV-visible-near infrared (UV-vis-NIR) optical absorption, steady state photoluminescence (PL), time-resolved photoluminescence (TRPL). Photocatalysis studies were performed in a commercial photocatalytic reactor.

2.2.1. Morphological and Structural Characterization

2.2.1.1. *Field Emission Scanning Electron Microscopy (FESEM)*

The FESEM is a very powerful tool for high resolution surface imaging of nanomaterials. The FESEM use a beam of electrons to probe objects on a very fine scale. The

use of electrons has two main advantages over optical microscopes: much larger magnifications are possible since electron wavelengths are much smaller than photon wavelengths and the depth of field is much higher. The electron wavelength depends on the electron velocity or the accelerating voltage as

$$\lambda_e = \frac{h}{mV} = \frac{h}{\sqrt{2qmV}} = \frac{1.22}{\sqrt{V}} nm \qquad \text{..... (2.2)}$$

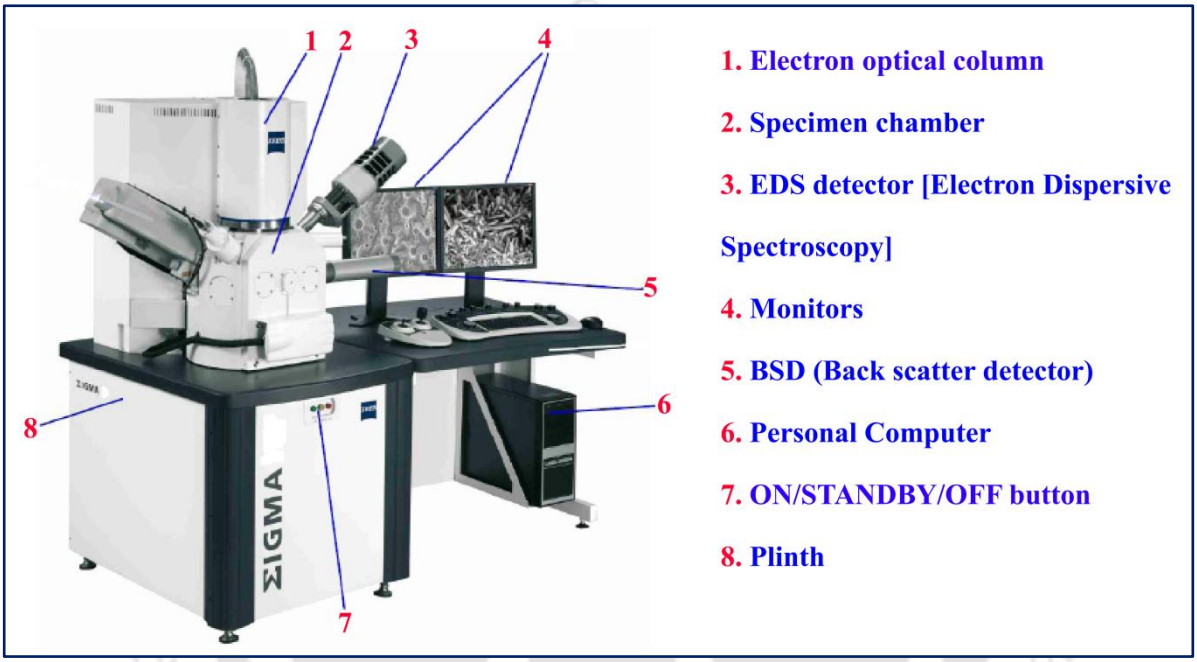

Fig. 2.5. An overview of the components of the Field Emission Scanning Electron Microscope (Sigma Zeiss, Germany)

Thus, for a 30 kV acceleration voltage, the resolution is extremely high. A photograph with the brief overview of the FESEM (Sigma Zeiss, Germany) used in the present study is shown in Fig. 2.5. In the FESEM, electrons are emitted from a field emission source under extreme vacuum. The vacuum allows the electrons movement along a column without scattering, which helps to prevent discharges inside the instrument. The field emission source is a tungsten filament (cathode) with sharp tip which is placed in a huge electrical potential gradient. The significance of extremely thin and sharp tip (diameter 10-100 nm) is that an electric field can be concentrated to an extreme level so that the work function of the material is lowered and electrons can leave the cathode. After emission, the electrons are accelerated by the two anodes. An accelerating voltage (0.5- 30 kV) between the cathode and anode is commonly used. This voltage combined

with beam diameter determines the resolution of the image. As the voltage increases, better point-to-point resolution can be obtained. Because of the smaller size of the electron source, the beam produced by this emitter is about 1000 times smaller in diameter than that in a standard scanning electron microscope (SEM), which markedly improves the image resulation. The beam is collimated by electromagnetic condenser lenses, focused by an objective lens, and scanned across the surface of the sample by electromagnetic deflection coils. The primary imaging method is by collecting emitted secondary electrons that are released by the sample. A secondary electron detector is placed near to the specimen. By correlating the sample scan position with the resulting signal, an image is formed on the screen that is strikingly similar to what would be seen through an optical microscope. The FESEM is equipped with a special objective or focusing lens that projects the magnetic field below the lens. Very high resolution is obtained by shortening the specimen–lens distance and using a specially designed in-lens. The distance is shortened by placing the specimen in the lens magnetic field. In this case, secondary electron detector is placed above the objective in-lens (called as in-lens detector), which makes difference in the image compared to the conventional image of the secondary electron detector. Very high resolution and contrast can be obtained by using in-lens detector. The type of electron source is the main difference between SEM and FESEM. In SEM, electrical current is used to heat up the filament and when the heat is enough to overcome the work function of the filament, electron escape from the material.

Interaction of the primary electron beam with atoms in the sample causes shell transitions which result in the emission of an X-ray. The emitted X-ray has an energy characteristic of the parent element. Detection and measurement of the energy permits elemental analysis by means of Energy Dispersive X-ray Spectroscopy (EDS). EDS provides rapid qualitative, or with adequate standards, quantitative analysis of elemental composition with a sampling depth of 1-2 microns. X-rays may also be used to form maps or line profiles, showing the elemental distribution in a sample surface.

For the FESEM imaging of Si NWs, as-synthesized Si NWs samples were directly mounted on the FESEM stub using a carbon tape. Here the carbon tape is used as adhesive to stick the sample and it also provides an electrical conduction path to the sample. For cross-sectional view of the sample, we have placed the sample vertically on the stub.

2.2.1.2. *Transmission Electron Microscopy (TEM)*

TEM is one of the best characterization tools for nanomaterials in which structural information can be acquired by high resolution imaging close to the atomic level (0.2 nm) as well as by electron diffraction. The high resolution TEM (HRTEM) known as lattice imaging, gives the structural information and presence of defects or dislocations. The growth orientation and lattice spacing can be studied from the lattice fringe image. The crystallographic information about the nanomaterials such as crystal structure (cubic, tetragonal, hexagonal or monoclinic etc.), crystallinity (single crystalline, poly-crystalline or amorphous) can be drawn from the selected area electron diffraction (SAED) patterns. In case of a crystalline material, electron diffraction will only occur at specific angles, which are the characteristic features for the crystal structures present. Moreover, elemental and chemical composition analysis down to sub-nanometer scale can be acquired with additional detector, such x-ray detector by EDX analysis. Fig. 2.6 shows the schematic diagram of a TEM machine. It works on the principle of optical projection; when an object is placed in front of a light source, its image is enlarged and shadow is created on the screen placed far behind the object. Electrons emitted from an electron gun are accelerated to high voltages (typically 100 to 400 kV) and focused on the sample by a number of condenser lenses.[42] A lanthanum hexaboride (LaB_6) crystal is used for thermionic electron emission. The emitted electrons pass through a series of lenses to be focused and scanned across the sample. The sample is placed on a small copper grid a few mm (~3 mm) in diameter. The static beam has a diameter of a few microns. The sample must be sufficiently thin (a few tens to a few hundred nm) to be transparent to electrons. The transmitted and forward scattered electrons form a diffraction pattern in the back focal plane and a magnified image in the image plane. With additional lenses, either the image or the diffraction pattern is projected onto a fluorescent screen for viewing or photographic recording.

In the present study, a TEM (JEM2100, JEOL, Japan) operating at 200 kV with high resolution CCD camera (Gatan, USA) is used for the normal TEM and HRTEM imaging. Sample for the TEM imaging was prepared by the following way: (a) the Si NWs were scratched from the Si wafer by a sharp razor blade; (b) the scratched Si NWs were dispersed in an acetone solvent; (c) a transparent dispersion of Si NWs was prepared by ultra-sonication for long duration and then drop casted on the carbon coated copper grid containing few hundreds of square shaped hollow meshes with dimension of ~1 μm; (d) after normal dry for prolong time,

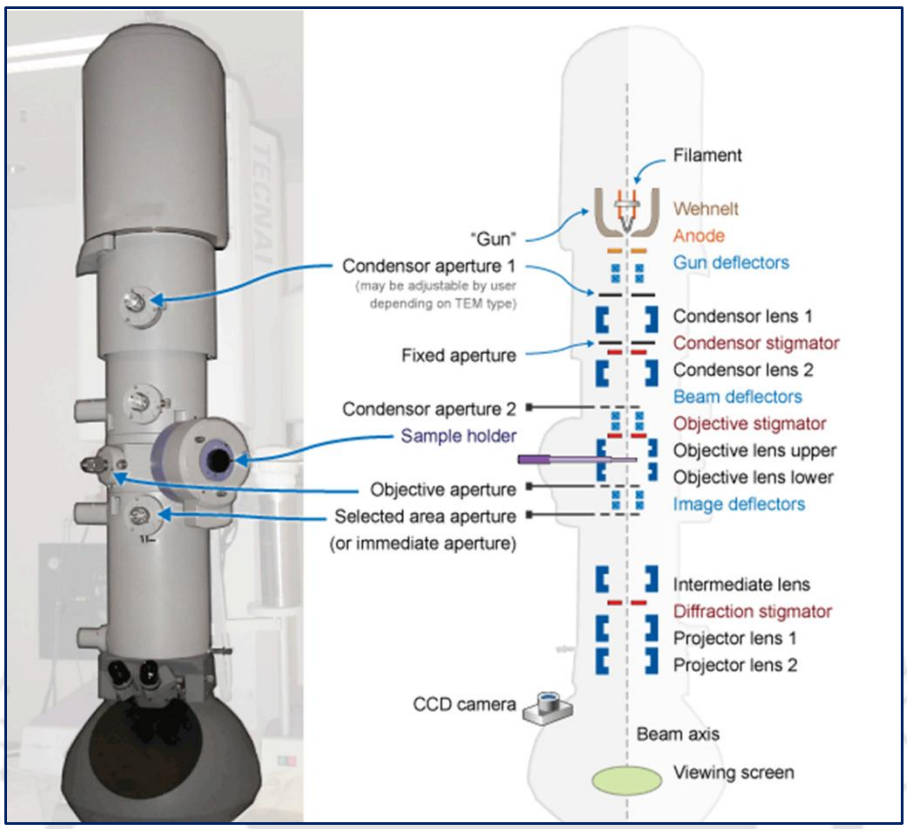

Fig. 2.6. Schematic diagram of a Transmission Electron Microscope showing its different components.

this grid is used for TEM imaging. The TEM and HRTEM images were processed by using '*Digital Micrograph* (Gatan, USA)' image analysis software. Improved resolution of the lattice image was obtained after processing using fast Fourier transformation (FFT). In addition, we used SAED pattern to understand orientation of the crystallographic orientation of the Si nanostructures.

2.2.1.3. *Atomic Force Microscopy (AFM)*

The AFM probes the surface of a sample with a sharp tip, a couple of microns long and often less than 100Å in diameter. The tip is at the end point of the cantilever that is ~100-200 μm long. The force between the tip and the sample surface causes the cantilever bend, or deflect. A detector measure the deflection as the tip scanned over the surface. The measured deflection allows a computer to generate a map of the surface topography. The force acting in this region is generally van der Walls force of the magnitude ~ 10^{-9} N. Depending upon the operation and the tip to sample distance there are two type of operation: (i) *Contact* and (ii) *Non-Contact* mode.

The force distance curve is shown in the Fig. 2.7(a) which define the region of operation in different modes.[43] When the tip is moving throughout the sample, the deflection of the cantilever is monitored using a laser focused at the top of the cantilever. The reflected light is detected by a high sensitive quadrant photodiode. The obtained laser signal is redirected into a well-constructed feedback loop to adjust the vertical piezoelectric scanner displacement, which keep the cantilever deflection constant. So the surface topography can be recorded by monitoring the motion of the piezoelectric scanner. Depending upon the mode of operation, there are two types:

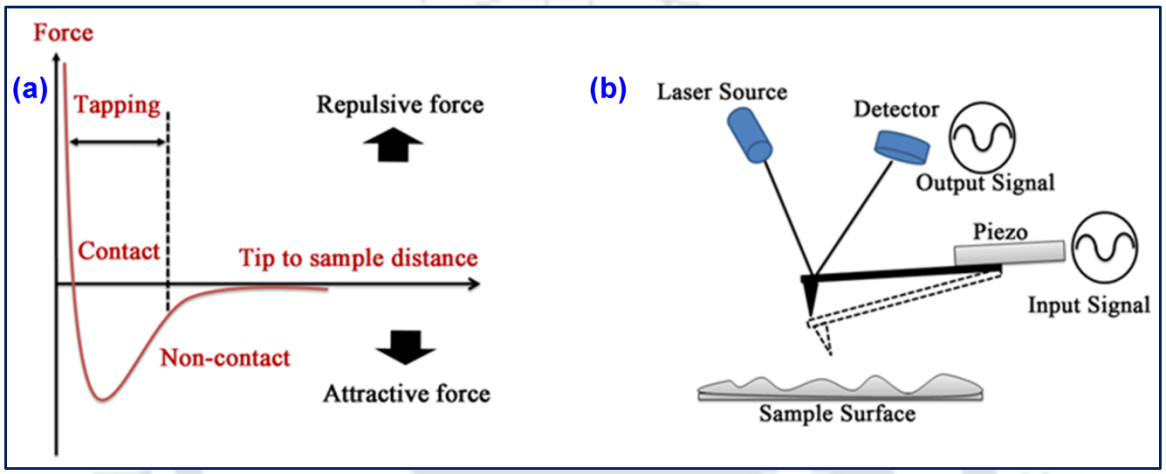

Fig. 2.7. (a) The qualitative dependence of the van der Waals force on inter-atomic distance. (b) A schematic diagram of the AFM operation in non-contact mode.

constant height and constant force modes. However, in contact mode the tip is so close to the sample surface that it feels the repulsive force, whereas in non-contact mode the cantilever vibrates near the surface of the sample (generally 50-150 Å above the sample) near the resonant frequency (100-400 kHz) with the amplitude of few ten to hundred angstrom. The operation in non-contact mode is shown in the Fig. 2.7(b).

In this study, AFM imaging of the samples were done by an *Agilent SPM5500* in non-contact mode using Si tips (Nanosensors, PPP-NCH-20). We have used AFM for understanding the size of the metal NPs on the surface of the Si wafers and calculation of the statistical parameters (growth exponents) of the rough surface of the MACE grown Si NWs samples at the early stages of etching. The AFM topography images were processed by the *WSXM* software.

2.2.1.4. *X-ray Diffraction (XRD)*

XRD is one of the most widely used non-destructive techniques for general characterization of crystalline material. The XRD patterns provide information on crystal phases, lattice parameters,

crystallite size and strain in the material. In XRD, a collimated beam of X-rays, with wavelength λ = 0.5-2.0 Å, is incident on a sample and is diffracted by the atoms of the crystalline phases in the sample according to 'Bragg's law',

$$2d\sin\theta = n\lambda, \qquad \text{..... (2.3a)}$$

where *d* is the spacing between atomic planes in the crystalline phase, θ is the angle of incidence of the x–ray beam with the atomic plane, *n* represents the order of diffraction (we consider only the first order diffraction, *n* =1, because the second order peaks are mostly difficult to detect experimentally). The intensity of the diffracted X–rays is measured as a function of the diffraction angle 2θ. In an X-ray diffraction pattern, the position and intensity of the diffraction peaks are characteristic for the crystallographic structure and the atomic composition of the material. In case of a multi-phase composition, the resulting pattern is a combination of the patterns of all structures present. Phase identification can be done by matching the XRD pattern with reference patterns of pure substances. Owing to the huge data bank available from JCPDS Powder Diffraction Files covering practically every phase of every known material, crystal

Fig. 2.8. A photograph of the X-ray Diffractometer (Rigaku RINT 2500, TTRAX III).

phase of the sample is identified from the peak positions of the diffractogram. Homogeneous or uniform elastic strain in the (hkl) direction can also be calculated from the shift in the diffraction peak positions, and the d_{hkl} spacing of the unstrained crystal. From the peak shapes and width of the diffraction peak, average crystallite size can be calculated.

X-ray diffraction patterns of the synthesized nanostructure samples were obtained using a commercial high power XRD (TTRAX III, Rigaku 2500) using a Cu $K_{\alpha 1}$ (λ = 1.5406 Å)

radiation. A photograph of the XRD instrument in our laboratory is shown in Fig. 2.8. All measurements were carried out at an accelerated voltage of 50 kV and tube current of 200 mA. The scanning step size was 0.01°. The exact peak position and full width half maxima (FWHM) of the XRD peak is obtained from the Lorentzian fitting to the experimental data, using following expression:

$$y = y_0 + \frac{2A}{\pi} \frac{w}{4(x-x_c)^2+x^2}, \qquad \text{..... (2.3b)}$$

where y_0 is the offset constant; x_c, w and A are the peak position, FWHM and area, respectively.

2.2.1.5. ***X-ray Photoelectron Spectroscopy (XPS)***

XPS is a key surface characterization tool, which combines surface sensitivity with the ability to quantitatively obtain both elemental and chemical state information for each element detected, through the chemical shift. It is widely used for studies of surface defects and chemical environment, because of its high sensitivity to surface (i.e., up to 10 nm from the sample surface). It also provides useful information about the depth profile (i.e., an evaluation of the variation of composition with depth) and the surface impurities present in the sample. The principle of XPS is based on the photoelectric effect outlined by Einstein in 1905 was developed by Siegbahn and his research group,[44] where the concept of the photon was used to describe the ejection of electrons from a sample surface when photons impinge upon it. This process can be expressed by the following equation:

$$BE = h\nu - KE - \Phi,$$

where BE is the binding energy of the electron in the atom, hν is the photon energy of X-ray source, KE is the kinetic energy of the emitted electron that is measured in the XPS spectrometer and Φ is the work function of the material being studied. For XPS, Al *K*α (1486.6 eV) or Mg *K*α (1253.6 eV) is generally used as the source of X-rays. The photon is absorbed by an atom of the sample, leading to emission of a core (inner shell) electron. The energy of the photoelectrons leaving the sample is determined using an appropriate electron energy analyzer and this gives a spectrum with a series of photoelectron peaks. For each and every element, there will be a characteristic binding energy associated with each core atomic orbital, i.e., each element will give rise to a characteristic set of peaks in the photoelectron spectrum at kinetic energies determined by the photon energy and the respective binding energies. The peak intensities

Fig. 2.9. Photograph of the X-ray photoelectron spectrometer (ULVAC-PHI, Inc.).

measure how much of a material is at the surface, while the peak positions indicate the elemental and chemical composition. Other values, such as the full width at half maximum (FWHM) are useful indicators of chemical state changes and physical influences.

In this study, XPS measurements were carried out with a PHI X-Tool automated photoelectron spectrometer (ULVAC-PHI, Inc.) using Al *K*α X-ray beam (1486.6 eV) with a beam current of 20 mA. Some of the samples were characterized with ESCALAB 3400 (Shimadzu, Japan) instrument using Mg *K*α X-ray beam (1253.6 eV). Carbon 1s spectrum was used for the calibration of the XPS spectra recorded for various samples. Fig. 2.9 shows the photograph of XPS instrument used for this study.

2.2.1.6. *Fourier Transform Infrared (FTIR) Spectroscopy*

FTIR is one of the powerful spectroscopic tools generally used to determine the structural bonding information, impurities and chemical functional groups in the sample. The FTIR is based on the "*Michelson interference"* combined with Fourier transformation of the source spectrum. FTIR interferogram consists of spectral information of the source along with the

transmittance characteristic of the sample. We used FTIR spectroscopy in reflectance mode of operation for our few samples to confirm the formation of SiO_x on the surface of Si NWs and Si NCs and Si-H related vibration modes in Si nanostructures. In this study, we used a commercial FTIR spectrometer (Perkin Elmer, Spectrum BX) to obtain the reflectance spectrum of the Si nanostructures at room temperature in the range 400-4000 cm^{-1} at a resolution of 2 cm^{-1}. Fig. 2.10 shows the photograph of the FTIR spectrometer. All the spectra were taken after background corrections.

Fig. 2.10. A photograph of the FTIR spectrometer (Perkin Elmer, Spectrum BX).

2.2.1.7. *Brunauer-Emmett-Teller (BET) Surface Area Analyzer*

Brunauer et al. (1938) published the BET theory, which is now established as a standard and reliable technique to characterize porous material and quantitatively analyze the actual surface area of solid substances, including the surface irregularity, porosity and the size of the materials.[45] Physical sorption of gas molecules on solid surface is not only determined by solid surface area, but also temperature, gas pressure and interaction between solid surface and gas. Therefore, for a fixed temperature, the amount of gas adsorbed at given pressure determines the surface area of the materials. Note that the sample is first purged with N_2 at 100-250 °C for few hours to remove surface moisture and volatile contamination. Then, it is cooled to the temperature of liquid N_2 (~77 K) to enable measurable adsorption. The gas adsorption process starts at very low relative pressure. The filling of micropores (diameter smaller than 2 nm) is the dominating effect at this stage. With increasing the relative pressure, the gas molecules start to be adsorbed on the solid surface. The total surface area of the sample can be calculated when a complete monolayer of gas molecules were formed on the sample surface. The mathematical form of the BET model is given in equation:

$$\frac{1}{V\left[\left(\frac{P_0}{P}\right)-1\right]} = \frac{1}{V_m C} + \frac{C-1}{V_m C}\left(\frac{P}{P_0}\right), \qquad \text{..... (2.4)}$$

where P/P_0 is the relative pressure of the inert gas (P_0 is the saturation pressure at a given temperature), V is the quantity of gas adsorbed, V_m is the quantity of gas adsorbed for a monolayer, C is an empirical BET constant indicating the strength of adsorbent-adsorbate interaction. BET model is usually employed to calculate the sample surface area with the data from the isotherm in the classic range of $0.05 < P/P_0 < 0.3$. Note that the gas adsorption process would not stop after monolayer adsorption. Additional molecules continue to be adsorbed to form multiple molecular layers. At higher relative gas pressure, the mesopores (diameter in between 2 nm and 50 nm) start to be filled due to the action called as capillary condensation. When the pores are fully filled, the equilibrium state is reached and the isotherm continue with the gas desorption process at a reducing pressure.

The BET gas sorption experiments in this work have been conducted by Quantachrome autsorb-iQ MP analyzer at 77K. The pore size distribution and total pore volume were estimated by the Barrett-Joyner-Halenda (BJH) model, which was built based on the modified Kelvin equation.[46] For sample preparation, the Si NWs were manually scraped off the Si wafers with a clean razaor blade and collected in a glass tube for degassing for 12 hours at 120°C before gas sorption experiment.

2.2.2. Optical Characterization

2.2.2.1. *UV-Vis-NIR Absorption Spectroscopy*

This technique provides useful information on the interaction of light with a material by measuring the reflection, absorption or transmission properties when light passes through the sample surface. The electronic band structure of any material is determined by the optical absorption of the material. The basic principle is that UV, visible or near infrared (NIR) light is used to excite electrons from valance band (VB) to conduction band (CB). In this case, the substrate should be transparent as the equipment works in transmission geometry. In our study, we have used corning glass and quartz as the substrates for understanding the optical absorption of ZnO thin film and different metal films. When we excite the sample with light of different wavelengths, the materials absorb the light corresponding to the energy of band gap or any state

intermediate to the band gap. Fig. 2.11 shows the photograph of the UV-Vis spectrometer (Shimadzu , Japan).

For photocatalysis studies, we carry out the measurement in organic dye solutions and monitor the changing absorbance of the dye after photocatalytic degradation under light illumination. When some organic dyes are dispersed in a transparent liquid and illuminate with light of different wavelengths, the dye reflects the lights of its color and absorbs/transmits the

Fig. 2.11. A photograph of the UV-Vis-NIR spectrometer (Shimadzu, Japan).

rest of the wavelengths depending upon their HUMO (highest occupied molecular orbital) and LUMO (lowest unoccupied molecular orbital) position due to the presence of different functional groups. We have used UV-Vis-NIR spectroscopy technique to understand the relative amount of colored organic dyes (such as, methylene blue, methyl orange etc.) by monitoring the change in the intensity of the absorption peaks.

2.2.2.2. *Diffuse Reflectance Spectroscopy (DRS)*

DRS is a technique generally used to study the reflectance or absorbance of opaque samples and to measure the band gap energy. The optical reflectance or absorbance is a result of interaction of light with the material. This technique is mostly applicable to powder samples and thin films. Usually UV-visible absorption spectroscopy requires a transparent substrate for the thin films and a transparent liquid medium to be dispersed for the powder samples. If the particle size of the sample is not small enough or not well dispersed in the solvent media, it precipitates and the absorption spectrum is difficult to interpret. In order to avoid these complications for powder samples and the opaque samples, it is desirable to use DRS, which enables to obtain absorbance as well as the band gap energy (E_g) of un-supported materials higher accuracy. Reflectance of samples can be measured using either an integrating sphere or a specular reflectance accessory. Integrating spheres are used for samples with a significant diffuse reflectance component.

Samples are placed at the back of the sphere and the light is reflected back off the sample and collected by the sphere. Measurements typically provide the total reflectance but if required the diffuse reflectance (specular excluded) portion can be measured independently. The latter

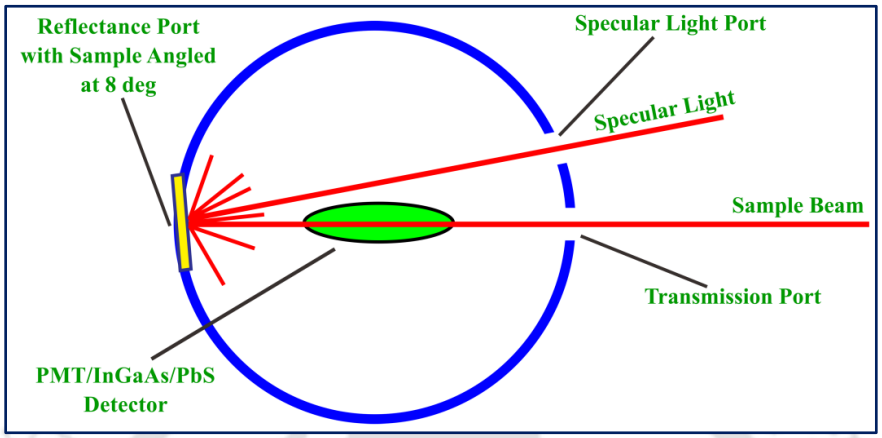

Fig. 2.12. A schematic diagram illustrating diffuse reflectance mechanism, excluding the specular reflectance.

measurement is achieved by allowing the specular component to exit the sphere through the open specular port. The theory which makes it possible to use diffuse reflectance spectra was proposed by Kubelka and Munk.[47] The absorbance can be calculated using Kubelka-Munk function:

$$F(R_\infty) = \frac{(1-R_\infty)^2}{2R_\infty} = \frac{k}{s} \qquad \text{..... (2.5)}$$

$F(R_\infty)$ is called the Kubelka-Munk (K-M) function, where $R_\infty = \frac{R_{sample}}{R_{standard}}$ is the reflectance, $k =$ K-M absorption coefficient and $s =$ K-M scattering coefficient. In the parabolic band structure, the E_g and k of a direct band gap and indirect band gap semiconductor are related through the well-known equations:[48]

$(F(R_\infty)h\nu)^2 = C_1(h\nu - E_g)$, *for direct band gap,* ..... (2.6a)

$(F(R_\infty)h\nu)^{1/2} = C_2(h\nu - E_g)$, *for indirect band gap,* ..... (2.6b)

where $h\nu$ is the photon energy, C_1 and C_2 are the proportionality constants.

We used a commercial spectrometer (SolidSpec, Shimazu) equipped with an integrating sphere for the DRS measurements. It performs the measurement in the UV/visible/NIR (i.e., 200-2500 nm wavelength range) region. The deuterium and tungsten halogen light sources are provided to perform the measurements in the UV/Visible/NIR region. An integrating sphere along with PMT (photomultiplier), InGaAs and PbS detectors are used to collect the diffuse light being reflected from the sample in all directions. A schematic diagram of diffuse

reflectance mechanism is shown in Fig. 2.12. We measured the absorbance of the samples from the reflectance spectra by using the K-M function ($F(R_\infty)$). The band gap is determined by the Tauc plot, which is calculated from the linear fit to the $(F(R_\infty)h\nu)^2$ vs $h\nu$ plot with $(F(R_\infty)h\nu)^2 = 0$ for direct band gap and $(F(R_\infty)h\nu)^{1/2}$ vs $h\nu$ plot with $(F(R_\infty)h\nu)^{1/2} = 0$ for indirect band gap.

2.2.2.3. *Micro-Raman Spectroscopy*

Raman spectroscopy is a vibrational spectroscopic technique generally used to study properties such as crystalline phases, strain, phonon confinement effect and defects present in the material. It is based on the Raman scattering process that corresponds to the interaction between the incident photons and optical phonons of the material. For the micro-Raman spectroscopy measurement, an intense laser beam is incident on the sample through a microscope with spot size about a few microns. The weak back-scattered light or signal is passed through a double

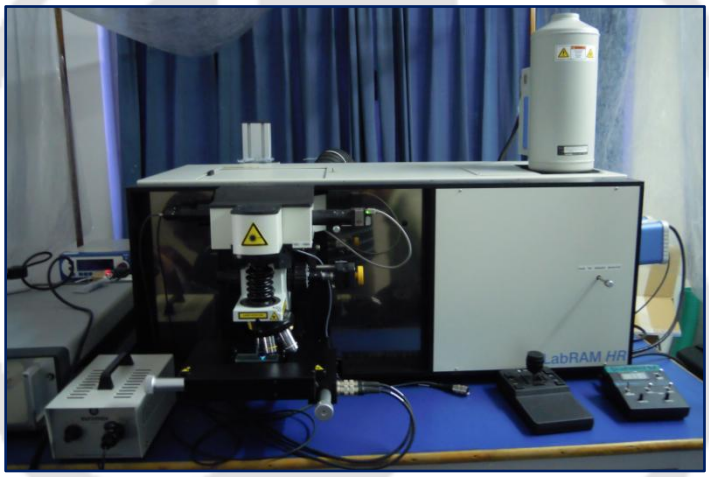

Fig. 2.13. A photograph of the micro-Raman spectrometer (LabRAM HR-800, Jobin Yvon, USA).

monochromator to reject the Raleigh scattered signal and the Raman shifted wavelengths are detected by a photodetector or CCD detector. Raman scattering is very sensitive to the crystal lattice microstructure via its vibrational properties. Inspection of line shapes of Raman spectra provides useful information concerning the crystallinity, amorphicity, stress/strain and dimension of nanostructured Si. Therefore, the Raman spectra of the MACE grown Si NWs are of great value for the understanding of the above parameters.

A high resolution micro-Raman (LabRAM HR-800, Jobin Yvon, USA) instrument with liquid nitrogen cooled CCD detector is used for the characterization of Si nanostructure samples. Fig. 2.13 is the photograph of micro-Raman set up used to acquire the Raman spectrum for the

present study. All the measurements are carried out at room temperature. Some of the samples are characterized using 488 nm and others using 514 nm Ar^+ laser at different laser powers.

2.2.2.4. *Photoluminescence Spectroscopy*

Photoluminescence (PL) spectroscopy is a contactless, nondestructive method of probing the electronic structure of a material. Light of suitable energy is directed onto a sample, where it is absorbed and imparts excess energy into the material in a process called photo-excitation. During photo-excitation, this excess energy can be released by the sample through the emission of light, or luminescence. The energy of the emitted light relates to the difference in energy levels between the two electron states involved in the transition between the excited state and the equilibrium state. Thus, suitable excitation energy is required to generate electron-hole pair within the material by exciting the electron from lower energy level (ground state/equilibrium state) to higher energy level (excited state) and the subsequent recombination comes out as emission (PL) with lower energy than the excitation energy. The quantity of the emitted light is related to the relative contribution of the radiative process between the various excited states (as defect states near the conduction act as a luminescence centers) and the equilibrium states. Features of the emission spectrum provide the information about the band gap energy, impurity level/ defect level detection, and electron-hole recombination mechanism. The most common radiative transition in semiconductors is between the states in the conduction and valence bands, with the energy difference being known as the band gap. Radiative transitions in semiconductors also involve localized defect levels within the band gap of the semiconductor. The PL energy associated with these levels can be used to identify specific defects, and the amount of PL can be used to determine their relative concentration. Analysis of PL helps to understand the underlying physics of the recombination mechanism. The fundamental limitation of PL analysis is its reliance on radiative events. Materials with poor radiative efficiency, such as low-quality indirect band gap semiconductors, are difficult to study via ordinary PL. Similarly, identification of impurity and defect states depends on their optical activity.

We used 325 nm He-Cd laser and 405 nm diode laser (Coherent, Cube) excitation with the help of a spectrometer (focal length: 15 cm; blaze wavelength: 500 nm; groove density: 150 g mm^{-1}) equipped with a cooled charge-coupled device (Princeton Instruments, PIXIS 100B) detector to acquire the PL spectra. Extended NIR PL measurements were carried out using a liquid N_2 cooled InGaAs detector (OMA-V-SE, Roper Scientific). Fig. 2.14 shows a photograph

of the PL instrument which is used in the present study. The PL measurements were carried at room temperature for

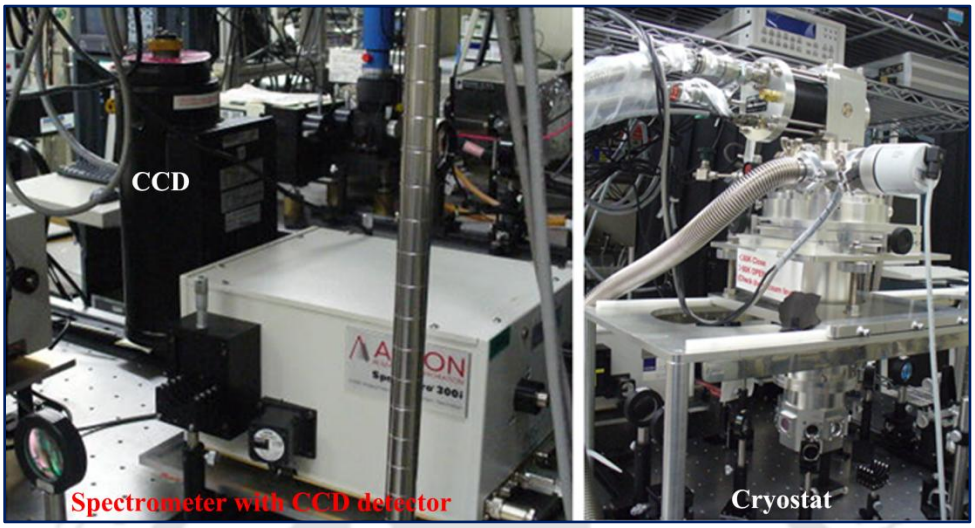

Fig. 2.14. A photograph of the low temperature photoluminescence spectrometer with CCD detector and cryostat.

most of the samples. We have also performed low temperature (10-280 K) PL measurement and room temperature PL under high vacuum (5×10^{-5} torr). Each spectrum was corrected for the detector response as a function of wavelength after background subtraction. The steady state PL peaks are usually of Gaussian shape expressed by

$$y = y_0 + A\,exp[-(\frac{(x-x_c)^2}{2w^2})] \qquad \text{..... (2.7)}$$

Where y_0 is the offset constant, x_c, w and A are the peak position, width and peak amplitude, respectively. The measured spectral profile of the PL spectrum is analyzed by fitting with Gaussian line-shape function or multiple Gaussian functions using PeakFit software.

2.2.2.5. *In-house Design and Development of Laser based PL Measurement Setup*

PL measurements of some of our samples were performed in a florescence spectrometer (Horiba Jobin Yvon Fluoromax-4). Due to the indirect band-gap nature of Si, the PL intensities of the Si NWs/NCs samples were very weak with Xenon-lamp as the excitation source. The defect induced PL of the samples were also very weak, which is difficult to detect. Since the intensity of the PL signal provides the qualitative information about the contribution of various states, more intense laser excitation based PL is generally preferred to study the Si NWs/NCs sample as compared to ordinary Xenon-lamp based PL system. We have used 405 nm DPSS

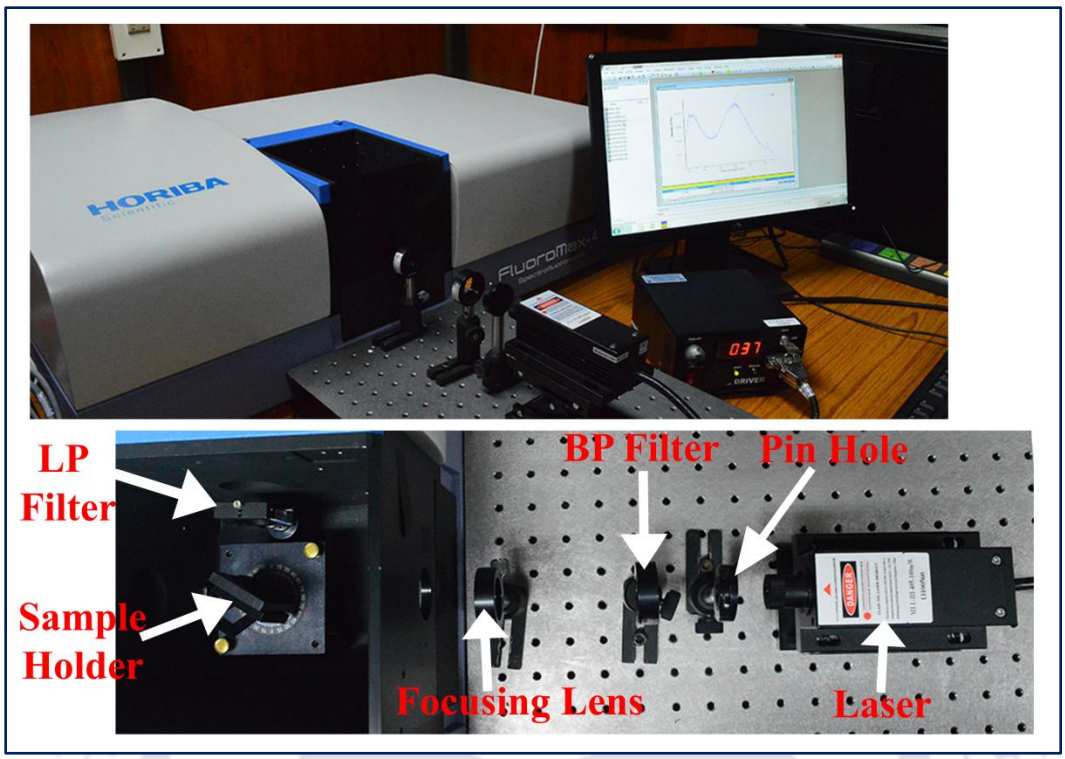

Fig. 2.15. A photograph of the PL spectrometer (Horiba Jobin Yvon Fluoromax-4) assembled with external laser source. The lower panel shows the components of the designed PL spectrometer.

(diode pumped solid state) laser as the excitation source. In case of 405 nm laser, we have used 405 nm band pass (BP) (Edmund optics) filter with a window of 4 nm. A long pass (LP) (Semrock, USA) filter of 409 nm with very sharp cut on was used in front of the detector (PMT). These filters are used to eliminate the laser line contribution in the PL spectra. Fig. 2.15 shows a photograph of the in-house developed PL measurement setup. Each spectrum was corrected for the detector response as a function of wavelength after background subtraction. 355 nm laser was also used as the excitation source in case of the heterostructure samples.

2.2.2.6. *Time-resolved Photoluminescence (TRPL) Spectroscopy*

Time resolved photo-luminescence (TRPL) is a useful characterization technique that provides the spectral and temporal evolution of the emission of a sample following its illumination by a short pulse of light. More precisely, the short pulse of light generates electron-hole pairs (excitons) that decay to lower energy levels of the sample. These electron-hole pairs can subsequently recombine and emit light. The emitted light is composed of a set of wavelengths corresponding to transition energies of the sample and, as a result, the measurement of the

optical spectrum as a function of time provides a means to measure the transition energies and their lifetimes. The measurement basically counts the number of photons of fixed wavelength with time. The emitted photon is analyzed by a spectrometer and detected by a micro-channel-plate photomultiplier tube (MCP-PMT) detector. A Multi-Channel Analyzer (MCA) board in the computer analyzes the output pulse voltages into various channels, which correspond to different times. In this way, the MCA can record each photon arriving at the MCP–PMT at a particular time. The number of output pulses from the MCP-PMT is directly proportional to the number of incident photons. Averaging over millions of photons, the measurement creates a histogram which shows how long excitons "live" after being created by the laser pulse. Thus, the carrier dynamics occurring during these processes provide not only information about the position of the peak emission, as in a normal steady state PL experiment, but also the lifetime of the excitons involved in the recombination.

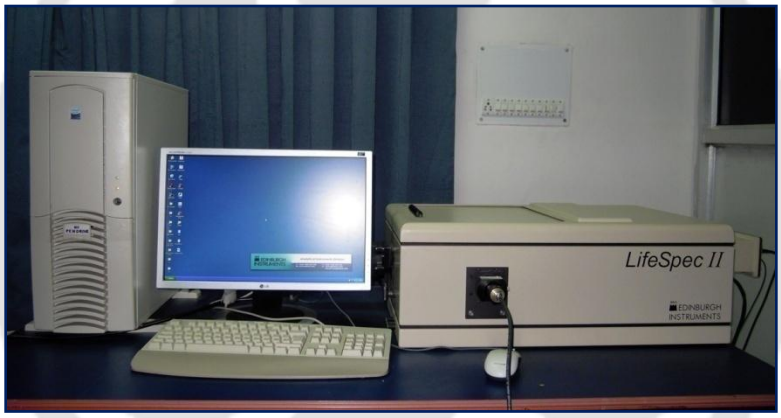

Fig. 2.16. A photograph of the Time-Resolved Photoluminescence spectrometer (LifeSpec II, Edinburgh Inst., UK).

The photograph of the TRPL spectroscopy (LifeSpec II, Edinburgh Inst., UK) instrument used in the present study is shown in Fig. 2.16. We used nanosecond pulsed laser (EPL series, Edinburgh Inst., UK) of wavelength 405 nm to excite the PL decay of the visible emission in the Si NWs/NCs and its heterostructures. This instrument has a time resolution of ~50 ps. The TRPL data usually follows an exponential decay behavior or combination of such function depending upon the number of decay channels available in the sample. The PL decay equation is expressed as

$$I(t) = I_1\, exp\left(-\frac{t}{\tau_i}\right) + I_2\, exp\left(-\frac{t}{\tau_2}\right) + I_3\, exp\left(-\frac{t}{\tau_3}\right) + \cdots \ldots\ldots\ldots\ldots + I_0 \qquad \ldots (2.8)$$

Where *I(t)* is the PL intensity, I_1,I_2,…. are decay channel amplitude, τ_1, τ_2,…are the decay time constant and I_0 accounts for the background noise. Measurement of τ provides information on the mechanism of recombination of carriers, electron transfer and energy transfer characteristics of different states.

2.2.2.7. *Photochemical Reactor*

"Photocatalysis" is a reaction which uses light to activate a substance which modifies the rate of a chemical reaction without being involved itself. And the photocatalyst is the substance which can modify the rate of chemical reaction using light irradiation. In a photochemical reactor when the photocatalyst is a semiconductor, the photocatalytic activity depends on the ability of the catalyst to create electron-hole pairs, which generate free radicals (e.g. hydroxyl radicals: •OH)

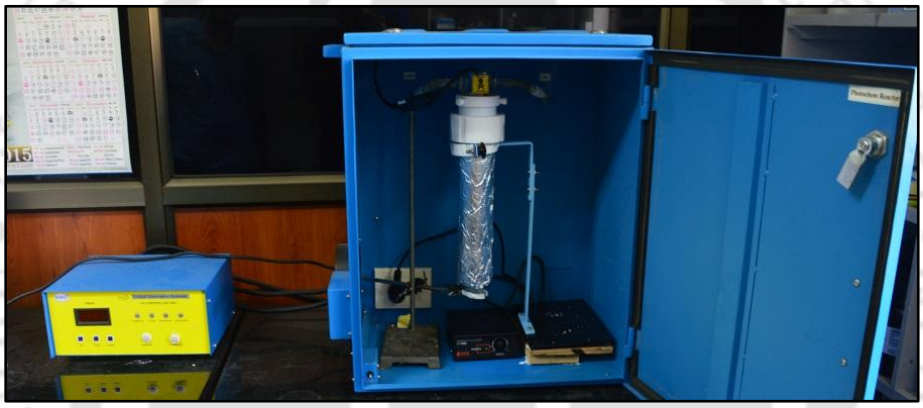

Fig. 2.17. A photograph of the Photochemical Reactor used for the photocatalysis study.

that are able to undergo secondary reactions. During the secondary reaction, these free radicals accelerate the oxidation and reduction process of the long-chain organic dyes and in this way the large dye molecules are broken down chemically into smaller molecules.

Photocatalytic degradation of different organic dyes (methylene blue, methyl orange etc.) using Si NWs was performed in a commercial photochemical reactor (Lelesil Innovative Systems, Mumbai). A time programmable visible lamp was used for illuminating the sample with excitation wavelength 390-730 nm. Fig. 2.17 shows a photograph of the photochemical reactor used for the present study.

References

1. Liu, X.; Coxon, P. R.; Peters, M.; Hoex, B.; Cole, J. M.; Fray, D. J. *Energy Environ. Sci.,* **2014,** 7, 3223.
2. Dussart, R.; Tillocher, T.; Lefaucheux, P.; Boufnichel, M. *J. Phys. D: Appl. Phys.,* **2014,** 47, 123001.
3. Eisenhawer, B.; Zhang, D.; Clavel, R.; Berger, A.; Michler, J.; Christiansen, S. *Nanotechnology,* **2011,** 22, 075706.
4. Schubert, L.; Werner, P.; Zakharov, N. D.; Gerth, G.; Kolb, F. M.; Long, L.; Gösele, U.; Tan, T. Y. *Appl. Phys. Lett.,* **2004,** 84, 4968.
5. Schwartz, G. C.; Schaible, P. M. *J. Vac. Sci. Technol.,* **1979,** 16, 410.
6. Choi, D.-G.; Yu, H. K.; Jang, S. G.; Yang, S.-M. *J. Am. Chem. Soc.,* **2004,** 126, 7019.
7. Gu, Q.; Dang, H.; Cao, J.; Zhao, J.; Fan, S. *Appl . Phys. Lett.,* **2000,** 76, 3020.
8. Das Kanungo, P.; Zakharov, N.; Bauer, J.; Breitenstein, O.; Werner, P.; Goesele, U. *Appl. Phys. Lett.,* **2008,** 92, 263107.
9. Morales, A. M.; Lieber, C. M. *Science,* **1998,** 279, 208.
10. Wu, Y.; Yang, P. *J. Am. Chem. Soc.,* **2001,** 123, 3165.
11. Wen, C. Y.; Reuter, M. C.; Tersoff, J.; Stach, E. A.; Ross, F. M. *Nano Lett.,* **2010,** 10, 514.
12. Li, X.; Bohn, P. W. *Appl. Phys. Lett.,* **2000,** 77, 2572.
13. Peng, K. Q.; Yan, Y. J.; Gao, S. P.; Zhu, J. *Adv. Mater.,* **2002,** 14, 1164.
14. Shao, M.-W.; Zhang, M.-L.; Wong, N.-B.; Ma, D. D.-d.; Wang, H.; Chen, W.; Lee, S.-T. *Appl. Phys. Lett.,* **2008,** 93, 233118.
15. Kim, J.; Han, H.; Kim, Y. H.; Choi, S. H.; Kim, J. C.; Lee, W. *ACS Nano,* **2011,** 5, 3222.
16. Kayes, B. M.; Filler, M. A.; Putnam, M. C.; Kelzenberg, M. D.; Lewis, N. S.; Atwater, H. A. *Appl. Phys. Lett.,* **2007,** 91, 103110.
17. Bandaru, P. R.; Pichanusakorn, P. *Semicond. Sci. Tech.,* **2010,** 25, 024003.
18. Otto, M.; Algasinger, M.; Branz, H.; Gesemann, B.; Gimpel, T.; Füchsel, K.; Käsebier, T.; Kontermann, S.; Koynov, S.; Li, X.; Naumann, V.; Oh, J.; Sprafke, A. N.; Ziegler, J.; Zilk, M.; Wehrspohn, R. B. *Adv. Optical Mater.,* **2015,** 3, 147.
19. Hasan, M.; Huq, M. F.; Mahmood, Z. H. *SpringerPlus,* **2013,** 2, 151.
20. Han, H.; Huang, Z.; Lee, W. *Nano Today,* **2014,** 9, 271.
21. Song, T.; Lee, S.-T.; Sun, B. *Nano Energy,* **2012,** 1, 654.
22. Qu, Y.; Zhoua, H.; Duan, X. *Nanoscale,* **2011,** 3, 4060.
23. Peng, K.-Q.; Lee, S.-T. *Adv. Mater.,* **2011,** 23, 198.
24. Huang, Z.; Geyer, N.; Werner, P.; de Boor, J.; Gosele, U. *Adv. Mater.,* **2011,** 23, 285.
25. Shao, M.; Ma, D. D. D.; Lee, S.-T. *Eur. J. Inorg. Chem.,* **2010,** 2010, 4264.
26. Schmidt, V.; Wittemann, J. V.; Gösele, U. *Chem. Rev.,* **2010,** 110, 361.
27. Schmidt, V.; Wittemann, J. V.; Senz, S.; Gösele, U. *Adv . Mater.,* **2009,** 21, 2681.
28. Ramanujam, J.; Shiri, D.; Verma, A. *Mater. Exp.,* **2011,** 1, 105.
29. Bachtouli, N.; Aouida, S.; Bessais, B. *Microporous Mesoporous Mater.,* **2014,** 187, 82.
30. Peng, K.; Zhang, M.; Lu, A.; Wong, N.-B.; Zhang, R.; Lee, S.-T. *Appl. Phys. Lett.,* **2007,** 90, 163123.
31. Hildreth, O. J.; Lin, W.; Wong, C. P. *ACS Nano,* **2009,** 3, 4033.
32. Ghosh, R.; Imakita, K.; Fujii, M.; Giri, P. K. *Phys. Chem. Chem. Phys.,* **2016,** 18, 7715.
33. Ghosh, R.; Giri, P. K. *RSC Adv.,* **2016,** 6, 35365.
34. Pal, A.; Ghosh, R.; Giri, P. K. *Appl. Phys. Lett.,* **2015,** 107, 072104.
35. Ghosh, R.; Pal, A.; Giri, P. K. *J. Raman Spec.,* **2015,** 46, 624.
36. Ghosh, R.; Giri, P. K.; Imakita, K.; Fujii, M. *Nanotechnology,* **2014,** 25, 045703.
37. Sanjay, K. S.; Dinesh, K.; Schmitt, S. W.; Sood, K. N.; Christiansen, S. H.; Singh, P. K. *Nanotechnology,* **2014,** 25, 175601.

38. Peng, K. Q.; Hu, J. J.; Yan, Y. J.; Wu, Y.; Fang, H.; Xu, Y.; Lee, S. T.; Zhu, J. *Advanced Functional Materials,* **2006,** 16, 387-394.
39. To, W.-K.; Tsang, C.-H.; Li, H.-H.; Huang, Z. *Nano letters,* **2011,** 11, 5252-5258.
40. Smith, Z. R.; Smith, R. L.; Collins, S. D. *Electrochimica Acta,* **2013,** 92, 139-147.
41. Chen, C.-Y.; Wu, C.-S.; Chou, C.-J.; Yen, T.-J. *Advanced Materials,* **2008,** 20, 3811-3815.
42. Schroder, D. K., *Semiconductor material and device characterization*. 3rd ed. ed.; Wiely-Interscience, New Jercy, USA, (2006).
43. García, R., *Amplitude Modulation Atomic Force Microscopy*. Wiley-VCH, Weinheim, Germany, (2010).
44. Siegbahn, K.; Nordling, C.; Fahlman, A.; Nordberg, R.; Hamrin, K.; Hedman, J.; Johansson, G.; Bergmark, T.; Kerlsson, S. E.; Lindgren, I.; B.Lindberg. *Nova Acta Regiae Soc. Sci., Ser,* **1967,** 20.
45. Brunauer, S.; Emmett, P. H.; Teller, E. *J. Am. Chem. Soc.,* **1938,** 60, 309.
46. Lowell, S.; E., S. J.; Thomas, M. A., *Characterization of porous solids and powders: surface area, pore size and density*. 3rd ed. ed.; Springer, Netherland, (2006).
47. Kubelka, P.; Munk, F. *Z. Tech. Phys.,* **1931,** 12, 593.
48. Tauc, J.; Grigorovici, R.; Vancu, A. *Physica Status Solidi (b),* **1966,** 15, 623.

भारतीय प्रौद्योगिकी संस्थान गुवाहाटी
Indian Institute of Technology Guwahati

Chapter 3

Controlled Growth of Mesoporous Si Nanowires Array by Metal Assisted Chemical Etching

The properties of Si nanowires (NWs) often depend on their preparation methods. The low cost production of large area, highly oriented array of Si NWs is extremely important to control the properties for device applications. We have used metal assisted chemical etching (MACE) method for the production of large area, ordered and uniform mesoporous Si NWs with high density of Si nanocrystals (NCs) on its surface. We have investigated the impact of etching condition and etching parameters on the morphologies and structure of the as-synthesize Si nanostructures. Growth mechanism and shape evolution is elucidated from the systematic studies of AFM, FESEM and TEM imaging. The structural characterizations of as-synthesized Si nanostructures are studied by using XRD, XPS, FTIR and micro-Raman spectroscopy to understand crystalline quality, structure, presence of defects and existence of terminated surface. This work will be valuable for controlled growth of mesoporous Si NWs and understanding the formation mechanism of various nanostructured Si synthesized under diverse growth conditions.

3.1. Introduction

The design and fabrication of 1D Si nanostructures in particular Si nanowires (NWs), have attracted intensive interest due to their unique architectures, extraordinary physical and chemical properties and potential applications in various areas of nanotechnology, such as light emitting diodes (LEDs), solar cell, Li-ion battery, artificial photosynthesis, environmental cleaning and biological/chemical/gas sensors.[1-14] To realize these promising high performance applications, the control of inherent crystal structure, morphology, surface area, and porosity through their nanostructures and understanding the formation mechanism are challenging today. Considerable effort has been made to explore novel and inexpensive approaches to fabricate large area, highly oriented array of Si NWs for dedicated applications. Over the past decades, Si NWs have been fabricated by several groups worldwide suing various methods, such as chemical vapor deposition (CVD), pulsed laser deposition (PLD), thermal evaporation, template assisted growth, molecular beam epitaxy (MBE), reactive ion etching (RIE), and metal assisted chemical etching (MACE) etc.[1, 11, 15-34] Out of several traditional approaches, CVD and MACE method are the

widely explored and largely usable methods for their versatility with controllability, repeatability, quality, low cost and mass production. Solution based MACE of Si overcomes the drawbacks of the other methods and has several advantages over any other established method for the fabrication of large area, well aligned and rapid production of high quality Si NWs.[1, 20, 21, 25-34]

3.2. Metal Assisted Chemical Etching

Due to the enormous control over the morphology and structure of the as-synthesize Si NWs, the solution based MACE has emerged as a promising and significant tool for the rapid production of large area, aligned and well controlled Si NWs and it has become the most common and of course inexpensive method for the production of high quality Si NWs.[1, 20, 21, 25-34] We have successfully grown highly ordered and oriented, single crystalline Si NWs by MACE of Si.[30-34] The details of the experimental setup, the growth condition and corresponding sample codes are provided in *Chapter 2, Section 2.1*. Note that MACE requires a galvanic displacement of noble metal NPs as a catalyst on the surface of the crystalline Si substrate and Ag, Au and Ag/Au have been demonstrated to be effective catalysts for MACE of Si.[30-34] Various oxidative agents have been mixed with HF to etch noble metal-loaded Si substrates, including $AgNO_3$ and H_2O_2. It is also to be noted that the MACE grown Si NWs are often decorated with arbitrary shaped self-grown Si NCs on the surface of Si NWs. However, the shape and size, length, diameter, density, crystallinity and the properties of the Si NWs strongly depends the (a) nature of the noble metal, (b) shape and size of the noble metal and the intermediate distance between them, (c) the etching solution and its concentration, (d) the doping type, resistivity and the orientation of the starting Si wafer, (e) temperature and (f) etching duration.[20, 21, 23, 25, 27, 28, 35-37]

3.3. Etching Mechanism

In order to fabricate the highly ordered array of Si NWs via MACE, it is very important to understand the growth mechanism of the Si NWs during MACE. Several models are reported regarding the mechanism of MACE and among all the reported models on the growth mechanism of Si NWs, microscopic electrochemical cell model is considered very important for understanding the formation of vertical Si NWs array.[1, 26, 27, 32, 38-41] In this self-assembled Ag induced selective etching process, continuous galvanic displacement of Si by Ag^+ via $Ag^+ \rightarrow Ag$ reduction occurs on the Si surface.[26, 32, 38, 40, 41] A schematic diagram of this growth process and

the overall reaction mechanism in terms of equations are discussed in *Chapter 2* (*Section* 2.1.1.3). Usually, oxidation and dissolution of Si occur at the bottom of the metal NPs and metal NPs diffuse through the Si by forming Si NWs. Fig. 3.1. shows the FESEM images which depicts the formation steps of Si NWs by Ag assisted chemical etching of Si wafers: (a-d) in $AgNO_3$ + HF solution and (e-h) in H_2O_2 + HF solution. It is clear from Fig. 3.1(b) and (f) (30 sec etched Si) that the pores are formed in the place of Ag NPs and vertical Si NWs are formed for higher etching duration, as observed in Fig. 3.1(c, d) and (g, h). It has been reported that the MACE grown Si NWs are covered by a thin layer of the amorphous Si or Si-H layers that is believed to prevent the lateral etching of the Si NWs.[32] This leads to straight vertical pores on the

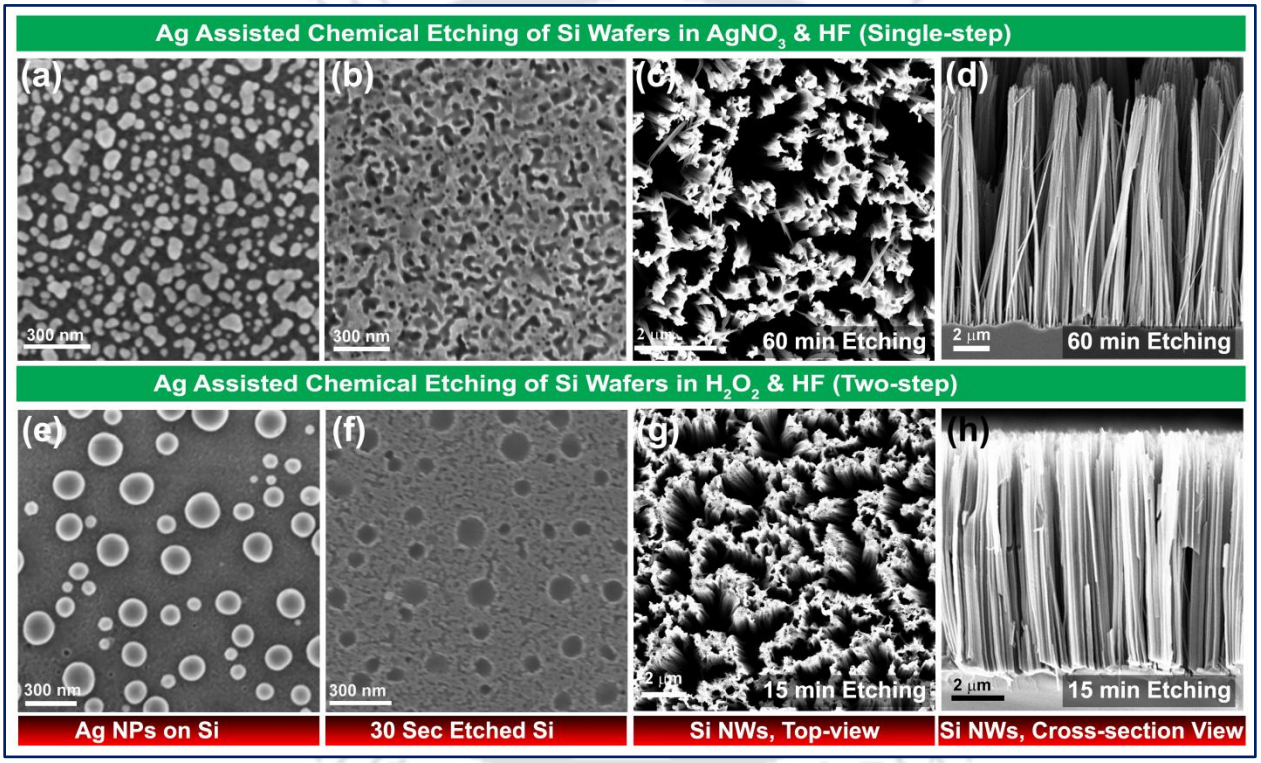

Fig. 3.1. FESEM images describing the formation steps of Si NWs by Ag assisted chemical etching of Si wafers: (a-d) in $AgNO_3$ + HF solution and (e-h) in H_2O_2 + HF solution.

Si surface resulting in array of vertical Si NWs. Note that the existing models mainly discuss about the etching mechanism in terms of mass transfer, hydrogen production, heat production and the diffusion of metal-catalyst by means of excess holes (h^+) in Si.[1, 26, 27, 32, 38-41] Since, the growth of Si NWs via MACE of Si is a statistical process, it is very important to understand the MACE mechanism by means of a scaling approach, which may provide an alternate view of growth mechanism.

3.4. Calculation of Growth Exponents at the Early Stage of Etching

We have investigated the early stages of growth of Si NWs by MACE in terms of the different scaling exponents e.g. roughness exponent, growth exponent and dynamical exponents using high resolution AFM imaging.[32] Fig. 3.2(a-f) shows representative AFM images of etched Si surface for different etching time. Here all the images are taken in 5×5 μm^2 areal surface that exhibits a rough type of surface morphology. The high resolution image of each sample scanned over 2×2 μm^2 area is shown as an inset in each case (left bottom corner). Height profile of each image along a line is shown at the bottom of the respective images.[32]

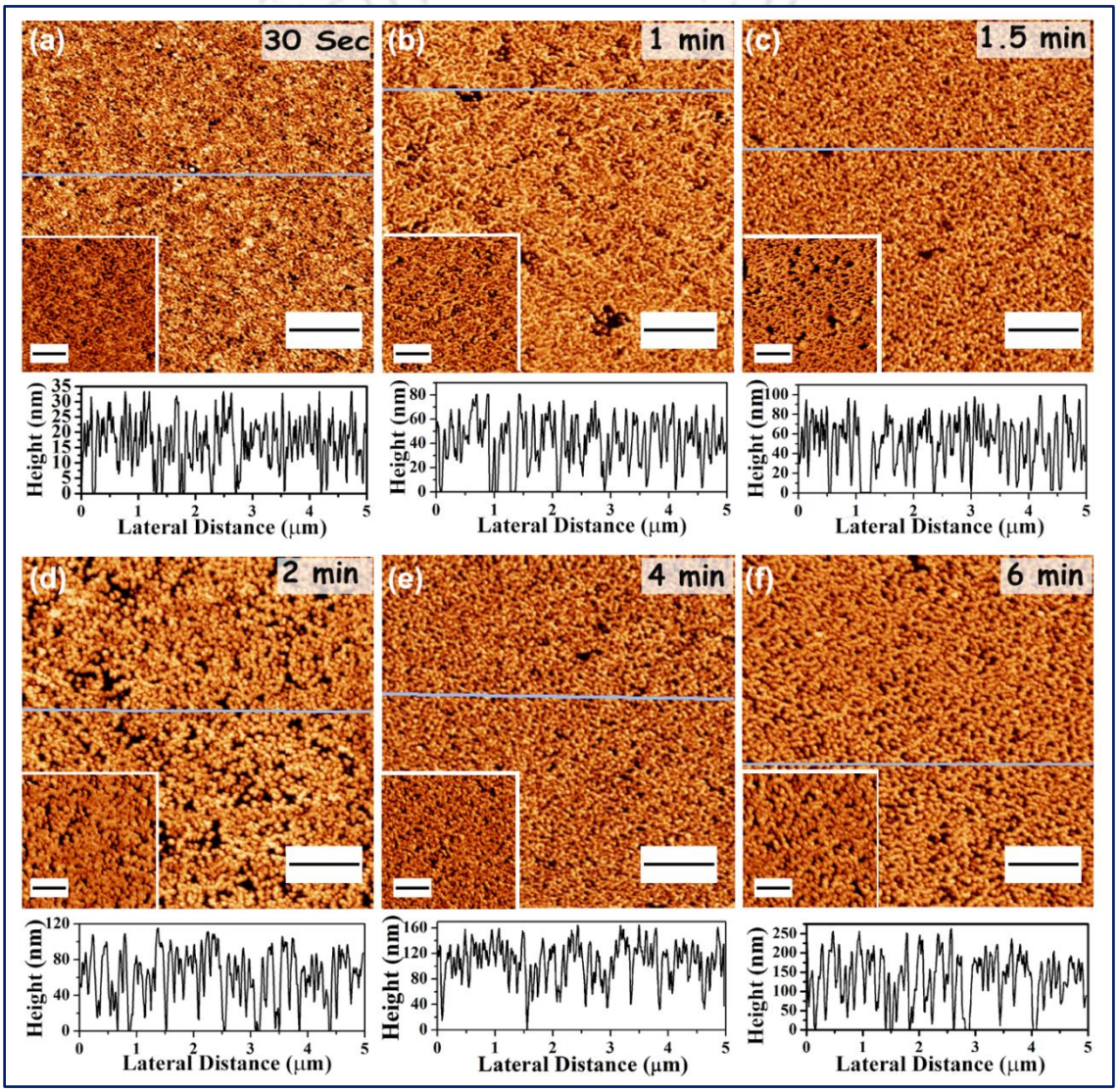

Fig. 3.2. (a-f) AFM images of etched Si surface, showing the surface morphology for different etching durations. Each image consists of 5×5 μm^2 scanned area and scale bar is 1.0 μm. The inset (left bottom corner) shows the magnified image (scale bar 0.5 μm) corresponding 2×2 μm^2 scanned area in each case. Height profile of each image is shown at the bottom of the respective images.

In order to gain insight into dynamic behavior of the surface evolution and characterize the roughness of the observed surface/interface, we define the local height *h(x,t)* along the moving direction of the surface to determine the different scaling exponents. These quantities are ascertained from height-height correlation function *G(r,t)*, which is defined as statistical average of the mean square of height difference between two positions in the interface separated by a distance *r* along horizontal direction as

$$G(r,t) = < [h(r,t) - h(0,t)]^2 >, \quad \text{..... (3.1)}$$

where *h*(*r*,*t*) and *h*(0,*t*) are the heights of the surface at the locations separated by a distance *r* and the brackets signify an average over pairs of points obtained from AFM image. In another way, for small length scale it also defined as

$$G(r,t) = [m(t)r]^{2\alpha} \text{ with } r << \xi(t), \quad \text{..... (3.2)}$$

where, ξ is the characteristic in-plane length scale, α is the roughness scaling exponent and *m(t)* is the local slope of the surface profile.[42-45] Lateral correlation length, ξ is the measure of the length beyond which surface heights are not significantly correlated and $m(\theta)$ is calculated from above mentioned relation.[42] Here, we have considered the dynamic behavior of the growth in terms of etching duration *t*, only at the early stages of growth. The height-height correlation function *G*(*r*,*t*) as a function of distance *r* calculated from the AFM images for different etching

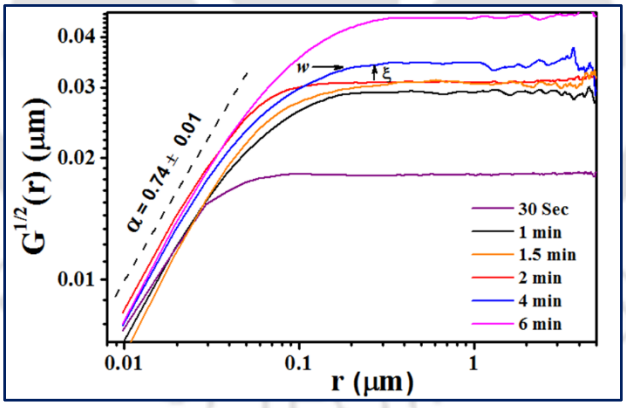

Fig. 3.3. Square root of height-height correlation function ($G^{1/2}$) as a function of lateral distance (*r*), as calculated from the AFM images for different samples etched for different time duration. Roughness exponent (α) is calculated from the power law fitting of the linear portion.

durations are plotted in Fig. 3.3.[32] In our analysis, we have checked about 9 to 12 AFM images for each sample, that were believe to be enough to give statistically reliable data to obtain *G*(*r*,*t*) plot and in this way the sampling induced effect in the *G*(*r*,*t*) calculation was avoided. Fig. 3.3 show $G^{1/2}(r,t)$ versus *r* plots for different samples with different etching duration. The roughness

exponent α was calculated from a fit to the linear part of the log-log plot of $G^{1/2}(r)$ versus r and we obtained the average α as 0.74 ± 0.01. We observe an upshift in the curves when we plot $G^{1/2}(r,t)$ *vs.* r for different etching times, as shown in Fig. 3.3 and it confirms the roughening in the growth process. In order to monitor the roughening process quantitatively, we have measured the interface width $w(t)$ as function of t following the conventional method.[46, 47] Here $w(t)$ is defined as the value of $G^{1/2}(r,t)$ at the first local maximum (shown by arrow marked in Fig. 3.3); $w(t) = G^{1/2}(t/2)$ whereas ξ marked by an upward arrow is the position of r at the first local minimum of $G^{1/2}(r)$.[48] This definition of roughness amplitude is preferred over the large r limit of $G(r)$, since artifacts at large length scales can affect the AFM data.

We have observed a power law behavior of interface width (w), as $w \sim t^{\beta}$. The exponent β characterizes the dynamics of the roughening process and is called growth exponent. Similar type of power law dependence is also observed in lateral correlation length ξ. It increases with t as $t^{1/z}$, where exponent 1/z is called dynamic exponent. The logarithmic variation of w as a function of t is shown in Fig. 3.4(a) for all etched samples.[32] The obtained value of growth exponent β is 0.30 ± 0.05. The dynamic exponent (1/z) is calculated as 0.32 ± 0.05 from the log-log plot of ξ versus t, as shown in Fig. 3.4(b). Fig. 3.4(a) shows the increasing nature of w with time t, that signifies the roughening nature of growth.[32] In order to identify the growth mode, we have plotted local slope (m) as a function of etching time, as shown in Fig. 3.4(c). If m(t) is

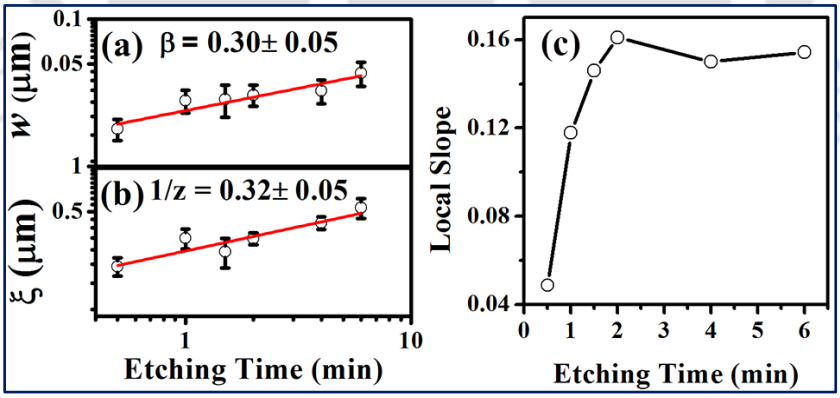

Fig. 3.4. Log-log variation of: (a) interface width (w), and (b) lateral correlation length (ξ) with etching time (t). The growth exponent (β) and dynamic exponent (1/z) are calculated from the slope of the respective curve. (c) Variation of local slope (m) as a function of etching time (t).

independent of etching time, it is called stationary type of growth. In stationary growth, for $r << \xi$ the height-height correlation function will merge for different t values. However, for the non-stationary case, $G^{1/2}(r)$ will shift upward as the local slope changes with etching duration.[43]

In the present case, the growth is obviously non-stationary. We also observe that the local slope at first increases and then saturates. This signifies that in the present case the growth process is roughening.[32] In the early stage of growth, size of the Si nanostructures is very small, and with time the size as well as local slope is increasing. However, after a certain time the diameter of the Si NW do not change (only vertical growth is dominated), as a result the local slope is saturated. For the nonequilibrium growth, the theoretically predicted values of the exponents are $\alpha = 2/3$ and $\beta = 1/5$.[49] and for liner growth the exponents are $\alpha = 1$ and $\beta = 1/4$.[50] However, our exponent values ($\alpha = 0.74$ and $\beta = 0.30$) are different from the above values. Thus, none of the theoretical models can properly support the type of growth observed here. Interestingly, growth due to roughening is still not well understood.[43] In case of nonequilibrium film growth, the growth equation is expressed as[45]:

$$\frac{\partial h}{\partial t} = D_s \nabla^4 h(r,t) + D_v \nabla^3 h(r,t) + \nu \nabla^2 h(r,t) + \lambda (\nabla h(r,t))^2 + R\Omega(h,t) + \eta(r,t), \quad \text{.....(3.3)}$$

where D_s expresses surface diffusion, D_v volume diffusion, ν evaporation and redeposition, and λ is a non-linear coupling term, R is the growth (or etching) rate, Ω the shadowing solid angle (which is a non-local term) and η a noise term, which generates the roughness. Here, each term plays different role in different growth models, such as KPZ or Lai-Das-Sharma etc.[42] Interplay between the parameters will generate different types of surface. However, for explaining columnar type of growth, shadowing instability theory may be more relevant, where either $D_s = D_v = 0$ or $D_v = \nu = 0$.[51-53] The shadowing mechanism, i.e., the primary nonlocal effect is very much applicable for mound type surface, where taller surface features block incoming flux to reach lower lying areas of the surface. As a result, surface with small height receive little or no particle flux, whereas the taller surface receive higher flux. Shadowing is an inherently nonlocal process, since the shadowing of a surface feature depends on the difference between the surfaces with different heights. In absence of lateral diffusion or evaporation, the surface evolves as a vertical structure.[54] Here our experimental results seem to closely resemble the shadowing instability model.[32] In case of MACE process, chemically generated Ag^+ ions create defect site at the outer surface of the Si substrate. The rate of formation of soluble H_2SiF_6 is accelerated at these defect sites as compared to the flat surface. This means that etching occurs preferentially at these sites due to lower binding energy of Si compared to the Ag of Ag^+ ions.[32] Thus, the bottom of the native column is etched preferentially over the top surface of Si. It is consistent with the

columnar growth that occurs as a result of shadowing during Si NWs growth, where the top of the native column grows more quickly than the bottom, which is equivalent to a faster etching of the bottom. The shadowing of the native column also prevents the lateral etching. Interestingly, similar type of shadowing effect has been reported in plasma etched Si surface by Drotar et al.[55] It was shown that vertical structure can be grown on Si with $\beta < 0.5$ by shadowing effect in plasma etched Si surface. Yao et al.[51] theoretically predicated a $\beta = 0.33 \pm 0.02$ using shadowing instability model. These values are very close to our experimental data, i.e., $\beta = 0.30 \pm 0.05$. The other growth exponents for columnar type or mound type surface growth under shadowing effect, as explained by Pelliccione et al., are also comparable to our experimental data.[54] Though the etching mechanism of Si by MACE is still under debate, shadowing instability theory explaining columnar growth of Si NWs by MACE provide an alternative understanding on the etching mechanism.[32]

3.5. Si Nanocrystal Decorated Si Nanowires

MACE grown Si NWs are decorated with the self-grown Si NCs due to the mesoporous nature of the Si NWs and the formation mechanism of small pores on Si NWs has been discussed by several groups.[21, 25, 27, 30-34, 56-58] The mesoporous Si NWs are formed due to lateral etching and this gives rise to the formation of arbitrary shaped Si NCs on the surface of the Si NWs.[25, 30-34, 56] As mentioned earlier, the process of MACE relies on the hole injection from metal ions to Si in presence of the oxidant and the SiO_2 dissolution by HF. Usually, oxidation and dissolution of Si occur at the bottom of the metal NPs and metal NPs diffuse through the Si by forming Si NWs. So, the whole reaction mechanism depends upon the formation rate of the metallic ions in the solution by which the Si wafer is oxidized. When the formation rate of metal ions is higher, the metallic ions not only inject holes to the Si underneath these metal ions but the excess ions can attack the sidewalls of the Si NWs also. As a result, the extra metal ions can nucleate near nucleation sites on the sidewalls of the Si NWs by collecting electrons and etch in the lateral direction of the Si NWs, leading to the formation of small pores on Si NW surfaces. The portion of Si surrounded by these pores on the surface of Si NWs is termed as the Si NCs. We have observed that the Si NWs are decorated with Si NCs. Fig. 3.5(a) shows the TEM image of a single Si NW of sample R1 (See *Table 2.1, Chapter 2*), while (b) shows a magnified view of the surface of the Si NW, depicting rough surface of the NWs due to sidewall etching and

confirming the presence of Si NCs on its surface. Fig. 3.5(c) shows the HRTEM lattice image of a single Si NC showing the clear lattice fringe image of the Si NCs.[33] We have observed from the HRTEM image of each type of Si NWs, we find that the shape of the Si NCs is arbitrary and

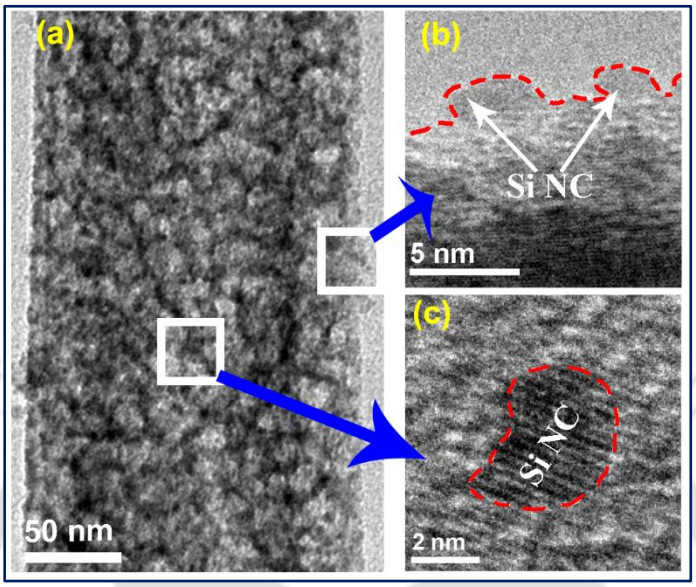

Fig. 3.5. (a) TEM image of a single Si NW of sample R1. (b) A magnified view of the Si NW, showing rough surface of the NWs due to sidewall etching and confirming the presence of Si NCs on its surface. (c) The HRTEM lattice image of a single Si NC and its shape is marked by a dashed line.[33]

it is more appropriate to express of their size in terms of cross-sectional areas (A). We have also calculated the equivalent diameter (D) of the Si NCs from the corresponding "A" considering a circular cross-section of the Si NCs. The size distributions of the Si NCs of all the samples are summarized in Table 3.1. Fig. 3.6 shows the size distribution for (a) sample P, (b) sample Q and (c) sample R, respectively. In each case, we have observed that the size of the Si NCs is distributed over a broad range and follows an asymmetric Gaussian distribution. Note that the shape and size of the Si NCs strongly depends of the mesoporous nature of the Si NWs i.e. the size of the pores, the intermediate distance between these pores and also the depth of the pores. So, the etching parameters which affect the porous nature of the Si NWs also have strong effect on the formation as well as the shape and size variation of the self-grown Si NCs.

Usually, crystal defects and impurities such as dopant elements in Si wafer at the Si surface are thought to serve as nucleation sites for the pore formation. Higher dopant concentration may create a larger thermodynamic driving force for pore formation, or at least increase the rate of etching and surface roughness. Similarly, higher dopant concentration lowers the energy barrier to charge injection across the Si surface. This results in higher porosity and

Table 3.1. *Details of the size distribution (cross-sectional area (A) and diameter (D)) of the Si NCs obtained from HRTEM images*

Starting Wafer	Etching Condition	Sample Code	Average A (nm^2)	Equivalent D (nm)
P-type, Si(100), 1-10 Ω-cm	Direct etching in 0.015M $AgNO_3$ + 5.55M HF for 60 min	**P**	37.90	6.95
	Ag assisted etching in 0.015M $AgNO_3$ + 5.55M HF for 60 min	**Q**	39.40	7.08
	Ag assisted etching in 4.6 M HF + 1.422 M H_2O_2 for 15 min	**R**	56.50	8.48
	Ag assisted etching in 4.6 M HF + 1.422 M H_2O_2 for 20 min	**R1**	30.17	6.20
P-type, Si(100), 0.01 Ω-cm	Ag assisted etching in H_2O_2 + HF (5:2 volume ratio) for 20 min	**S1HF5**	24.40	5.58
P-type, Si(111), 0.001 Ω-cm	Ag assisted etching in H_2O_2 + HF (5:2 volume ratio) for 20 min	**S2HF5**	06.92	2.97
P-type, Si(100), 1-10 Ω-cm	Ag/Au assisted etching in H_2O_2 + HF (1:4 volume ratio) for 20 min	**AgAuSi**	62.18	8.90

hence the average size of the Si NCs decreases, while its density increases.[25, 30-34, 56] Accordingly, the average size of the Si NCs decreases with decreasing resistivity, $D_{R\ (1\text{-}10\ \Omega\text{-cm})} > D_{S1HF5\ (0.01\ \Omega\text{-cm})} > D_{S2HF5\ (0.001\ \Omega\text{-cm})}$, as observed from Table 3.1.

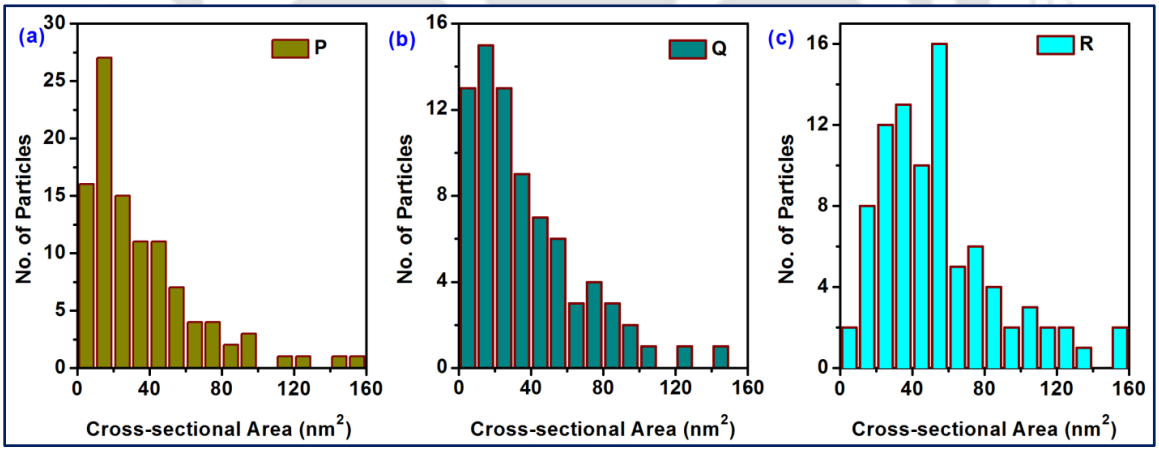

Fig. 3.6. The no. distribution Si NCs as function of cross-sectional area (A) for sample (a) P, (b) Q and (c) R, calculated from the respective HRTEM images.

Note that the relative concentration of the etching solution also has a strong effect on the size and density of the Si NCs.[31] In case of Ag assisted etching, the pre-deposited Ag NPs oxidized by the oxidant (such as, H_2O_2) becomes Ag^+ in the close proximity of the Ag NPs. For a fixed value of the H_2O_2, we have investigated the effect of HF concentration on the size and

density of the Si NCs. With the increase in HF concentration, relative concentration of H_2O_2 decreases and hence the concentration of the Ag^+ ions decreases.[31] As a result, less fraction of Ag^+ ions nucleate at the defect sites and the density of pores decreases. Hence, the average size of the Si NCs increases and the Si NCs density decreases with increasing HF concentration. [23, 25, 27, 30-34, 56] However, it is very difficult to calculate the size distribution of the Si NCs for each concentration of HF from the HRTEM images since the variation in the HF concentration also affects the porosity of the Si wafer and the formation of the Si NWs indeed. We have investigated the size distribution of the Si NCs for different concentration of the HF solution through indirect ways, such as PL and Raman analysis using quantum confinement effect (discussed in the next *Chapter*).[31, 33]

The average size and the density of the Si NCs also strongly depend on the etching duration. During the etching, as the time progresses more number of nucleation sites is generated on the sidewall of Si NWs and porosity increases. As a result, Si NCs formed at the initial stage of etching are divided into a smaller sized Si NCs. So, the density of smaller sized Si NCs increases, while the density of larger size Si NCs decreases with increasing etching duration.[33, 34] Accordingly, we have observed that the average size of the Si NCs decreases with increasing etching duration.[33] In all cases, the size distribution of the Si NCs follows a skew-symmetric distribution with positive skewness.[33] We have compared the size distribution measurement obtained from the direct evidence (HRTEM analysis) with that of the indirect measurement, such as PL and Raman analysis and we have found a significant matching in the results obtained from different measurement tools (discussed in details in *Chapter* 5).[33]

3.5.1. Surface Porosity Analysis by BET

Since porosity of the Si NWs surface determines the size and density of the Si NCs, it is crucial to study the porosity in a quantitative manner. Porosity also affects other properties of the Si NWs, including surface area and chemical reactivity. Brunauer-Emmett-Teller (BET) gas sorption is a well-established surface porosity measurement method.[59-62] In the present study, Si NWs (~14 mg) were scraped from the wafer and collected from the sample S1HF5 and the BET analysis was performed. The N_2 adsorption-desorption isotherms of the sample S1HF5 are shown in Fig. 3.7(a). The shape of the isotherms depends on the pore sizes of the nanostructure. The isotherms of the nanostructures with mesopores and micropores (size >2 nm) exhibit an abrupt increase in the high-pressure region (>0.7 P/P_0 value) that can be attributed to the capillary

condensation and multilayer adsorption of N_2 in the micropores. In order to understand the average pore size and corresponding size distribution, Barrett-Joyner-Halenda (BJH) analysis was carried out on BET data. The BJH pore size distribution profiles for sample S1HF5 are shown in Fig. 3.7(b). A mean surface area of 448.648 m^2/g was obtained from the multi-point BET analysis, which is very high as compared to the results obtained by Qu et al.[61] and Zhong et al.[59] This high surface area is significant for the enhanced photocatalytic activity of the sample S1HF5 (discussed in chapter 6). However it is clear from Fig. 3.7(b) (inset) that the pore size distribution is divided into two regions; (I) pore diameter < 5 nm and (II) pore diameter > 5 nm. The average pore diameter is found to be ~3.7 nm for part I and ~10.5 nm for part II as determined by the distribution profile. Interestingly, the average diameter of the Si NCs obtained from the HRTEM was 5.6 nm, which is comparable to the average pore size for part I. It can be

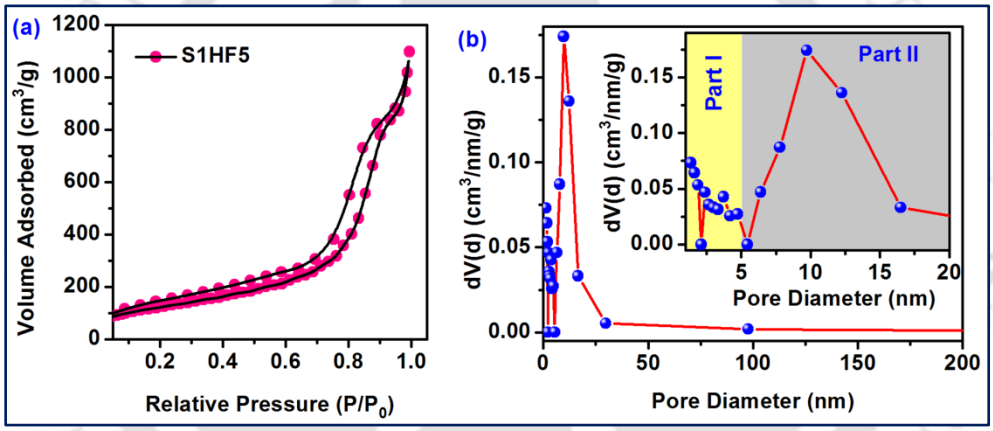

Fig. 3.7. (a) N_2 adsorption/desorption isotherms of porous Si NWs obtained from sample S1HF5 (b) Corresponding BJH pore size distribution. Inset shows the pore size distribution in the range 0-20 nm. The pore size distribution is divided into two parts; part I: pore diameter < 5 nm (yellow box) and part II: pore diameter > 5 nm (grey box).

noted that HRTEM technique has a limitations in probing ultra-small pore sizes. Note that the size distribution of the Si NCs calculated from PL analysis (Chapter 4 and Chapter 5) reveals that the visible PL originates due to the ultra-small Si NCs and comparatively larger size Si NCs are responsible for the NIR emission of the MACE grown Si NWs/NCs. It should be noted that BET surface area analysis requires large amount of porous sample in powder phase, which makes it difficult to measure for all samples.

3.6. Effect of Etching Parameters on the Morphology and Structure of Si NWs

There are several factors affecting the etching, which decide the morphology and structure of the Si NWs as well as the Si NCs. We have investigated the following parameters to see its influence

on the size and shape evolution of the Si NWs: (a) the doping nature of the Si wafer (from which the Si NWs/NCs are grown); (b) the nature of noble metal nanoparticles, the size of the noble metal and their interspacing, the nature of etching solution as well as its concentration; and (c) the external parameters including the etching duration. We have studied the structure of the Si NWs/NCs samples by means of Raman, FTIR, XRD and XPS in order to understand the structural quality, presence of surface defects and the strain in the surface.

3.6.1. Effect of Etching Duration

Etching duration is one of the important factors that control the length, diameter and porosity of the etched Si NWs. In order to understand its effect on the morphology of the Si NWs/NCs, we have varied the etching duration keeping the other parameters same. Fig. 3.8(a-e) shows the FESEM cross-sectional images of the as-grown Si NWs for different etching duration in 0.015 M $AgNO_3$ + 5.55 M HF. We have used Boron doped p-type Si(100) wafer with resistivity 1-10

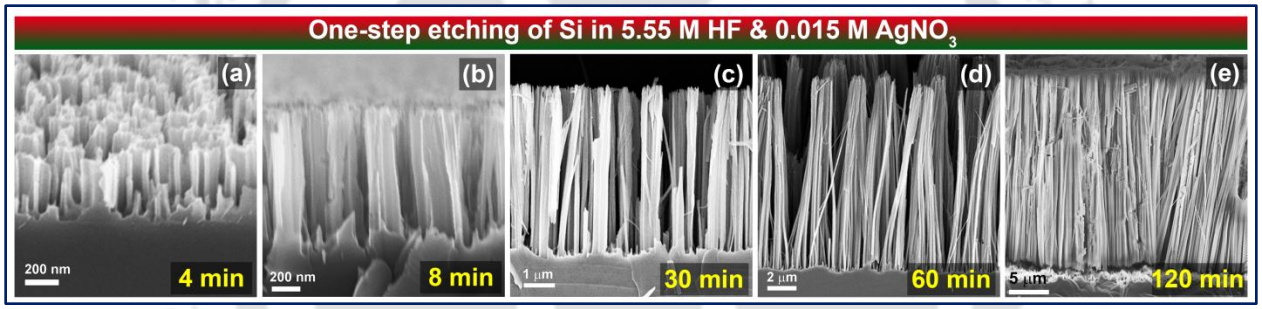

Fig. 3.8. FESEM cross-sectional images of the as-grown Si NWs for different etching duration in 0.015 M $AgNO_3$ + 5.55 M HF: (a) 4 min, (b) 8 min, (c), 30 min (d) 1 hr and (e) 2 hr.

Ω-cm in each case. It is observed that the length of the Si NWs varies almost linearly with the etching duration (Fig. 3.10(a)). As mentioned earlier, in the early stage of growth, size of the Si NWs is very small, and with time the size as well as local slope increases (as seen in Fig. 3.4(c)).[32] However, after a certain time (>2 min for the present case), the diameter of the Si NW do not change significantly (only vertical growth dominates). As a result, the local slope is saturated as observed in Fig. 3.4(c). Due to the preferential etching of Si wafer, long Si NWs are formed after prolonged duration of etching.

We have also checked the effect of etching duration on the two-step MACE of p-type Si(100) wafer with resistivity 1-10 Ω-cm in 1.422 M H_2O_2 + 4.6 M HF. Fig. 3.9(a-d) shows the FESEM cross-sectional images of the as-grown Si NWs for different duration of etching. In this

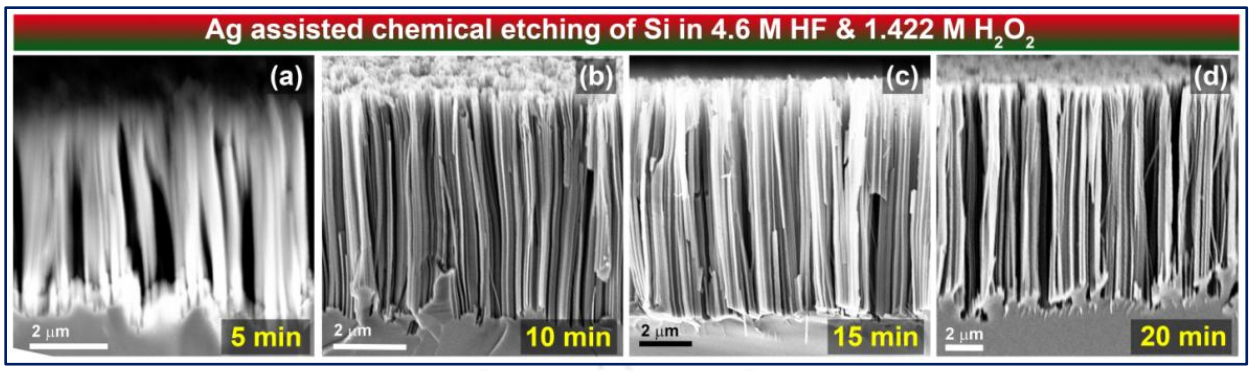

Fig. 3.9. FESEM cross-sectional images of the as-grown Si NWs for different duration of etching in 1.422 M H_2O_2 + 4.6 M HF: (a) 5 min, (b) 10 min, (c), 15 min and (d) 20 min.

case also we have observed that long vertical Si NWs are formed with almost uniform diameter. We have measured the length of the Si NWs independently using cross-sectional FESEM images and the actual length of Si NWs as a function of etching duration is shown as Fig. 3.10. Fig. 3.10(a) shows the length of the Si NWs as a function of time in 0.015 M $AgNO_3$ + 5.55 M HF, while 3.10(b) shows the same in 1.422 M H_2O_2 +4.6 M HF. It can be noted that the length of the Si NWs increases linearly with increasing etching duration. The etch rate is calculated in each case from the linear fit and it is observed that the etch rate is ~4.3 times higher for HF/H_2O_2 etched Si NWs as compared to the HF/$AgNO_3$ etched Si NWs. Note that the etch rate also depends on with the other parameters, such as the wafer doping type and doping density of the Si wafer, relative etchant concentration, temperature etc.

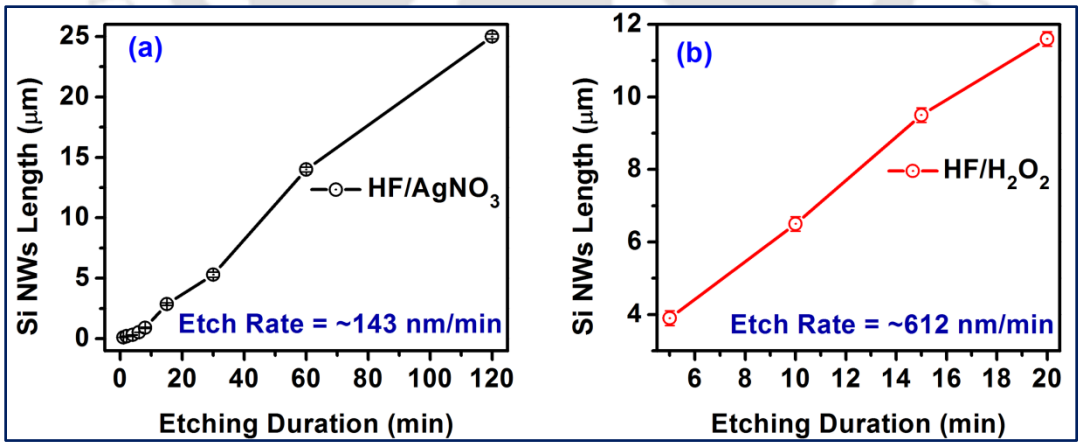

Fig. 3.10. The length of Si NWs as a function of etching duration in (a) 0.015 M $AgNO_3$ + 5.55 M and (b) 1.422 M H_2O_2 + 4.6 M HF. The length of Si NW increases almost linearly with etching time.

As mentioned in *Section* 3.5, the Si NWs are covered with arbitrary shaped Si NCs on its surface and the average size and the density of the Si NCs also depend on the etching duration.

The average size of the Si NCs decreases with the etching duration, while the density of the Si NCs increases.[33, 34]

3.6.2. Effect of Metal Nanoparticle Species on the MACE Growth

The surface morphologies of the MACE grown Si NWs are different for different metal catalysts under identical etching conditions.[30] In earlier studies, mostly Ag and Au have been used as the noble metal catalysts for the growth of Si NWs by MACE. More recently, Ag/Au bilayer metal has been attempted to overcome some of the drawbacks of conventional Ag or Au assisted Si etching to fabricate arrays of uniform Si NWs.[23] In order to investigate the case of bilayer metal, we have compared Ag, Au and Ag/Au assisted etching of the Si wafers.[30] In this process, an ultra-thin layer of metal [Ag (10 nm), Au (2 nm), and Ag (10 nm) followed by Au (2 nm)] film was first deposited by thermal evaporation under high vacuum on the Si substrates. In case of bilayer metal, first Ag layer (10 nm) was deposited and then Au layer (2 nm) was deposited over the Ag layer without breaking the vacuum. These ultra-thin metal layers form interconnected nanostructures on Si substrates leaving open area for Si etching. Subsequently, all as-deposited substrates were immersed in a solution containing HF and H_2O_2 (4:1 volume ratio) for 5 min at RT. The Ag, Au and Ag/Au bilayer assisted MACE grown samples are named as AgSi, AuSi and AgAuSi respectively. Fig. 3.11(a) shows the FESEM image of the Au NPs on the Ag NPs coated Si wafer prior to etching. Fig. 3.11(b-d) shows the FESEM top view images of AgSi, AuSi and AgAuSi, respectively, after etching. Fig. 3.11(e) shows the FESEM cross sectional image of the vertically aligned Si NWs array in AgAuSi (etched for 30 min). The insets of (b) and (c) show the magnified view of a portion of the corresponding images. The scale bar is 200 nm in each case.[30] It is clear that after 5 min etching, AgSi and AuSi show porous like structure on the Si surface, without having any well-formed Si NWs. In contrast, the AgAuSi shows vertically aligned long Si NWs for the same etching duration. We have performed the growth experiment for higher etching time (30 min) and observed vertically aligned, long (~25 μm) and straight Si NW arrays for the AgAuSi, as depicted in Fig. 3.11(e). Thus, the morphology of the MACE grown Si NWs strongly depends on the nature of the noble metal catalyst. Fig. 3.11(f) shows the TEM image of a single Si NW in AgAuSi, which confirms that the surface of the Si NW is rough due to the side wall etching and it gives rise to arbitrary shaped Si NCs on the surface of Si NWs, as indicated by the arrows. Fig. 3.11(g) shows a magnified view of the Si NCs grown on the

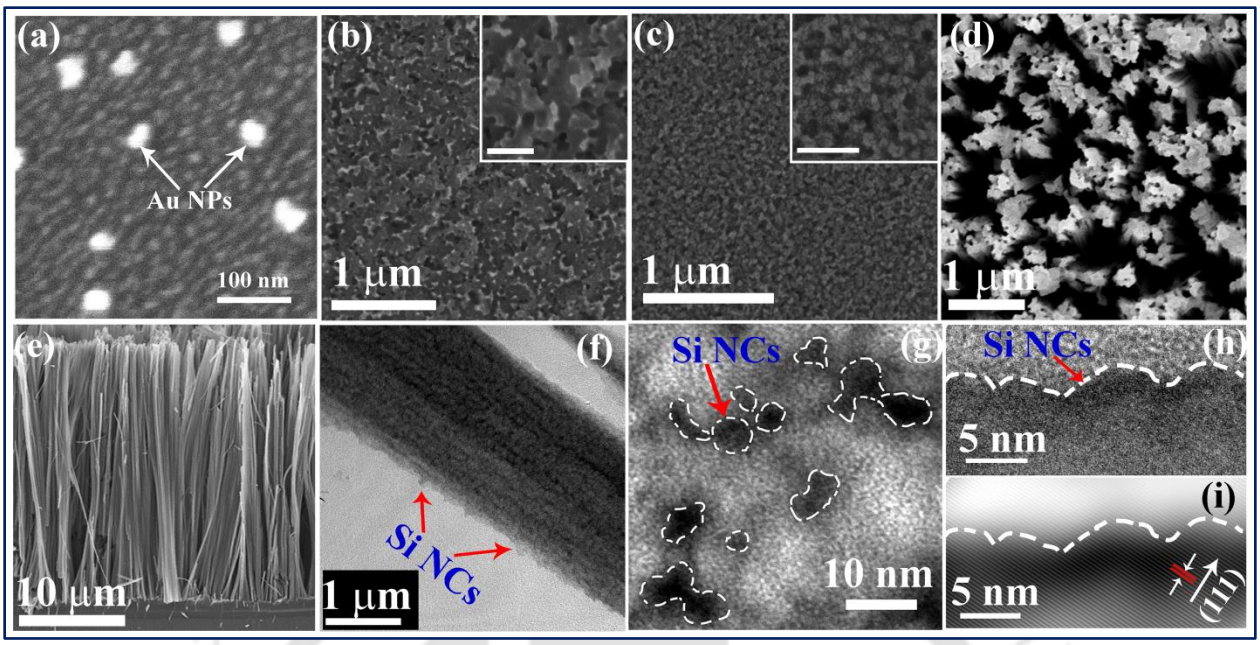

Fig. 3.11. FESEM top view images of (a) AgAu on Si (10 nm Ag + 2 nm Au), before etching (b) sample AgSi, (c) sample AuSi and (d) sample AgAuSi, respectively after 5 min etching. The insets of (b) and (c) show the magnified view of a portion of the corresponding images. The scale bar is 200 nm in each case. (e) FESEM cross-sectional images of the vertically aligned Si NWs array in AgAuSi after etching for 30 min. (f) Corresponding TEM image of single Si NW showing Si NCs due to side wall etching. (g) Higher magnification TEM image showing arbitrary shaped Si NCs (marked by white dashed boundary). (h, i) HRTEM image and corresponding IFFT image of the surface protrusions of the Si NW showing single crystalline Si NCs.

surface of the Si NWs. The arbitrary shapes of the Si NCs are indicated by white dashed lines. Note that the average dimension of the Si NCs is < 5 nm. Fig. 3.11(h) and (i) show the HRTEM lattice image and corresponding IFFT image showing the high crystallinity of the Si NW as well as Si NCs. The lattice spacing (d = 2.95 Å) in Fig. 3.11(i) confirms that the Si NW/NCs are single crystalline and (111) oriented. The reduced d-spacing (2.95 Å instead of 3.11 Å) implies a compressive strain in the lattice, which is due to the anisotropic etching and the native oxide layer grown on the Si NW/NC surface.[30, 34] Note that there are some advantages of using Ag/Au bimetal catalyst for Si etching as compared to the conventional single metal Ag or Au catalysts. In case of Ag and Au assisted etching, porous like structure on Si surface is formed without proper NW formation for 5 min etching, while vertically aligned long Si NWs decorated with Si NCs were formed in case of AgAu bimetal assisted etching under the same etching conditions.[30] The conventional Ag or Au assisted Si etching has several drawbacks, e.g., (i) Ag layer is very unstable in air due to its tendency to become Ag oxide, (ii) Ag metal undergoes dissolution induced structural failure during Si etching for an extended period of time. The problem becomes

significant when the amount of Ag is reduced inside the pores of the Si NWs, which results in the highly porous and nonuniform Si NWs.[23] (iii) Due to the poor cohesion of Au with Si and high etch rate, in case of pure Au assisted Si etching the Si NWs are not uniform and instead of Si NWs, porous Si layer is formed.[37] On the other hand, Ag/Au bilayer metal catalyst allows to overcome the drawbacks of the conventional Ag or Au assisted Si etching. Interestingly, in case of Ag/Au bilayer assisted etchings, Ag nanoparticles (NPs) are sandwiched between the Au layer and Si, which gives rise to the following advantages: (i) Ag is in direct contact with Si and protected by the more stable Au layer which prevent Ag layer from oxidation, (ii) Ag plays the role of etching front, as well as guiding the morphology of the following Au layer. Slow etch rate of Ag compared to Au makes the catalyst film stable during prolonged etching: the etching happens only in the vertical direction,[37] (iii) The overlying Au layer protects the dissolution of Ag in the etchants and provides mechanical cohesion for the discontinuous underlying Ag layer. Before performing the etching, the morphology and topography of the metal coated Si is checked. It is clear from Fig. 3.11(a) that the Au layer forms isolated Au NPs (average radius 15-25 nm) on the top of the interconnected Ag NPs (average radius 5-10 nm) layer. During the etching, the regions with bimetal NPs forms nanostructures that show interesting optical properties of the Si NWs.[30] However in this case also the bilayer assisted Si NWs are decorated with the Si NCs with average size 8.9 nm as mentioned in Table 3.1.[30] These Si NCs strongly influence the optical properties of the bimetal assisted chemically etched Si NWs.[30]

3.6.3. Effect of Etching Concentration

The morphology of the MACE grown Si NWs strongly depends on the etchant concentration.[30, 31] We have investigated the morphologies of the as-etched Si wafers for different HF concentrations keeping the H_2O_2 amount and other etching parameters fixed.[31] We have used Ag NPs as the noble metal and different volume ratio of HF & H_2O_2 for the etching of p-type Si(100) wafer with resistivity 0.01 Ω-cm for 20 min in RT (sample codes S1HF2…..S1HF8, as shown in *Table 2.1, Chapter 2*). Fig. 3.12 shows FESEM top-view (a-e, 1st row) and cross-sectional (f-j, 2nd row) images of surface morphology of the group of sample S1 (p-type, (100) and 0.01 Ω-cm).[31] The formation rate of Ag^+ ions from the Ag NPs is higher for higher concentration of H_2O_2. It also depends upon the wafer resistivity. When the HF concentration is very small (2:2), the relative concentration of H_2O_2 is high as compared to the case of 2:8. As a result, the formation rate of Ag^+ from the Ag NPs is higher, but the overall percentage of HF+

H_2O_2 with respect to water is lower as compared to the other concentration of HF and this leads to the lower density of the Ag^+. As a result, the movement of Ag NPs is arbitrary on the Si

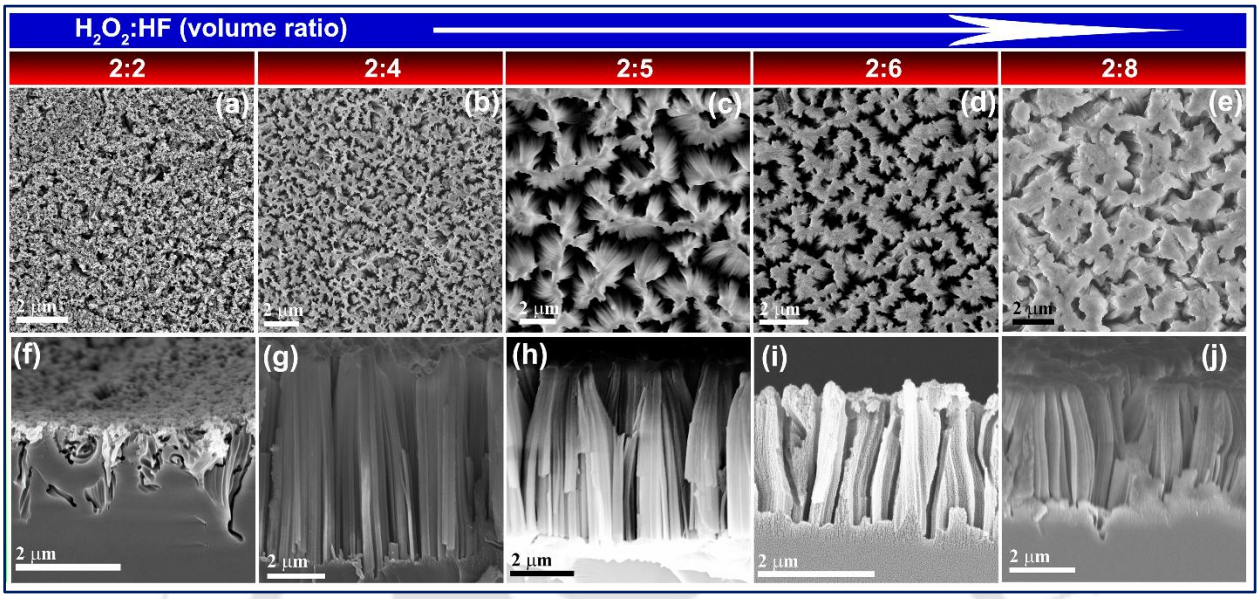

Fig. 3.12. Comparison of FESEM top-view (a-e, 1st row) and cross-sectional (f-j, 2nd row) images of surface morphology of the group of samples S1 with different etching concentration.

wafer and porous Si structure is formed instead of Si NWs (Fig. 3.12(a) and (f)) at low HF concentration.[31] With the increase in the HF concentration, the pores become more well defined and uniform, and thus vertical NWs are formed (Fig. 3.12(g-j)).[31] Note that when the HF concentration is high (e.g., 2:7, 2:8), the formation rate of Ag^+ from the Ag NPs is slower. Accordingly, the Si NWs diameters are higher and the lengths are lower (Fig. 3.12(i, j)) as compared to the low concentration HF cases (Fig. 3.12(g, h)).[31] It is also clear that the NWs are slightly bent at the top portions and for higher concentration of HF (2:8) the Si NWs form bundles (Fig. 3.12(e) and (j)). So, we optimized the ratio of H_2O_2 and HF (2:4, sample code S1HF4 or 2:5 sample code S1HF5) for the growth of micron long Si NWs with ~50-300 nm diameter by Ag assisted two-step etching of Si and we have studied the optical properties of these Si NWs for different applications.

We observed mesoporous structure of the Si NWs for each concentration of HF from the TEM images.[31] 3.14(a) shows the TEM image of a single Si NWs in sample S1HF5.[31] It is clear that the surface of the Si NW is rough due to the side wall etching and it gives rise to arbitrary shaped Si NCs on the surface of Si NWs.[31] It was discussed in *Section* 3.5 that the average size of the Si NCs increases and the Si NCs density decreases with increasing HF concentration.[23, 25,

[27, 30-34, 56] Interestingly, these Si NCs have significant effect in the PL, Raman and photocatalytic properties of the mesoporous Si NWs.

3.6.4. Orientation Controlled Growth of Si NWs

In order to understand the effect of Si wafer orientation on the morphology and structure of the Si NWs, we have performed the Ag assisted two-step MACE of Si(111) wafer in different etching concentration of HF + H_2O_2 (sample code S2HF2…..S2HF8, as shown in T*able 2.1, Chapter 2*). Fig. 3.13(a-e) shows the FESEM cross-sectional images of surface morphology of the group of sample S2.[31] Interesting changes in growth direction and morphology have been observed when the H_2O_2:HF concentration ratio is systematically changed from 2:2 to 2:8.[31] At lower HF concentration (2:2), nearly straight but slightly slanted Si NWs are formed (Fig. 3.13(a)). With the increase of HF concentration, the NWs become slanted, kinked and zigzag directed but in case of Si(100), we observed straight and vertical NWs in each case as shown in Fig. 3.13.[31] The mechanism behind different orientations of the NWs in this case can be explained in the following way. According to the Si crystal structure, the (100) planes have two back bonds to the atoms underneath, while atoms on (111) planes have three back bonds.[63] The

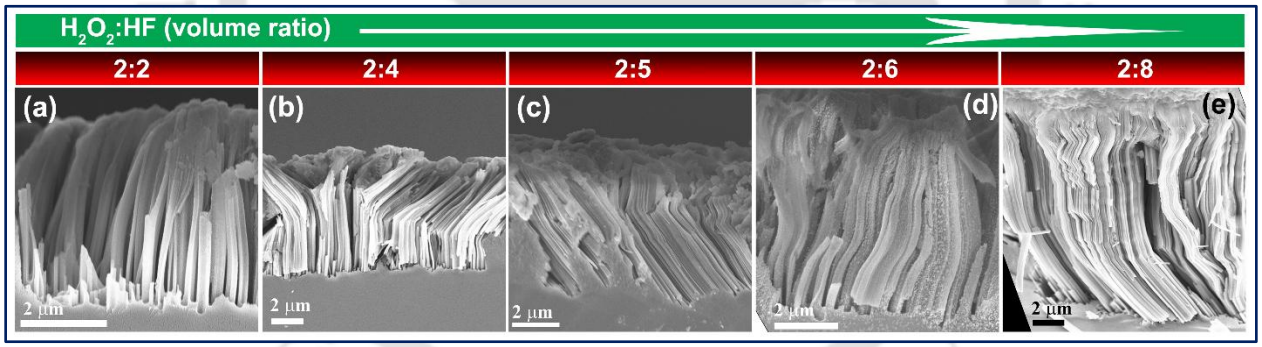

Fig. 3.13. (a-e) Comparison of FESEM cross-sectional images of surface morphology of the group of samples S2 for different etching concentration.

Si atoms of (100) planes underneath the Ag NPs in HF/H_2O_2 solution are easier to dissolve as compared with the Si atoms of (111) planes. As a result, the Si NWs are always vertical for Si(100) wafer as the etching takes place vertically. In case of Si(111) wafer, the etching is highly anisotropic. When the HF concentration is low, the Si oxide formed on the etching front (underneath the Ag NPs) is not dissolved completely and the hole injection from the oxidant to Si as well as dissolution of Si oxide is slower. As a result, etching happens on the preferable <100> direction and the NWs are vertical for sample S2HF2. When the HF concentration is increased, the rate at which Si oxidation takes place is same as the dissolution rate. In this case,

the anisotropic etching of Si occurs and kinked Si NWs are formed. When the HF concentration becomes sufficiently high, the dissolution of Si occurs rapidly and the NWs become zigzag.[31, 63] Fig. 3.14(a) and (b) shows the TEM images of a single Si NW taken from sample S1HF5 and S2HF5, respectively. The Si NW is straight for S1HF5, while it is zigzag in nature in case of S2HF5 and the angle in each corner of the zigzag NW is shown in Fig. 3.14(b). It is clear that the surface of the Si NW is rough due to the side wall etching and it gives rise to arbitrary shaped Si NCs on the surface of Si NWs.[31]

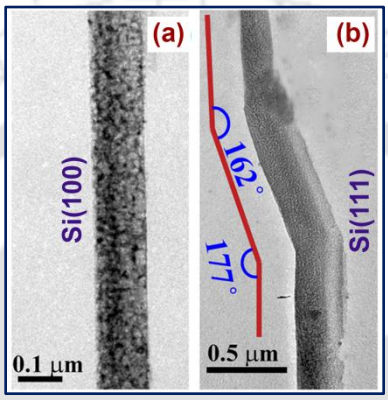

Fig. 3.14. (a-b) TEM images of a single Si NW taken from sample S1HF5 and S2HF5, respectively. The Si NW is straight for S1HF5, while it is zigzag in nature in case of S2HF5 and the angle in each corner of the zigzag NW is shown in (b).

3.6.5. Effect of the Resistivity of Si Wafer

As mentioned before in *Section* 3.5, the crystal defects and impurities, such as dopant elements in Si wafer at the Si surface, are thought to serve as nucleation sites for the pore formation during etching. Thus the lower resistivity wafers with higher doping concentration are etched faster than that of the higher resistivity wafer. Table 3.2 shows the length of the Si NWs for different resistivity wafers in different H_2O_2:HF solution. We have found that for fixed H_2O_2:HF concentration, the lower resistivity samples (2nd row) show longer Si NWs. It is to be noted that the wafer resistivity also have effect on the morphology and structure of the Si NCs on the surface of the Si NWs.[31] Fig. 3.15(a) and (b) shows the HRTEM images of sample S1HF5 and S2HF5.[31] The rough surfaces of the Si NWs are marked by the white dashed line indicating the formation of Si NCs.[31] Fig. 3.15(c, d) shows the corresponding SAED pattern of the Si NW/NCs. The orientations of the planes of the crystalline Si NWs/NCs are shown in the SAED pattern. The lattice spacing d = 2.90 Å in Fig. 3.15(a) and d = 2.95 Å in Fig. 3.15(b) confirms that the Si NW/NCs are strained, single crystalline and (111) oriented. The reduced d-spacing (2.90 Å and

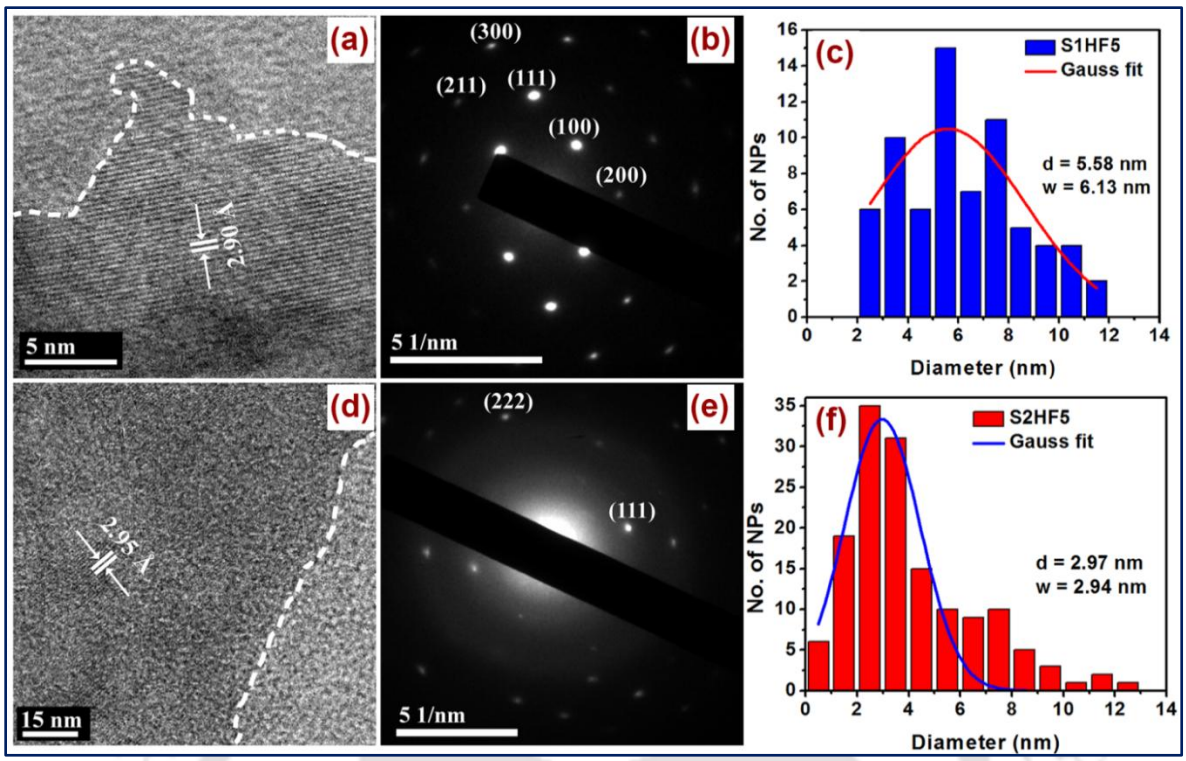

Fig. 3.15. HRTEM images of: (a) a straight Si NW in S1HF5 and (b) a zigzag Si NW in S2HF5 on its edge. The reduced lattice spacing (2.90 Å for sample S1HF5 and 2.95 Å for sample S2HF5) is seen in each cases. The presence of arbitrary shaped Si NCs on the surface of Si NW is indicated by a white dashed boundary. (c-d) The corresponding SAED pattern indicating the different orientations of the crystalline Si NWs/NCs. The size distribution of the Si NCs on the surface of the Si NWs for (e) S1HF5 and (f) S2HF5. The corresponding Gaussian fit (line) to the size distribution with the average diameter and FWHM is also shown for comparison.

2.95 Å instead of 3.11 Å) implies a compressive strain in the lattice, which is related to the anisotropic etching and native oxide layer grown on the Si NW/NC surface.[34] The size distribution of Si NCs measured from sample S1HF5 and S2HF5 are shown in Fig. 3.15(e) and

Table 3.2: *Length of the Si NWs for different wafer resistivity in different H_2O_2:HF solution.*

Si wafer Resistivity (Ω-cm)	Length of the Si NWs in μm for different H_2O_2:HF Concentration				
	2:2	**2:4**	**2:5**	**2:7**	**2:8**
0.01	--	7.1±0.1	5.6±0.1	2.5±0.1	3.5±0.1
0.001	4.4±0.2	8.2±0.4	6.8±0.4	6.2±0.4	15.5±0.4

(f), respectively. The average diameter (d) of the Si NCs are calculated by a Gaussian fit to the size distribution in Fig. 3.15(e) and (f) and the mean value of d in S1HF5 is ~5.58 nm, while it is ~2.97 nm in S2HF5. The full width at half maximum (w) of the distribution is also high in case

of sample S1HF5 (6.13 nm) as compared to the sample S2HF5 (2.94 nm). These observations are consistent with the discussion in *Section* 3.5.

3.8. Controlling the Diameter of the Si NWs

The cross-sectional dimension of the Si NWs grown by MACE depends on the intermediate space between the pores on Si wafer, since the formation of pores depends upon the shape, size and interspacing of the pre-deposited metal islands on the Si wafer. Usually, self-assembling polymers and lithography are commonly used for patterning the noble metal on Si wafer to control the diameter of the Si NWs and the spacing between them.[28, 29, 36, 64, 65] Without the protective layer or proper masking, MACE is anisotropic and the nanostructures formed in this case are highly nonuniform. We have used a very simple, fast and inexpensive process i.e. rapid thermal annealing (RTA) for the formation of Ag NPs islands on the Si substrate from the very

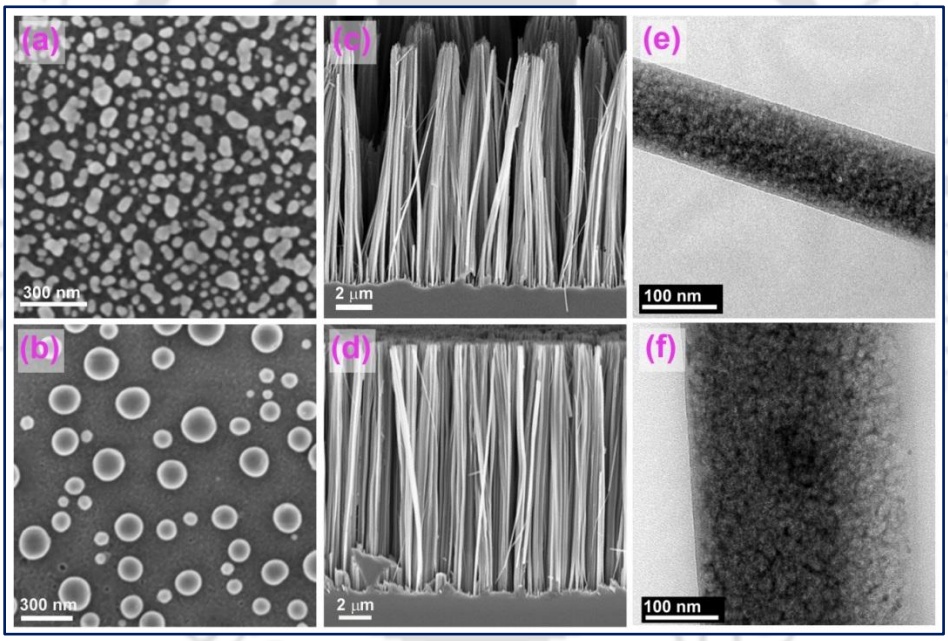

Fig. 3.16. FESEM images of Ag NPs on Si wafer (a) before RTA and (b) after RTA. (c) and (d) The Si NWs grown in on the corresponding wafers under identical condition. (e) and (f) The TEM images of the individual Si NW collected from the corresponding samples.

thin film of Ag film. In this case, at first a thin layer of Ag NPs were formed on the substrates by dipping the Si substrates in a solution containing 0.015 M $AgNO_3$ + 5.55 M HF for 4-5 seconds. RTA of Ag coated Si wafers was performed for 1 min at 500℃. We have used heating and cooling rate ~30℃/sec for our experiment. Fig. 3.16(a) and (b) shows the Ag NPs coated Si wafer before and after RTA. It is clear that the Ag NPs are collapsed to form the stable larger

NPs due to RTA. The agglomeration of the smaller Ag NPs happens to form bigger Ag droplets because of the minimization in total surface energy. The etching of the RTA treated as well as untreated wafers was carried out in 0.015 M $AgNO_3$ + 5.55 M HF for 1 hour at RT. Fig. 3.16(c) and (d) shows the FESEM cross-sectional image of sample P (Ag NPs without RTA) and Q (Ag NPs with RTA), respectively. Fig. 3.16(e) and (f) shows the TEM images of a single Si NWs of the corresponding samples. It is clear from Fig. 3.16(c) and (d) that the lengths of the Si NWs are almost same in both cases, while the average diameter of the Si NWs is higher for sample Q. We have observed that the diameter of the Si NWs is varying in the range ~20-250 nm for sample P and for sample Q it is ~50-350 nm. The Si NCs decorated mesoporous Si NWs are formed in both the cases and the dimension of the Si NCs are also almost same for both the samples (average diameter of Si NCs in sample P ~6.95 nm and it is ~7.08 nm for sample Q).

3.9. Structural and Compositional Analysis of Si NWs

We have studied the structure and composition of the Si NWs/NCs samples by means of EDX, XRD, XPS, Raman and FTIR in order to understand the structural quality, crystallinity, presence of strain, presence of terminated surface and the presence of surface defects such as NBOHC and V_O, which affect the photophysical properties of the Si NWs/NCs.

3.9.1. Energy Dispersive X-ray Analysis

For the compositional investigation, we have performed the EDX analysis on the as-grown Si NWs/NCs. Fig. 3.17(a) and (b) shows the EDX spectra measured on top surface of S1HF5 and S2HF5 confirming the presence of the Si and O on the Si NWs surface. The inset shows the corresponding elemental composition in atomic percentage.[31] Fig. 3.17(c) and (d) depict the compositional color mapping of the surface of sample S1HF5 and S2HF5. The insets in Fig. 3.17(c) and (d) show the color mapping of individual element “Si” (left corner), and “O” (right corner).[31] Fig. 3.17(e) shows the EDX spectra measured on the top surface of sample AgAuSi.[30] The EDX analysis of each sample confirms that the Si NWs are covered with a thin layer of oxide layer which is highly oxygen deficient. For example, sample S1HF5 is covered with Si_2O and sample S2HF5 is covered with SiO, as revealed form the compositional analysis. Thus, the oxygen content of the samples is quite different in two cases, which is consistent with the XPS analysis discussed later.[31] We have attempted to remove the residual metal NPs from the Si NWs samples, though these metal NPs cannot be removed fully and can have signature in EDX

spectra. The EDX spectra in Fig. 3.17(e) confirm that the Ag and Au NPs are present on AgAuSi.[30]

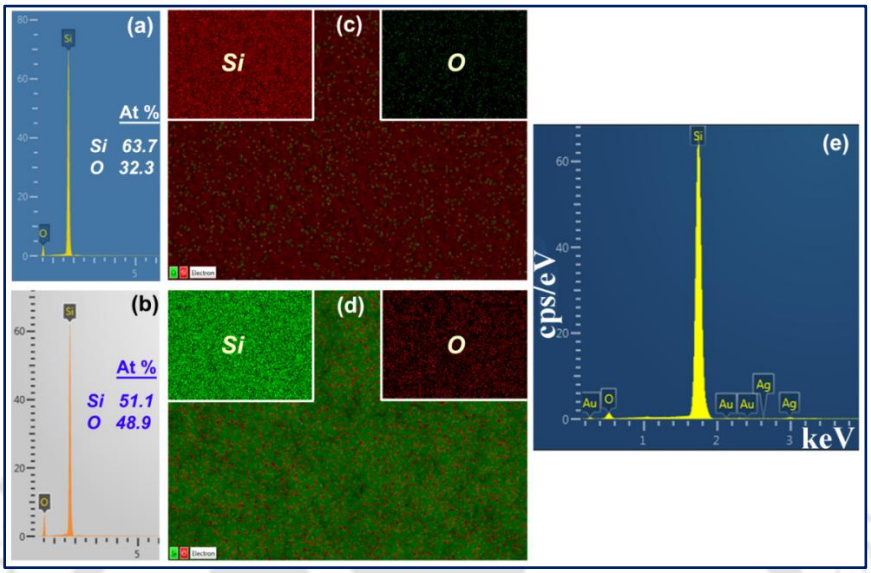

Fig. 3.17. EDX spectra of the samples: (a) S1HF5 and (b) S2HF5. The inset shows the corresponding elemental composition (in atomic percentage). The compositional color mappings of the surface of samples: (c) S1HF5 and (d) S2HF5. The insets of (c) and (d) show the color mapping of individual element Si (left corner) and O (right corner), respectively. (e) EDX spectrum of sample AgAuSi confirming the presence of the Ag and Au elements on AgAuSi.

3.9.2. X-ray Diffraction Pattern

For the investigation of the crystalline quality, phase and presence of impurity in the as synthesized Si NWs/NCs, we performed XRD analysis. Fig. 3.18 shows the comparison of the XRD pattern of different samples. The curves are vertically translated for better visualization of the small peaks. It is clear that the as-grown Si NCs/NWs are highly crystalline in nature and the sharp peaks are indicated by the vertical dashed lines (JCPDS ref. no. 26-1481 and 77-2109). It is also clear that all the samples are covered by a thin layer of SiO_2 and samples show broad peaks (shaded rectangles) at $2\theta \sim 21.5^{\circ}$ and $2\theta \sim 55.5^{\circ}$, which correspond to (100) and (103) plane of SiO_2, respectively (JCPDS ref. no. 86-1629 and 86-1630). We also checked the XRD pattern of sample S1HF5 before removing the Ag NPs (bottom curve in Fig.3.17). We observed sharp peaks due to Ag at $2\theta \sim 38.2^{\circ}$ due to Ag(111), $2\theta \sim 44.3^{\circ}$ due to Ag(200) and $2\theta \sim 64.5^{\circ}$ due to Ag(220) (JCPDS ref. no. 04-0783). Note that the XRD peaks corresponding to Ag are also present in some of the samples, which confirms that residual Ag NPs cannot be fully removed by post growth HNO_3 etching.

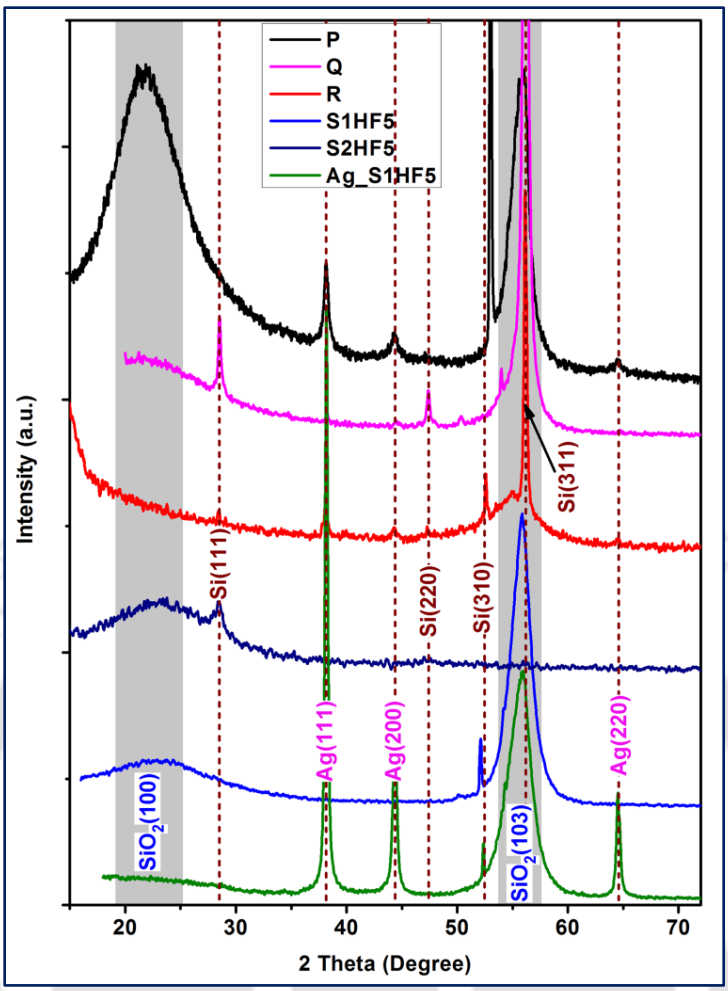

Fig. 3.18. XRD pattern of the different samples. The curves are vertically shifted for clarity. The sharp peaks are indicated by dashed vertical lines and broad peaks by shaded rectangle.

3.9.3. X-ray Photoelectron Spectroscopy

In order to investigate the chemical composition and the nature of defects in Si NWs/NCs, XPS studies were carried out on some samples. Fig. 3.19(a) shows the comparison of the core level Si 2p XPS spectra of different Si NWs/NCs samples, while 3.19(b) shows the corresponding O 1s spectra. The XPS spectrum of bulk Si is also shown in each case for the comparison. The spectra are normalized and vertically translated to enable comparison. XPS studies confirm that the Si NWs as well as the Si NCs are covered by a native sub-oxide layer of Si, i.e., SiO_x ($0<x<2$) layer. The neutral Si and its different oxidation of Si (Si^{0+} (Si), Si^{1+} (Si_2O), Si^{2+} (SiO), Si^{3+} (Si_2O_3), and Si^{4+} (SiO_2)) are shown by the dashed vertical lines in Fig. 3.19(a).[30, 31, 34, 66, 67] However, the compositional analysis of XPS also confirms the presence of the sub-oxide in each

case. It is interesting to note that Si^{0+} XPS peak is very weak for sample P, which implies that the sample P is covered with a thick sub-oxide layer.[34] XPS analysis thus confirms the presence of SiO_x layer on the Si NWs/NCs and this SiO_x layer is responsible for the compressive strain in the Si NWs/NCs, as revealed from the HRTEM analysis. From the O1s spectrum in Fig. 3.19(b), the XPS peak at ~532-533 eV is attributed to O^- ions in the Si-O bonds due to the sub-oxide layer of Si, which is consistent with the Si 2p core level spectrum.[30, 31, 34] We have studied the effect of

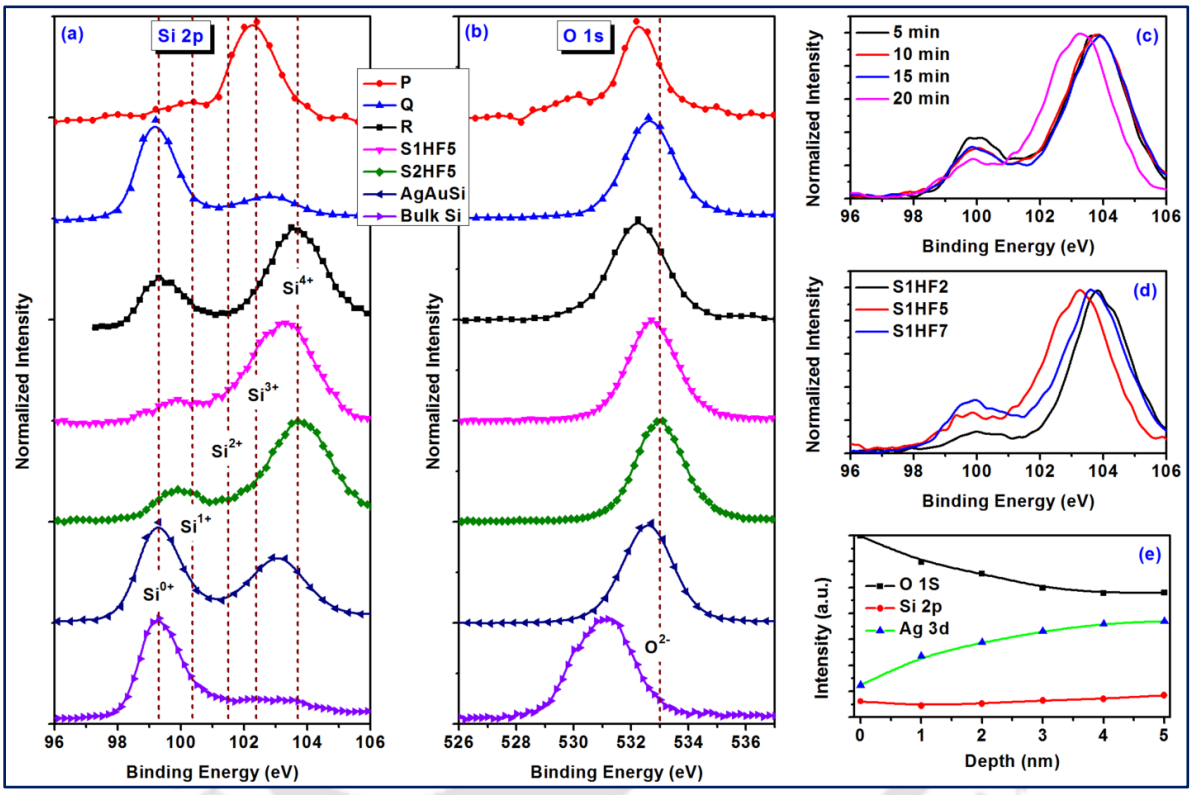

Fig. 3.19. (a) Core level Si 2p XPS spectra of different Si NWs/NCs samples. (b) Corresponding O 1s spectra. The legends in (b) are same as that of (a). The spectra are normalized and vertically shifted to enable comparison. Different oxidation states of Si in (a) and O in (b) are shown by the dashed vertical lines. (c) Core level Si 2p XPS spectra of different Si NWs/NCs samples grown for different etching duration. (d) Comparison of the Si 2p XPS spectra of samples S1HF2, S1HF5 and S1HF7 (different HF concentration). (e) Depth profile of O, Si and Ag atoms in the sample R from surface.

etching duration on the XPS spectra of Si NWs/NCs. Fig. 3.19(c) shows the core level Si 2p XPS spectra of different Si NWs/NCs samples grown for different etching duration. With increasing duration of etching, the intensity of the Si^{0+} peak decreases due to the formation of thicker SiO_x layer. We also investigated the effect of relative etching concentration on the XPS of Si NWs/NCs and Fig. 3.19(d) shows the comparison of the Si 2p XPS spectra of the samples S1HF2, S1HF5 and S1HF7 (different HF concentration, keeping the other parameters

unchanged). The Si^{0+} peak intensity is higher for higher HF concentration. During the etching, SiO_2 is formed in the etching front (beneath metal NPs) and it is dissolved by the HF present in the solution. When the HF concentration is low, the dissolution rate is relatively low and due to this the thick sub-oxide layer in formed for sample S1HF2, which results the low intensity in Si^{0+} peak. Fig. 3.19(e) shows the depth profile of O 1s, Si 2p and Ag 3d core level XPS spectra for the sample R. It is clear from the depth profile data that the Si 2p intensity is almost constant up to the depth of 5 nm. On the other hand, the oxygen concentration decreases systematically with depth from the surface layer. Thus, the sub-oxide layer extends only up to a few nm from the Si NW/NC surface. In contrast, the Ag concentration is low at the surface, increases slowly with depth finally saturates at a depth of almost 5 nm.

In order to understand the relative contribution of the different surface states (defects and terminated surfaces), we have fitted the Si 2p core level XPS spectrum of each sample by Gaussian peaks (using the appropriate Shirley background). The fitted parameters are tabulated in Table 3.3. Fig. 3.20(a) shows the fitted Si 2p core-level spectrum of AgAuSi, which exhibits

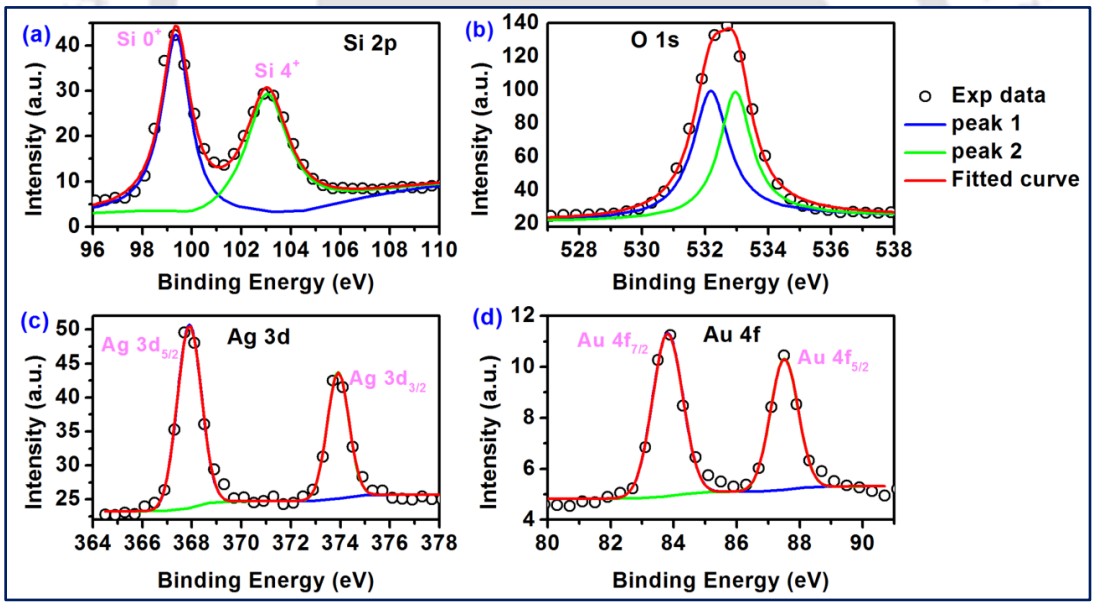

Fig. 3.20. Core level XPS spectra of sample AgAuSi: (a) Si 2p; (b) O 1s; (c) Ag 3d and (d) Au 4f. The legends for fitted peaks are same in each case. Each curve is fitted with two Gaussian peaks after choosing appropriate baseline (Shirley).

two peaks at ~99.4 eV and ~103.0 eV corresponding to Si^{0+} and Si^{4+} (SiO_2) states, respectively.[30, 66, 67] The asymmetric shape of O 1s spectrum for AgAuSi in Fig. 3.20(b) is fitted by choosing the appropriate XPS baseline (Shirley). The peaks at 533.0 eV and 532.2 eV for

AgAuSi are assigned to O^- ions in the SiO_2 bonds and O^- ions in the oxygen deficient regions, (e.g., Si_2O_3), respectively.[30, 68, 69] From the XPS compositional analysis, the atomic ratio of oxygen to Si is found to be <2 in each sample (Table 3.3). Fig. 3.20(a) also confirms that the atomic ratio of oxygen to Si is 1.5 (Si_2O_3). This leads to NBOHC (≡Si–O∗, where "∗" represents an unpaired hole) related defects in the SiO_x layer. The peak around ~100 eV is also sometimes attributed to the Si-H bonds.[31] This is consistent with the PL spectra that show defect related visible emission (discussed in *Chapter* 4). Fig. 3.20(c, d) shows the Ag 3d and Au 4f XPS core level spectra confirming the presence of Ag and Au NPs in the AgAuSi.[30] Despite the post growth etching of Si NWs in HNO_3 solution, Ag and Au NPs reside on the surface and at the bottom of the Si NWs. It was shown from XPS depth profile in Fig. 3.19(e) that the density of metal NPs increases with depth from the top surface of the Si NWs.[70] This is because the metal NPs resides on the pores of the Si NWs. These NPs influence the PL and photocatalytic properties of the Si NWs/NCs.

Table 3.3: *The summary of the fitted peak parameters of Si 2p XPS core level spectra of different samples.*

Sample Code	Peak Information						Si:O (Atomic ratio)
	Si^{0+} (eV)	Si^{1+} (eV)	Si^{2+} (eV)	Si^{3+} (eV)	Si^{4+} (eV)	Si-H (eV)	
Bulk Si	99.2	100.2	-	102.1	103.5	-	1.08
P	99.7	-	101.8	102.6	-	-	1.88
Q	99.2	100.5	-	101.9	103.1	-	0.83
R	99.3	-	101.1	102.6	103.7	100.0	1.54
S1HF5	99.3	-	101.4	-	103.3	99.9	1.80
S2HF5	99.4	-	101.4	-	103.8	100.1	1.85
AgAuSi	99.4	-	-	-	103.0	-	1.58

3.9.4. Raman Spectroscopy

Raman scattering is sensitive to the crystal lattice microstructure of Si via its vibrational properties. In order to assess the crystallinity/amorphicity, presence of H-terminated surface and the dimension of Si NCs on the Si NWs surface, micro-Raman measurements are very important for the MACE grown Si NWs. It has been reported that the MACE grown Si NWs are covered by a thin layer of the amorphous Si or Si-H layers that is believed to prevent the lateral etching of the Si NWs.[32] In order to confirm the above we performed micro-Raman studies on the as-

grown Si NWs via one-step etching of Si in $AgNO_3$/HF solution.[32] Fig. 3.21 shows the Raman spectra of the Si NWs grown after different etching durations at the early stage of growth.[32] Several multi-phonon bands are present in the spectra (~300, ~433, ~520, ~617, ~670, ~826 and ~964 cm^{-1}), some of which are not detected in the bulk Si spectrum (i.e., before etching). The LO, 2LA and 2LO modes shown in Fig. 3.21 are mostly due to the amorphous Si or the surface chemical bonds (such as, Si–H).[33, 71] The peak intensity increases with increasing duration of

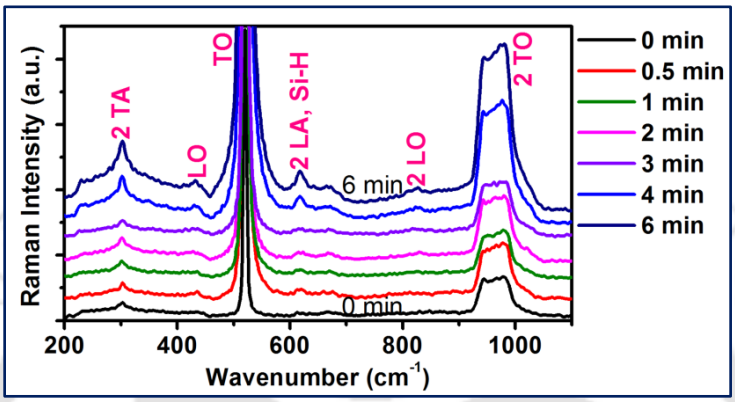

Fig. 3.21. Comparison of the Raman spectra for the as-grown Si NWs via one-step etching of Si in $AgNO_3$/HF solution for different time durations. The curves are vertically shifted for clarity of presentation.

etching. Note that the TO mode at 520 cm^{-1}, the first-order Raman mode of crystalline Si, is extended down to ~460 cm^{-1}. The TO peak (~480 cm^{-1}) corresponding to the amorphous Si may be overshadowed by the high intensity 1st order Raman peak of crystalline (core) Si (~520 cm^{-1}). Due to the presence of the amorphous Si and Si-H layer on Si NWs surface, the Ag^+ ions do not affect the sidewall of the as grown Si NWs considerably and the etching occurs preferentially along the vertical direction. This leads to straight vertical pores on the Si surface resulting in an array of vertical Si NWs.[32]

Inspection of line shapes of Raman spectra provides useful information concerning the crystallinity, amorphicity, and dimension of nanostructured Si. We have observed that the 1st order Raman spectra of each sample are red shifted and showed lower energy asymmetry as compared to the bulk Si.[1, 30, 31, 33, 34] Fig. 3.22(a) depicts a comparison of the 1st order Raman spectra of S2 etched with different concentration of HF,[31] while Fig. 3.22(b) shows a comparison of the Raman spectra for the Si NWs samples grown for different etching duration in HF/H_2O_2 solution (15 min etched sample corresponds to sample R).[33] Raman spectra of different samples were compared by taking the first order Raman peak of the bulk Si at 520.5 cm^{-1} as reference

(dotted vertical line). Note that the 1st order Raman spectrum of each sample shows a red shift and asymmetry in the lower energy range. These Raman shifts (Δω) and asymmetry can be

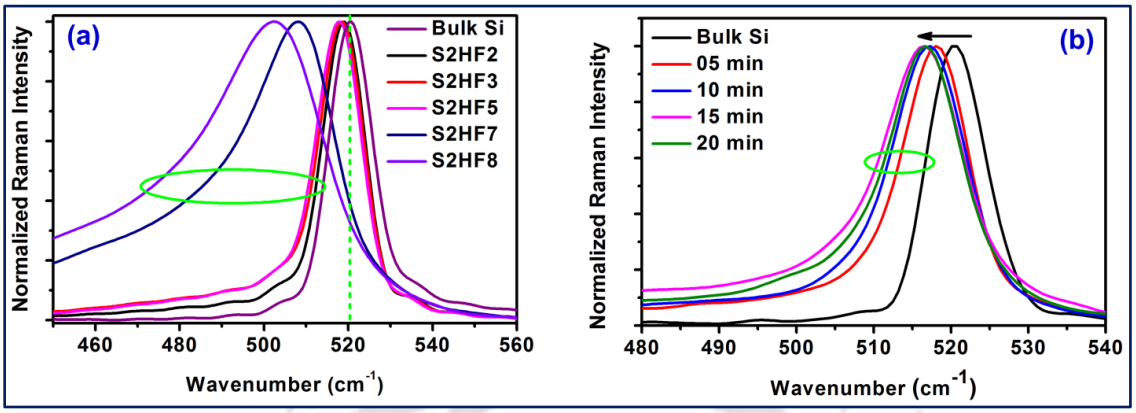

Fig. 3.22. (a) Comparison of the 1st order Raman spectra with 514 nm laser excitation at a laser power of 1.2 mW for the Si NWs in group S2 grown with different concentrations of HF. (b) Comparison of the Raman spectra with 488 nm laser excitation at a laser power of 0.083 mW for the Si NWs samples grown for different etching duration in HF/H_2O_2 solution (15 min etched sample corresponds to sample R). The bulk Si Raman spectrum is also shown for comparison. The spectra are normalized to assess the peak shift from the bulk Si 1st order Raman peak at 520.5 cm^{-1} (indicated by dotted vertical line).

explained based on the competing effect of phonon confinement and strain on the Si NWs/NCs.[30, 31, 33, 34, 72-74] The Δω is positive (blue shift) for compressive strain and negative (red shift) for tensile strain.[30, 33, 34, 74] However, the phonon confinement can cause the Raman peak shift toward the lower wavenumber. The details of the Raman shift are explained in the light of phonon confinement effect, strain and laser heating in *Chapter* 5.[33] Not that the TO and 2TO

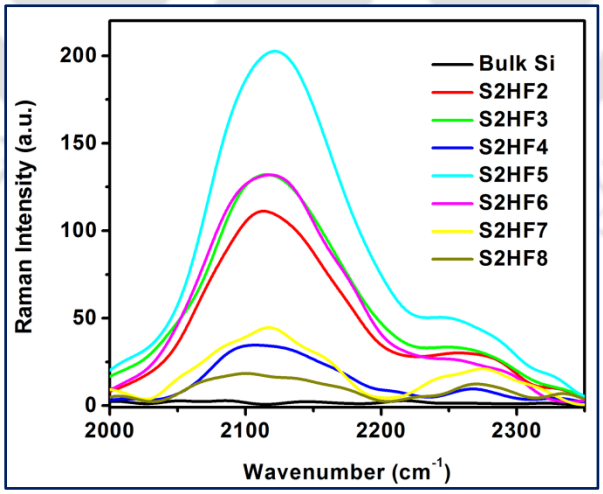

Fig. 3.23. Comparison of the Raman spectra in range 2000-2350 cm^{-1} for the Si NWs grown with different concentrations of HF (S2 group). The peak at ~2112 cm^{-1} indicates the presence of Si-H bonds in the respective samples.

Raman modes of the samples in Fig. 3.22(a) (S2HF7 and S2HF8) are deformed and the shifts are beyond the phonon confinement limit.[31] It implies that the Si NWs top surface become amorphous in nature. Note that the tail of the 1st order Raman peak in each case is extended down to 460 nm (Fig. 3.21, 3.22(a, b)), which falls in the region TO Raman mode of amorphous Si (480 cm^{-1}). Higher concentration of HF creates higher fraction of amorphous Si-H regions in the MACE grown Si NWs.[31]

Interestingly, the presence of Si-H bonds in the Si NWs/NCs grown by MACE is also evidenced by the Raman data in the range 2000-2400 cm^{-1}.[30, 31, 75] Fig. 3.23 shows the Raman spectra in the range 2000-2350 cm^{-1} of the samples in group S2.[31] Each sample shows the stretching modes of Si-H present at ~2112 cm^{-1}.[31, 76] The Si-H bonds play a crucial role in the photocatalytic process (discussed in *Chapter* 7).

3.9.5. Fourier Transform Infrared Spectroscopy

In order to further understand the structural quality and the presence of different characteristic

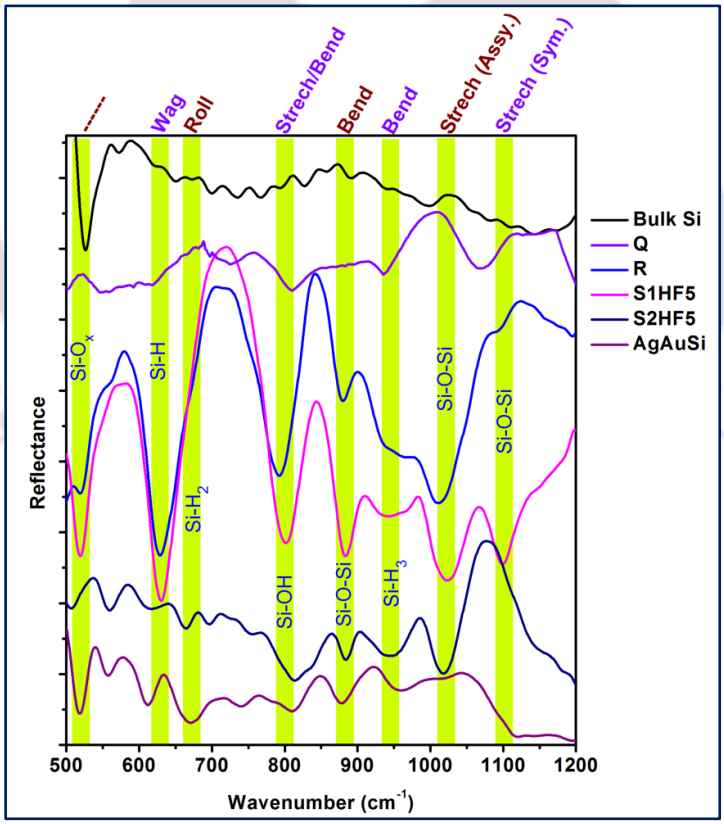

Fig. 3.24. Comparison of the FTIR reflectance spectra for samples Q, R, S1HF5, S2HF5 and AgAuSi showing different vibrational modes. The curves are vertically translated to enable comparison. The green vertical boxes indicate the position of the characteristic modes of Si. The nature of the corresponding characteristic modes is shown on the top of each vertical box.

modes of Si, FTIR Spectroscopy of the MACE grown samples is employed. Fig. 3.24 shows the FTIR spectra recorded in reflection mode for the as-synthesized Si NWs/NCs samples. The characteristic modes of Si present in these samples are indicated by the green vertical boxes. The nature of the corresponding characteristic modes is shown on the top of each vertical box. It is clear that the MACE grown Si NWs are covered by a thin layer of SiO_x and it is also surrounded by the Si-H terminated surface. The vibrational modes are consistent with the earlier reports and our Raman data.[30, 31, 76, 77] Thus, the FTIR analysis of MACE grown Si NWs strongly support the fact that the samples are covered by a layer of amorphous Si-H and SiO_x, which are consistent with the XPS and XRD analyses. These results are very important to explain the simultaneous presence of strong PL and photocatalytic activity of the MACE grown Si NWs/NCs.

3.10. Conclusion

We have fabricated large area, highly oriented and controlled array of Si NWs by a very simple, easy, fast and cost effective MACE process. The Si NWs are highly crystalline and decorated with arbitrary shaped quantum size Si NCs, which have strong effect on the optical properties of the Si NWs/NCs. We have investigated the impact of etching conditions and etching parameters on the diameter, orientation and structure of the as-synthesize Si nanostructures. The etching mechanism of Si by MACE resembles the shadowing instability model explaining columnar growth of Si NWs by MACE. Ag/Au bimetal assisted etching of Si provides improved morphology over conventional single Ag or Au metal layer as a catalyst for the MACE growth of Si NWs/NCs. MACE grown Si NWs/NCs covered by a layer of amorphous Si-H and SiO_x and NBOHC defects are present within the SiO_x layer, which are very significant to explain the simultaneous photoluminescence and photocatalytic properties of MACE grown Si. The density of the Si NCs, defect centers and Si-H terminated sites are tunable and can be controlled by the etching parameters. These Si NWs/NCs are extremely important for device applications, as it possess tunable optical properties.

References

1. Ghosh, R.; Giri, P. K. *Sci. Adv. Today,* **2016,** 2, 25230.

2. Otto, M.; Algasinger, M.; Branz, H.; Gesemann, B.; Gimpel, T.; Füchsel, K.; Käsebier, T.; Kontermann, S.; Koynov, S.; Li, X.; Naumann, V.; Oh, J.; Sprafke, A. N.; Ziegler, J.; Zilk, M.; Wehrspohn, R. B. *Adv. Optical Mater.,* **2015,** 3, 147.
3. Chen, C. C.; Yeh, C. C.; Chen, C. H.; Yu, M. Y.; Liu, H. L.; Wu, J. J.; Chen, K. H.; Chen, L. C.; Peng, J. Y.; Chen, Y. F. *J. Am. Chem. Soc.,* **2001,** 123, 2791.
4. Wu, Y.; Yang, P. *Chem. Mater.,* **2000,** 12, 605.
5. Schmidt, V.; Wittemann, J. V.; Gösele, U. *Chem. Rev.,* **2010,** 110, 361.
6. Peng, K.-Q.; Lee, S.-T. *Adv. Mater.,* **2011,** 23, 198.
7. Shao, M.; Ma, D. D. D.; Lee, S.-T. *Eur. J. Inorg. Chem.,* **2010,** 2010, 4264.
8. Peng, K.-Q.; Wang, X.; Li, L.; Hu, Y.; Lee, S.-T. *Nano Today,* **2013,** 8, 75.
9. Dhara, S.; Giri, P. K. *Rev. Nanosci. Nanotechnol. ,* **2013,** 2, 147.
10. Niu, J.; Sha, J.; Yang, D. *Physica E Low Dimens. Syst. Nanostruct.,* **2004,** 23, 131.
11. Liu, X.; Coxon, P. R.; Peters, M.; Hoex, B.; Cole, J. M.; Fray, D. J. *Energy Environ. Sci.,* **2014,** 7, 3223.
12. Schmidt, V.; Wittemann, J. V.; Senz, S.; Gösele, U. *Adv . Mater.,* **2009,** 21, 2681.
13. Galopin, E.; Barbillat, J.; Coffinier, Y.; Szunerits, S.; Patriarche, G.; Boukherroub, R. *ACS Appl. Mater. Interfaces,* **2009,** 1, 1396.
14. Shao, M.; Cheng, L.; Zhang, X.; Ma, D. D. D.; Lee, S. T. *J. Am. Chem. Soc.,* **2009,** 131, 17738.
15. Dussart, R.; Tillocher, T.; Lefaucheux, P.; Boufnichel, M. *J. Phys. D: Appl. Phys.,* **2014,** 47, 123001.
16. Choi, D.-G.; Yu, H. K.; Jang, S. G.; Yang, S.-M. *J. Am. Chem. Soc.,* **2004,** 126, 7019.
17. Gu, Q.; Dang, H.; Cao, J.; Zhao, J.; Fan, S. *Appl . Phys. Lett.,* **2000,** 76, 3020.
18. Das Kanungo, P.; Zakharov, N.; Bauer, J.; Breitenstein, O.; Werner, P.; Goesele, U. *Appl. Phys. Lett.,* **2008,** 92, 263107.
19. Wen, C. Y.; Reuter, M. C.; Tersoff, J.; Stach, E. A.; Ross, F. M. *Nano Lett.,* **2010,** 10, 514.
20. Li, X.; Bohn, P. W. *Appl. Phys. Lett.,* **2000,** 77, 2572.
21. Peng, K. Q.; Yan, Y. J.; Gao, S. P.; Zhu, J. *Adv. Mater.,* **2002,** 14, 1164.
22. Shao, M.-W.; Zhang, M.-L.; Wong, N.-B.; Ma, D. D.-d.; Wang, H.; Chen, W.; Lee, S.-T. *Appl. Phys. Lett.,* **2008,** 93, 233118.
23. Kim, J.; Han, H.; Kim, Y. H.; Choi, S. H.; Kim, J. C.; Lee, W. *ACS Nano,* **2011,** 5, 3222.
24. Kayes, B. M.; Filler, M. A.; Putnam, M. C.; Kelzenberg, M. D.; Lewis, N. S.; Atwater, H. A. *Appl. Phys. Lett.,* **2007,** 91, 103110.
25. Qu, Y.; Zhoua, H.; Duan, X. *Nanoscale,* **2011,** 3, 4060.
26. Bachtouli, N.; Aouida, S.; Bessais, B. *Microporous Mesoporous Mater.,* **2014,** 187, 82.
27. Huang, Z.; Geyer, N.; Werner, P.; de Boor, J.; Gosele, U. *Adv. Mater.,* **2011,** 23, 285.
28. Peng, K.; Zhang, M.; Lu, A.; Wong, N.-B.; Zhang, R.; Lee, S.-T. *Appl. Phys. Lett.,* **2007,** 90, 163123.
29. Hildreth, O. J.; Lin, W.; Wong, C. P. *ACS Nano,* **2009,** 3, 4033.
30. Ghosh, R.; Imakita, K.; Fujii, M.; Giri, P. K. *Phys. Chem. Chem. Phys.,* **2016,** 18, 7715.
31. Ghosh, R.; Giri, P. K. *RSC Adv.,* **2016,** 6, 35365.
32. Pal, A.; Ghosh, R.; Giri, P. K. *Appl. Phys. Lett.,* **2015,** 107, 072104.
33. Ghosh, R.; Pal, A.; Giri, P. K. *J. Raman Spec.,* **2015,** 46, 624.
34. Ghosh, R.; Giri, P. K.; Imakita, K.; Fujii, M. *Nanotechnology,* **2014,** 25, 045703.
35. Li, X. *Curr. Opin. Solid State Mater. Sci.,* **2012,** 16, 71.
36. Chen, C.-Y.; Liu, Y.-R. *Phys. Chem. Chem. Phys.,* **2014,** 16, 26711.
37. Kim, S. M.; Khang, D. Y. *Small,* **2014,** 10, 3761.
38. Sanjay, K. S.; Dinesh, K.; Schmitt, S. W.; Sood, K. N.; Christiansen, S. H.; Singh, P. K. *Nanotechnology,* **2014,** 25, 175601.
39. Peng, K. Q.; Hu, J. J.; Yan, Y. J.; Wu, Y.; Fang, H.; Xu, Y.; Lee, S. T.; Zhu, J. *Adv. Func. Mater.,* **2006,** 16, 387.

40. To, W. K.; Tsang, C. H.; Li, H. H.; Huang, Z. *Nano Lett.,* **2011,** 11, 5252.
41. Smith, Z. R.; Smith, R. L.; Collins, S. D. *Electrochim. Acta,* **2013,** 92, 139.
42. Pelliccione, M.; Lu, T.-M., *Evolution of thin film morphology: modeling and simulation,*. Springer-Verlag, New York, (2008).
43. Jeffries, J. H.; Zuo, J. K.; Craig, M. M. *Phys. Rev. Lett. ,* **1996,** 76, 4931.
44. Zhao, Y.; Wang, G.-C.; Lu, T.-M., *Characteriztion of Amorphus and Crystalline Rough Surface: Principles and Application*. Academic Press, London, (2001).
45. Barabási, L.; Stanley, H. E., *Fractal Concepts in Surface Growth*. Cambridge University Press, (1995).
46. Lee, I. J.; Yun, M.; Lee, S. M.; Kim, J. Y. *Phys. Rev. B,* **2008,** 78, 115427.
47. Datta, D. P.; Chini, T. K. *Phys. Rev. B,* **2004,** 69, 235313.
48. Kim, J.; Cahill, D.; Averback, R. *Phys. Rev. B,* **2003,** 67.
49. Lai, Z.; Das Sarma, S. *Phys. Rev. Lett.,* **1991,** 66, 2348-2351.
50. Wolf, D. E.; Villain, J. *Europhys Lett,* **1990,** 13, 389-394.
51. Yao, J. H.; Guo, H. *Phys. Rev. E,* **1993,** 47, 1007.
52. Karunasiri, R. P. U.; Bruinsma, R.; Rudnick, J. *Phys. Rev. Lett. ,* **1989,** 62, 788.
53. Bales, G. S.; Bruinsma, R.; Eklund, E. A.; Karunasiri, R. P. U.; Rudnick, J.; Zangwill, A. *Science* **1990,** 249, 264.
54. Pelliccione, M.; Karabacak, T.; Gaire, C.; Wang, G. C.; Lu, T. M. *Phys. Rev. B,* **2006,** 74, 125420.
55. Drotar, J. T.; Zhao, Y. P.; Lu, T. M.; Wang, G. C. *Phys. Rev. B,* **2000,** 62, 2118.
56. Hochbaum, A. I.; Gargas, D.; Hwang, Y. J.; Yang, P. *Nano Lett.,* **2009,** 9, 3550.
57. Chen, C.-Y.; Wong, C.-P. *Nanoscale,* **2015,** 7, 1216.
58. Kumar, V.; Saxena, S. K.; Kaushik, V.; Saxena, K.; Shukla, A. K.; Kumar, R. *RSC Adv.,* **2014,** 4, 57799.
59. Zhong, X.; Qu, Y.; Lin, Y.-C.; Liao, L.; Duan, X. *ACS Appl. Mater. Int.,* **2011,** 3, 261.
60. Lowell, S.; E., S. J.; Thomas, M. A., *Characterization of porous solids and powders: surface area, pore size and density*. 3rd ed. ed.; Springer, Netherland, (2006).
61. Qu, Y.; Zhong, X.; Li, Y.; Liao, L.; Huangbc, Y.; Duan, X. *J. Mater. Chem.,* **2010,** 20, 3590.
62. Kamal Kumar, P.; Ramesh, G.; Giri, P. K. *Nanotechnology,* **2016,** 27, 315703.
63. Huang, Z.; Shimizu, T.; Senz, S.; Zhang, Z.; Geyer, N.; Gösele, U. *J. Phys. Chem. C,* **2010,** 114, 10683.
64. Xie, C.; Nie, B.; Zeng, L.; Liang, F.-X.; Wang, M.-Z.; Luo, L.; Feng, M.; Yu, Y.; Wu, C.-Y.; Wu, Y.; Yu, S.-H. *ACS Nano,* **2014,** 8, 4015.
65. Chern, W.; Hsu, K.; Chun, I. S.; Azeredo, B. P. d.; Ahmed, N.; Kim, K. H.; Zuo, J.-m.; Fang, N.; Ferreira, P.; Li, X. *Nano Lett.,* **2010,** 10, 1582.
66. Barbagiovanni, E. G.; Goncharova, L. V.; Simpson, P. J. *Phys. Rev. B,* **2011,** 83, 035112.
67. Kim, S.; Kim, M. C.; Choi, S. H.; Kim, K. J.; Hwang, H. N.; Hwang, C. C. *Appl. Phys. Lett,* **2007,** 91, 103113.
68. Bancroft, G. M.; Nesbitt, H. W.; Ho, R.; Shaw, D. M.; Tse, J. S.; Biesinger, M. C. *Phys. Rev. B,* **2009,** 80, 075405.
69. Choi, Y. R.; Zheng, M.; Bai, F.; Liu, J.; Tok, E.; Huang, Z.; Sow, C.-H. *Sci. Rep.,* **2014,** 4, 4940.
70. Ghosh, R.; Giri, P. K.; Imakita, K.; Fujii, M. *J. Alloy Compd.,* **2015,** 638, 419.
71. Volodin, V. A.; Koshelev, D. I. *J. Raman Spec.,* **2013,** 44, 1760.
72. Shchepetov, A.; Prunnila, M.; Alzina, F.; Schneider, L.; Cuffe, J.; Jiang, H.; Kauppinen, E. I.; Torres, C. M. S.; Ahopelto, J. *Appl. Phys. Lett. ,* **2013,** 102, 192108.
73. Hessel, C. M.; Wei, J.; Reid, D.; Fujii, H.; Downer, M. C.; Korgel, B. A. *J. Phys. Chem. Lett.,* **2012,** 3, 1089.
74. Chen, Y.; Peng, B.; Wang, B. *J. Phys. Chem. C,* **2007,** 111, 5855.

75. Brodsky, M. H.; Cardona, M.; Cuomo, J. J. *Phys. Rev. B,* **1977,** 16, 3556.
76. Salcedo, W. J.; Fernandez, F. J. R.; Galeazzo, E. *Braz. J. Phys.,* **1997,** 27, 158.
77. Fobelets, K.; Li, C. B.; Coquillat, D.; Arcade, P.; Teppe, F. *RSC Adv.,* **2013,** 3, 4434.

भारतीय प्रौद्योगिकी संस्थान गुवाहाटी
Indian Institute of Technology Guwahati

Chapter 4

On the Origin of the Broadband Visible And Near Infrared Photoluminescence From Mesoporous Si Nanowires

In this chapter, the photoluminescence (PL) properties of the arrays of vertically aligned single crystalline Si nanowires (NWs) decorated with arbitrary shaped quantum size Si nanocrystals (NCs) are presented. A strong broad band and tunable visible to near infrared (NIR) (1.3-2.4 eV) PL is observed from these Si NWs/NCs at room temperature (RT). The origin of this visible-NIR PL is explained in the light of quantum confinement (QC) effect in Si NCs and the nonbridging oxygen hole center (NBOHC) in the oxide matrix. Distinct NIR PL consisting of peaks at ~1.1 eV is attributed to TO/LO phonon assisted radiative recombination of free carriers condensed in the electron-hole plasma in etched Si NWs observed at RT. We have studied the effect of growth conditions, decay statistics, temperature and other tunable measurement conditions on the PL characteristics to arrive at the conclusions. Our results help to resolve long standing debate on the origin of visible-NIR PL from Si NWs.

4.1. Introduction

Despite the indirect band gap nature of bulk Si, Si nanostructures emit light with wavelength tunability depending on its size, doping and surface conditions.[1-21] Efficient visible PL has been observed at RT in various forms of nanostructured Si, such as porous Si[11, 12, 22], Si NCs[4, 10, 13-18, 21] and Si NWs [4, 23]. However, the mechanism of PL from Si NWs is often debated. While several studies emphasize the effect of QC of carriers on the visible PL from Si NWs, strong influence of defects in the PL has been recognized in other studies.[4-11, 16, 24] Phonon-assisted radiative recombination has also been proposed as a powerful mechanism of PL in Si NCs.[19, 20] Recent studies have shown that Si NCs produced by the side wall etching of Si NWs during MACE process strongly contribute to the visible PL.[4-10] Often Si NCs/NWs are covered with a native oxide layer and NBOHC defects and oxygen vacancy (V_O) within oxide matrix in a core-shell Si/SiO_x nanostructure is also found to be responsible for the visible PL at RT.[1-10] Dhara et al.[25] explained the reddish PL emission of Si NCs in SiO_2 matrix by a three level system consisting of valence band, conduction band of Si NC and the intermediate defect state related to the Si-O

interface. Though visible PL is common in nanostructured Si, NIR PL is not commonly observed at RT. However, Demichel et al. reported NIR PL at low temperature (T) from core-shell Si/SiO_x NWs and it was interpreted as phonon assisted radiative recombination of confined electron-hole plasma in Si NW core.[19] The understanding of the origin of visible-NIR PL from MACE grown Si NWs decorated with Si NCs has huge importance for the application of lighy emitting diodes, PL based sensor etc.

4.2. Sample Preparation for Photoluminescence Studies

The Si NWs/NCs samples were grown by MACE process. We have used both a single-step and a two-step MACE for the growth of Si NWs. The details of the growth technique and the growth parameters are described in *Chapter 2, Section 2.1* and the corresponding sample codes have been provided in the same *Section (Table 2.1).* We have also tuned the (a) nature of the noble metal, (b) the etching solution and its concentration, (c) the doping type, resistivity and the orientation of the Si wafer and (d) etching duration for understanding their effect on the PL properties. The dimensions of the Si NCs for different samples are described in *Chapter 3, Section 3.5.* The experimental setup and measurement procedure for PL study are presented in *Chapter 2, Section 2.2.1*.

4.3. Origin of Visible Photoluminescence from Self-Grown Si Nanocrystal Decorated Si Nanowires

Si NWs decorated with Si NCs on its surface exhibit strong broadband PL in the visible region at RT.[4-6, 8, 10, 26, 27] Fig. 4.1 shows the broad visible PL from the samples P, Q and R. Sample R shows seven fold stronger and red shifted visible PL compared to sample P and Q. Due to large diameter and indirect nature of the bandgap of the Si NWs, strong visible PL is unlikely to originate from the Si NWs. It is already mentioned that the Si NWs are decorated with arbitrary shaped Si NCs due to the sidewall etching, and the dimensions of the self-grown Si NCs are comparable/smaller than the excitonic Bohr diameter in Si (~9.8 nm). Therefore, the QC effect of carriers in the Si NCs, instead of that in Si NWs, is most likely responsible for the visible PL shown in Fig. 4.1. Si NWs/NCs are covered by an oxide layer (SiO_x, where $0<x<2$). So, the V_O and NBOHC defects in the oxide matrix can contribute to the visible PL. It may be noted that in the present work, Si NCs are compressively strained due to the oxide over-layer, as discussed in

Chapter 3 and the strain is expected to cause a red shift in bandgap of Si NCs.[20] Phonon-assisted radiative recombination has also been proposed as a powerful mechanism of PL in Si NCs.[19, 20]

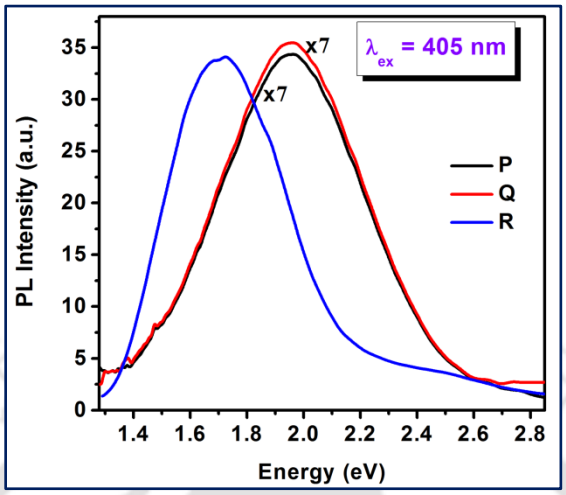

Fig. 4.1. Comparison of the PL spectra for samples P, Q and R. The PL peak is red shifted and intensity is seven times stronger in R as compared to that in P and Q.

4.3.1. Quantum Confinement Model

In order to quantitatively analyze the origin of the tunable visible PL from different samples, QC model is the most successful model. Note that the NCs shape is arbitrary with a broad distribution in sizes and the average cross-sectional area of the Si NCs is ~ 38 nm^2 in sample P, while that in sample R is ~57 nm^2. Thus, average sizes of the NCs in all the samples are lower than the excitonic Bohr radius of 4.9 nm (equivalent cross-sectional area ~75.4 nm^2). If the QC effect is dominant, the sample P with lower size Si NCs would give rise to higher energy PL peak than the sample R. This is fully consistent with the data presented in Fig. 4.1. The broad PL peak arises due to the large size distribution in the Si NCs, as explained later. Therefore, Si NCs, instead of the Si NWs, are most likely source of strong visible PL observed in Fig. 4.1.[10]

From the heterogeneous relations between the diameter (d) of the Si nanostructure (quasi-1D in Si NW and quasi-0D in Si NC) and corresponding PL peak energy (E_g) expressed as

$$E_g(peak) = E_g(bulk) + Cd^{-\alpha}, \qquad \text{.....(4.1)}$$

where C and α are constants. This relation assumes a circular cross-section of the NWs or NCs and different groups have reported different values of the constants from Si NWs/NCs grown by methods different from the MACE method used here.

In general, the shape of the NCs may not be strictly cylindrical or spherical in nature, as seen in the present case. So, a general formulism is needed by which E_g of the nanostructure can

be predicted for any shape and size. We choose the cross-sectional area (A) as the most appropriate parameter to replace the parameter "d" resulting in the following equation:

$$E_g(peak) = E_g(bulk) + C'A^{-\alpha'} \quad \ldots\ldots\ldots\ldots\ldots\ldots (4.2)$$

where C′ and α′ are new constants. Here A is the cross-sectional area that is equivalent to a $\pi d^2/4$ for a circular cross-section.

4.3.2. Quantitative Analysis of the Photoluminescence Spectra

Since sample R shows strongest PL, we analyze its size dependence by measuring the size distribution of the corresponding Si NCs.[10] To emulate the PL line shape, size distribution of the NCs has been considered. Fig. 3.6(c), *Chapter 3, Section 3.5* shows the typical distribution of the cross-sectional area of the Si NCs on the side wall of the Si NWs of the sample R. The NC area is measured from the high magnification TEM image of the Si NW surface.[10] It is evident from Fig. 3.6(c), *Chapter 3, Section 3.5* that majority of the Si NCs have cross-sectional area A below 80 nm^2 (~ 86%) and it follows the typical asymmetric Gaussian distribution.[10] Since

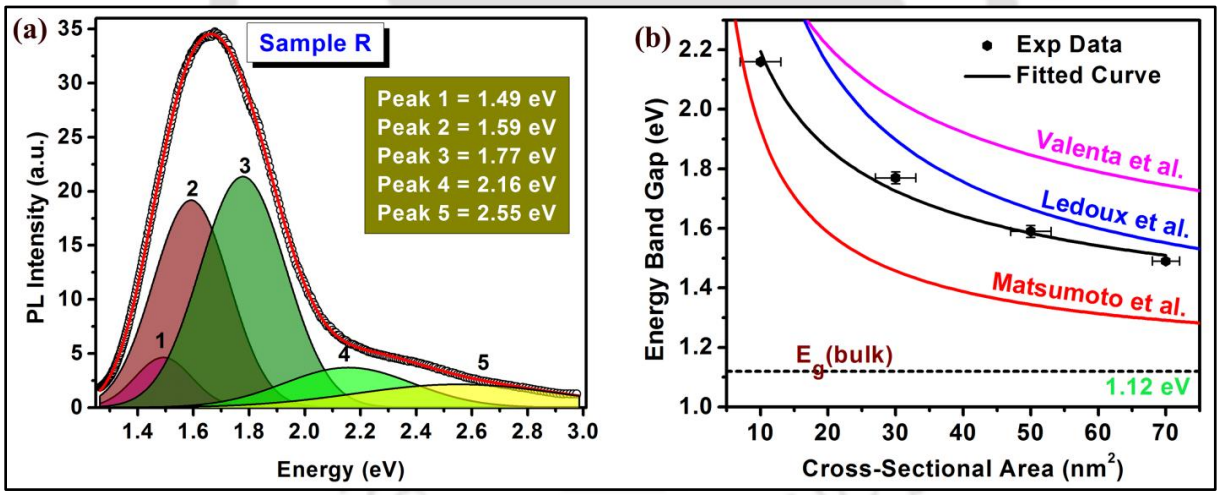

Fig. 4.2. (a) PL spectra of the sample R fitted with five different Gaussian peaks; peak 1, 2, 3, 4 arising from four different groups (cross-section) of Si NCs, and peak 5 originates from SiO_x layer. (b) The variation of the energy band gap with the cross sectional areas of the Si NCs. The black line represents the best fit to the experimental data (black hexagons) using Equation 2. For comparison, results reported from other groups are also shown.

the major contribution comes from the NCs belonging to this region of size distribution (below 80 nm^2), we divide this portion into four equal sub-portions with an interval 20 nm^2 and attempt to fit the PL band in sample R by four Gaussian bands and the center of the fitted peaks are indicated in Fig. 4.2(a).[10] Note that the additional peak (peak 5) at 2.55 eV is very weak at RT,

though it becomes more distinct and intense at low temperature (will be discussed later). Based on the earlier reports and our study, broad band peak at ~2.55 eV is attributed to the oxygen vacancy (V_O defect) in the SiO_x layer grown on the surface of Si NWs/NCs.[10, 28] Thus, the first four PL bands arise due to the specified groups of the NCs. Since the energy band gap reduces with the increase in NC size, the PL peak centers vary as a function of the cross-sectional area of Si NCs.[10]

The variation of the PL peak positions with cross sectional areas of the Si NCs are demonstrated in Fig. 4.2(b) (black hexagons). We fitted the data points by Equation 4.2 and found out the constants C′ as 3.58 eV/nm and α′ as 0.52.[10] A comparison between our results and the earlier reported results on the variation of E_g with the corresponding A (converted from the corresponding diameter d) are presented in Fig. 4.2(b) and values of the constants C′ and α′are presented in Table 4.1. It clearly shows that our results closely follow the results recently

Table 4.1: Comparison of the constants determined from Eqn. 4.2 with those reported in the literature.

Constants	Our Result	Valenta et al.[29]	Ledoux et al.[16]	Matsumoto et al.[18]
C′ (eV/nm^2)	3.58	2.23	3.15	1.69
α′	0.52	0.46	0.70	0.80

reported by Valenta et al. for free-standing Si NCs grown by a different method.[29] Fig. 4.2(b) also reveals that the nature and the position of the experimental curves are not deviated much from the other reported results and the values of the constants derived by our model are fully consistent with the earlier reports. The deviation of our results from those of Valenta et al. shown in Fig. 4.2(b) can be partly accounted from the strain effect.[29] Another source of discrepancy may be the shape dependence of the bandgap, since Si NCs in the present case have arbitrary shape. Note that Si NCs studied by Valenta et al. were not embedded in any matrix and hence strain effect is negligible there. Thus, under the limiting condition of circular cross-section and strain free Si NCs, our results would match very well with the reported results.[10] We believe that this general formalism using cross-sectional area A as a parameter is more versatile than the commonly assumed diameter d as a parameter for prediction of energy gap and corresponding PL spectra. This is particularly relevant for the Si NCs grown by MACE that are nonspherical in nature.

Such an analysis was carried out for other two samples P and Q as well. In both the cases, the distributions in A is Gaussian but asymmetric in nature. The average A in each case is shown in Table 3.1 and Fig. 3.6, *Chapter 3, Section 3.5.* Despite different growth conditions, sample P and Q have similar visible PL spectra due to the fact that they possess similar size Si NCs decorated on the surface of the Si NWs. The relative change in the PL bands shown in Fig. 4.1 is fully consistent with the change in A for different samples. Thus, our results show that QC effect is the most dominant mechanism of the visible PL from the Si NCs decorated on the Si NWs.[10] Note that in the present case Si NCs are attached to the Si NW core, and thus the influence of the Si NW core on the observed PL cannot be ignored. We believe that efficient radiative recombination takes place at the quasi-0D Si NCs due to the covering of the SiO_x layer, before the carriers diffuse to the 1D Si NWs through the weak link on the surface.[10]

4.4. Contribution of NBOHC Defects to the Photoluminescence

Note that the as-grown Si NWs/NCs here are covered with oxygen deficient SiO_x layer. Oxygen vacancy (V_O) in the interface between Si and amorphous SiO_x or NBOHC defect within SiO_x matrix in core-shell Si/SiO_x nanostructure may also contribute to the observed visible PL.[1-3] In order to understand the contributions of different species in the broad visible PL, we have deconvoluted the PL spectra of sample AgAuSi. Fig. 4.3 shows that the broad visible PL spectra of AgAuSi consist of three peaks centered at 1.74 eV (peak 1), 1.92 eV (peak 2) and 2.50 eV

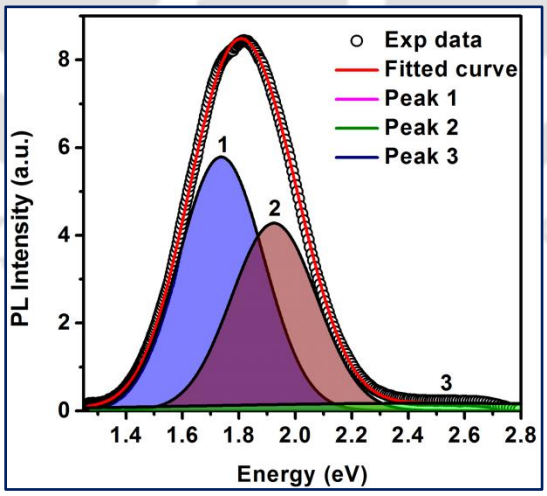

Fig. 4.3. PL spectrum at RT for the sample AgAuSi fitted with three different Gaussian peaks: peak 1, 2, 3.

(peak 3).[5] The peak 1 is attributed to the QC effect in the Si NCs embedded in SiO_x matrix.[4-6, 8, 10, 16] The deep red PL at 1.92 eV (peak 2) is attributed to the NBOHC in the SiO_x.[1-3, 5, 6] The peak

3 in the PL spectra originates from the V_O defects in the SiO_x structure.[28] The deconvoluted PL spectra of AgSi and AuSi have also shown similar behavior.[5] The resultant visible PL spectrum in each case is determined by the relative contribution and interplay of the above three species.[5] It may be noted that PL spectral position depends on the doping type and doping density of the initial Si wafers and etching parameters during MACE.[5-7, 10] To confirm the PL peak assignments, PL measurement was carried out on samples grown with different etching conditions.[5-8, 10] Fig. 4.4(a) and (b) show the fitted PL spectra of the sample S1HF5 and S2HF5, respectively. The low intensity peak 1 is an artifact of the measurement arising from the incident laser (2nd harmonic of 405 nm, i.e., 810 nm). Peak 2 is attributed to the QC effect in the Si NCs embedded in SiO_x matrix.[4-6, 8, 10, 16] The deep red PL at ~1.93 eV (Peak 3) is attributed to the NBOHC defects in the SiO_x layer.[1-3, 5, 6] Further explanations are provided later.

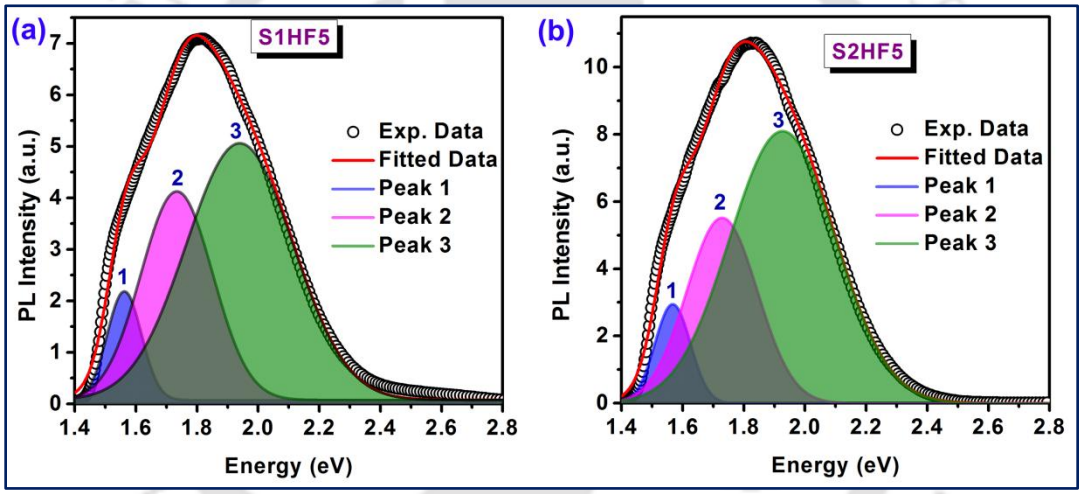

Fig. 4.4. PL spectra fitted with three different Gaussian peaks for samples: (a) S1HF5 and (b) S2HF5.

4.5. Tunability of the Visible Photoluminescence from Mesoporous Si NWs

PL spectral position and PL efficiency strongly depends on the morphology of the Si NWs/NCs samples and the surface properties. In *Chapter 3*, we have explained the effect of the different growth parameters on the morphology and structures of the samples, such as (a) the doping nature of the Si wafer (from which the Si NWs/NCs are grown); (b) the nature of noble metal, the size of the noble metal NPs and their interspacing, the nature of etching solution as well as its concentration; and (c) the etching duration. We have studied the structure of the Si NWs/NCs samples by means of Raman, FTIR, XRD and XPS in order to understand the presence of surface defects such as NBOHC and V_O, which affect the PL spectra. Therefore, understanding the effect

of the above mentioned parameters on the PL spectra of the Si NWs/NCs samples is crucial to understand the PL emission phenomena of Si nanostructures. Note that the PL measurement conditions also influence the PL spectral position and PL intensity and we will explain its effect on the PL spectral evolution.

4.5.1. *Etching Duration*

We studied the effect of etching duration on the Si NWs/NCs morphology and the corresponding PL spectra. The NW length increases linearly with etching time duration (see *Chapter 3*, Fig. 3.9).[30] Fig. 4.5(a) shows the PL spectra of samples grown for different etching duration (15 min etched sample refers to sample R). Fig. 4.5(b) shows a comparison of the length of the Si NWs and the respective integrated PL intensities as a function of etching time. It shows a sublinear increase in visible PL intensity with increase in etching duration from 5 min to 20 min, though the Si NW length follows the linear behavior. If the visible PL is originated from Si the NWs, the visible PL intensity (integrated) would have increased linearly, since the length

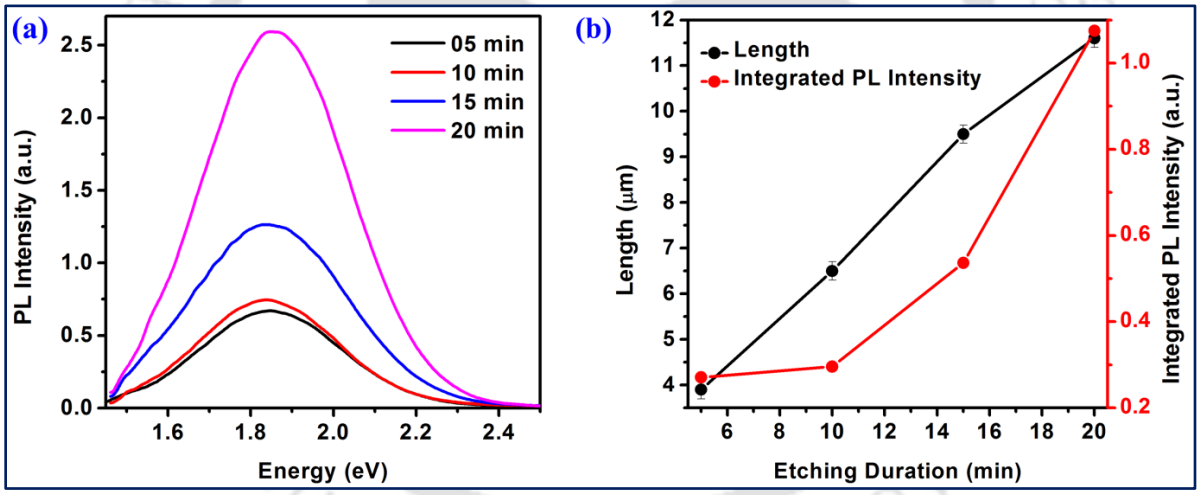

Fig. 4.5. (a) Comparison of the visible PL spectra with a 405 nm laser excitation for samples grown for 5, 10, 15, 20 min. (b) Comparison of the Si NWs length and the respective integrated PL intensities of the samples as a function of etching duration.

increases linearly with etching time. However, our results show a sublinear behavior, indicating that visible PL may not originate from the Si NWs. So the visible PL originates from the QC effect in Si NCs and/or the presence of defects in the Si-SiO_x interface. Note that the larger size Si NCs (which do not show QC effect related PL) break into pieces for higher etching duration. As a result, the density of Si NCs (comparable to quantum size) increases with etching duration, which results in enhanced visible PL.[5, 8, 10] On the other hand, higher length causes higher surface

area and the no. of defect sites may also be increased, which also indicate the enhanced intensity in PL.[5, 6, 10] It is also to be noted that the higher absorption (discussed later) by samples grown with higher etching duration are also partly responsible for the increased PL intensity.[5, 10]

4.5.2. *Etchant Concentration*

It is clear that the etchant concentration has strong influence in the morphology and surface states of the Si NWs. In order to understand its effect on PL spectra, we have taken the PL spectra of Si NWs samples grown with different concentration of HF during MACE process without altering the other parameters. Fig. 4.6(a) and (b) show a comparison of the visible PL spectra of the samples in group S1 and S2, respectively, grown using different concentrations of HF.[6] Each sample shows strong visible PL band covering the range 1.4-2.4 eV. It is clear form Fig. 4.6(a, b) that the PL intensity of the samples depends on the HF concentration during the growth.[6] A nonmonotonic change in PL intensity with HF concentration can be understood from the following competing effects: the formation and dissolution rate of Si oxide

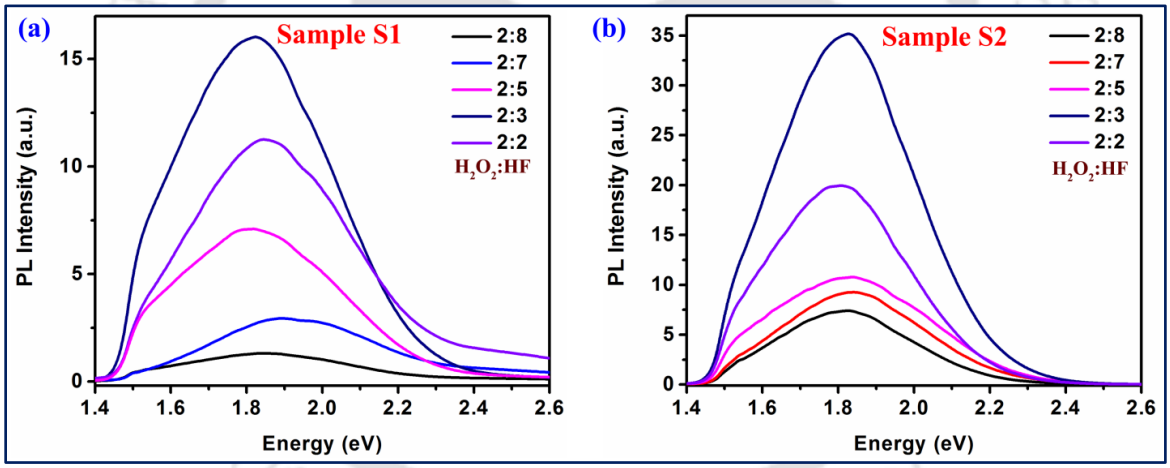

Fig. 4.6. Comparison of the PL spectra of the Si NWs grown at different concentrations of HF for group: (a) S1 and (b) S2.

formed at the etching front is not same for different HF concentration. At lower HF concentration, the dissolving rate of Si oxide formed at the etching front is slow. Owing to the undissolved Si oxide, the NBOHC defect density is higher at lower concentration of HF. As a result, the PL intensities would be higher for the samples grown using lower HF concentration.[5] However, at very low concentration of HF (2 mL and 3 mL HF for group S1), the formation of Si NWs is incomplete and only a porous-like Si surface is formed (Fig. 3.12(f), *Chapter 3*).[6] Due to the incomplete NW formation, the lateral etching is also very less and thus the density of Si

NCs is very low. This gives rise to the lower intensity of PL.[5] It has been pointed out in our previous section that the PL intensity increases with increase in the length of the Si NWs due to the higher density of Si NCs and NBOHC defects.[5, 8] When the density of the NCs and the NBOHC defects are significant, the resulting PL intensity attains a maximum. At higher HF concentration, NBOHC defect decreases and as a result the resultant PL intensity decreases. Thus, the integrated PL intensity shows a maximum for a certain concentration of HF in S1 and S2 group of samples. Note that at very high HF concentration (2:7 and 2:8), the top portions of the Si NW layer become amorphous in nature that may be partly responsible for the low intensity PL of the respective samples.[6]

4.5.3. *Wafer Resistivity/Doping Concentration*

PL spectral position and intensity depend on the doping density of the starting Si wafers. Fig. 4.7 depicts the comparison of the PL spectra of the Si NWs samples, which are grown by using different resistivity wafers under identical etching condition. It is clear that the PL intensity increases with increasing doping concentration. It is also seen from Fig. 4.6 that the PL intensity of each sample in group S2 (resistivity ~ 0.001 Ω-cm) is higher than that of the corresponding samples in group S1 (resistivity ~ 0.01 Ω-cm).[6] It is clear from Fig. 4.7 that the

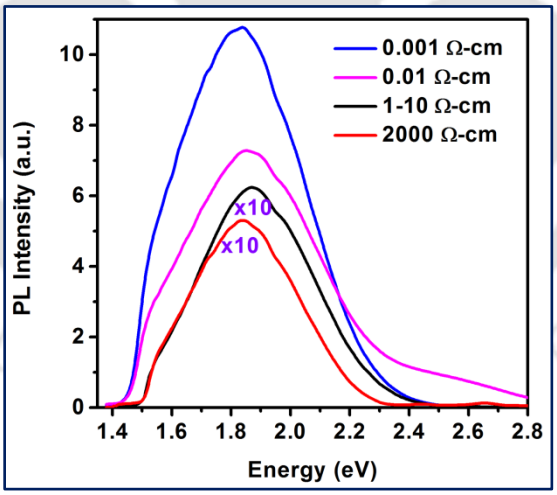

Fig. 4.7. Comparison of the PL spectra of the Si NWs samples, which are grown by using different wafer resistivity under identical etching condition. Some of the spectra are scaled up to enable comparison.

PL peak position does not change systematically with doping concentration. As mentioned before, the dopant sites act as the nucleation site for the sidewall etching of the Si NWs. Therefore, with increasing the doping density, the Si NCs' density increases, which results in the

enhanced PL intensity for the low resistive wafers.[6] This is consistent with our other reports.[5, 8] On the other hand, the formation and dissolving rate of Si oxide formed at the etching front is not same for each type of wafers. Under identical conditions of etching, the formation rate of Si oxide in faster for the lower resistivity wafers as compared to the higher resistivity wafers.[6] As a result the overall dissolving rate is slow for the lower resistive wafers as compared to the higher resistive wafers, which results in the higher NBOHC defect density.[5, 6] Therefore, the PL intensity is higher for the lower resistivity wafers as compared to the higher resistivity wafers.[6]

4.5.4. *Oxide Layer Thickness*

In order to gain further insight into the origin of PL and its efficiency, we performed post growth etching of the samples in 10% HF solution for 30 sec to remove the native oxide layer and performed the PL measurement immediately after etching, under identical conditions. Fig. 4.8(a) and (b) show comparison of the PL spectra of the samples Q and AgAuSi before and after HF treatment, respectively.[5, 10] Interestingly, there is about ~3 fold (in sample Q) and ~7 fold (in

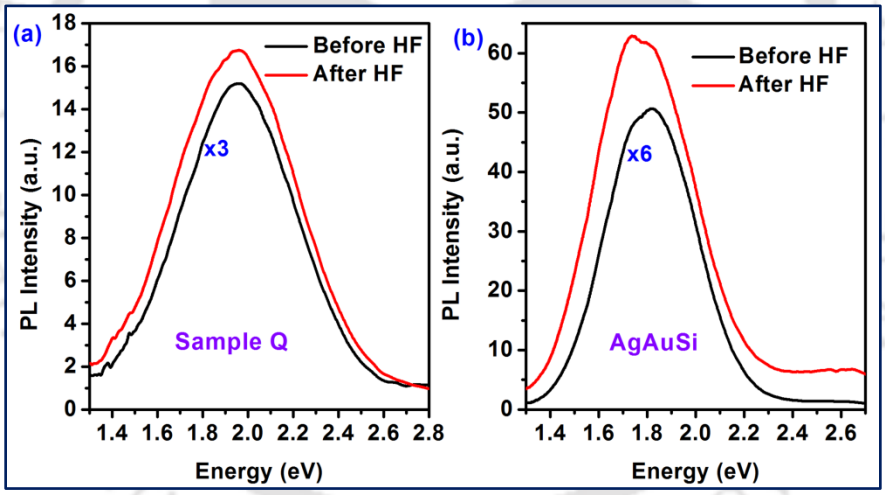

Fig. 4.8. Comparison of the PL spectra before and after HF etching for samples (a) Q and (b) AgAuSi. The spectra are scaled up to enable comparison.

sample AgAuSi) enhancement in the intensity of PL immediately after HF etching.[10] Normalization of the peak intensity reveals no considerable shift in the mean peak position. Therefore, a small change in the spectral shape is observed for sample AgAuSi.[5] In order to understand the shape evolution of PL spectrum after etching, the PL spectrum was fitted with three Gaussian peaks before and after HF treatment.[5] It is clear from the fitted curves and fitting parameters that the relative intensity of peak 1 (due to QC effect) with respect to that of peak 2 (due to NBOHC defects) is enhanced after HF etching (Table 4.2).[5] It is clear from Table 4.2 that

the intensity ratio of peak 1 to peak 2 is ~2.3 in case of HF etched AgAuSi, while it is ~1.35 in AgAuSi (before etching).[5] It is due to the fact that the dilute HF etching partially removes the

Table 4.2: *Summary of the fitted parameters for PL spectra of different samples.*

Samples	Peak 1		Peak 2		Peak 3	Intensity Ratio, Peak 1/ Peak 2
	Center (eV)	Intensity	Center (eV)	Intensity	Center (eV)	
AgAuSi	1.74	5.79	1.92	4.28	2.50	1.35
AgAuSi_HF	1.72	47.10	1.90	20.5	2.57	2.29
AgAuSi_HF, 150 sec laser exposed	1.74	15.20	1.86	18.30	2.68	0.83
AgAuSi, 100 mW laser exposed	1.74	11.30	1.89	10.50	2.66	1.07
Peak Identity/Origin	**Si NCs**		**NBOHC**		**O_V**	

native oxide layer and reduces the relative contribution of PL due to the NBOHC defects in the oxide layer.[5] On the other hand, due to removal of SiO_x layer after HF etching, contribution of Si NCs to PL is enhanced and this results in enhanced intensity of peak 1 arising from the QC effect. Thus, the PL intensity is enhanced for both the samples after HF etching.[5, 10] Note that the SiO_x layer may contain some nonradiative defects, which may quench the PL partly and PL is enhanced after partial removal of the nonradiative defects.[5, 10]

4.5.5. *Nature of Noble Metal during MACE*

The effect of different noble metals on the morphology of the Si NWs/NCs is discussed in *chapter 3*. Fig. 4.9 shows the comparison of the broad visible PL spectra from AgSi, AuSi and AgAuSi. Note that PL intensity of AgAuSi is about two orders of magnitude higher than that of the AgSi and AuSi. The spectra of AgSi and AuSi are scaled up by a factor of 10 to enable comparison. The origin of the strong enhancement of the PL intensity can be understood in the following way. In case of Ag/Au bilayer assisted etching, the surface etching of Si NWs is more precise and uniform and this gives rise to well-formed long Si NWs even for short etching time.[5, 31, 32] In case of Ag and Au assisted etching, porous like structure on Si surface is formed, while vertically aligned long Si NWs decorated with Si NCs were formed in case of AgAu bimetal assisted etching under the same etching conditions, as shown in Fig. 3.11, *Chapter 3*.[5] Due to large surface area of the Si NWs covered with high density of Si NCs, PL emission is strong in AgAuSi as compared to the single metal case where NW growth is incomplete.[5] Owing to large

surface area of the Si NWs and higher density of NBOHC defect sites, the AgAuSi shows stronger visible PL intensity compared to the other samples where NW growth is incomplete.[5]

It is clear from XPS and EDX analyses presented in *chapter 3 (Section 3.9.1 and 3.9.2)* that the MACE grown Si NWs have residual metal NPs (Ag, Au) lying at the bottom of the NWs and partly at the surface of the NWs/NCs.[5, 10] Localized surface plasmon resonance (SPR) originating from these metal NPs may also enhance the PL intensity of the MACE grown Si NWs.[33] We have observed a high intensity SPR absorption peak centered at ~1.75 eV for the AuAg bilayer film on quartz substrate, which has strong overlap with the PL spectrum of the AgAuSi.[5] Since the maximum PL enhancement of the Si NCs may occur in the region of SPR absorption band of the metal NPs, the AgAuSi shows the highest PL intensity with enhancement over broad wavelength.[5] This is consistent with the diffused reflectance spectrum of the AgAuSi discussed later. We note a PL enhancement by a factor of ~94 in AgAuSi as compared to that of AgSi, as shown in Fig. 4.9.[5] Time resolved PL measurements (discussed later) on these samples shows much faster PL decay in AgAuSi in comparison to the case of AgSi and AuSi.[5] Note that the broad enhancement can partly be caused by the photon recycling process. The photons emitted from the Si NCs with higher energy can produce other photons with comparatively smaller energy.[5] Thus, the enhanced PL intensity in AgAuSi is primarily due to the SPR induced enhanced absorption of the Si NWs/NCs in presence of AuAg NPs. For Si NCs in a SiO_2 matrix,

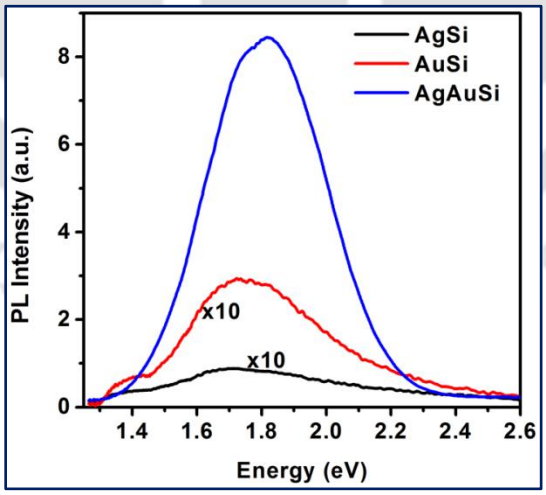

Fig. 4.9. Comparison of the PL spectra for samples AgSi, AuSi and AgAuSi. PL spectra of AgSi and AuSi are scaled up by a factor 10 to enable comparison.

the highest reported PL intensity enhancement in presence of nanoscale Ag island arrays is 7-fold[34], while in case of Si NWs with Ag NPs it is only 4-fold.[23] Huh et al.[35], Potrick et al.[36], and

Goffard et al.[37] reported enhancement by a factor of 2, 3.9 and 6, respectively, in light emission efficiency form Si NCs light-emitting diodes via SPR by employing Au NPs. Similar enhancement by a factor of 3 in PL intensity in Si NWs/Au NPs composite was reported by Au-catalyzed chemical etching method.[38] The enhancement in PL efficiency was explained in terms of radiative energy exchange between Si NCs and metal NPs due to enhanced radiative coupling of exciton-plasmon.[36, 38] In the present case, overall enhancement in PL intensity (by a factor of 94) is remarkable and cannot be fully explained by SPR effect of Ag/Au bilayer alone. However, the contributions by other factors, may be responsible for this enormous enhancement, such as longer length/high density of Si NWs/NCs, enhanced radiative recombination and increase of the light extraction efficiency due to scattering by metal NPs.[5]

4.5.6. *PL Excitation Spectra*

In order to understand the effect of excitation laser wavelength on the PL spectra, we have collected the PL excitation (PLE) spectrum of AgAuSi keeping the emission peak fixed at 690 nm (~1.8 eV). Fig. 4.9(a) shows the PLE spectra of sample AgAuSi. We have observed a broad peak centered at 392 nm for the 690 nm emission. Note that the PL spectra of all the samples were taken with laser excitation of 405 nm for obtaining high PL intensity. Fig. 4.9(b)

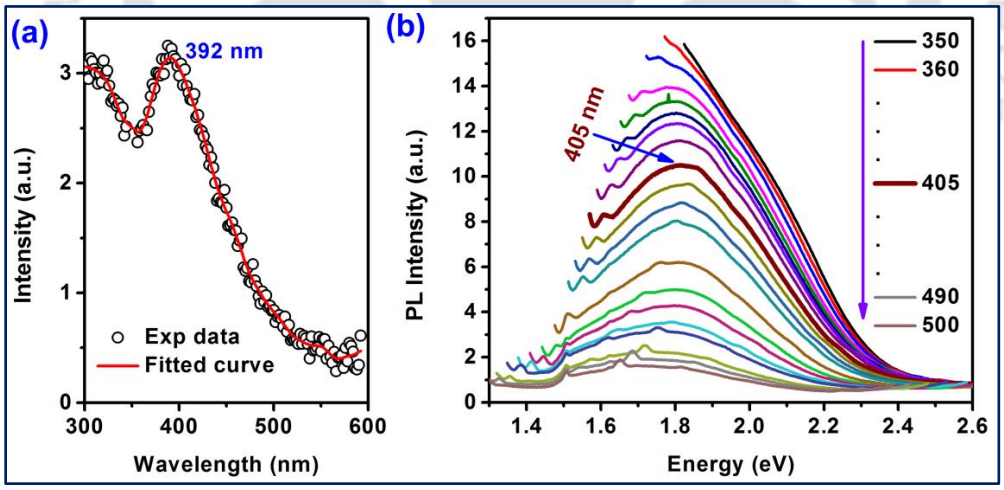

Fig. 4.9. (a) PL excitation spectrum of sample AgAuSi. (b) Comparison of the PL spectra for the sample S1 with different excitation wavelength ranging from 350 nm to 500 nm. The data is collected at the interval of 5 nm in the range 380-420 nm and it is 10 nm in rest of the cases.

shows the comparison of the PL spectra of the sample S1 with different excitation wavelength ranging from 350 nm to 500 nm. It is clear that the PL intensity decreases with increasing excitation wavelength. Note that the peak position is almost unaltered during this experiment

although the spectral shape is slightly changed in higher wavelength. However, we have performed our PL experiment under laser excitation of 405 nm for all the samples in order to get all the significant information with considerable PL intensity.

4.5.7. *Laser Excitation Power*

In order to understand the effect of laser heating and any nonlinear effect on the PL spectra, the PL measurements were performed with different excitation power ranging from 5 to 100 mW (at source).[5] Fig. 4.10(a) shows the evolution of the PL spectra with different excitation power for the sample AgAuSi with 405 nm laser excitation. Fig. 4.10(b) shows the variation of the peak intensity with excitation power. In this case, the shape of the PL spectra is not changed considerably at different laser power.[5] Note that the intensity of the PL spectra increases sub-linearly with increasing laser power (at source) and it reaches a kind of saturation at high power

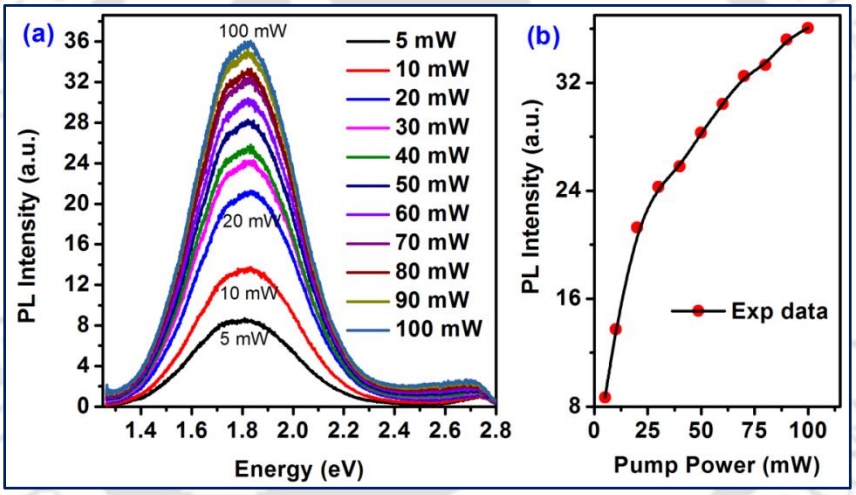

Fig. 4.10. (a) Excitation power dependent PL spectra of sample AgAuSi. (b) The PL peak intensity as a function of laser power (at source).

(100 mW).[5] This is mainly due to the laser induced heating that partially oxidize the Si NWs due to the measurement under ambient condition.[39] The nonradiative defects in the SiO_x layer may partially quench the PL intensity and PL intensity enhancement is reduced at higher power.[5] This is consistent with the results of HF etching induced changes in PL intensity. In order to understand the shape evolution of PL spectrum taken at different laser power, the PL spectrum of AgAuSi with highest (100 mW) laser power was fitted with three Gaussian peaks and the fitted parameters are shown in Table 4.2.[5] It is clear from the fitted curves and fitting parameters that the relative intensity of peak 1 (due to QC effect) with respect to that of peak 2 (due to NBOHC

defects) is reduced for higher laser excitation power (Table 4.2).[5] This is mainly due to the laser induced heating that partially oxidize the Si NWs and remove the NBOHC defects due to the measurement under ambient condition. Thus, the strong PL from the MACE grown Si NCs/NWs arises from the QC effect of carriers in Si NCs as well from NBOHC defects in the SiO_x layer.[5]

4.5.8. *Laser Exposer Time: Temporal Decay*

In order to ascertain further the contribution of various species in the PL from bilayer assisted MACE grown Si NWs (AgAuSi), we monitored the temporal change in PL spectra at an interval of 5 sec, while illuminating the sample continuously with laser excitation at 405 nm (5 mW at source) under ambient condition.[5] Fig. 4.11(a) shows the temporal decay of PL spectra acquired from AgAuSi_HF, while (b) shows the variation of PL intensity as a function of time.[5] Note that the PL spectral shape is changed after prolonged (150 sec) exposure to laser in ambient condition

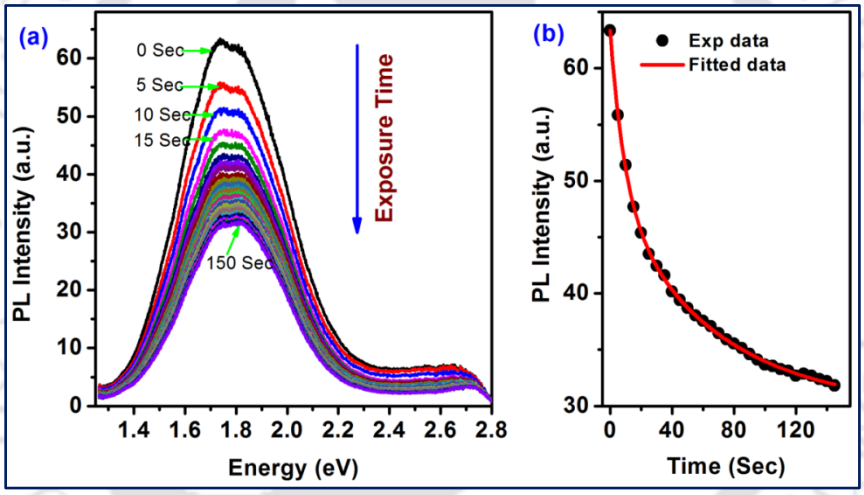

Fig. 4.11. (a) Time evolution of the PL spectra of HF etched AgAuSi acquired in ambient condition at an interval of 5 sec. (b) The intensity of PL as a function of laser illumination time, t and the fitted data points show a bi-exponential decay.

(Fig. 4.11(a)).[5] In order to understand the shape evaluation, we have fitted the PL spectra of the sample after 150 sec laser exposure.[5] Fitted parameters are shown in Table 4.2. It is noticed that the NBOHC defect related peak (~1.9 eV) intensity is not changed considerably (slightly decreased), though the QC effect related peak(~1.74 eV) intensity is strongly reduced with laser exposer time.[5] The local heating due to the prolonged laser exposure may promote local oxidation and create SiO_x layer that may contain nonradiative defects in it and these defects partially quench the PL intensity. This is fully consistent with the results of the post-growth etching experiments discussed earlier. Note that the surface oxidation may reduce the porosity of

the Si NWs, which may reduce the PL intensity of the Si NCs.[39] As the laser exposer time progresses, the rate of decrease of PL intensity goes down.[5] The Si NCs may be oxidized partially due to the laser induced local heating and the PL arising from the NBOHC defects in SiO_x layer decides the PL spectral line shape.[5] We observed that the PL intensity decays bi-exponentially with increase with laser exposure time, as shown in Fig. 4.11(b). The possible reasons for bi-exponential decay are as follows: (i) the oxidation of Si NCs and the partial removal of NBOHC defects due to the laser induced local heating for prolonged illumination are mainly responsible for this and (ii) the increase of nonradiative recombination due to local heating.

4.5.9. *Absorption Spectra of Si NWs*

In order to understand the relative change in the visible PL intensity for different samples, absorption coefficient was assessed by measuring the diffused reflectivity under oblique incidence. Fig. 4.12(a) shows a comparison of the optical reflectivity as a function of wavelength for the bulk Si wafer and sample P, Q and R.[10] Two-step MACE grown Si NWs in HF/H_2O_2 solution (sample R) show significantly lower reflectivity at all wavelengths (6.2% at 405 nm) as compared to the bulk Si wafer (41.9% at 405 nm). Fig. 4.12(b) shows a comparison of the optical reflectivity as a function of wavelength for the samples grown for different etching duration keeping the other parameters same (15 min etched sample refers to sample R). Due to multiple reflections on the inner surface of the Si NWs and a broad range of size distribution of the Si NCs, the absorption is significantly high in case of Si NWs/Si NCs over the entire range of wavelength.[10, 40] Interestingly, sample R shows the lowest reflectivity (Fig. 4.12(a)) among all the samples below 450 nm indicating higher absorption that may be responsible for the enhanced visible PL intensity from sample R as compared to sample P and Q (Fig. 4.1).[10] Due to high optical absorption by the Si NCs and trapping of light by the Si NWs array, the samples appear dark in color with naked eye. Note that the MACE grown Si NWs may have residual metal NPs lying at the bottom of the NWs and partly at the surface of the NWs/NCs. These metal NPs may cause higher absorption in the visible range due to the surface plasmon resonance (SPR).[5, 10, 23] However, since the NWs were etched in HNO_3 solution after growth, its contribution may not be significant, though not negligible for sample R. In fact our XPS studies reveal the presence of Ag near the top surface of the NWs for sample R and this may partly be responsible for the strongest visible PL and lowest reflectivity in R.[10] Low reflectivity implies higher absorption and

excitation of carriers finally leading to the enhanced radiative recombination or PL in sample R.[10, 23] It is also revealed from Fig. 4.12(b) that the absorption increases with the length of the Si NWs and this results on the enhanced PL intensity shown in Fig. 4.5(a). The higher density of the Si NCs due to the higher length of the Si NWs causes the higher absorption. Similarly, higher length causes the longer path for the exposed light to increase the multiple reflections.

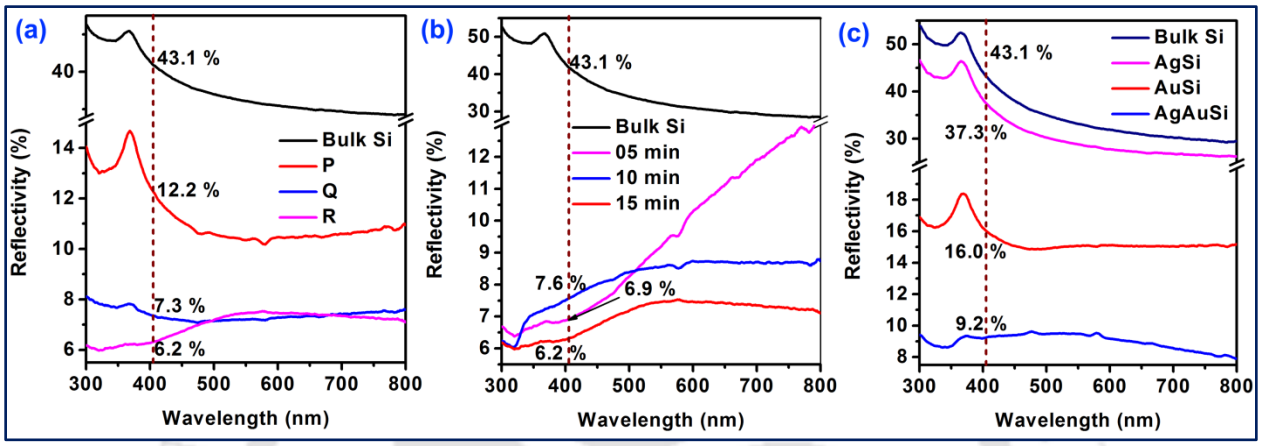

Fig. 4.12. Comparison of the diffused reflectance spectra for the samples: (a) P, Q and R; (b) the samples with different etching duration (different length) and (c) AgSi, AuSi and AgAuSi. The reflectivity of the bulk Si wafer is also presented for comparison. The dashed vertical line in each case shows the reflectivity of the respective samples at wavelength 405 nm.

In order to better understand the relative intensity of PL for samples grown with different metal NPs, diffused reflectivity measurements of the samples AgSi, AuSi and AgAuSi were performed under oblique incidence. Fig. 4.12(c) shows a comparison of the diffused reflectivity as a function of energy for the bulk Si wafer and the AgSi, AuSi and AgAuSi.[5] Interestingly, AgAuSi shows the lowest reflectivity (9.2 % at 405 nm) among all samples indicating strongest absorption (possibly due to the SPR enhancement of the bimetal NPs) that may be responsible for the enhanced visible PL intensity from AgAuSi compared to AgSi and AuSi (as seen in Fig. 4.9).[5]

4.5. Low Temperature Photoluminescence

In order to understand the contributions of radiative and nonradiative processes in the visible PL, we have studied the temperature (T) dependence of the PL spectra. The line shape, intensity and peak centers of the PL spectra are strongly dependent upon T, as illustrated in Fig. 4.13(a) for sample R in the range 10 K to 295 K.[10] The room temperature PL spectrum of sample R has a broad peak centered at ~1.6 eV (as seen in Fig. 4.1). At lower T, the PL spectra of sample R have

two distinct bands centered at ~1.54 eV (band X) and ~2.56 eV (band Y) with strongly enhanced intensities.[10] We notice that intensity of band Y increases at lower T, though the center position of the band does not change appreciably.[10] On the other hand, both intensity and center of band X changes strongly with T, as shown by the vertical line (dashed) in the Fig. 4.13(a) and the spectral shape is also changed.[10] Thus, band Y may have intrinsic origin and as discussed before, it is most likely to originates from the V_O defects in SiO_x layer on the surface of the Si NCs.[10, 28]

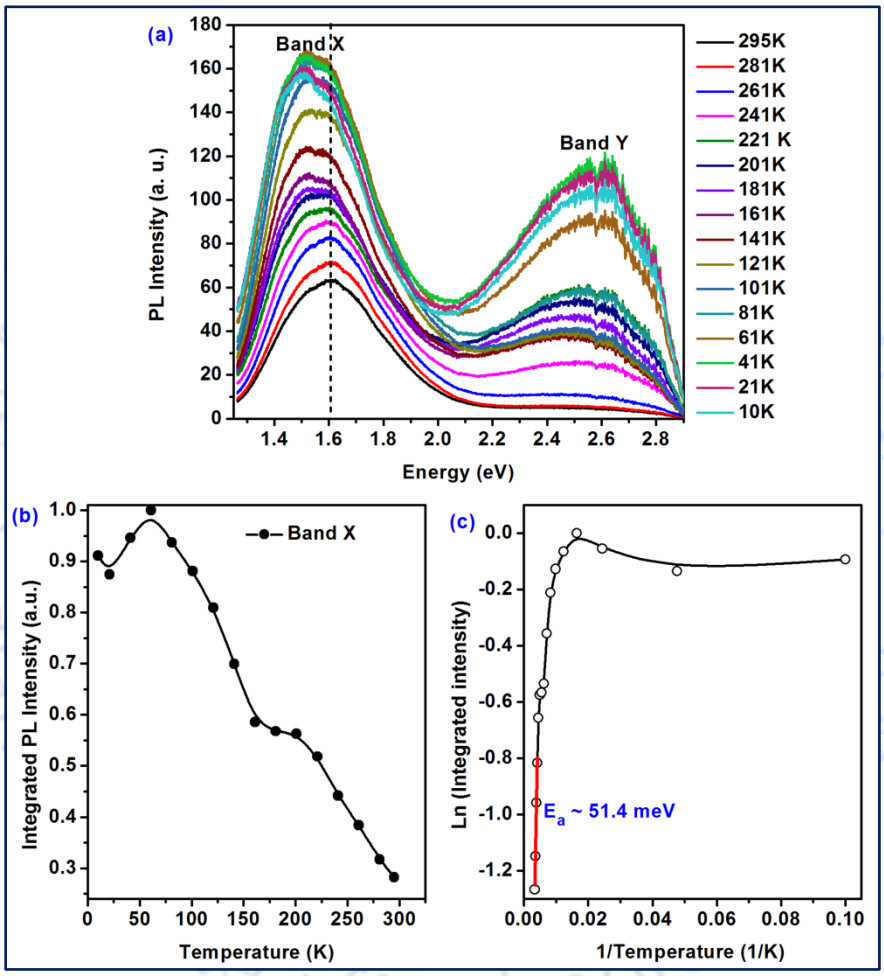

Fig. 13. (a) Temperature dependent visible PL spectra of sample R. Vertical dashed line shows a red-shift of the center of band X with lowering temperature. (b) Variation of integrated PL intensity with T for sample R, (c) corresponding Arrhenius plot showing an activation energy (E_a) of 51.4 meV.

The band X that shows a red shift at low T contradicts the well-known Varshni formula.[41] Fig. 4.13(b) shows the variation of integrated PL intensity of band X with T and Fig. 4.13(c) shows the corresponding Arrhenius plot.[10] At low T, the integrated PL intensity is dramatically increased compared to that of RT and it shows a maximum at ~61 K. It indicates that the nonradiative recombination becomes active at T>61 K resulting in the decrease in PL intensity at

higher T.[10] The temperature dependence of the integrated intensity represents Arrhenius type dependence [29] at higher T, which is represented by the equation

$$\frac{I(T)}{I_0} = \frac{1}{1 + C\,exp(-E_a/k_bT)} \qquad \text{..... (4.3)}$$

The activation energy E_a is found to be ~ 51.4 meV (Fig. 4.13(c)) and this is consistent with the earlier reports.[4] Both the intensity variation and PL peak shift with T can be described by the interplay of radiative recombination of strongly localized excitons within the crystalline Si NCs and the T dependent non-radiative exchange interactions between electrons and holes via the defect states due to the thin sub-oxide layer upon the Si NCs.[10] The effective decay constant (τ_{eff}) depends upon both the T dependent radiative decay constant (τ_r (T)) and non-radiative decay constant (τ_{nr} (T)) according to the relation

$$\frac{1}{\tau_{eff}(T)} = \frac{1}{\tau_r\,(T)} + \frac{1}{\tau_{nr}\,(T)}, \qquad \text{..... (4.4)}$$

where τ_r (T) is the radiative lifetime and τ_{nr} (T) is the non-radiative lifetime of the NC system at any T.[42, 43] The variation of integrated intensity with T can be divided into three regimes: τ_r -dominated regime for T<61 K, τ_r -domination to τ_{nr} -domination for 61<T<161 K, τ_{nr} -dominated regime for T>161 K.[10] According to Hartel et al.[43] τ_r -dominated regime is T<70 K, τ_r -domination to τ_{nr} -domination is for 70<T<150 K and τ_{nr} -dominated for T>150 K, which are very similar to our results.[10] So, the transition from τ_{nr} -domination to τ_r -domination results in the red shift of the peak center from ~1.60 eV to ~1.52 eV in case of band X (Fig. 4.13(a)).[10] Thus, the intensities of the band X and band Y varies with T according to the domination of the radiative and nonradiative recombination in different T regions.[10] This calls for a multi-level transition model to describe the above phenomena that arises from the localized states due to the porous nature of the Si NWs[44, 45]

4.6. Near-Infrared Photoluminescence

Besides the visible PL, some samples exhibited strong NIR PL at RT measured using a liquid N_2 cooled InGaAs detector. Fig. 4.14(a) shows a comparison of NIR PL spectra at RT for the direct etched samples P, P1 and P2 (P1 refers to higher and P2 refers to lower concentration of $HF/AgNO_3$ as compared to P during Si NWs growth). It is clear that sample P shows very high intensity PL peaked at ~1.1 eV, while P1 and P2 show much lower PL intensity.[10] It should be mentioned that we did not observe such NIR PL signal from any other sample in this specific

range. Thus, Si NWs grown under one-step etching shows NIR PL at RT, in addition to the visible PL.[10] Due to large diameter and indirect bandgap nature, Si NWs may not exhibit phonon assisted recombination/PL at RT. Therefore, NIR PL is usually not observed from Si NWs at

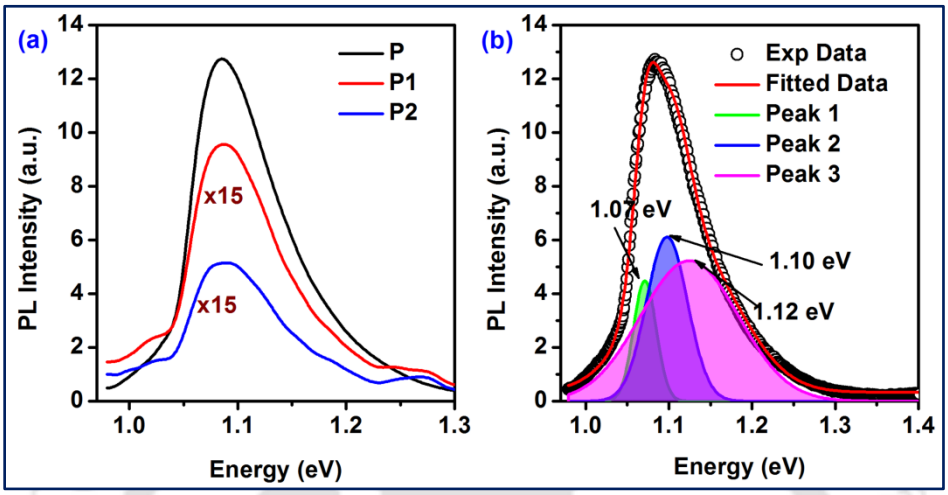

Fig. 4.13. (a) Comparison of the NIR PL spectra of sample P, P1 and P2. Spectra for sample P1 & P2 are scaled up by a factor of 15 to enable comparison (b) NIR PL spectra of sample P fitted with three Gaussian bands.

RT.[10] In order to understand this strong NIR PL at RT of sample P, we fitted the asymmetric peak with three Gaussian bands centered at 1.07 eV, 1.10 eV and 1.12 eV.[10] Fig. 4.13(b) shows the fitted NIR PL spectrum of sample P indicating the peak positions of the deconvoluted peaks.[10] Usually phonon-assisted radiative recombination is expected to be responsible behind the appearance of these peaks.[10] Demichel et al. reported similar NIR PL bands at low T in core-shell Si/SiO_2 NWs grown by CVD and attributed the 1.12 eV peak to the transverse acoustic (TA), 1.07 eV peak to transverse and longitudinal optical (TO/LO) phonon assisted recombination of intrinsic carriers of the electron hole plasma (EHP) phase and 1.10 eV peak to LO phonon assisted recombination of intrinsic carriers of the free exciton (FE).[19, 20, 46] Similar results were reported for CVD grown Si NWs surface passivated with SiO_2 layer and usually prominent at low T (<25 K). However, we observed strong NIR PL in chemically etched Si NWs even at RT without any surface passivation step. The XPS analysis (*Section 3.9.C, Chapter 3*) indicates that the Si NWs in sample P are covered with thick layer of SiO_x and this may provide spatial confinement of carriers needed to form EHP in the Si NW core.[10] We believe that in the present case, besides the surface native oxide layer, the high crystalline core of the Si NWs decorated with small Si NCs possessing higher bandgap may provide QC effect of the carriers that aids in yielding EHP and FE PL even at RT.[10] In the present case, Si NWs/NCs are covered

with a native SiO_x layer as opposed to the high temperature oxidation and passivation steps adopted by Demichel et al.[20] Thus, strong visible as well as NIR PL can be obtained from the same Si NWs decorated with Si NCs grown by a simple chemical method without involving sophisticated growth and processing steps.[10]

Further, we have observed a relatively weak but broad NIR PL signal at ~1.45 eV as detected by the NIR detector for sample R.[8, 10] This is in contrast to the relatively sharper but strong PL band at ~1.1 eV shown for sample P.[10] Fig. 4.14 shows the comparison of the NIR PL

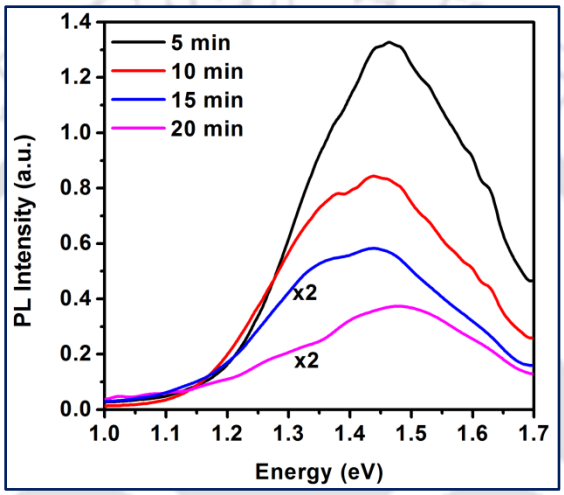

Fig. 4.14. Comparison of the NIR PL spectra of samples grown by two-step MACE in HF/H_2O_2 solution for different etching time (15 min etched sample refers to R). PL spectra of 15 and 20 min etched sample are scaled up to enable comparison.

spectra of samples grown by two-step MACE in HF/H_2O_2 solution for different etching time (15 min etched sample refers to R).[8] This broad PL band centered at ~1.45 eV is possibly arising from the larger Si NCs decorated on the Si NWs.[8] The broad line shape of the PL band is consistent with the wide size distribution of the Si NCs. It is clear from Fig. 4.5(a) that the intensity of the visible PL increases with etching duration, while Fig. 4.14 indicates that the NIR PL intensity decreases with increasing with etching duration. This is because the average size of the Si NCs decreases with increasing etching duration.[8] As discussed in the earlier chapter, during the etching, as the time progress more number of nucleation sites generate on the sidewall of Si NWs and porosity increases. As a result, the larger Si NCs are divided into a smaller Si NCs. So, the density of smaller Si NCs increases whereas the larger size Si NC's density decreases with etching time.[8] As a result, visible PL intensity increases with etching duration, while NIR PL intensity decreases.[8]

4.7. Time Resolved Photoluminescence

Time resolved PL studies were undertaken to determine the contribution of different species in the PL decay of the Si NWs/NCs for understanding the origin of the PL spectra from the Si NWs/NCs. Fig. 4.15(a) shows the PL decay of sample R at different emission wavelengths with a window width of 10 nm.[10] Each decay curve could be fitted well with a bi-exponential decay with time constants in the range of a few μs. The fitted parameters are summarized in Table 4.3. Unlike the earlier reports on Si NCs that usually show stretched exponential decay, interestingly our data fits to abi-exponential decay. Recently Linnros et al. reported mono-exponetial decay from single Si quantum dot, though large variation in life time (5-45 μs) from dot to dot was observed, even for the same emission energy.[47] In the present case, Si NCs are less interacting though weakly attached to the Si NW core. Due to less interaction among Si NCs and highly crystalline core, PL decay here is nearly single exponential for a small group of Si NCs as

Table 4.3: Details of the fitted parameters calculated from the TRPL decay of different samples

Sample	Emission Wavelength (nm)	τ_1	τ_2	τ_{eff}
R	650	13.01 μs	2.55 μs	5.19 μs
	690	17.39 μs	2.69 μs	7.88 μs
	730	24.26 μs	3.12 μs	12.3 μs
	850	62.5 μs	--	62.5 μs
AgSi	650	3.29 ns	0.53 ns	1.47 ns
AuSi	650	2.93 ns	0.39 ns	1.26 ns
AgAuSi	650	2.22 ns	0.34 ns	0.92 ns
P	1135	172 ns	--	172 ns

compared to the stretched exponential decay usually observed for ensemble measurements.[10] The data in Fig. 4.15(a) clearly shows that the decay time constants are lower for higher energy PL peak. The higher energy PL arises mainly from a group of smaller size Si NCs and smaller size NCs have smaller lifetime. This is fully consistent with the earlier report.[48] PL decay measured at 1.69 eV (730 nm) is contributed primarily by two peaks corresponding to 1.59 and 1.77 eV (peak 2 and peak 3 in Fig. 4.2 with the time constants τ_1 = 3.13 μs and τ_2 = 24.27 μs (Table 4.3).[10] The fitting parameters in Table 4.3 show that amplitude of τ_1 component is higher than that of τ_2, consistent with the relative amplitudes of the peak 2 and peak 3.[10]

We estimated the effective lifetimes (τ_{eff}) using the relation[49],

$$\tau_{eff} = \frac{A_1\tau_1 + A_2\tau_2}{A_1 + A_2} \qquad \text{.....(4.5)}$$

where A_1 and A_2 are the amplitude of the decay with lifetime τ_1 and τ_2, respectively. The values of τ_{eff} are shown in Table 4.3. Interestingly, the systematic change in τ_{eff} confirms the quantum size effect for the Si NCs in PL spectra i.e. decay life time increases with increasing Si NCs size and our results are consistent with Hartel et al.[43] Thus, the TRPL data supports the size dependent PL from Si NCs decorated on the Si NWs and this further confirms the role of QC effect in the observed visible PL from Si NCs.

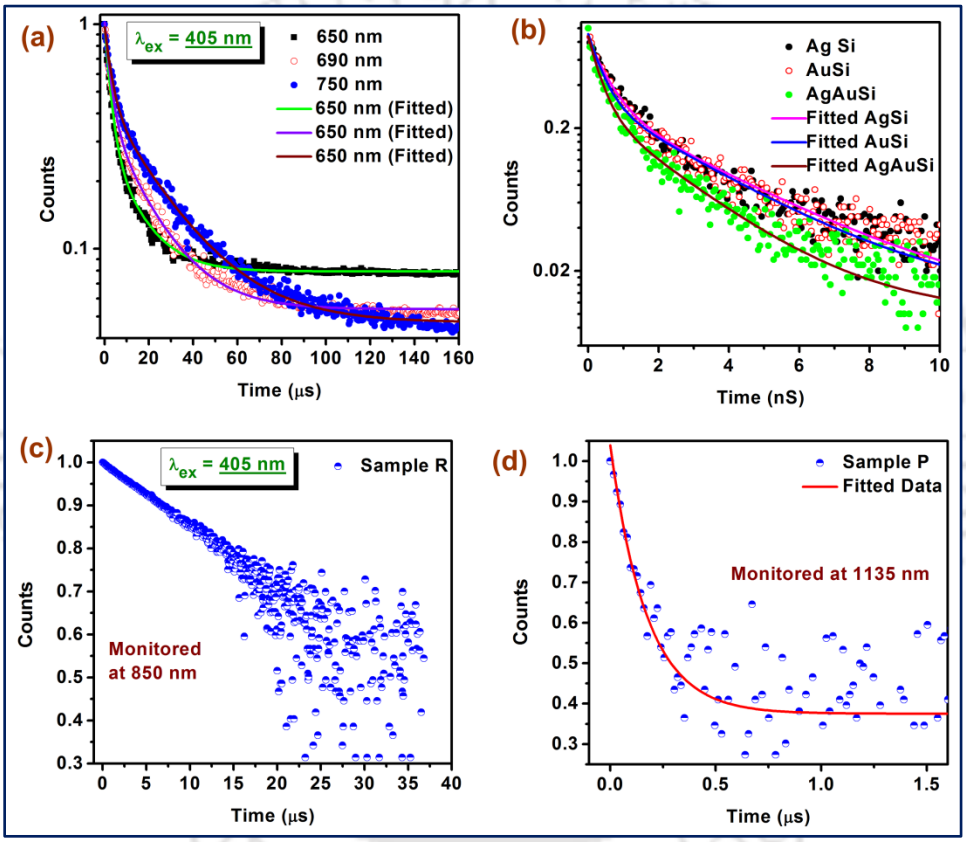

Fig. 4.15. (a) Comparison of PL decay (symbols) of the sample R at emission wavelengths 650, 690 and 730 nm. (b) Comparison of the TRPL decay for AgSi, AuSi and AgAuSi monitored 1.91 eV (650 nm). Solid lines refer to bi-exponential fit to each curve. TRPL decay in (c) sample R is monitored at 850 nm and (d) sample P is monitored at 1135 nm.

In order to understand the effect of NBOHC defects and contribution of plasmonic metal NPs in the TRPL decay, we have compared the TRPL data for sample AgSi, AuSi and AgAuSi.[5] Fig. 4.15(b) shows the comparison of the decay of PL intensity as a function of time for AgSi, AuSi and AgAuSi monitored at emission energy 1.91 eV.[5] Each decay curve could be fitted well with a bi-exponential decay with time constants in the range of a few ns.[5] The fitting parameters

are shown in Table 4.3. Note that the τ_{eff} is in ns timescale, which suggests that there is a huge contribution of NBOHC defect in the PL spectra of Si NWs/NCs. Due to the contribution of two distinct species with different time constants of decay (τ_1, τ_2), the PL decay fits to a bi-exponential function. The slower component (τ_1) is attributed to the QC effect and the faster component τ_2 is attributed to the NBOHC defects. Note that there is a considerable reduction in τ_1 as well as τ_2 for AgAuSi as compared to that of AgSi or AuSi. It has been reported that the radiative emission rate of Si NCs is increased after Au incorporation.[37] In the present case, Ag/Au NPs are present on the surface of the Si NCs attached with the Si NWs. These metal NPs can accelerate the radiative recombination rate of Si NCs.[5] This might be partly responsible for the high intensity of PL in AgAuSi (Fig. 4.9). To understand the contribution of two different species in the PL decay of AgAuSi, we have studied the PL decay monitored at different emission energies.[5] We have observed that τ_{eff} follows the trend expected from the QC effect i.e. τ_{eff} increases with increasing size of the Si NCs.[5] Thus, it can be concluded that the broad visible-NIR PL from the AgAuSi arises from the combine effect of QC in Si NCs and the NBOHC defects in SiO_x structure.[5]

In order to understand the origin of NIR PL from the MACE grown samples, we have taken the TRPL spectra of the sample R and P by monitoring the emission in the NIR range. Fig. 4.15(c) and (d) shows the TRPL decay in for sample R monitored at 850 nm and sample P monitored at 1135 nm, respectively. The fitted parameters are shown in Table 4.3. We observed a τ_{eff} = 62.5 μs for sample R for the TRPL decay at 850 nm and it follows the trend of QC effect in Si NCs for sample R. Therefore, the NIR PL of sample R (Fig. 4.14) centered at ~1.45 eV (850 nm) is originated from the larger size Si NCs, since the τ_{eff} increases with size of the Si NCs. On the other hand, the τ_{eff} = 172 ns for sample P monitored at 1135 nm (~1.1 eV), which is not in the range of 5-45 μs and thus ~1.1 eV PL for sample P is not due to QC effect in Si NCs.[47] This is consistent with the steady state NIR PL analysis.

4.8. Illustration of PL Mechanism using the Energy Band Diagram

Fig. 4.16(a) shows a schematic diagram of the Si NCs decorated Si NWs produced by MACE process. Note that these Si NWs/NCs are covered with SiO_x, which consist of NBOHC defect. The visible-NIR PL from MACE grown Si NWs/NCs arise from the combine effect of QC of carriers in the Si NCs (~1.1-2.4 eV) and the NBOHC defect in the SiO_x layer. Fig. 4.16(b) shows

a schematic energy band diagram at the interface of Si-SiO_x showing the contributions of Si NCs and NBOHC defects in SiO_x layer to the observed visible-NIR PL from the MACE grown Si NWs/NCs. Fig. 4.16(c) shows a schematic diagram of the relationship between the PL bands and the morphology (not to scale) of the Si NWs decorated with Si NCs and covered with an SiO_x layer. It essentially shows that the strong visible PL in sample R is due to the high density of Si NCs and NBOHC defects and the strong NIR PL in sample P originates from the Si NWs covered with a thick SiO_x layer. Note that phonon-assisted radiative recombination is expected to be responsible behind the distinct 1.1 eV PL for sample P.

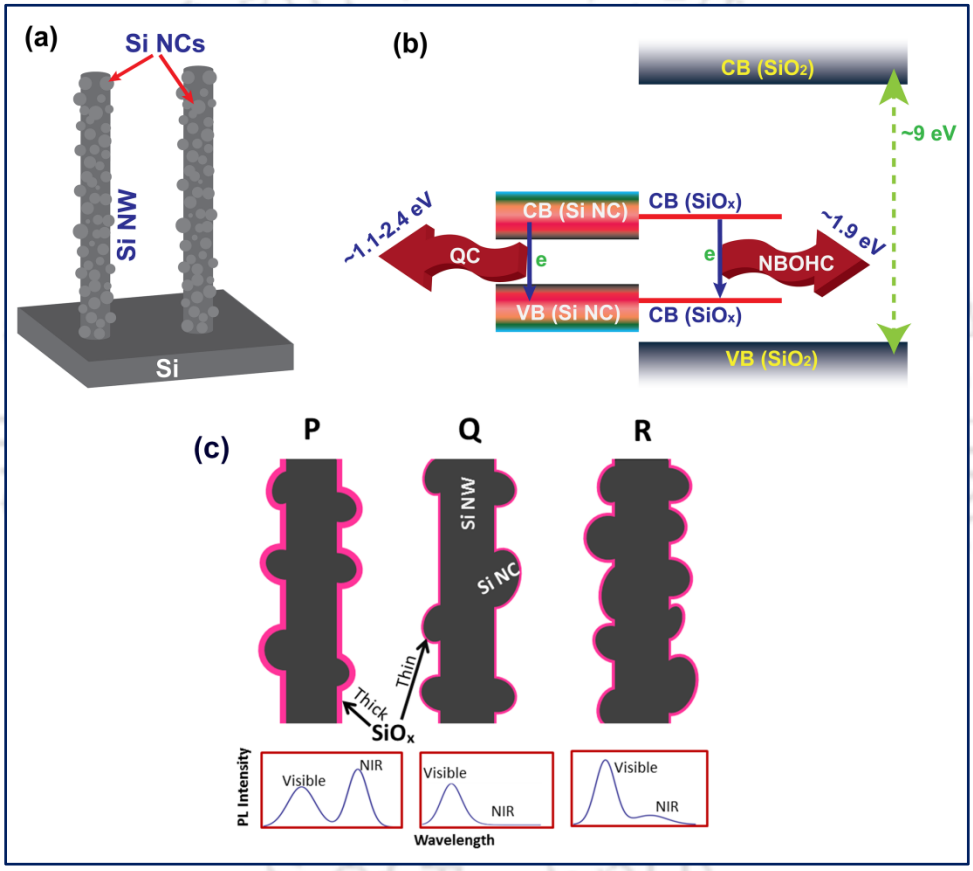

Fig. 4.16. (a) Schematic diagram of the Si NCs decorated Si NWs. (b) Schematic of energy band diagram at the interface of Si-SiO_x showing the different PL components originating from Si NCs and defects in SiO_x. ''VB'' and ''CB'' refer to valence and conduction band, respectively. (c) Schematic diagram of the cross-section (not to scale) of the Si NWs decorated with Si NCs and covered with an SiO_x layer for the sample P, Q and R, respectively. The lower panel shows a schematic diagram of the relative intensities of visible and NIR PL bands in each case.

4.9. Conclusion

The MACE grown Si NWs decorated with self-grown and arbitrary shaped quantum size Si NCs show strong and tunable visible-NIR PL at RT. In each case, it is revealed that the broad band

and tunable visible-NIR PL originates from the combined effect of QC in Si NCs and the NBOHC defects in the SiO_x layer. Interestingly, one-step etched Si NWs grown in $AgNO_3$/HF are covered with thick layer of Si sub-oxide and it shows additional NIR PL at ~1.1 eV distinctly different from the size dependent visible-NIR PL from Si NCs and this is ascribed to phonon assisted radiative recombination of EHP inside the core of the Si NWs. Our conclusions are strongly supported by the XPS, Raman, FTIR (*Section 3.9.C, D and E, Chapter 3*), DRS and HRTEM analysis. The effect of different growth parameters on PL spectra is extensively studied to understand the spectral position, shape and intensity of PL. Our observations help to resolve long standing debate on the origin of visible-NIR PL from Si NWs. This MACE grown Si NWs/NCs are beneficial for the low-cost production of photodiode, LED and other optoelectronic applications in the field of nanotechnology.

References

1. Walavalkar, S. S.; Hofmann, C. E.; Homyk, A. P.; Henry, M. D.; Atwater, H. A.; Scherer, A. *Nano Lett.,* **2010,** 10, 4423.
2. Suzuki, T.; Skuja, L.; Kajihara, K.; Hirano, M.; Kamiya, T.; Hosono, H. *Phys. Rev. Lett.,* **2003,** 90, 186404.
3. Skuja, L.; Suzuki, T.; Tanimura, K. *Phys. Rev. B,* **1995,** 52, 15208.
4. Kuznetsov, A. S.; Shimizu, T.; Kuznetsov, S. N.; Klekachev, A. V.; Shingubara, S.; Vanacken, J.; Moshchalkov, V. V. *Nanotechnology,* **2012,** 23, 475709.
5. Ghosh, R.; Imakita, K.; Fujii, M.; Giri, P. K. *Phys. Chem. Chem. Phys.,* **2016,** 18, 7715.
6. Ghosh, R.; Giri, P. K. *RSC Adv.,* **2016,** 6, 35365.
7. Ghosh, R.; Giri, P. K. *Sci. Adv. Today,* **2016,** 2, 25230.
8. Ghosh, R.; Pal, A.; Giri, P. K. *J. Raman Spec.,* **2015,** 46, 624.
9. Ghosh, R.; Giri, P. K.; Imakita, K.; Fujii, M. *J. Alloy Compd.,* **2015,** 638, 419.
10. Ghosh, R.; Giri, P. K.; Imakita, K.; Fujii, M. *Nanotechnology,* **2014,** 25, 045703.
11. Canham, L. T. *Appl. Phys. Lett.,* **1990,** 57, 1046.
12. Wolkin, M. V.; Jorne, J.; Fauchet, P. M.; Allan, G.; Delerue, C. *Phys. Rev. Lett.,* **1999,** 82, 197.
13. Brus, L. E.; Szajowski, P. F.; Wilson, W. L.; Harris, T. D.; Schuppler, S.; Citrin, P. H. *J. Am. Chem. Soc.,* **1995,** 117, 2915.
14. Hill, N. A.; Whaley, K. B. *Phys. Rev. Lett.,* **1995,** 75, 1130.
15. Ehbrecht, M.; Kohn, B.; Huisken, F.; Laguna, M. A.; Paillard, V. *Phys. Rev. B,* **1997,** 56, 6958.
16. Ledoux, G.; Gong, J.; Huisken, F.; Guillois, O.; Reynaud, C. *Appl. Phys. Lett.,* **2002,** 80, 4834.
17. Yang, S.; Li, W.; Cao, B.; Zeng, H.; Cai, W. *J. Phys. Chem. C,* **2011,** 115, 21056–21062.
18. Matsumoto, T.; Suzuki, J. I.; Ohnuma, M.; Kanemitsu, Y.; Masumoto, Y. *Phys. Rev. B,* **2001,** 63, 195322.
19. Demichel, O.; Oehler, F.; Noé, P.; Calvo, V.; Pauc, N.; Gentile, P.; Baron, T.; Peyrade, D.; Magnea, N. *Appl. Phys. Lett.,* **2008,** 93, 213104.

20. Demichel, O.; Calvo, V.; Noé, P.; Salem, B.; Fazzini, P. F.; Pauc, N.; Oehler, F.; Gentile, P.; Magnea, N. *Phys. Rev. B,* **2011,** 83, 245443.
21. Kusova, K.; OndiC, L.; Klimesova, E.; Herynkova, K.; Pelant, I.; Danis, S.; Valenta, J.; Gallart, M.; Ziegler, M.; Honerlage, B.; Gilliot, P. *Appl. Phys. Lett.,* **2012,** 101, 143101.
22. Cullis, A. G.; Canham, L. T.; Calcott, P. D. J. *J. Appl. Phys.,* **1997,** 82, 909.
23. Chern, W.; Hsu, K.; Chun, I. S.; Azeredo, B. P. d.; Ahmed, N.; Kim, K. H.; Zuo, J.-m.; Fang, N.; Ferreira, P.; Li, X. *Nano Lett.,* **2010,** 10, 1582.
24. Guichard, A. R.; Kekatpure, R. D.; Brongersma, M. L.; Kamins, T. I. *Phys. Rev. B,* **2008,** 78, 235422.
25. Dhara, S.; Lu, C. Y.; Nair, K. G. M.; Chen, K. H.; Chen, C. P.; Huang, Y. F.; David, C.; Chen, L. C.; Baldev, R. *Nanotechnology,* **2008,** 19, 395401.
26. Najar, A.; Slimane, A. B.; Hedhili, M. N.; Anjum, D.; Sougrat, R. *J. Appl. Phys.,* **2012,** 112, 033502.
27. Ghosh, R.; Giri, P. K. *Adv. Sci. Lett.,* **2016,** 22, 71.
28. Tsybeskov, L.; Vandyshev, J. V.; Fauchet, P. M. *Phys. Rev. B,* **1994,** 49, 7821.
29. Valenta, J.; Bruhn, B.; Linnros, J. *Nano Lett.,* **2011,** 11, 3003.
30. Rykaczewski, K.; Hildreth, O. J.; Wong, C. P.; Fedorov, A. G.; Scott, J. H. J. *Nano letters,* **2011,** 11, 2369-2374.
31. Qu, Y.; Zhoua, H.; Duan, X. *Nanoscale,* **2011,** 3, 4060.
32. Kim, J.; Han, H.; Kim, Y. H.; Choi, S. H.; Kim, J. C.; Lee, W. *ACS Nano,* **2011,** 5, 3222.
33. Mulazimoglu, E.; Nogay, G.; Turan, R.; Emrah Unalan, H. *Appl. Phys. Lett. ,* **2013,** 103, 143124.
34. Biteen, J. S.; Lewis, N. S.; Atwater, H. A.; Mertens, H.; Polman, A. *Appl. Phys. Lett.,* **2006,** 88, 131109.
35. Huh, C.; Choi, C.-J.; Kim, W.; Kyu Kim, B.; Park, B.-J.; Jang, E. H.; Kim, S.-H.; Yong Sung, G. *Appl. Phys. Lett.,* **2012,** 100, 181108.
36. Potrick, K.; Huisken, F. *Phys. Rev. B,* **2015,** 91, 125306.
37. Goffard, J.; Gérard, D.; Miska, P.; Baudrion, A.-L.; Deturche, R.; Plain, J. *Sci. Rep.,* **2013,** 3, 2672.
38. Bassu, M.; Strambini, M. L.; Barillaro, G.; Fuso, F. *Appl. Phys. Lett.,* **2010,** 97, 143113.
39. Choi, Y. R.; Zheng, M.; Bai, F.; Liu, J.; Tok, E.; Huang, Z.; Sow, C.-H. *Sci. Rep.,* **2014,** 4, 4940.
40. Peng, K.-Q.; Lee, S.-T. *Adv. Mater. ,* **2011,** 23, 198–215.
41. Varshni, Y. P. *Physica,* **1967,** 34, 149-154.
42. Hartel, A. M.; Gutsch, S.; Hiller, D.; Zacharias, M. *Physical Review B,* **2012,** 85, 165306.
43. Hartel, A. M.; Gutsch, S.; Hiller, D.; Zacharias, M. *Physical Review B,* **2013,** 87, 035428.
44. He, H.; Liu, C.; Sun, L.; Ye, Z. *Applied Physics Letters,* **2011,** 99, 123106.
45. Lin, L. H.; Sun, X. Z.; Tao, R.; Li, Z. C.; Feng, J. Y. *Journal of Applied Physics,* **2011,** 110, 073109.
46. Demichel, O.; Calvo, V.; Besson, A.; Noe, P.; Salem, B.; Pauc, N.; Oehler, F.; Gentile, P.; Magnea, N. *Nano Lett.,* **2010,** 10, 2323.
47. Sangghaleh, F.; Bruhn, B.; Schmidt, T.; Linnros, J. *Nanotechnology,* **2013,** 24, 225204 (5pp).
48. Rinnert, H.; Jambois, O.; Vergnat, M. *Journal of Applied Physics,* **2009,** 106, 023501-7.
49. Galli, S.; Maspero, A.; Giacobbe, C.; Palmisano, G.; Nardo, L.; Comotti, A.; Bassanetti, I.; Sozzani, P.; Masciocchi, N. *Journal of Materials Chemistry A,* **2014,** 2, 12208-12221.

Chapter 5

Quantitative Analysis of the Phonon Confinement Effect in Arbitrarily Shaped Si Nanocrystals Decorated on Si Nanowires and its Correlation with the Photoluminescence Analysis

Quantitative analysis of quantum confinement (QC) effect in the Si NCs is very important in order to understand the size distribution of the Si NCs. It was shown that the MACE grown Si NWs are decorated with arbitrary shaped Si NCs and it exhibited strong visible-NIR PL. QC of carriers in the Si NCs was believed to be primarily responsible for the observed PL emission. Raman spectra of the Si NCs decorated on Si NWs exhibit a red shift and an asymmetric broadening of 1st order Raman peak as well as the other multi phonon modes when compared with that of the bulk Si. Quantitative analysis of confinement of phonons in the Si NCs is very important to account for the measured Raman peak shift and asymmetric broadening. In this chapter, the size distribution of Si NCs is calculated from Raman and PL spectral analysis using the phonon and electron confinement models, respectively. The distribution follows a log-normal distribution and expressed in terms of mean diameter (D_0) and skewness (σ). The correlation between Raman and PL spectra allows spectroscopic evaluation of the accurate size distribution of the Si NCs on the surface of the Si NWs, even for arbitrary shaped Si NCs. Finally, the results are correlated with the HRTEM analysis. These results are useful for the design of high performance optoelectronic devices based on the Si NWs/NCs.

5.1. Introduction

Raman scattering is sensitive to the crystal lattice microstructure of Si via its vibrational properties. Inspection of line shapes of Raman spectra provides useful information concerning the crystallinity, amorphicity, presence of H-terminated surface and dimension of nanostructured Si. The Raman spectra of bulk crystalline Si and Si nanostructures have been studied extensively and are well understood. It is well known that the Si NWs grown by MACE are usually covered with arbitrary shaped Si NCs due to the side wall etching. These NW/NCs exhibit significantly different optical characteristics over the bulk Si in Raman spectra. Therefore, the Raman spectra

of the MACE grown Si NCs decorated Si NWs are of great value for the further understanding of the above mentioned parameters i.e. crystallinity, amorphicity, stress/strain, presence of H-terminated surface and dimension of nanostructured Si. Raman studies of Si nanostructures usually show a downshift and an asymmetric broadening of the first order Raman peak. It is understood that temperature, lattice stress and phonon confinement play a major role in the observed downshift as well as asymmetric broadening of the peak. Raman spectroscopy is not only a convenient non-destructive powerful method for measuring the size of the Si NCs, but also a sensitive tool for the defects (due to the amorphous SiO_x layer), composition and local conditions such as laser heating.[1-11] Several reports have been published on the size dependent Raman spectra of nanostructured materials.[1-7] Most of the reports dealt with spherical Si NCs or the Si NCs embedded in SiO_2 matrix.[1, 2, 9, 10] To the best of our knowledge, there is no detailed Raman study of highly ordered vertical Si NWs array decorated with arbitrary shaped Si NCs grown by MACE method. Thus, Raman spectroscopy can become one of the preferred choices to characterize and understand the Si NCs and Si NWs by analyzing the confinement of phonon in Si NCs and the strain due to amorphous SiO_x layer. On the other hand, the MACE grown Si NWs decorated with arbitrary shaped and ultrasmall size Si NCs can emit both visible and NIR PL depending on the size of the Si NCs and the PL results has been explained on the basis of primarily the quantum confinement (QC) effect.[12-16] However, the NBOHC defect has also strong contribution to the broad visible PL of the Si NWs/NCs.[13, 17-19] Thus the relation between Si nanostructure's bandgap and its size is still under debate. Therefore, a study on the confinement effect of electrons and holes in PL spectroscopy and the confinement of phonons monitored through the Raman spectroscopy can provide a valuable correlation between the two techniques and a quantitative estimation of the average size of Si NCs with their size distribution would be possible.

In this chapter, we will establish a direct correlation between the PL and Raman spectra of Si NC/NWs in the light of QC of carriers and phonon confinement effect, respectively. We have fabricated highly ordered arrays of micron-long Si NWs with diameter in the range 20-400 nm by MACE from single crystalline Si wafers at RT under different etching conditions and these NWs are decorated with arbitrary shaped self-grown Si NCs. The light emission properties of these Si NCs are explained using primarily the QC effect.[13, 14] Since the PL emission energy is directly related to size of the Si NC, we attempt to find out the size distribution of the Si NCs

in each sample in terms of its mean diameter (D_0) and skewness (σ), considering that the size distribution of Si NCs follows the typical log-normal distribution. In the Raman spectra, the observed downshift and the asymmetric broadening of the first-order phonon mode in MACE grown Si NWs/NCs are explained taking into the account of quantitative analysis using phonon confinement effect. In order to eliminate the effect of laser heating (both homogeneous and inhomogeneous heating), we perform the Raman measurements with a very low laser power (0.08 mW).[20] We fit the 1st order Raman data with Dogan model[21] and numerically estimate the Si NCs size distribution in terms of D_0 and σ.[20] We compare the size distribution in each sample estimated from the Raman and PL spectra and also compare the results with that of sizes obtained directly from the high resolution transmission electron microscopy (HRTEM) analysis. Such a correlation is useful for the calculation of accurate size distribution of the semiconductor nanostructures for different semiconductors.

5.2. Growth of Si NC Decorated Si NWs

For the present study, Si NWs were grown from boron-doped p-type Si (100) wafers with resistivity 1-10 Ω-cm. The Si wafers were cleaned by typical RCA process as discussed in the earlier chapter. For Si NW growth, we used a two-step metal assisted chemical etching (MACE) process. At first, a thin layer of Ag NPs was formed on the Si wafers by dipping the wafers in a

Table 5.1. *Details of the growth parameters and the size distribution of the Si NCs in terms of* mean diameter (D_0) and skewness (σ), as *obtained from different techniques.*

Sample code	Etching solution	Etching duration (min)	Si NWs length (μm)	Si NC's D_0 (nm)			σ (nm)		
				Raman	PL	HRTEM	Raman	PL	HRTEM
M1	Two-step Etching, 4.6 M HF & 1.422 M H_2O_2	5	3.9 ± 0.2	6.8	5.8	8.9	0.45	0.23	0.3
M2		10	6.5 ± 0.2	4.8	5.8	8.1	0.4	0.23	0.3
M3		15	9.5 ± 0.2	4.2	5.7	6.9	0.42	0.24	0.35
M4		20	11.6 ± 0.2	4.3	5.7	6.2	0.4	0.24	0.27

solution containing 0.015 M $AgNO_3$ + 5.55 M HF for 3-5 seconds.[20] The Ag NPs coated Si wafers were subsequently immersed in to a solution containing 1.422 M H_2O_2 + 4.6 M HF. Depending on the etching durations (5 min to 20 min), the Si NWs samples are termed as M1,

M2, M3 and M4. The details of the samples are presented in Table 5.1. The residual Ag NPs on the top and sidewall surface of the Si NWs, and pores in between them were removed by dipping Si NWs into diluted (10%) HNO_3 solution for 5 min. The samples were dried in Ar gas flow after ringing in DI water.[20]

5.3. Morphology

5.3.1 FESEM Analysis

Micron long Si NWs decorated with arbitrary shaped quantum sized Si NCs is formed by MACE. The formation mechanism of Si NWs as well as the Si NCs on its surface is discussed in the *chapter 3, section 3.5*.[13, 17, 18, 20, 22, 23] Fig. 5.1 (a-d) shows the FESEM cross-sectional micrographs of M1, M2, M3 and M4, respectively. The length of the corresponding Si NWs is shown in Table 5.1.

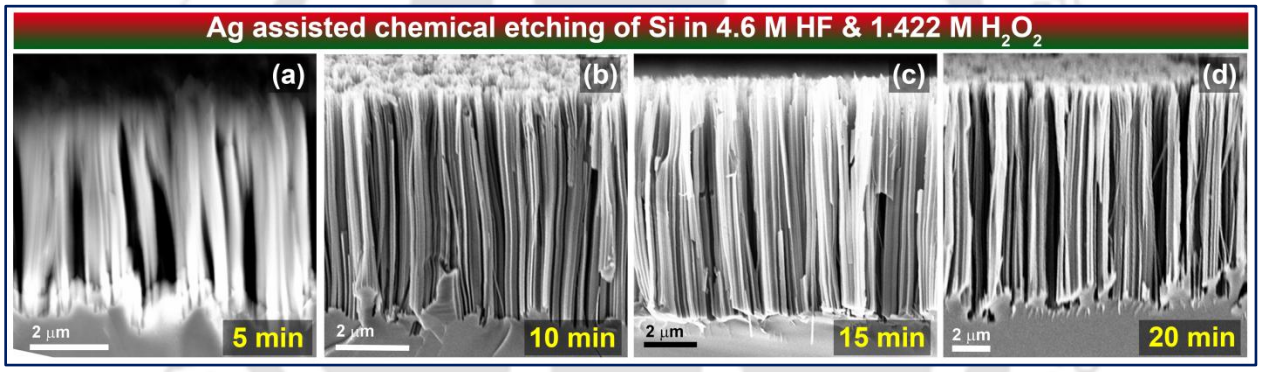

Fig. 5.1. FESEM cross-sectional micrographs of sample (a) M1, (b) M2, (c) M3 and (d) M4.

5.3.2. TEM Analysis

Mesoporous nature of the Si NWs with uniform diameter are confirmed from the TEM images of individual Si NWs collected from each sample. The formation of the Si NCs on the surface of the Si NWs strongly depends upon the mesoporous structure of the NWs. The shape and size of the Si NCs depend on the size of the pore and intermediate distance between the pores, which in turn depend on the etching conditions.[13, 17, 18, 20, 23] Fig. 5.2 shows the TEM images of individual Si NW acquired from samples (a) M1, (b) M2, (c) M3 and (d) M4.[20] Fig. 5.2(e) shows the enlarged portion of the Si NW collected from sample M4 and it is clear that the surface of the Si NWs is rough due to the presence of the arbitrary shaped Si NCs originating from the side wall etching of the NWs. Fig. 5.2(f) shows the HRTEM image of the surface of the Si NWs. The typical

dimension of a single Si NC is marked by a dashed line.[20] Fig. 5.2(g) shows the corresponding inverse first Fourier transformed (IFFT) image of the selected area of Fig. 5.2(d). Fig. 5.2(h) and (i) show the selected area electron diffraction (SAED) pattern and energy dispersive X-ray (EDX) spectrum, respectively, of the sample M4.[20] The EDX spectrum confirms the presence of SiO_x layer on the top of the Si NWs/NCs. It is clear from Fig. 5.2(g) and (h) that the Si NCs are

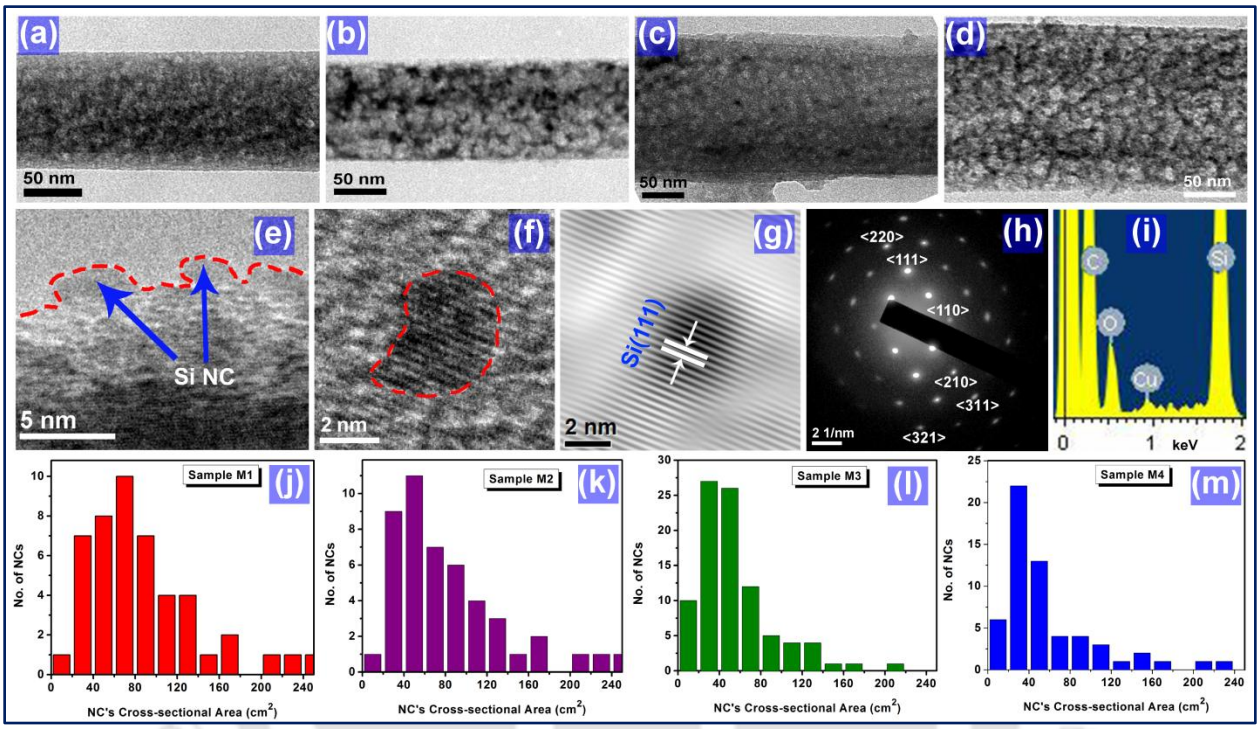

Fig. 5.2. TEM image of a single Si NW collected from samples (a) M1, (b) M2, (c) M3 and (d) M4. (e) A magnified view of the (d), showing rough surface of the NWs due to sidewall etching and confirming the presence of Si NCs on its surface. (f) The HRTEM lattice image of a single Si NC and its shape is marked by dashed line. (g) Corresponding HRTEM lattice image of the Si NC indicating growth in (111) direction. (h) SAED pattern of the Si NCs showing different planes of Si. (i) EDX spectrum of the Si NW/NCs showing the SiO_x layer on the surface of the Si NWs/NCs. The distribution of cross-sectional area "A" of the Si NCs on the surface of the Si NWs calculated from samples (j) M1, (k) M2, (l) M3 and (m) M4, respectively.

single crystalline and the typical dimension of the Si NC is easily visualized.[20] Calculation of d-spacing from the lattice image in Fig. 5.2(g) shows a reduced lattice constant (3.01 Å), implying a compressive strain in the lattice. This may be related to the anisotropic etching and native oxide layer grown on the Si NWs/NCs surface.[13, 20] The SAED pattern in Fig. 5.2(h) confirms that several crystal planes are present in the Si NC's lattice structure. Since the Si NCs formed on the surface of the Si NWs are of arbitrary shape and size, we represent the size of the Si NCs in terms cross-sectional areas (A) instead of the diameter of the NCs. Fig. 5.2(j-m) represents the distribution of "A" for the samples M1, M2, M3 and M4, respectively. The shapes of the Si NCs

are arbitrary and varying in wide range of sizes depending upon the growth condition, as shown in Fig. 5.2. We have also calculated the equivalent diameter (D_0) of the Si NCs from the corresponding "A" considering the circular cross-section of the Si NCs. The size distributions follows a log-normal distribution and it is expressed in terms of mean diameter, D_0 and skewness, σ as shown in Table 5.1.

5.4. Raman Spectral Analysis

Raman scattering is sensitive to the crystal lattice microstructure of Si via its vibrational properties and by inspection of line shapes of Raman spectra one can get the useful information including the crystallinity, amorphicity, and dimension of nanostructured Si. The Raman spectra of all the Si NWs/NCs samples were measured at low laser power along with a bulk Si wafer for suitable comparison. The Raman spectra of all the samples were corrected and compared by taking the first order Raman peak of the bulk Si at 520.5 cm^{-1}.[24] Fig. 5.3(a) shows the Raman spectra for the samples M1, M2, M3, M4 and bulk Si with 488 nm laser excitation at a power of 0.083 mW.[20] The curves are vertically shifted to enable comparison. Fig. 5.3(b) shows the magnified view of 1st order Raman spectra at RT for these samples. The spectral resolution of the Raman data is 0.7 cm^{-1}. The 1st order Raman peak of all the samples is red shifted and asymmetric towards lower wavenumbers. However, the peak arises from the first-order Raman scattering of the longitudinal optical (LO) and the transverse optical (TO) phonon modes of Si, which are degenerate at the Brillouin zone center in crystalline Si. Fig. 5.3(a) shows that several multi-phonon bands are present in the Si NWs/NCs samples (290-300 cm^{-1}, 620-640 cm^{-1} and 950-970 cm^{-1}), which are not detected in the bulk Si Raman spectrum. These bands are mostly due to the amorphous Si, Si NC embedded in SiO_x matrix or the surface chemical bonds (such as Si-H).[25-27] Note that the band corresponding to the 1st order Raman mode in Fig. 5.3(a) is extended down to ~410 cm^{-1}, which suggest that the Si NCs are covered by a thin layer of amorphous Si.[20] However, there are other factors that can have strong effect on the 1st order Raman spectra of the Si NWs/NCs.

In order to understand the excitation wavelength dependence of the Raman spectra, we performed the Raman measurement with 514 nm excitation in addition to the 488 nm laser excitation. Fig. 5.4(a) and 5.4(b) show the comparison of normalized 1st order Raman spectra of the samples at 488 and 514 nm laser excitations, respectively.[20] In case of 514 nm laser excitation, the Si NWs/NCs shows all the multi phonon peaks and the 1st order Raman peak of all

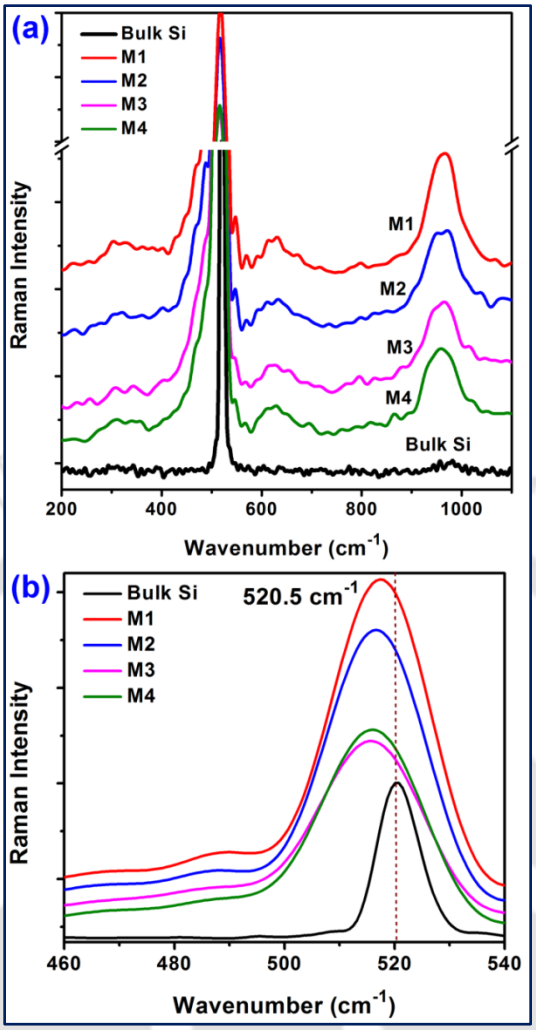

Fig. 5.3. (a) Comparison of the Raman spectra for the samples M1, M2, M3 and M4 with that of the bulk Si with 488 nm laser excitation at a laser power of 0.083 mW. The curves are vertically shifted to enable comparison. (b) Comparison of the 1st order Raman spectra (smoothed) for different samples.

the samples are red shifted and asymmetric towards lower wavenumbers, which are almost identical to the results obtained with 488 nm laser excitation.[20] The red shift and asymmetric broadening of the 1st order phonon mode in the Raman spectra of the Si NWs/NCs can be explained in terms of three sets of effects:

(a) phonon confinement effect only

(b) phonon confinement and compressive strain effects

(c) phonon confinement, compressive strain and inhomogeneous laser heating effects.

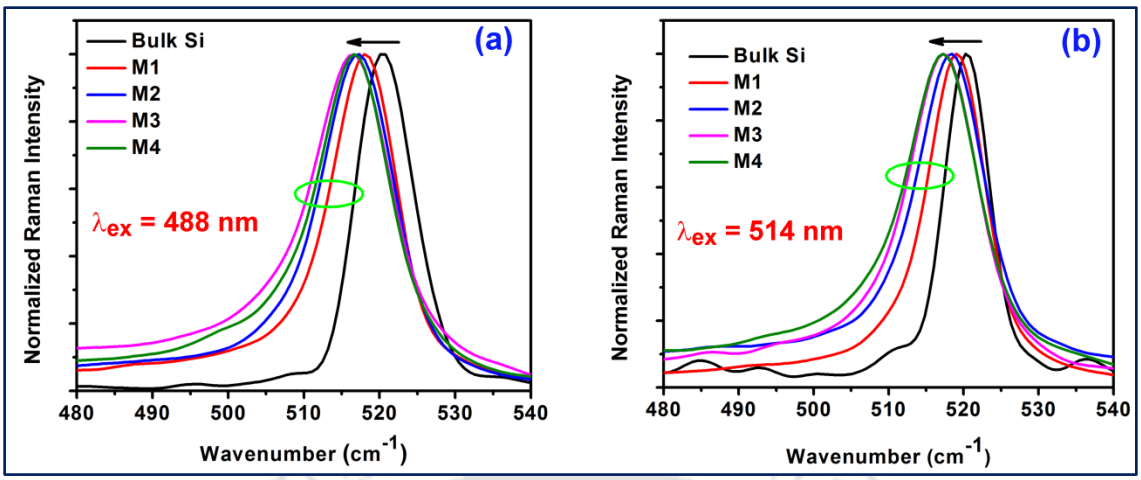

Fig. 5.4. Comparison of the normalized 1st order Raman spectra of different samples with laser power 0.083 mW and laser excitations: (a) 488 nm and (b) 514 nm. The green oval shows the asymmetry and broadening of the spectra and the arrow represents the peak shift towards lower wavenumber.

5.4.1. *Effect of Lattice Strain*

As mentioned before, the Si NWs/NCs are covered with a native oxide layer and the compressive stress from the oxide matrix could also be responsible for the shift in the 1st order Raman peak to higher wavenumber and it may be competing with the downshift of wavenumber due to phonon confinement.[8-10, 13, 17, 18, 20] From the additional shift of the Raman peaks ($\delta\omega = \omega - \omega_0$), the lattice strain for the bulk Si can be approximately calculated using the following equations[8],

$$\delta\omega = -3\gamma(a - a_0)/a \quad \text{..... (5.1)}$$

where a is the lattice constant of the strained Si, γ is Gruneisen constant ($\gamma \sim 1.0$), and a_0 (5.42 Å) is the lattice constant of single-crystalline Si. The lattice constant of sample M3 and M4 calculated from HRTEM analysis are 5.21 Å and 5.35 Å. The corresponding shifts of the 1st order Raman peak due to the strain effect are estimated to be 0.12 cm^{-1} and 0.04 cm^{-1} for M3 and M4, respectively. However, the 1st order Raman mode of the respective samples in Fig. 5.3(b) show shifts of ~4 cm^{-1} and ~3.9 cm^{-1}, respectively. Thus, the strain effect on the observed shifts is considered to be insignificant for these samples.[13]

5.4.2. *Effect of Laser Heating*

Laser exposure of solid samples can cause inhomogeneous heating resulting in a down shift and a broadening of the Raman peaks. This is indeed important in the present case due to high absorption of the Si NWs/NCs in the entire visible range. In order to understand the effect of laser power on the Raman spectra, we have performed the Raman measurements with different

laser powers ranging from 0.083 mW to 5 mW. The laser spot diameter is about 6 µm, when the sample was focused by a lens with 50X magnification. Fig. 5.5 shows the 1st order Raman spectra of the samples (a) M1, (b) M2, (c) M3 and (d) M4 at different laser powers. With

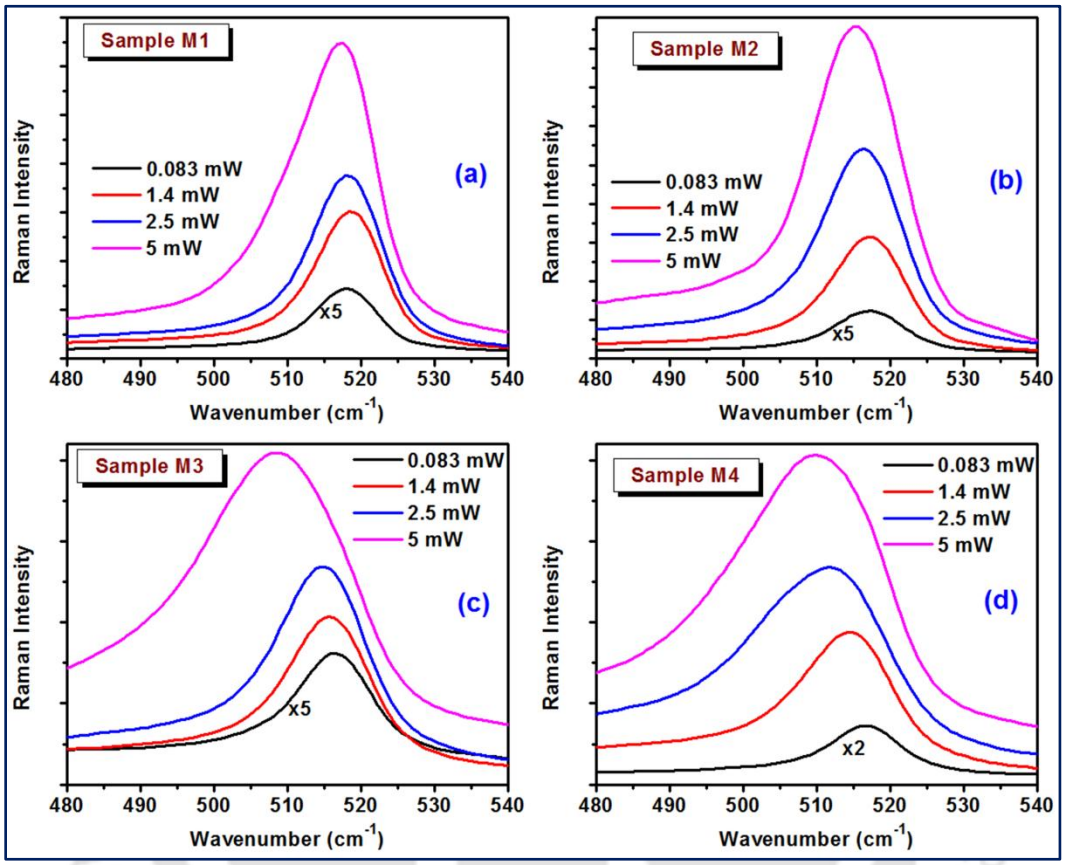

Fig. 5.5. Comparison of the Raman spectra for samples (a) M1, (b) M2, (c) M3 and (d) M4 with different laser powers at 488 nm excitation. The curve corresponding to the 0.083 mW is scaled up to enable comparison.

the increase of the laser power: (i) the peak intensity increases; (ii) peak position shifts downwards; (iii) the line width (FWHM) increases; and (iv) the asymmetry increases. Note that vertically ordered Si NWs array grown by reactive ion etching did not show any significant change in Raman spectra at different laser power.[28] However, in the present case, the MACE grown Si NWs decorated with Si NCs are very sensitive to the laser heating as compared to its bulk counterpart.[20] This is primarily due to size effect, giving a much lower thermal conductivity of the Si NCs than that of the bulk Si and poor thermal contact with the substrate. Further, Si NC has higher absorption than bulk Si in the entire visible region. This may cause a local rise in temperature. Thus, the rise in local temperature must be taken into account when interpreting the Raman spectra.[20] Note that in case of laser power 0.083 mW, the corresponding laser power density is ~293 W/cm^2. This is sufficiently low and comparable to that used by Ilker et al.[21] Note

that a fraction of the laser radiation is specularly reflected, and a significant amount of the power absorbed by the specimen is reradiated. Thus, only a fraction of the incident power is actually converted to heat.[29] On the other hand, since the Si NWs/NCs are not free standing, maximum amount of heat was dissipated to the Si wafer beneath the Si NWs/NCs. Thus, the contribution of the local heating in the Raman spectra is not considerable at 0.083 mW, though not fully eliminated at this power. Note that high laser powers can create free carriers. These carriers can interfere with the Si phonon line and create an asymmetric Fano line shape and this should show an increase of the low wavenumber asymmetry in the Si NWs/NCs spectrum at higher power.[20, 30, 31] In order to minimize such effects on Raman spectra, we have performed the Raman measurements at a very low laser power i.e. 0.083 mW.[20]

5.4.3. *Quantitative Analysis of the Raman Spectra*

In the literature, theories have been developed for the calculation of the Raman energy shift due to the phonon confinements in nanostructures.[1, 2, 5-7] The active phonon in the Raman scattering process of bulk materials is in the center of the first Brillouin Zone (BZ) with q~0, where q is the phonon wave vector. Classical electromagnetic radiation theory predicts a Lorentzian-shaped Raman peak from an oscillating dipole[32]:

$$I(\omega, q) = I_0 \int_{BZ} L(\omega, q) d^3q \,, \qquad \text{..... (5.2)}$$

$$L(\omega, q) = \frac{1}{\pi} \frac{\Gamma/2}{[\omega - \omega(q)]^2 + [\Gamma/2]^2} \,, \qquad \text{..... (5.3)}$$

where the L(ω, q) is a Lorentzian function of wavenumber ω, phonon dispersion relation ω(q), and the characteristic full width at half maximum (FWHM) Γ. According to the phonon dispersion relation of Si, ω(q) can be expressed as:

$$\omega(q) = \omega_0 [1 - 0.23 \left(\frac{q a_0}{2\pi}\right)^2] \,, \qquad \text{..... (5.4)}$$

where ω_0 = 520.5 cm^{-1} and a_0 = 0.542 nm are the wavenumber and lattice constant, respectively, of bulk crystalline Si. Eqn. (5.2) represents the Raman spectrum for semi-infinite crystals i.e. systems under long range translational symmetry. In a finite-size crystal, the translational symmetry of the lattice is no longer conserved due to the presence of grain boundaries that results in confinement of phonons, and triggers a red-shift (to the lower wavenumbers) of the characteristic phonon mode with decreasing size.[20] The red-shift of the Raman spectrum with decreasing NC size was first explained by the phonon confinement (PC)

model or Richter (RWL) model.[5] After incorporating the NCs size distribution by means of NC's mean size (D_0) and the skewness (σ) into the one-phonon confinement model (PCM) described by Faraci et al.,[6] the intensity of phonon wavenumbers of Si NCs with different sizes with a defined size distribution is expressed as[1, 21]:

$$I(\omega) = \int_0^{\infty} F(D)L(\omega, D)dD, \quad \text{..... (5.5)}$$

where, F(D) represents a typical log-normal size distribution in terms of D, D_0 and σ; and L(ω, D) represents the generalized Lorentzian. Since the Raman peak intensity and broadening depend roughly as D^{-3} and D^{-4} respectively, the distribution of D is important. However, the expression of F(D) and L(ω, D) can be written as follows[1, 21]:

$$F(D) = \frac{1}{\sigma D\sqrt{2\pi}} exp\left(-\frac{log(D/D_0)^2}{2\sigma^2}\right), \quad \text{..... (5.6)}$$

$$L(\omega, D) = \frac{A(D)}{\pi} \frac{\Gamma_{NC}(D)/2}{(\omega - \omega_{NC}(D))^2 + (\Gamma_{NC}(D)/2)^2}, \quad \text{.... (5.7)}$$

The explicit expressions for the intensity A(D), peak broadening $\Gamma_{NC}(D)$, and peak position $\omega_{NC}(D)$ could be expressed in terms of D as[21]:

$$A(D) = 1.4\times10^{-2}D^{-3}, \quad \text{..... (5.8a)}$$

$$\Gamma_{NC}(D) = \Gamma_0 + 60.0D^{-4}, \quad \text{..... (5.8b)}$$

$$\omega_{NC}(D) = \omega_0 + 34.8D^{-2}, \quad \text{..... (5.8c)}$$

Where Γ_0 = 3 cm^{-1}, is assumed to be the theoretical broadening of the 1st order phonon peak of bulk crystalline Si[6, 21] and ω_0 = 520.5 cm^{-1}. In order to find out effective FWHM (Γ_0) of bulk Si

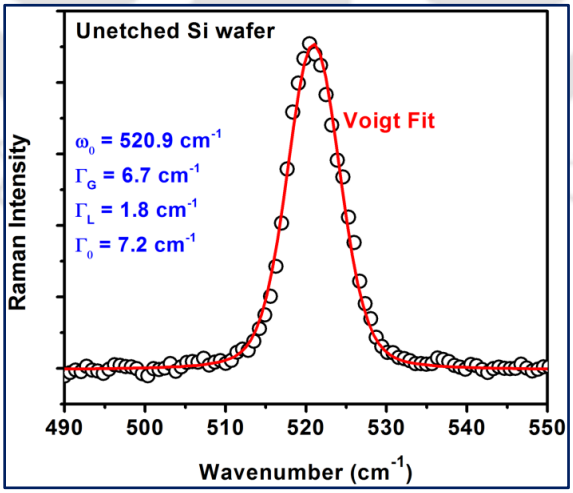

Fig. 5.6. The 1st order Raman spectrum of unetched Si wafer with laser power 0.083 mW and its Voigt fit (combination of Gaussian and Lorentzian peaks). The errors in the fitting in ω_0, Γ_G (FWHM of the Gaussian), Γ_L (FWHM of the Lorentzian) are 0.02, 0.5 and 0.6 cm^{-1} respectively.

including instrumental broadening effect, we fitted the 1st order Raman spectrum of the unetched bulk Si wafer by a Voigt peak (a combination of Gaussian and Lorentzian line shape). Fig. 5.6 shows the 1st order Raman spectrum of unetched bulk Si wafer with laser power 0.083 mW and its Voigt fit. The effective Γ_0 for the bulk Si is calculated to be 7.2 cm^{-1} for our spectrometer[33]. The error in fitting of ω_0, Γ_G (FWHM of the Gaussian), Γ_L (FWHM of the Lorentzian) are 0.02,

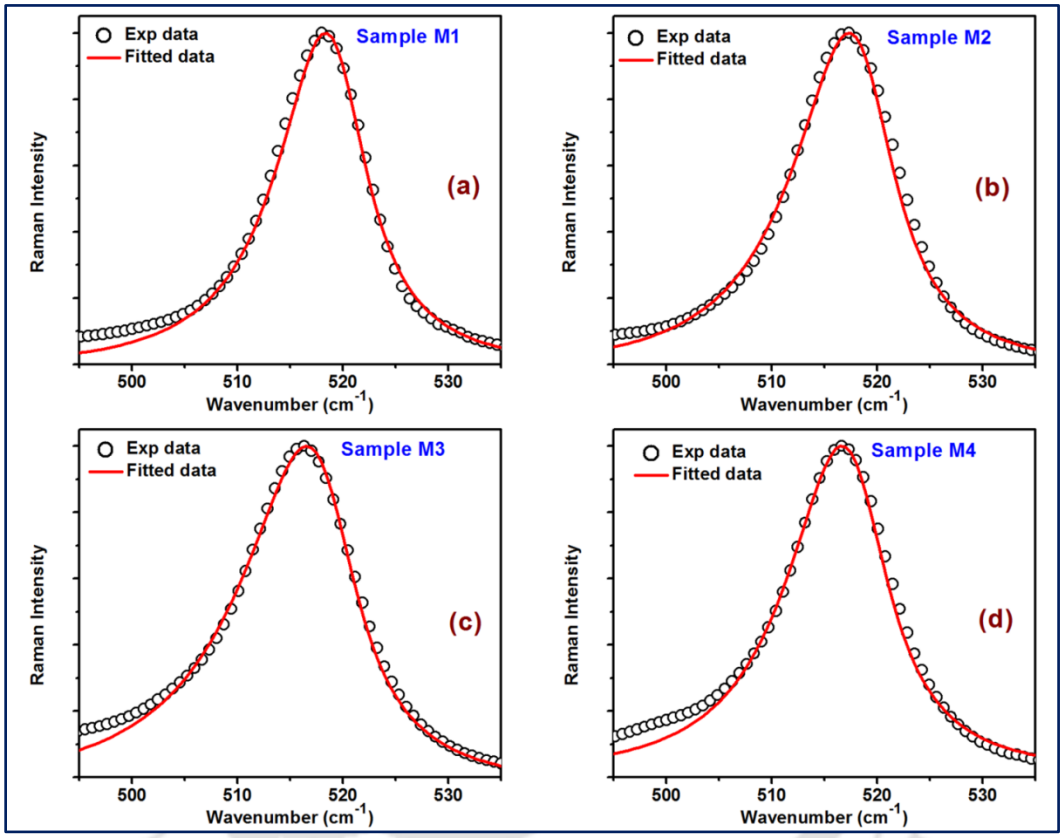

Fig. 5.7. (a)-(d) Fitting of the 1st order Raman spectrum using eqn. (5.5) by tuning the values of D_0 and σ for the samples M1, M2, M3, and M4, respectively.

0.5 and 0.6 cm^{-1} respectively. Taking Γ_0 as 7.2 cm^{-1}, we put the values of A(D), $\Gamma_{NC}(D)$ and $\omega_{NC}(D)$ into the eqn. (5.7) and then replace the values of F(D) and L(ω, D) from eqn. (5.6) and (5.7) into the eqn. (5.5) and attempt to fit the 1st order Raman spectrum of each samples shown in Fig. 5.3(b) by eqn. (5.5).[20] We have tuned the values of D_0 and σ to obtain best fit for the 1st order Raman spectrum of each sample. The fitted 1st order Raman spectrum of each sample is shown in Fig. 5.7(a-d). The fitting yields the size distribution of the Si NCs in terms of the D_0 and σ, details of which are presented in Table 5.1.[20] The mean diameter of the Si NCs decreases with increasing the etching duration, which is consistent with the PL and HRTEM analysis.

5.5. Photoluminescence Analysis

The Si NWs decorated with arbitrary shaped Si NCs on its surface exhibit strong broadband PL at RT in the visible to NIR region.[13, 14, 17, 18] Fig. 5.8(a) shows the broad visible PL spectra from the samples M1, M2, M3 and M4, while Fig. 5.8(b) shows corresponding NIR PL spectra, respectively. Fig. 5.8(c) shows the comparison of the integrated PL intensities as a function of etching duration, where the intensities of the visible and NIR PL show opposite trend with etching duration. The inset of Fig. 5.8(c) shows the variation of Si NWs length with the etching duration. We studied the effect of etching time on the morphology (in *Chapter 3, Section 3.6.1*) and PL spectra (in *Chapter 4, Section 4.5.1*) of the NWs.[13] The NW length increases almost linearly with etching time duration (inset of fig. 5.8(c)). Due to large diameter of the Si NWs and indirect nature of its bandgap, strong visible PL at room temperature is unlikely to originate from the Si NWs. On the other hand, the dimensions of the self-grown Si NCs are comparable/smaller than the excitonic Bohr diameter of Si (~9.8 nm). So, the QC effect of carriers can give rise to efficient visible-NIR PL from the Si NCs depending on its sizes.[13, 14] Since these Si NCs are usually embedded in an amorphous Si sheath or SiO_x layer, the surface (NBOHC) defects can also cause the reddish PL.[13, 17, 18, 20, 34] The origin of PL emission from the MACE grown Si NWs/NCs is explained elaborately in chapter 4. Non-bridging oxygen hole center (NBOHC) within the SiO_x is reported to be a possible source for the visible PL centered at ~1.9 eV.[17, 18, 35] In the present case the PL band is extended from ~1.1-2.5 eV. In addition to the NBOHC defect mediated PL emission at ~1.9 eV, the QC of carriers at the ultrasmall Si NCs with a wide range of size distribution is primarily believed to be responsible for the strong visible PL in the MACE grown Si NWs/NCs.[20]

QC model is the most successful model for explaining size dependent PL spectra of Si nanostructures. The heterogeneous relations between the diameter (D) of the Si nanostructure (quasi-0D in Si NC) and corresponding PL peak energy (E_{NC}) can be expressed as

$$E_{NC} = E_g(bulk) + CD^{-\alpha}, \quad \text{..... (5.9)}$$

where C and α are constants. Note that in our case the shape of the Si NCs is arbitrary with a broad distribution in size/cross-section. Due to the arbitrary shape, we choose the cross-sectional area (A) as the most appropriate parameter to replace the parameter "D" resulting in the following equation:

$$E_{NC} = E_g(bulk) + C'A^{-\alpha'}, \quad \text{..... (5.10)}$$

where C′ and α′ are new constants. Here A is the cross-sectional area of the Si NCs replacing $\pi D^2/4$ for the circular cross-section. To emulate the PL line shape, size distribution of the NCs must be considered. As discussed in in the *Chapter 4, Section 4.3.2*, we found the new constants as C′ = 3.58 eV/nm^2 and α′ = 0.52, which are very much consistent with the literature report.[36] It

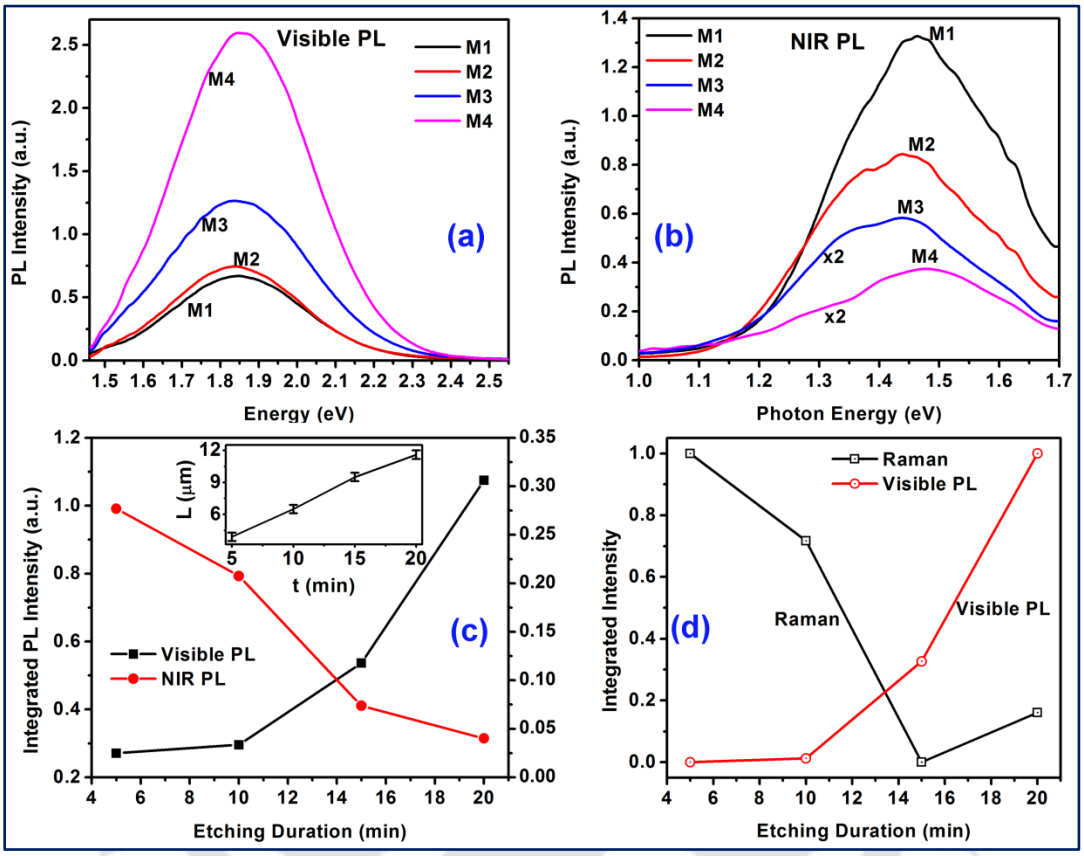

Fig. 5.8. Comparison of the (a) visible PL and (b) NIR PL spectra for the samples M1, M2, M3 and M4 at RT with a 405 nm laser excitation. NIR PL spectra of sample M3 and M4 are scaled up by a factor 2 to enable comparison. (c) Comparison of the integrated PL intensities of the samples with etching duration. The inset shows the variation of Si NWs length (L) with etching time (t). (d) Comparison of the integrated intensity of the 1st order Raman spectrum and visible PL spectrum as a function of etching duration.

is clear that with increasing etching duration, the density of the Si NCs increases and correspondingly intensity of the visible PL increases. Note that the NIR PL intensity decreases with increasing the etching duration, since the bigger size NCs that give rise to NIR PL breaks into smaller size NCs during longer period etching.[13, 20] Since the shape of the Si NCs are arbitrary, we take the dimension of the Si NCs in terms of their cross-sectional areas (A) and Fig. 5.1(j-m) shows the distribution of the A for the Si NCs measured from the TEM image of the samples M1, M2, M3 and M4, respectively (bar graph). Both the TEM results and the variation

of the PL intensity with NCs size indicate that the Si NCs size distribution is skewed symmetric and σ is positive.[20] Note that the NIR PL originates from the comparatively larger size Si NCs. It is clear from Fig. 5.8(c) that the integrated intensity of the visible PL increases with etching duration, while the NIR PL decreases. This is because the average size of the Si NCs decreases with increasing etching duration, i.e., the positivity of σ of the size distribution of the NCs increases with etching duration.[20] During the etching, as the time progress more number of nucleation sites is generated on the sidewall of Si NWs and the porosity increases. As a result, the larger Si NCs are divided into a smaller Si NCs. So, the density of smaller Si NCs increases at the cost of decrease in density of the large size Si NCs with etching time. As a result, the positivity of σ in the size distribution increases and it leads to the enhancement of visible PL and decrease in NIR PL with etching time.[20]

5.6. Correlation between the Raman and PL Analysis: Calculation of the Size Distribution of Si NCs

The correlation between Raman and PL spectra of Si is very important to understand the structural, electronic and optical properties of Si as well as the distribution of the size of the nanostructured Si. The MACE grown Si NWs decorated with ultra-small Si NCs show strong visible PL due to the QC effect and considerable red shift of 1st order Raman peak depending upon the size of the Si NCs.[20] In order to calculate the average size of the Si NCs including its size distribution, we attempt to correlate the PL and Raman spectra of the MACE grown Si NWs decorated with arbitrary shaped Si NCs. Fig. 5.8(d) shows the variation of integrated intensity of visible PL and 1st order Raman peak in the range 480-540 cm^{-1} as a function etching duration.[20] Note that due to higher density of Si NCs formed during longer duration etching, integrated PL intensity increases systematically with etching time, as discussed before. However, the decrease of Raman intensity with etching time cannot be explained if we consider that the length of the Si NWs is increasing with increasing etching time. The decreased Raman intensity can be explained properly if the decreases in size of the NCs are taken into account. Earlier reports suggest that the 1st order Raman peak intensity increases strongly with length of the Si NWs grown by MACE.[37, 38] Earlier report also suggests that the Raman intensity decreases with the decrease in diameter of the Si NW.[28] In our case, it is found that the D_0 of the Si NC's decreases with etching time, though the length of the Si NWs increases, and this decrease in NCs size is responsible for the

reduced Raman intensity. Note that the surface corrugation of the NWs may also be partly responsible for the reduced intensity of the Raman peak with increasing NW length.[20] Due to the presence of the Si NCs on the surface of the Si NWs, multiple reflections in the Si NW are reduced and hence a smaller length of the NW/NCs contributes to the scattering intensity. Further, the Si NCs have high absorption in the entire visible range. As a result, the Raman scattering intensity decreases with the length of the Si NWs.[20] This result also confirms that both the Raman and PL spectra of MACE grown Si NWs are dominated by the contribution from the self-grown Si NCs.[20] Further, the probable optical loss induced by the residual Ag NPs possibly cause a decrease in the Raman intensity from the samples, since the Ag particles can't be removed fully even after keeping the samples in HNO_3 for prolonged duration.[20, 37]

PL and Raman spectral analysis are two effective ways to measure the size distribution of the NCs indirectly due to the QC and phonon confinement effects, respectively. PL peak position is related to the size of the Si NCs by eqn. (10), where C´ = 3.58 eV/nm^2 and α´ = 0.52. From eqn. (10), taking equivalent circular cross-section, diameter distribution of the Si NCs can be expressed as:

$$D = \frac{2}{\sqrt{\pi}}\left(\frac{E_{NC}-1.12}{3.58}\right)^{(-0.96)}, \quad \text{..... (5.11)}$$

We attempt to fit the PL spectra in Fig. 5.8(a) for different samples using the eqn. (5.10) and fit these spectra with typical log-normal curve considering that the size distribution of Si NCs is skewed symmetric.[20] The maximum possible errors in fitting of D_0 and σ are 0.02 nm and 0.004 nm, respectively.[20] We attempt to fit the experimental Raman data in Fig. 5.3(b) by the eqn. (5.5) and for a suitable choice of D_0 and σ, best fitted curves are obtained.[20] Fig. 5.9(a-d) show a comparison of the calculated size distribution of the Si NCs from the Raman & PL data, in terms of the D_0 for the samples M1, M2, M3 and M4, respectively.[20] Assuming equivalent circular cross-section of the Si NCs, the size distribution of the Si NCs for various samples are calculated from HRTEM analysis and are shown in Fig. 5.9(a-d) for comparison.[20] Table 5.1 shows the calculated values of D_0 and σ of the size distribution of the Si NCs in each case.[20] The calculated size distributions of the Si NCs analyzed from NIR PL of all the samples are also shown in Fig. 5.10.[20] The NIR PL intensity is low and the Si NCs responsible for the NIR PL are quite large and unlikely to produce any significant Raman peak shift and broadening.[20] If the density of ultra-small (<2 nm) Si NC's is too low, the scattering intensity is too low to affect the

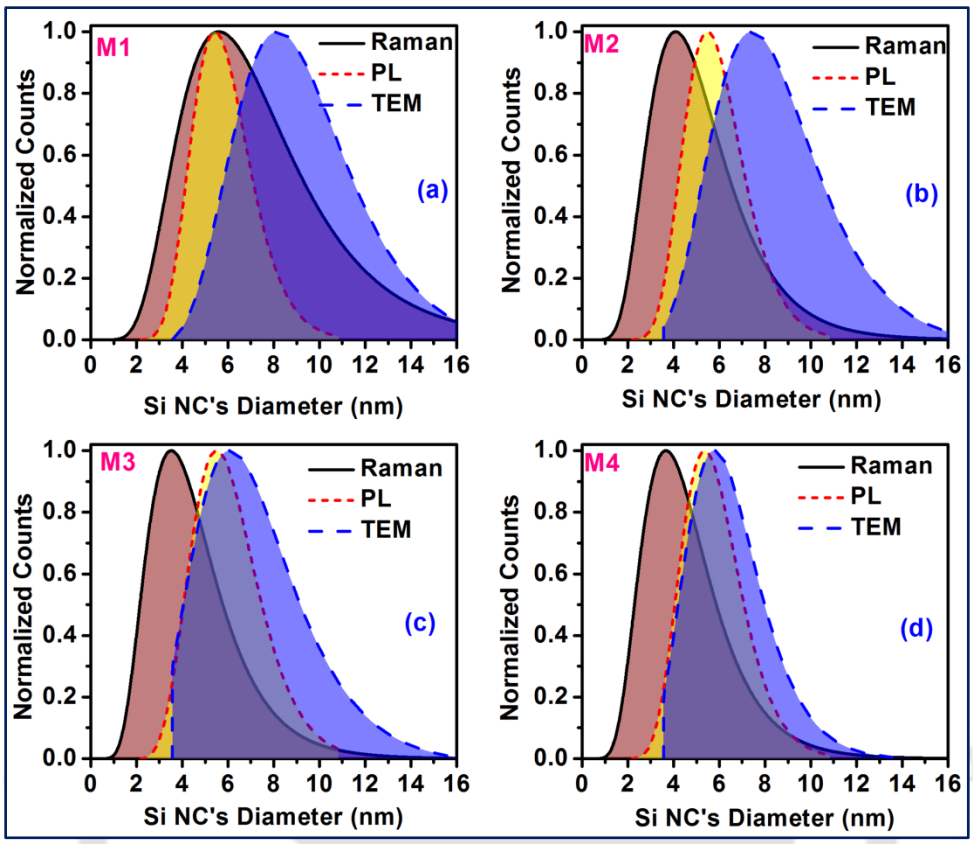

Fig. 5.9. Comparison of the size distribution (D_0, σ) of the Si NCs calculated from the Raman spectrum, PL spectrum and TEM images (assuming equivalent circular cross-section of the Si NCs) for (a) M1, (b) M2, (c) M3 and (d) M4, respectively.

Raman spectra and the small Si NCs are not clearly visible from the TEM images either.[20] However, the Raman spectrum is very sensitive to the size of the Si NCs in the quantum size range and significant shift as well as broadening in the 1st order peak can be observed due to the presence of the small Si NCs (<2 nm) due to the phonon confinement effect. So, when the sizes of the Si NCs are very small, estimation of the sizes from Raman spectra is more accurate.[20] For comparatively larger Si NCs, PL spectrum is more sensitive than the Raman spectrum, because PL emission energy $\propto D^{-1.04}$ (see eqn. (5.11)), while Raman peak shift $\propto D^{-2}$ (see eqn. 5.8c).[20] Similarly, Raman peak intensity is $\propto D^{-3}$ and FWHM $\propto D^{-4}$ (see eqn. (5.8)).[20] So, the Si NCs with comparatively larger size (>6 nm) will have more pronounce effect on the PL spectra as compared to the Raman spectra.[20] Thus, a proper estimation of Si NCs size distribution is difficult, purely from Raman or PL or TEM analysis independently. Therefore, combining the size distribution of Si NC's estimated from the Raman analysis and the same analyzed from the visible-NIR PL spectra give a better estimate of actual size distribution.[20] It may be noted the

sizes obtained from HRTEM analysis are typically higher than the sizes obtained from Raman and PL analysis. This is due to the fact that crystallite sizes are usually smaller than the grain

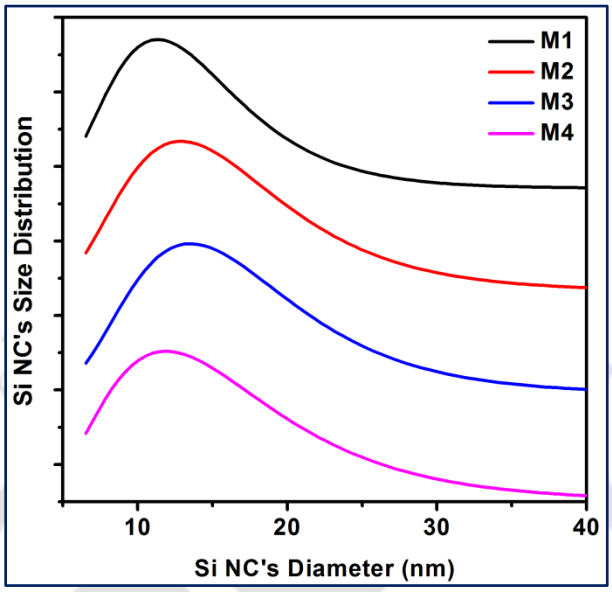

Fig. 5.10. The Comparison of the calculated normalized size distribution of the Si NCs on the surface of the Si NWS in terms of their D of the samples M1, M2, M3 and M4 respectively, which are obtained from the respective NIR PL spectrum. The curves are vertically shifted to enable comparison.

sizes determined from the microscopic techniques.[20] Further, if we consider the NIR PL to calculate the size distribution, the average size will turn out to be high than that found only from the visible PL spectrum. Thus, the PL and HRTEM analysis are consistent.

5.7. Conclusion

In this chapter, we have presented a clear correlation between the Raman and PL spectra of Si NCs decorated on Si NWs array grown by a MACE method. With increasing etching duration the porosity of the Si NWs and the density of the Si NC's increase, while mean diameter of the Si NC's decreases and positivity of skewness increases. This causes an increase in intensity the visible PL peak and decrease in NIR PL, while the Raman peak is shifted to lower energy with asymmetric broadening and a decrease of 1st Raman peak intensity. Raman and PL results are quantitatively analyzed using the phonon and electron confinement models, respectively and the correlation between two was shown to be fairly good. The size distributions of Si NCs are estimated in terms of the mean diameter and skewness from the PL and Raman spectra and compared with the size distribution obtained from the HRTEM analysis. Such a

correlation between Raman and PL spectra allows spectroscopic evaluation of the accurate size distribution of the Si NCs on the surface of the Si NWs even for arbitrary shaped Si NCs.

References

1. Ke, W.; Feng, X.; Huang, Y. *J. Appl. Phys.,* **2011,** 109, 083526-5.
2. Faraci, G.; Gibilisco, S.; Pennisi, A. R.; Faraci, C. *J. Appl. Phys.,* **2011,** 109, 074311.
3. Piscanec, S.; Cantoro, M.; Ferrari, A. C.; Zapien, J. A.; Lifshitz, Y.; Lee, S. T.; Hofmann, S.; Robertson, J. *Phys. Rev. B,* **2003,** 68, 241312.
4. Compaan, A.; Lee, M. C.; Trott, G. J. *Phys. Rev. B,* **1985,** 32, 6731.
5. Richter, H.; Wang, Z. P.; Ley, L. *Solid State Commun.,* **1981,** 39, 625.
6. Faraci, G.; Gibilisco, S.; Russo, P.; Pennisi, A. R.; La Rosa, S. *Phys. Rev. B,* **2006,** 73, 033307.
7. Cheng, W.; Ren, S. F. *Phys. Rev. B,* **2002,** 65, 205305.
8. Chen, Y.; Peng, B.; Wang, B. *J. Phys. Chem. C,* **2007,** 111, 5855.
9. Hessel, C. M.; Wei, J.; Reid, D.; Fujii, H.; Downer, M. C.; Korgel, B. A. *J. Phys. Chem. Lett.,* **2012,** 3, 1089.
10. Arguirov, T.; Mchedlidze, T.; Kittler, M.; Rölver, R.; Berghoff, B.; Först, M.; Spangenberg, B. *Appl. Phys. Lett.,* **2006,** 89, 053111.
11. Sahoo, S.; Dhara, S.; Mahadevan, S.; Arora, A. K. *J. Nanosci. Nanotechnol.,* **2009,** 9, 5604.
12. Ghosh, R.; Giri, P. K.; Imakita, K.; Fujii, M. *J. Alloy Compd.,* **2015,** 638, 419.
13. Ghosh, R.; Giri, P. K.; Imakita, K.; Fujii, M. *Nanotechnology,* **2014,** 25, 045703.
14. Kuznetsov, A. S.; Shimizu, T.; Kuznetsov, S. N.; Klekachev, A. V.; Shingubara, S.; Vanacken, J.; Moshchalkov, V. V. *Nanotechnology,* **2012,** 23, 475709.
15. Ledoux, G.; Guillois, O.; Porterat, D.; Reynaud, C.; Huisken, F.; Kohn, B.; Paillard, V. *Phys. Rev. B,* **2000,** 62, 15942.
16. Ghosh, R.; Giri, P. K. *Adv. Sci. Lett.,* **2016,** 22, 71.
17. Ghosh, R.; Imakita, K.; Fujii, M.; Giri, P. K. *Phys. Chem. Chem. Phys.,* **2016,** 18, 7715.
18. Ghosh, R.; Giri, P. K. *RSC Adv.,* **2016,** 6, 35365.
19. Ghosh, R.; Giri, P. K. *Sci. Adv. Today,* **2016,** 2, 25230.
20. Ghosh, R.; Pal, A.; Giri, P. K. *J. Raman Spec.,* **2015,** 46, 624.
21. Ilker, D.; Sanden, V. d.; Mauritius, C. M. *J. Appl. Phys.,* **2013,** 114, 134310.
22. Hochbaum, A. I.; Gargas, D.; Hwang, Y. J.; Yang, P. *Nano Lett.,* **2009,** 9, 3550.
23. Pal, A.; Ghosh, R.; Giri, P. K. *Appl. Phys. Lett.,* **2015,** 107, 072104.
24. Cai, Q.; Li, L. H.; Yu, Y.; Liu, Y.; Huang, S.; Chen, Y.; Watanabe, K.; Taniguchi, T. *Phys. Chem. Chem. Phys.,* **2015**.
25. Dey, P. P.; Khare, A. *Appl. Surf. Sci.,* **2014,** 307, 77.
26. Khajehpour, J.; Daoud, W. A.; Williams, T.; Bourgeois, L. *J. Phys. Chem. C,* **2011,** 115, 22131.
27. Adachi, M. M.; Anantram, M. P.; Karim, K. S. *Nano Lett.,* **2010,** 10, 4093-4098.
28. Khorasaninejad, M.; Walia, J.; Saini, S. S. *Nanotechnology,* **2012,** 23, 275706.
29. Hart, T. R.; Aggarwal, R. L.; Lax, B. *Physical Review B,* **1970,** 1, 638-642.
30. Compaan, A.; Lee, M. C.; Trott, G. J. *Physical Review B,* **1985,** 32, 6731-6741.
31. Piscanec, S.; Cantoro, M.; Ferrari, A. C.; Zapien, J. A.; Lifshitz, Y.; Lee, S. T.; Hofmann, S.; Robertson, J. *Physical Review B,* **2003,** 68, 241312.
32. Gouadec, G.; Colomban, P. *Prog. Cryst. Growth Charact. Mater.,* **2007,** 53, 1.
33. Olivero, J. J.; Longbothum, R. L. *J. Quant. Spectrosc. Radiat. Transfer,* **1977,** 17, 233.

34. Gan, L.; Sun, L.; He, H.; Ye, Z. *J. Mater. Chem. C,* **2014,** 2, 2668.
35. Suzuki, T.; Skuja, L.; Kajihara, K.; Hirano, M.; Kamiya, T.; Hosono, H. *Phys. Rev. Lett.,* **2003,** 90, 186404.
36. Valenta, J.; Bruhn, B.; Linnros, J. *Nano Lett.,* **2011,** 11, 3003.
37. Osminkina, L.; Gonchar, K.; Marshov, V.; Bunkov, K.; Petrov, D.; Golovan, L.; Talkenberg, F.; Sivakov, V.; Timoshenko, V. *Nanoscale Res. Lett.,* **2012,** 7, 524.
38. Lin, G. R.; Lin, Y. H.; Pai, Y. H.; Meng, F. S. *Opt. Exp.,* **2011,** 19, 597.

Chapter 6

The Visible Light Photocatalytic Performance of the Mesoporous Si Nanowires

Photocatalysis has attracted much interest because of its potential application in clean energy production and to degrade organic pollutants for water purification. Si NW is an ecofriendly, photostable, inexpensive and nontoxic material and is able to utilize near UV, visible and NIR light for the degradation of organic pollutants. In this chapter, we have shown that the photogenerated excitons within the mesoporous Si NWs grown by metal assisted chemical etching (MACE) could be energetic enough to drive applicable photoelectrochemical reactions for the degradation of organic dyes. The Si-H bonds present on the surface of the Si NWs/NCs facilitate the visible light photocatalytic activity by efficient separation of photogenerated e-h pairs. We have studied the effect of growth conditions of Si NWs/NCs on the photodegradation performance of the Si NWs/NCs. We also address the issue of simultaneous photoluminescence (PL) and photocatalysis from the same Si NWs/NCs grown by MACE.

6.1. Introduction

Photocatalysis by semiconductors has attracted much interest because of its potential application in clean energy production and degradation of organic pollutants in water. Mainly wide bandgap semiconductors (e.g., TiO_2) are commonly used as photocatalysts because of their wide ranging band gaps and stability towards chemical and photochemical corrosion. Si NW is an ecofriendly, photostable, inexpensive and nontoxic material and is able to absorb near UV, visible and NIR light for the degradation of organic pollutants.[1-7] High aspect ratio Si NCs decorated Si NWs with Si-H terminated surface grown by MACE have shown excellent photocatalytic nature under visible light illumination.[1-8] Earlier studies suggest that Si-H bonds present on the surface of Si NWs/NCs serve as the photoelectrochemical reaction centers during photodegradation.[1-8] In addition, ultralow reflection/ broadband absorption over the entire visible range and the unaltered metal NPs during etching also contribute to the photocatalytic efficiency of MACE grown Si NWs/NCs.[2, 3, 7] However, the MACE grown Si NWs/NCs have shown efficient PL and excellent photocatalytic activity and due to this, MACE grown Si NWs have drawn significant attention

for the energy and environmental applications.[1-14] Therefore, it is very important to understand the origin of enhanced visible-NIR PL and visible light photocatalysis from the same Si NWs/NCs sample. We focus on the origin of excellent visible light photocatalysis by MACE grown Si NWs and its dependence on various etching conditions. These results open up the possibility of using the MACE grown Si NWs array for light emitting diodes, solar cell, organic waste treatment and hydrogen production by photocatalytic water splitting etc.

6.2. Visible Light Photocatalysis

6.2.1. Sample Preparation for Photocatalysis Studies

The Si NWs/NCs samples were grown by MACE process. We have used both single-step and two-step MACE process for the growth of Si NWs. The details of the growth technique and growth parameters are described in *Chapter 2, Section 2.1* and the corresponding sample codes have been provided in the same *Section.* We have also tuned the (a) nature of the noble metal, (b) the etching solution and its concentration, (c) the doping type, resistivity and the orientation of the Si wafer and (d) etching duration for understanding their effect in the photocatalytic performance of the Si NWs/NCs.

6.2.2. Photocatalysis Setup

Photocatalytic efficiency of the Si NWs samples was carried out in a commercial photochemical reactor (Lelesil Innovative Systems, Mumbai). A time programmable visible lamp (Xe lamp, 250 W) was used for illuminating the sample with excitation wavelength 390-730 nm. The photograph of the photochemical reactor is shown in Fig. 2.17 in *Chapter 2*. Methylene Blue (MB) and Methyl Orange (MO) were used as the target dye molecules for the photodegradation.

6.2.3. Photodegradation Procedure

At first, a 100 mL aqueous solution of organic dye was made with 10^{-5} M concentration. The solution was stirred at moderate speed with a magnetic stirrer for an hour under dark condition. For the degradation study, a small piece (area ~1.5 cm^2) of Si NWs sample was kept in a beaker (size 500 mL) containing 100 mL of 10^{-5} M solution and it was exposed to visible light for a defined time duration inside the photochemical reactor. We have used a stirrer at slow speed for the circulation of the solution. 5 mL of dye solution was taken out at an interval of 20 min. The illumination process was continued upto 200 minutes. We have recorded UV-vis absorption

spectra of the dye solution collected at a regular interval in a Shimadzu 2450 UV-vis spectrophotometer. The photodegradation analysis was performed by using the highest intensity absorption peak as the reference for the reference dye in the visible range. The photo degradation performance of a bare Si wafer with same size was also checked as the blank sample. We have also performed the photocatalytic experiment using the industry standard photocatalyst P25 (TiO_2) under the identical condition.[15] Fig. 6.1 shows the FESEM (a) top view and (b) cross-

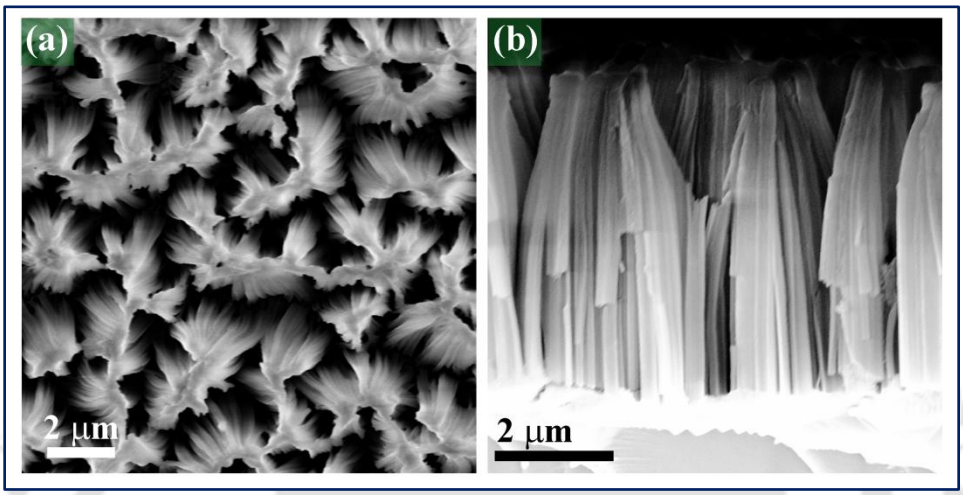

Fig. 6.1. FESEM (a) top-view and (b) and cross-sectional view images of Si NW in S1HF5.

sectional image of the sample S1HF5. We have calculated the NWs covering area ~119.63 μm^2 in Fig. 6.1(a) and length of the Si NWs is ~5.52 μm in Fig. 6.1(b) using ImageJ software. So the amount of the Si NWs (for sample S1HF5, surface area 1.5 cm^2) used as photocatalyst is ~1.32 mg. As the P25 available in powder form, we have taken the same amount of P25 for the comparison of the photodegradation efficiency of our sample.

6.3. Visible Light Photocatalysis of Methylene Blue (MB)

When a photon with energy equal to or greater than the band gap of the Si NWs/NCs reaches the catalyst's surface, it results in the generation of an electron in the conduction band and a hole in the valence band. The induced hole receives an electron from the adsorbed water and results in •OH free radical groups, which is mostly responsible for the degradation of the MB in aqueous solution.[2, 7, 8, 16] Fig. 6.2 shows the photodegradation of MB under visible light illumination in presence of the Si NWs/NCs photocatalysts. Fig. 6.2 depicts the UV-vis absorbance spectra of MB at an interval of 20 min of illumination using photocatalysts: (a) bulk Si, (b) sample S1HF5 and (c) sample S2HF5. It is clear that the Si NWs show excellent photodegradation of MB under

visible light illumination as compared to that of bulk Si. Digital photographs of the change in MB color (decoloration) due to the photodegradation at an interval 20 min for S1HF5 and S2HF5 are shown in Fig. 6.2(d) and (e), respectively. It is believed that the electron-deficient Si-H surface states present on the samples serve as an electron sink and hence accelerate the separation of photoinduced e-h pairs, which facilitate the photocatalytic activity of the Si NWs/NCs.[2, 7] Finally, the reactive •OH radicals oxidize and degrade the MB by destructing the

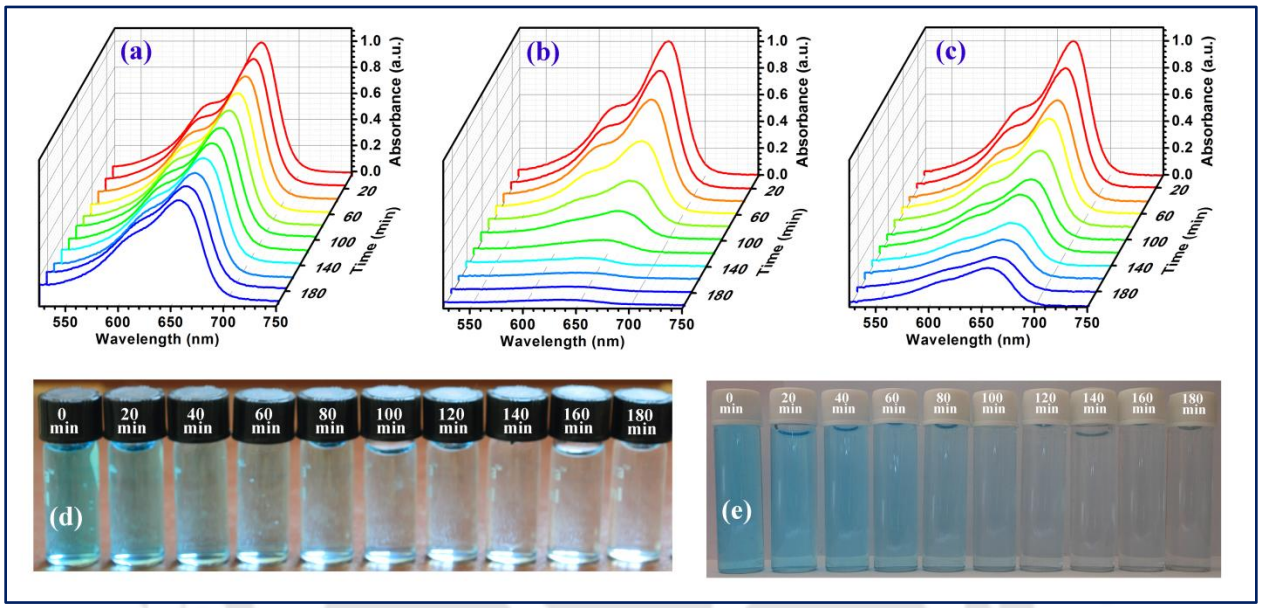

Fig. 6.2. Photodegradation of MB: UV-vis absorbance spectra of MB at an interval of 20 min of light exposure using photocatalyst (a) bulk Si, (b) sample S1HF5 and (c) sample S2HF5. Digital photograph of MB solution collected in an interval of 20 min during photodegradation by samples (d) S1HF5 and (e) S2HF5.

chain of the organic molecule. [2, 7, 8, 16] Our XPS, FTIR and Raman (discussed in *Chapter 3*) spectra confirm that the Si-H bonds are present on the Si NCs/NWs and XPS spectra along with PL analysis confirm that the SiO_x over layer contains NBOHC defectes (discussed in *Chapter 4*). This is consistent with the earlier reports.[7, 8, 16] It has been reported that H-terminated Si NCs covered by Si sub-oxide is possibly the best Si based photocatalyst compared to the other Si structure (bulk Si and Si nanostructure).[7] Kang et al reported photocatalytic activity of size controlled Si quantum dots (Si QDs) that exhibited tunable emission from near-infrared to blue wavelength.[17]

Note that the metal NPs present (confirmed from the EDX, XRD and XPS analyses discussed in C*hapter 3*) within pores between the Si NWs and on the surface of the Si NCs can also enhance the photocatalytic activity.[2, 7] Because of the differences in their Fermi levels, it can

introduce a Schottky barrier between the metal NPs and Si NWs/NCs. The built-in potential at the Schottky diode junction can facilitate the efficient separation of photogenerated e-h pairs and influence the degradation of the dye strongly.[2, 7] Furthermore, the electronegativity of the noble metals (Au, Ag or Ag/Au bimetal) is higher than that of Si.[2] Hence, these metal NPs can accelerate the separation of photoinduced e-h pairs better, which can increase the photocatalytic activity of the mesoporous Si NWs.[2, 3, 7, 8] It is clear from Fig. 4.12, *Chapter 4*, that the MACE grown Si NWs/NCs show ultralow reflectance, i.e., very high absorption over the entire visible range. This could also contribute to the enhanced photocatalytic activity in case of MACE grown Si NWs.[2, 7] Similarly, SPR related broad visible absorption due to the unaltered metal NPs can also function as the catalysts to facilitate certain redox reactions to degrade MB dye.[2, 7, 16] In the present experiment, we used a small piece of Si NW/NCs sample compared to the total volume of the MB dye. If bigger size of NW/NC sample is used, higher efficiency degradation can be achieved from the MACE grown Si NWs/NCs.

6.4. Effect of Different Growth Parameters on the Photocatalytic Performance

The photodegradation efficiency of the Si NWs/NCs samples strongly depends on the morphology of the as-grown samples and the surface properties. In this *section*, we will explain the effect of the different etching parameters on the photocatalytic properties of the Si NWs/NCs samples, such as (a) etching duration, (b) content of etching solution, (c) etching solution concentration, (d) doping type and doping density of the Si wafer (from which the Si NWs/NCs are grown) and (e) the nature of noble metal used for MACE. However, there are several possible reasons behind the enhanced photodegradation performance of the Si NWs/NCs, such as:

1. Enhanced surface area
2. Tunable bandgap and enhanced absorption range
3. Amount of dye and amount of the catalyst
4. Carrier exchange in the interface of the material
5. Ionic condition of the dye as well as the material

6.4.1. *Etching Duration*

Note that the photocatalytic activity of the Si NWs/ NCs samples strongly depends on the surface area of the Si NWs/NCs in contact with the MB solution. The length of the Si NWs increases

linearly with the etching (MACE) duration and we have studied the photocatalytic efficiency of the Si NWs grown for different etching duration keeping the etchant concentration unaltered.[7, 10, 18] Fig. 6.3 shows the comparison of the photodegradation efficiency of sample S1HF5 grown for different etching duration (5, 10, 15 and 20 min). Higher etching duration causes higher length of the NWs, higher surface area and higher density of Si NCs, which result in enhanced absorption

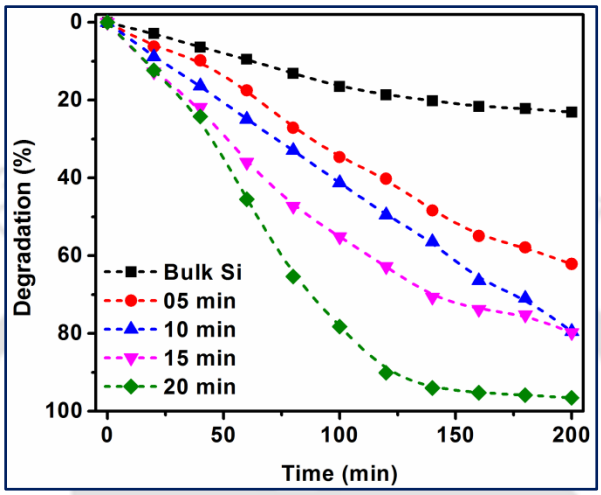

Fig. 6.3. Comparison of the photodegradation efficiency of Si NWs grown for 5, 10, 15 and 20 min in H_2O_2/HF solution (2:5 volume ratio) with that of the bulk Si.

and creation of more e-h pairs finally leading to the higher photodegradation efficiency.[2, 7, 9, 10] A mean surface area of 448.648 m^2/g was obtained for the sample S1HF5 from the multi-point Brunauer-Emmett-Teller (BET) analysis (*Section 3.5.1, Chapter 3*), which is very high compared to the results obtained by Qu et al.[16] and Zhong et al.[19] for mesoporous Si NWs. Note that this high surface area and high porosity indicate the high density of H-bonded sites on the Si NWs/NCs in contact with the dye molecule. As a result, the photodegradation efficiency is higher for the Si NWs samples etched for larger duration.[7] The enhanced absorption due to the higher length and higher density of Si NCs (as shown in Fig. 4.12, *Chapter 4*) also results in the increased photodegradation efficiency of the respective samples.

6.4.2. *Etching Solution*

It is noted that surface properties are different for the Si NWs/NCs grown in different etching solution, as discussed in the previous chapters. The surface states have strong influence on the photodegradation properties of the Si NWs/NCs in contact with the MB solution. We have studied the photodegradation behavior of the Si NWs/NCs grown in HF/$AgNO_3$ (sample Q) and

HF/H_2O_2 (Sample S1HF8) solution. Fig. 6.4 shows a comparison of the photodegradation performance of these two samples including that of the bulk Si. It is clear that the sample S1HF8 shows higher degradation efficiency as compared to the sample Q although the length of the sample Q (~14 µm) is ~4 times higher than that of S1HF8 (~3.5 µm). Note that we got enhanced absorption (Fig. 4.12(a), *Chapter 4*) over the entire visible range for the sample S1HF8 as compared to that of sample Q.[10] Therefore, it can be concluded that higher absorption & the higher density of Si-H bonds in S1HF8 are responsible for the improved photocatalytic performance of the corresponding Si NWs/NCs.

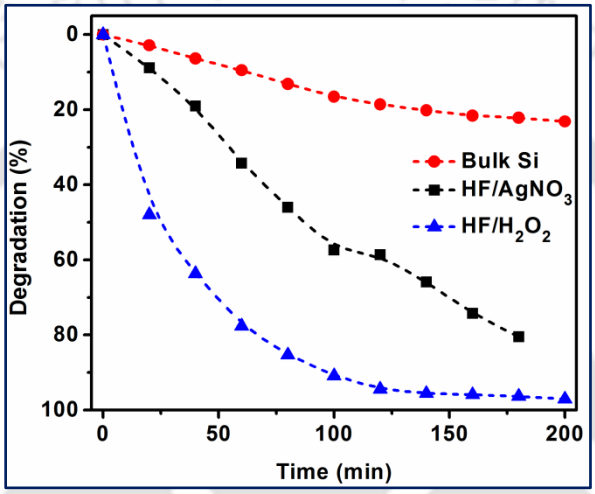

Fig. 6.4. Comparison of the photodegradation efficiency as a function of time for Si NWs grown in different etching solutions.

6.4.3. *Etchant Concentration*

The etchant concentration has strong effect on the morphology and surface features of the Si NWs. In order to understand its effect in the photocatalytic performance, we have performed the photodegradation experiments for the Si NWs samples grown with different concentration of etchants. Fig. 6.5(a) shows the comparison of the visible light photodegradation of MB in presence of Si NWs grown by using different concentration of HF keeping the H_2O_2 amount fixed (group S1).[7] Fig. 6.5(b) shows the same for group S2.[7] In the present case, in both type of samples S1 and S2, the photocatalytic efficiency increases with the increase in HF concentration during etching.[7] Higher concentration of HF causes higher density of Si-H bonds and it results in higher degradation efficiency.[7] As discussed before, the surface properties of the etched Si NWs/NCs depend upon the formation and dissolving rate of Si oxide formed at the etching front, which is not same for different HF concentration. At lower HF concentration, the dissolving rate

of Si oxide formed at the etching front is slow. Owing to the undissolved Si oxide, the NBOHC defect density is higher at lower concentration of HF.[7] As a result, the PL intensities would be higher for the samples grown using lower HF concentration (*Section 4.5(b), Chapter 4*).[2, 7] When the HF concentration is high enough, excess amount of H^+ ions are available in the solution to dissolve the Si oxide formed at the etching front. The extra H^+ ions bind with the Si surface to form Si-H bonds, which are responsible for the dye degradation. The formation rate of H^+ ions is higher for higher HF concentration and thus the H-terminated surface, which results in better efficiency for the MB degradation.[7]

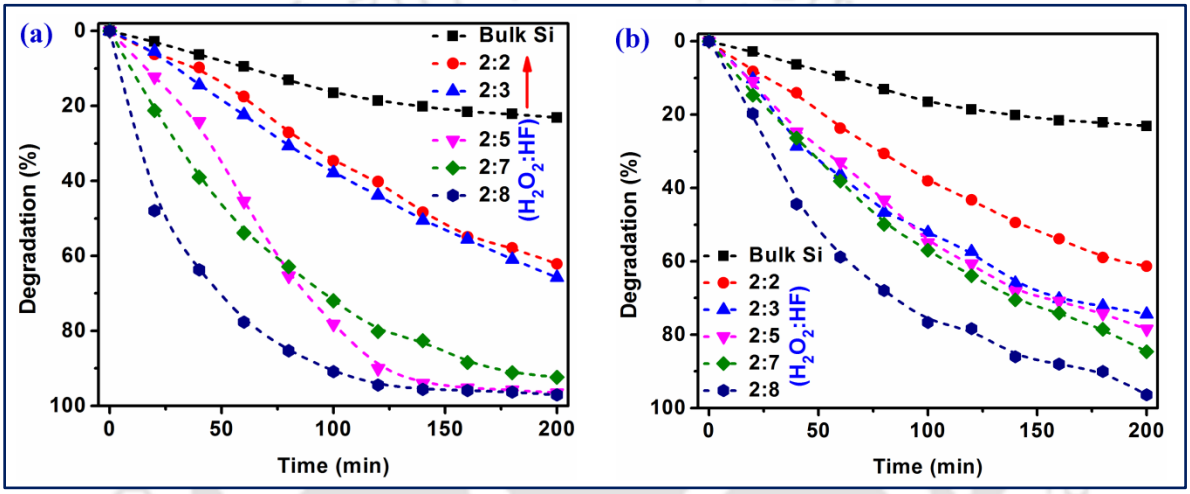

Fig. 6.5. Comparison of the visible light photodegradation of MB in presence of Si NWs/NCs for group: (a) S1 and (b) S2.

6.4.4. *Si Wafer Resistivity*

Fig. 6.6 depicts a comparison of the photodegradation efficiency of the samples as a function of relative HF concentration (volume fraction) for different wafer resistivity (0.01 Ω-cm i.e. samples in group S1 and 0.001 Ω-cm i.e. samples in group S2) keeping the other parameters of etching identical. The degradation of MB was marked after 60 min light illumination. It is clear that the photodegradation efficiency is higher for higher resistivity (group S1) when the HF concentration is relatively high (>4 mL).[7] It is already mentioned that the dopant sites may act as the nucleation sites for the sidewall etching of the Si NWs. Therefore, when the doping density is low (sample in group S1), the formation rate of Si oxide at the etching front is relatively low and excess amount of H^+ ions available in the solution attack the Si surface to form Si-H bonds.[7] Thus, enhanced efficiency in MB degradation is observed in higher resistivity Si NWs as compared to the lower resistivity Si NWs.[7] Note that the photodegradation efficiency is slightly

lower for higher resistivity case (group S1) when the HF concentration is very low (<5 mL). We have observed an incomplete growth of Si NWs with higher resistivity wafers, when the HF

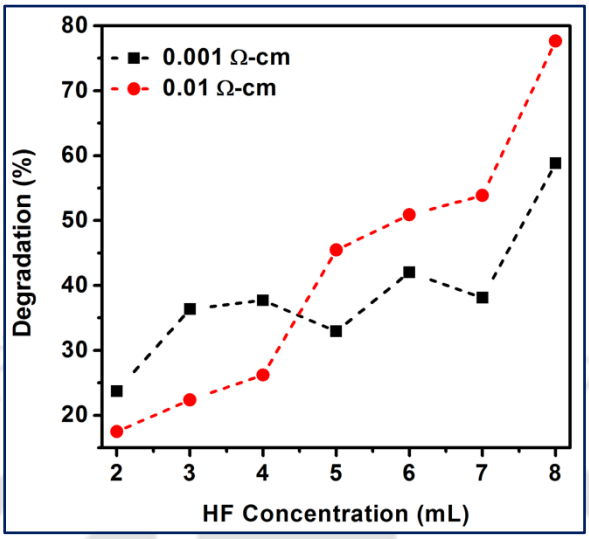

Fig. 6.6. Comparison of the photodegradation efficiency of the Si NW samples as function of relative HF concentration (volume fraction) for different resistivity Si wafers. The degradation of MB was measured after 60 min light illumination.

concentration is low (Fig. 3.12, *Chapter 3*). On the other hand, the length of the Si NWs in group S2 is higher than that of group S1 at each HF concentration (Table 3.2, *Chapter 3*). As a result, the enhanced surface area in group S2 is responsible for the slightly enhanced photodegradation efficiency in case of sample of group S2 when the HF concentration is very low. Note that the photodegradation efficiency is higher for the samples of group S1 than that of in group S2 at higher HF concentration. Higher formation rate of H^+ ions than the formation rate of Si oxide at the etching front is mainly responsible for this (the formation rate of Si oxide is higher in case of lower resistivity wafer).

6.4.5. *Nature of Noble Metals during MACE Growth*

The effect of different noble metals in the morphology of the Si NWs/NCs is discussed in *chapter 3*. In *Chapter 4, Section 4.5.1,* we have shown the superiority of the sample AgAuSi in PL properties as compared to the samples AgSi and AuSi. However, the photogenerated excitons within the mesoporous Si NWs for sample AgAuSi could be energetic enough to drive applicable photoelectrochemical reactions due to its wide range of optical absorption with high intensity. Fig. 6.7 shows a comparison of the photocatalytic degradation efficiency of MB for AgSi, AuSi, AgAuSi and bulk Si wafer under visible light illumination for 1 hr.[2] In this case, a small piece

(0.8 cm^2) of sample containing Si NWs/NCs was put in a beaker containing 25 mL of MB solution and it was exposed to visible light (390-720 nm) for 1 hour continuously. However, in the present case, AgAuSi shows the highest photodegradation (~43 % in 1 hr) of MB compared

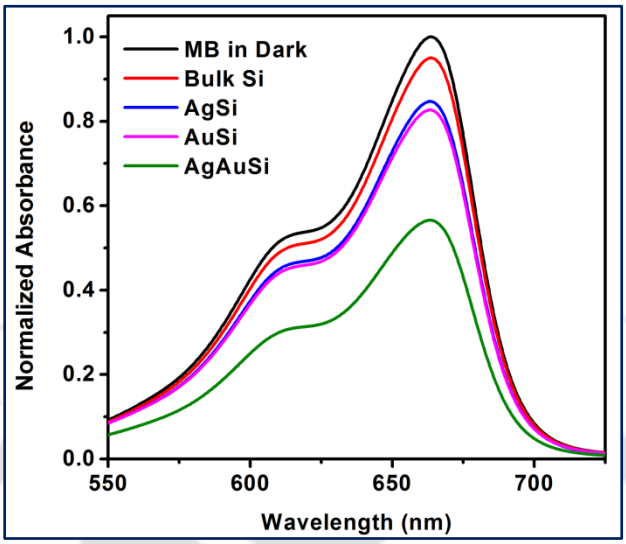

Fig. 6.7. Comparison of the photo degradation of MB by AgSi, AuSi and AgAuSi with that of the bulk Si wafer under 1 hour visible light illumination.

to that of AgSi (~15 %) or AuSi (~18 %).[2] It was shown earlier (Fig. 3.12, *Chapter 3*) that the aspect ratio of the Si NWs is highest for AgAuSi case as compared to the other samples. On the other hand, the NWs growth is incomplete for the sample AgSi and AuSi. Due to large surface area of Si NWs covered with high density of Si NCs, the density of Si-H is higher in AgAuSi as compared to the other samples where NW growth is incomplete and this is believed to give rise to efficient photocatalysis by AgAuSi.[2] As discussed above (*Section 6.3*), the metal NPs (Ag, Au and AgAu) (as shown in XPS spectra, Fig. 3.20, *Chapter 3*) present within pores between the Si NWs and on the surface of the Si NCs can enhance the photocatalytic activity.[2] Furthermore, the electronegativity of Au is higher than that of Ag or Si. Hence, Au or Ag/Au bilayer can accelerate the separation of photoinduced e-h pairs better, which can increase the photocatalytic activity of the nanoporous Si NWs.[2, 3, 8] It is clear from Fig. 4.12(c), *Chapter 4*, that the AgAuSi possesses ultralow reflectance as compared to the AgSi and AuSi, i.e., very high absorption over the entire visible range. The results clearly demonstrate that the Ag/Au bilayer assisted grown Si NWs are much more efficient photocatalysts than the Ag or Au assisted grown Si NWs.[2] Furthermore, the Ag/Au NPs shows SPR related broad visible absorption and these metal NPs

can also function as the catalysts to facilitate certain redox reactions to degrade the organic pollutants.[2, 16]

6.5. Visible Light Photocatalysis of Methyl Orange (MO)

Photocatalytic efficiency depends on the ionic conditions of the dye as well as the sample. In the present study, Si-H primarily takes part in the photocatalysis, which is anionic in nature in presence of light. Note that MB is slightly cationic in nature. We have measured the photodegradation efficiency of the MACE grown Si NWs/NCs for the degradation of a dye of different ionic nature under identical condition as it was in case of MB. Methyl Orange (MO) is anionic in nature. Fig. 6.8 shows a comparison of the photodegradation performance of MB and

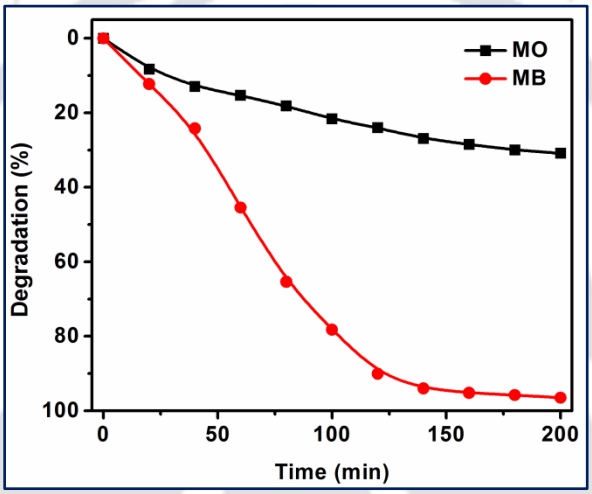

Fig. 6.8. Comparison of the photodegradation efficiency of MB and MO by S1HF5.

MO by S1HF5 under identical condition. It is evident that the photodegradation efficiency of the Si NWs/NCs photocatalyst is higher for the cationic dye MB as compared to the anionic dye MO.[2, 7] Since, in presence of light, Si-H is anionic there is columbic repulsion between the anionic MO molecules and anionic Si surface. Thus the adsorption rate of MO dye molecules at the Si surface is slower compared to that of MB, which results in the slower degradation of MO.

6.6. Photocatalytic Rate Constant

It is very convenient to compare the efficiency of different photocatalysts by the degradation rate constant (k). The photodegradation data follow the first-order rate kinetics and the corresponding rate constant k was obtained by fitting the concentration data to the rate equation:

$$ln(C_t/C_0) = -kt \quad \text{..... (6.1)}$$

where k is apparent rate constant, C_t is the actual concentration at time t, and C_0 the initial concentration of MB. We have calculated the rate constant for each sample in groups S1 and S2 and the results are shown in Fig. 6.9.[7] The photodegradation rate constant of the industry standard photocatalyst P25 (TiO_2) is also shown in Fig. 6.9.[15] It is clear from Fig. 6.9 that the value of k is higher for higher concentration of HF during MACE due to the stronger presence of H-terminated surface.[7] The k value is considerably higher for S1 group as compared to the S2 group ofsamples.[7] As discussed in *Section 6.4D,* enhanced efficiency in MB degradation was

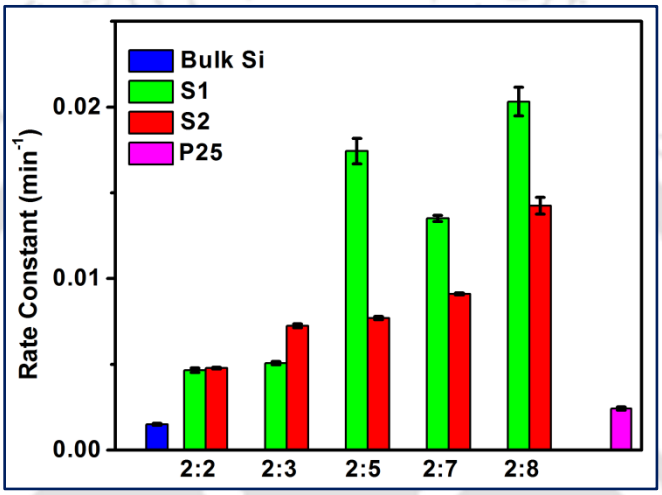

Fig. 6.9. Comparison of the photodegradation rate constant for S1 and S2 at different HF concentration. The rate constant of standard P25 measured in MB solution is also shown for comparison.

observed in higher resistivity Si NWs (samples S1) as compared to the lower resistivity Si NWs (samples S2) due to the higher density of Si-H bonds.[7] Similarly, We observed higher values of k in case of S1 as compared to that of S2.[7] Note that the increment in k value for increasing HF concentration is higher for S1 group as compared to the S2 group samples.[7]

Note that we have observed a change in the photodegradation efficiency with the length of the Si NWs (Fig. 6.3). We have calculated the rate constant k corresponding to the photodegradation data in Fig. 6.3 and plotted in the Fig. 6.10 as function of etching duration. It is clear that though the length of the Si NWs varies almost linearly with the etching duration, k increases sub-linearly with increasing etching time. If the photodegradation depends only on the surface area of the Si NWs/NCs, then the increment in k would follow a linear behavior. However, we notice a different behavior in k with etching time. Thus, photodegradation not only

depends on the surface area of the photocatalyst, but also of the surface states (in the present case Si-H bonds) as well as its density.

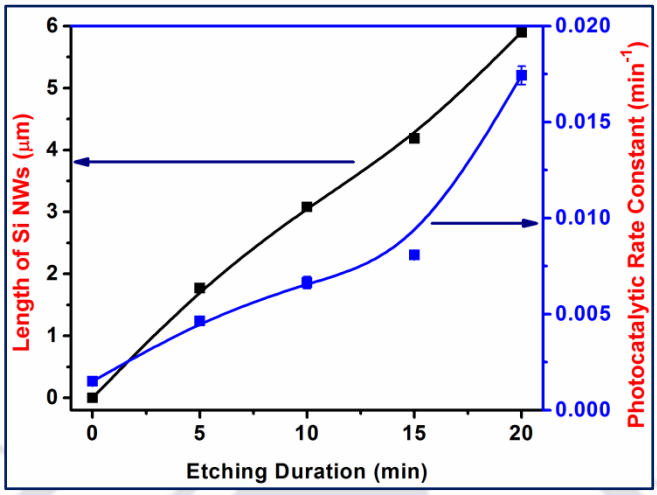

Fig. 6.10. Comparison of the photocatalytic rate constant and the length of the Si NWs as a function of etching duration. The symbols report the experimental data & the lines are drawn to guide the eye.

6.7. Surface Evolution of the Si NWs after Photocatalysis

It is clear that the H-terminated surface present on the surface of Si NWs/NCs are responsible for the efficient photocatalysis and it is expected that the H-terminated surface will be passivated by the Si oxide. For further confirmation, we have performed the structural analysis of the Si NWs/NCs photocatalyst before and after photocatalysis. Fig. 6.11(a-b) shows the comparison of the FTIR spectra for AgAuSi before and after (sample code AgAuSi_MB) photocatalysis of MB showing different vibrational modes in two different regions of wavenumbers.[2] FTIR spectra confirm that the Si-H bonds present in the Si NCs/NWs structure (as discussed in *Section 3.9.E, Chapter 3*) and the vibrational modes associated with the H-terminated surface of Si are eliminated partially after the photocatalysis.[2] It is also confirmed that the vibrational modes associated with the Si-O are enhanced. Fig. 6.11(c) depicts the comparison of the Raman spectra for AgAuSi before and after photocatalysis of MB, which confirms the presence of Si-H bonds.[2] It is consistent with the FTIR results that the vibrational modes associated with the H-terminated surface of Si are reduced but not fully eliminated after the photocatalysis.[2] Fig. 6.11 shows the comparison of the Si 2p core level XPS spectra for sample S1HF5 (d) and S2HF5 (e), before and after photodegradation of MB. In both samples, the peak corresponding to neutral Si is reduced and the peak corresponding to the Si oxide is enhanced. This confirms the formation of Si oxide and partial elimination of Si-H bonds after the photocatalysis. The FTIR, Raman and XPS results

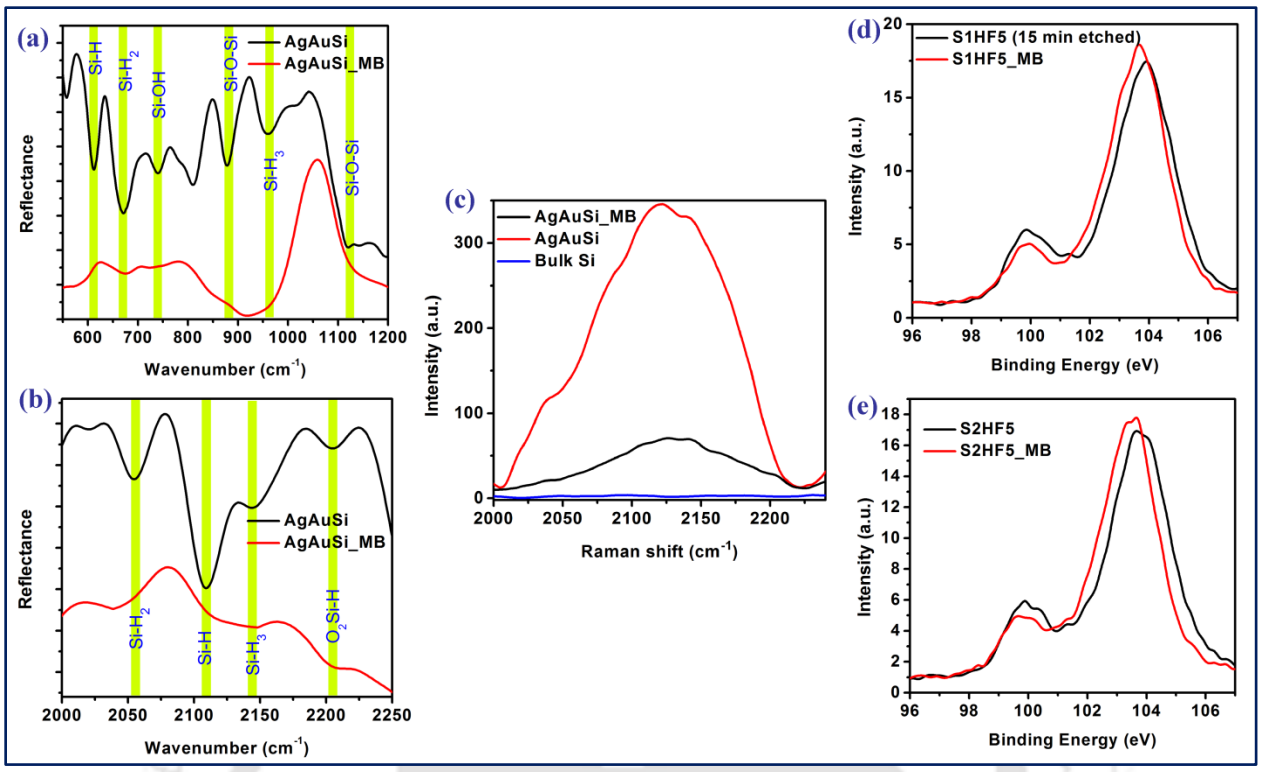

Fig. 6.11. (a-b) Comparison of the FTIR spectra for AgAuSi before and after the photocatalysis of MB showing different vibrational modes in two different regions of wavenumbers. The green vertical boxes indicate the position of the different characteristic modes of Si. (c) Comparison of the Raman spectra for AgAuSi before and after photocatalysis of MB. Comparison of the Si 2p core level XPS spectra for (d) sample S1HF5 and (e) S2HF5, before and after photodegradation of MB.

are consistent with our explanation that the excellent photocatalytic properties of the MACE grown Si NWs/NCs are mostly due to the Si-H bonds and partly due to the high absorption by the Si NWs/NCs. It is also confirmed that the Si-H bonds are reduced after photocatalysis, but not eliminated fully and this results in the recyclability of theses MACE grown Si NWs in photodegradation of the organic dyes, as discussed below.[7]

6.8. Recyclability of Si NW Photocatalyst

In order to evaluate the stability and recyclability of the photocatalyst (MACE grown Si NWs), the photodegradation of MB was repeated for multiple cycles. After each cycle, the sample is taken out and rinsed in DI water. Fig. 6.12(a) shows the comparison of photodegradation of MB in S1HF5 for different cycles.[7] It is clear from Fig. 6.12(a) that 96.5% MB is degraded in first cycle and 59.8% after 5th cycle.[7] Thus there is a reduction in photodegradation efficiency after

each cycles. This is because of the formation of Si oxide and elimination of Si-H surface states (as discussed in *Section 6.7*).[7] The FTIR, Raman and XPS results in *Section 6.7* confirm that the

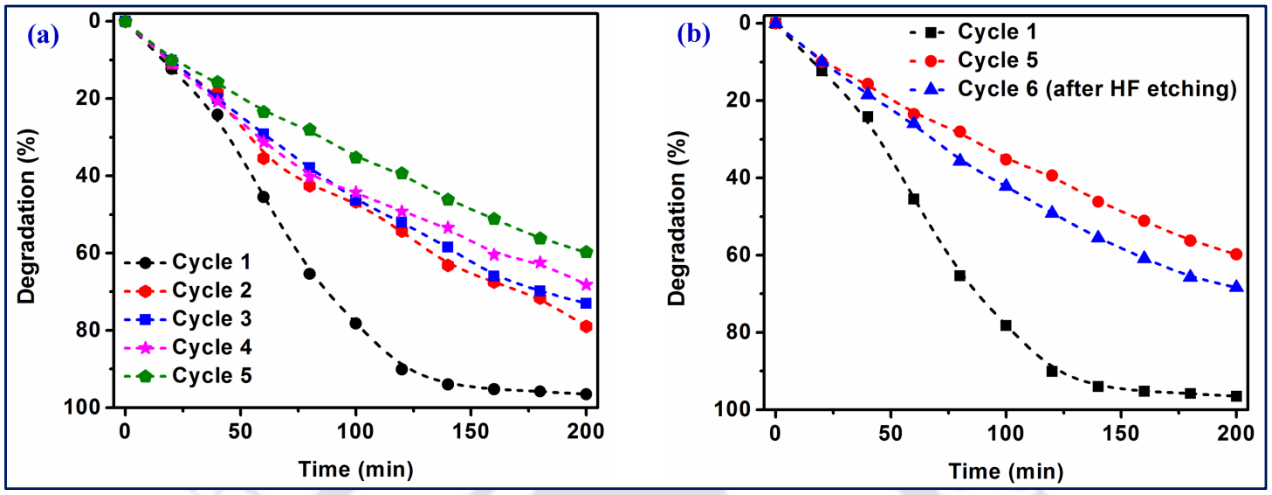

Fig. 6.12. (a) Comparison of the photodegradation of MB of sample S1HF5 for different cycle. (b) Improvement in the stability after HF etching.

Si-H bonds are reduced after photocatalysis. The unaltered H-terminated surfaces are responsible for the photodegradation of MB in case of later cycles.[7] The efficiency of the Si NWs/NCs photocatalyst decreases with the cycle number. It is well known that immersion of Si NWs in diluted HF solution results in partial removal of the oxide layer. Fig. 6.12(b) shows the increase in photodegradation efficiency after Si oxide removal by HF. Note that HF treatment creates new H-terminated Si surface, which can take active part in MB degradation.[7, 20] Thus, dilute HF treatment can partly recover the stability though the recovery is not full.

6.9. Illustration of Photocatalysis Mechanism using Energy Band Diagram

For a direct bandgap semiconducting material, a fast radiative recombination of the excited e-h pairs (in the form of PL), and an easy separation of the photoexcited e-h pairs with minimum recombination (photocatalysis) are equally likely. Efficient separation of photogenerated e-h pairs is very much necessary to facilitate enough redox reaction for the degradation of the dye. In case of the MACE grown Si NWs/NCs, the exchange of photogenerated e-h pairs is favorable due to the presence of Si-H bonds, which could lead to the enhanced photodegradation in those MACE grown Si NWs/NCs samples.[21] On the basis of the above demonstrated efficient photodegradation by MACE grown Si NWs/NCs samples under visible irradiation and other reports, a possible mechanism can be proposed. [1-8, 21] The schematic diagram of the MACE

grown Si NWs decorated with arbitrary shaped Si NCs along with the band alignment is shown in Fig. 6.13. The possible charge separation in presence of Si-H bonds and the dye degradation mechanism is also schematically illustrated in Fig. 6.13. The reaction mechanism is as follows:

$$Si \xrightarrow{h\nu} e^- + h^+ \quad \text{..... (6.2)}$$

$$Si\text{-}H + e^- + h^+ \longrightarrow Si\text{-}H + e^- + h^+ \text{ (separation of e-h pairs)} \quad \text{..... (6.3)}$$

$$H_2O \longrightarrow H^+ + OH^- \quad \text{..... (6.4)}$$

$$OH^- + h^+ \longrightarrow \bullet OH \quad \text{..... (6.5)}$$

$$\text{Organic dye} + \bullet OH \longrightarrow \text{degradation products} \quad \text{..... (6.6)}$$

When a photon with energy equal to or greater than the band gap of the Si NWs/NCs reaches the catalyst's surface, it results in the generation of an electron in the conduction band and a hole in the valence band. The Si-H bonds present in the samples serve as an electron sink and hence

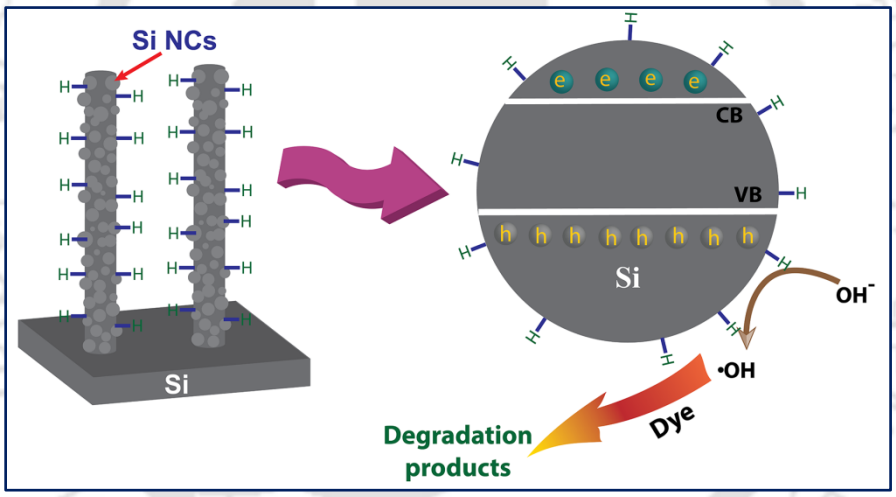

Fig. 6.13. Illustration of photocatalysis mechanism by MACE grown H-terminated Si NWs/NCs describing the e-h pair production, effective charge separation and dye degradation.

accelerate the separation of photoinduced e-h pairs and thus prevents the fast recombination. The H_2O molecules react with the photogenerated electrons and holes and holes can be trapped by hydroxyl groups to form hydroxyl radicals. A sufficient number of hydroxyl radicals are thus generated and they decompose the adsorbed organic pollutants. However, there are several other factors for the enhanced photodegradation of organic dyes by the MACE grown Si NWs/NCs, such as the Schottky barrier effect due to the presence of unaltered metal NPs left after etching; the metal NP's SPR related broad and enhanced absorption; enhanced charge separation due to the higher electronegativity of the metal NPs and the high surface area of the photocatalyst. Due

to the high porosity & high surface area of the Si NWs/NCs, the overall efficiency is significantly high as compared to the bulk Si.

6.10. Comparison of Photocatalytic Performance of Mesoporous Si NWs & Commercial P25

P25 (TiO_2) is the most common photocatalysts used in the industry for the degradation of organic dyes in the water.[15] Due to its wide bandgap (3.2 eV), it can utilize the UV lights only. On the other hand, MACE grown Si NWs are ecofriendly, photostable, inexpensive and nontoxic material and are able to utilize near UV, visible and NIR light for the degradation of organic pollutants. We have compared the photocatalytic efficiency of the MACE grown Si NWs sample with that of the commercial photocatalyst P25 and the results are shown in Fig. 6.14. For a fare comparison, we have taken the same amount of P25 as that of the Si NWs (sample S1HF5) (Fig. 6.1) by weight. Interestingly and impressively, it is found that the performance of the MACE

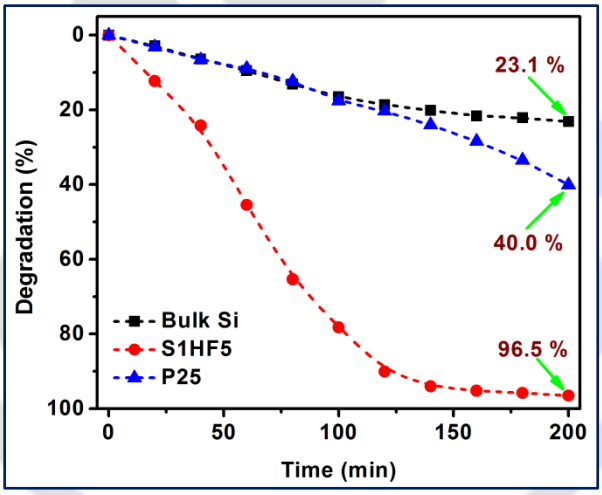

Fig. 6.14. Comparison of the photodegradation of MB by sample S1H5F, P25 and bulk Si.

grown Si NWs is significantly stronger than that of commercial P25 samples. Note that we used a visible light source (390-730 nm) for the photodegradation study. We have calculated and compared the photodegradation rate constant for P25 and sample S1HF5 and found that the value of k is 0.017 min^{-1} for the sample S1HF5, while it is 0.002 min^{-1} for P25. Thus k for the sample S1HF5 is ~8.5 times higher than that of P25. Earlier report suggests that the visible light photocatalytic rate constant of P25 in MB solution is 0.0076 min^{-1}, which is very much consistent with our results.[22] Note that in the present experiment, we used a small piece of Si NW/NCs sample compared to the total volume of the MB dye. If bigger size of sample is used,

higher efficiency degradation can be achieved from the MACE grown Si NWs/NCs. We have observed that the MACE grown Si NWs photocatalysts are stable up to several cycles. Thus, Si NWs/NCs grown by cost effective, rapid and less time consuming MACE method can replace the commercial photocatalyst P25 for utilizing the visible spectrum of solar light for environmental cleaning.

6.11. Correlation between PL Intensity and Photocatalytic Performance of Mesoporous Si NWs

It is interesting to note that the MACE grown samples show highly efficient visible-NIR PL as well as impressive photocatalytic efficiency under the visible light illumination. Note that the PL process requires a fast radiative recombination of the excited e-h pairs, while the photocatalysis requires an easy separation of the photoexcited e-h pairs with minimum recombination.[2, 7] Thus, if the former process is dominant, the later process is expected to be less effective. Earlier reports suggest that two such contrastive phenomena can be simultaneously present in a single system.[2, 23] Anpo et al. reported PL and photocatalytic activity of highly dispersed TiO_2 anchored onto porous vycor glass.[23] Yin et al. reported enhanced visible PL and strong photocatalytic activity

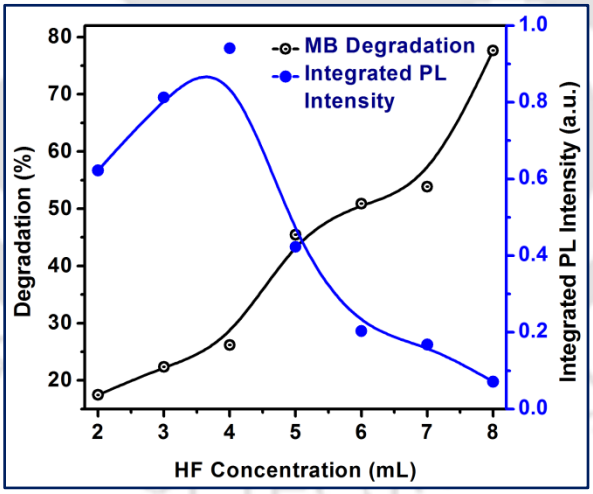

Fig. 6.15. Comparison of the integrated PL intensity and photodegradation(%) of MB as a function of HF concentration keeping the H_2O_2 concentration fixed for samples in group S1.

of V_2O_5-loaded ZnO NRs and attributed it to coupling between ZnO NRs and V_2O_5 NPs.[24] In the present case, it has been reported that the H-terminated surface in mostly responsible for the excellent photocatalytic activity of the MACE grown Si NWs[2, 3, 7, 8], while the QC effect in Si NCs and the NBOHC defects are mainly responsible for the efficient PL.[2, 7, 10, 14, 25] We have

found that the photodegradation efficiency of the MACE grown Si NWs/NCs increases with the concentration of HF (Fig. 6.5 and Fig. 6.6) but the PL intensity decreases (Fig. 4.6(a, b), *Chapter 4*). As expected, we indeed found that the efficiencies of the above two processes are complementary to each other for different samples.[7] Fig. 6.15 shows the variation of integrated PL intensity and the photodegradation efficiency (after 60 min light illumination) of the samples in group S1 as a function of relative HF concentration. It is clear from Fig. 6.15 that as the HF concentration increases, the integrated PL intensity decreases, while the photodegradation efficiency systematically increases. As mentioned earlier, higher HF concentration causes higher density of Si-H bonds, which results in higher photodegradation efficiency, while lower HF concentration causes higher Si NCs density and higher density of NBOHC defect sites, which results in the strong PL intensity.[7] Thus, depending on the requirement, one can tune the etchant concentration in the MACE process to suit one's need. We have also observed that the PL intensity decreases with increasing resistivity of the Si wafer (Fig. 4.7, *Chapter 4*), while the photocatalytic activity follows the opposite trend (Fig. 6.6). This is consistent with our observation in photocatalytic rate constant in Fig. 6.9. These results are consistent with our explanation about the two contrasting phenomena PL and photocatalysis, which may be taking place at two different location of the sample. Our results demonstrate the supremacy of MACE process for the fabrication of multifunctional Si NWs and open up the possibility of using the MACE grown Si NWs array for various light emitting and visible light photocatalytic applications, such as organic waste treatment and hydrogen production by photocatalytic water splitting etc.

6.12. Conclusion

The MACE grown Si NWs decorated with self-grown and arbitrary shaped quantum size Si NCs perform as an efficient and strong photocatalyst for the degradation of organic dyes. The MACE grown Si NWs/NCs are able to utilize the entire visible light for the degradation of organic pollutants and its degradation efficiency is in fact higher than the commercial photocatalyst P25 with the use of visible light. It is revealed that the Si-H bonds present on the surface of the Si NWs/NCs facilitate the photocatalytic activity by efficient separation of photogenerated e-h pairs. Our results confirm the complementarity of the two contrasting phenomena, PL and photocatalysis from the same Si NWs/NCs. The effects of different growth parameters on photodegradation performance of Si NWs/NCs are extensively studied to tune the efficiency,

stability of the photocatalyst for passible commercialization. The MACE grown Si NWs/NCs can be highly beneficial for the artificial photosynthesis and environmental cleaning applications.

References

1. Ghosh, R.; Giri, P. K. *Sci. Adv. Today,* **2016,** 2, 25230.
2. Ghosh, R.; Imakita, K.; Fujii, M.; Giri, P. K. *Phys. Chem. Chem. Phys.,* **2016,** 18, 7715.
3. Megouda, N.; Cofininier, Y.; Szunerits, S.; Hadjersi, T.; ElKechai, O.; Boukherroub, R. *Chem. Comm.,* **2011,** 47, 991.
4. Liu, D.; Li, L.; Gao, Y.; Wang, C.; Jiang, J.; Xiong, Y. *Angew. Chem. Int. Ed. ,* **2015,** 54, 2980.
5. Liao, F.; Wang, T.; Shao, M. *J. Mater. Sci: Mater. Electron.,* **2015,** 26, 4722.
6. Brahiti, N.; Hadjersi, T.; Menari, H.; Amirouche, S.; El Kechai, O. *Mater. Res. Bul.,* **2015,** 62, 30.
7. Ghosh, R.; Giri, P. K. *RSC Adv.,* **2016,** 6, 35365.
8. Shao, M.; Cheng, L.; Zhang, X.; Ma, D. D. D.; Lee, S. T. *J. Am. Chem. Soc.,* **2009,** 131, 17738.
9. Ghosh, R.; Pal, A.; Giri, P. K. *J. Raman Spec.,* **2015,** 46, 624.
10. Ghosh, R.; Giri, P. K.; Imakita, K.; Fujii, M. *Nanotechnology,* **2014,** 25, 045703.
11. Demichel, O.; Calvo, V.; Besson, A.; Noe, P.; Salem, B.; Pauc, N.; Oehler, F.; Gentile, P.; Magnea, N. *Nano Lett.,* **2010,** 10, 2323.
12. Walavalkar, S. S.; Hofmann, C. E.; Homyk, A. P.; Henry, M. D.; Atwater, H. A.; Scherer, A. *Nano Lett.,* **2010,** 10, 4423.
13. Valenta, J.; Bruhn, B.; Linnros, J. *Nano Lett.,* **2011,** 11, 3003.
14. Skuja, L.; Suzuki, T.; Tanimura, K. *Phys. Rev. B,* **1995,** 52, 15208.
15. Liu, Y.; Chen, K.; Xiong, M.; Zhou, P.; Peng, Z.; Yang, G.; Cheng, Y.; Wang, R.; Chen, W. *RSC Adv.,* **2014,** 4, 43760.
16. Qu, Y.; Zhong, X.; Li, Y.; Liao, L.; Huangbc, Y.; Duan, X. *J. Mater. Chem.,* **2010,** 20, 3590.
17. Kang, Z.; Tsang, C. H. A.; Wong, N. B.; Zhang, Z.; Lee, S.-T. *J. Am. Chem. Soc.,* **2007,** 129, 12090.
18. Pal, A.; Ghosh, R.; Giri, P. K. *Appl. Phys. Lett.,* **2015,** 107, 072104.
19. Zhong, X.; Qu, Y.; Lin, Y.-C.; Liao, L.; Duan, X. *ACS Appl. Mater. Int.,* **2011,** 3, 261.
20. Xu, H.; Xiao, H.; Pei, H.; Cui, J.; Hu, W. *Micropor. Mesopor. Mater.,* **2015,** 204, 251.
21. Kamal Kumar, P.; Ramesh, G.; Giri, P. K. *Nanotechnology,* **2016,** 27, 315703.
22. Yang, Y.; Zhang, T.; Le, L.; Ruan, X.; Fang, P.; Pan, C.; Xiong, R.; Shi, J.; Wei, J. *Sci. Rep.,* **2014,** 4, 7045.
23. Anpo, M.; Aikawa, N.; Kubokawa, Y.; Che, M.; Louis, C.; Giamello, E. *J. Phys. Chem.,* **1985,** 89, 5017.
24. Yin, H.; Yu, K.; Hu, J.; Song, C.; Guo, B.; Wang, Z.; Zhu, Z. *Dalton Trans.,* **2015,** 44, 4671.
25. Suzuki, T.; Skuja, L.; Kajihara, K.; Hirano, M.; Kamiya, T.; Hosono, H. *Phys. Rev. Lett.,* **2003,** 90, 186404.

Chapter 7

Photoluminescence Signature of Resonant Energy Transfer in ZnO Thin Film Coated Mesoporous Si Nanowires Array

The light emitting properties of the MACE grown Si NWs can be improved with tunable colors by creating heterostructure (HS) with suitable material in appropriate configuration. Hexagonal zinc oxide (ZnO) with wide bandgap has received significant attention for the photoluminescence (PL) modification of Si NWs/NCs by creating HSs. In this *Chapter* we have investigated the photoluminescence properties of Si/ZnO core-shell NW HSs. Higher band gap ZnO film is sputter deposited on the Si NCs decorated Si NWs. Bare Si NW/NCs and Si NCs/ZnO HSs show extremely high broad band absorption in the entire visible region. PL studies on the Si NCs/ZnO HSs reveal significant red shift and in some cases reduced intensity of the PL band due to the ZnO layer in close proximity of the Si NCs. This is accompanied by a reduction in the PL lifetime of the Si NCs after ZnO coating. We have examined the mechanism of PL red shift and reduction in the PL lifetime from Si NWs/NCs due to ZnO over layer coating. Interestingly, no measurable red shift in PL is observed in absence of the resonance in the PL emission energy of ZnO and that of Si NCs. The modified PL from the HSs is explained through an energy band diagram on the basis of resonant energy transfer from the defect assisted recombination of the carries in the ZnO over-layer that excites the Si NCs in the close proximity and subsequent de-excitation process via radiative recombination. These findings have important bearing on the development of cost effective Si-based hybrid optoelectronic devices using wide band gap heterostructured oxide semiconductors.

7.1. Introduction

Si nanostructures have been shown enormous potential applications in wide areas of nanotechnology, such as solar cells, LED, photodetectors, sensors, artificial photosynthesis, environmental cleaning and so on.[1-4] Bare Si NWs based nano devices may have several drawbacks, such as poor performance, low device quality and short life cycle. To improve the varies drawbacks related to the Si NW based devices and to fulfill new requirement in ever rising energy and environmental applications, many strategies have been developed in the past few

decades and the most widely used one is to develop heterostructures (HSs) by incorporating suitable external materials including semiconductors, metals and other functionalities on Si NWs. Among different semiconductors, hexagonal zinc oxide (ZnO) has received significant attention for fabricating different HSs with enhanced device performance in photovoltaics[5, 6], photodetectors[7], LEDs[8-13], supercapacitors[14], H_2 production[15], gas sensor[16] etc. PL spectra of ZnO are usually composed of a visible blue-green band, related to a deep level defect emission, and ultraviolet (UV) emission from the ZnO excitonic emission.[17-22] ZnO films on Si substrates may introduce a large stress between the ZnO and Si due to the large mismatch in the thermal expansion coefficients and the lattice constants. There are only a few reports concerning the PL and electroluminescence from ZnO/Si NW HSs. [5-16, 23, 24] The reported studies have mostly used sophisticated techniques, e.g., atomic layer deposition and metal-organic chemical-vapor deposition, to grow the ZnO layers over Si nanostructures. Use of a relatively simple and low-cost technique such as radio frequency (RF) magnetron sputtering is least explored in the literature. The exploration of Si-based ZnO nano HSs is of significant interest in developing future nanoscale hybrid optoelectronic devices.

Forster type resonant energy transfer (FRET) is a mechanism, which describes the energy transfer between two light sensitive fluorophores.[25-30] FRET involves the nonradiative transfer of excitation energy from a donor fluorophore excited after absorption of a higher energy photon, to a ground state acceptor fluorophore, placed in close proximity and which can radiatively emit a lower energetic photon. FRET is realized by dipole-dipole interactions and depends on the degree of spectral overlap between donor's PL and acceptor's absorption. FRET efficiency depends on the sixth power of the separation distance between the donor and acceptor pair.[25-30] FRET has been invoked mostly in organic/inorganic[29, 30] hybrids, while only a few reports are available on inorganic/inorganic[25, 26] hybrids. In case of Si/ZnO NW core-shell HSs, the defect induced energy levels in ZnO are in close proximity of the band edge of Si, which can facilitate FRET.[25, 27-30] In order to explain the PL spectral features of Si/ZnO HSs, we have invoked FRET for the first time.[9]

In this chapter, we study the morphological, structural and PL properties of Si NCs/ZnO HSs by growing ZnO thin films by a sputter deposition method on the Si NWs/NCs. The high density Si NW/ZnO HSs not only act as an excellent anti-reflection layer over the entire UV to visible and near infrared (NIR) region but also efficient visible light emission can be easily tuned

from these HSs. Due to the specific band alignment in the HSs and close overlap of PL bands from Si NCs and ZnO layers, the Si NCs/ZnO HSs show modified PL features and this has been explained systematically invoking the FRET mechanism. The red-shift of the PL intensity and reduction in the PL lifetime of the Si NCs in presence of the ZnO layer are successfully explained on the basis of FRET mechanism.[9]

7.2. Experimental Procedure

7.2.1. Growth of Si NCs decorated Si NWs

Si NWs were grown from boron-doped p-type Si (100) wafers with resistivity 1-10 Ω-cm and 0.01 Ω-cm. Typical MACE process was used to grow the aligned Si NWs decorated with arbitrary shaped quantum sized Si NCs on its surface, as discussed in the earlier chapters.[9, 31-36] MACE is performed using both one-step and two-step processes. In case of the one-step process, the cleaned p-type Si wafers were immersed into a solution containing 0.015 M $AgNO_3$ and 5.55 M HF. In case of the two-step process, at first a thin layer of Ag NPs were formed on the Si substrates by dipping the substrates in a solution containing

Table 7.1: Details of the growth parameters of Si NWs/NCs.

Sample Code	Wafer Used	Etching Condition	Etching Duration
P	p-type Si(100), 1-10 Ω-cm	One step MACE in HF/$AgNO_3$	60 min
Q	p-type Si(100), 1-10 Ω-cm	Two step MACE in HF/$AgNO_3$	60 min
R	p-type Si(100), 0.01 Ω-cm	Two step MACE in HF/H_2O_2	5 min
P1	p-type Si(100), 1-10 Ω-cm	One step MACE in HF/$AgNO_3$	30 min

0.015 M $AgNO_3$ and 5.55 M HF for a few seconds and subsequently the substrates were treated by rapid thermal annealing (RTA) for one minutes at 500 °C. Due to the RTA treatment, the Ag NPs form spherical droplets on the Si wafer. Subsequently, the substrates were immersed into the solution containing 0.015 M $AgNO_3$ and 5.55 M HF as well as 1.422 M H_2O_2 and 4.6 M HF at room temperature (RT). Details of the sample information including used wafer, type of etchant, etching condition and etching duration are tabulated in Table 7.1.

7.2.2. Growth of ZnO Thin Film on Mesoporous Si NWs

The ZnO thin film was deposited on the above prepared samples by RF magnetron sputtering using a commercial ZnO target (99.999% purity), and these ZnO coated samples are termed as

P/ZnO, Q/ZnO and R/ZnO, respectively. The sputtering was carried out at a RF power of 50 W for 30 min with chamber pressure 1 Pa at a substrate temperature (T) 200 °C. We have optimized growth of ZnO layer by RF sputtering and found that such a low RF power gives rise to reasonable deposition rate and good quality (polycrystalline) film. The substrate temperature was kept at 200 °C to obtain better crystallinity of the ZnO layer. The thickness of the ZnO film on a reference Si substrate was measured by a profilometer (Vecco, Dektak 150) and the thickness (t) was found to be ~175 nm.[9]

7.3. Morphology

7.3.1. FESEM Imaging

We have studied the surface morphology of the Si NW/ZnO HS by means of the FESEM analysis. Fig. 7.1(a) and (b) show the FESEM top-view image of the ZnO film on plane Si wafer and Si NWs (sample Q/ZnO), respectively.[9] Small ZnO grains were formed in each case. We have also grown ZnO film of different thickness on the Si NWs. Fig. 7.2(a) and (b) represent the FESEM cross sectional images of the sample Q/ZnO with ZnO thickness ~175 nm and ~525 nm,

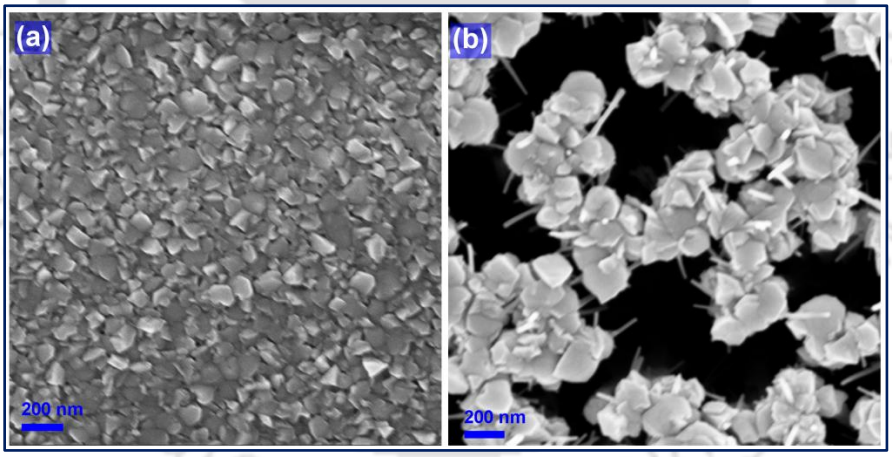

Fig. 7.1. FESEM top-view micrographs of (a) ZnO film on Si wafer and (b) sample Q/ZnO.

respectively, while (c) represent the cross sectional FESEM micrograph of sample R/ZnO.[9] Fig.7.2 (d-f) depicts the corresponding enlarged view of a selective portion of images in (a-c). It is clear that the ZnO shell thickness is not uniform across the Si NWs. ZnO thickness is higher towards the top of the Si NWs. It is also noted that the full length of the Si NWs is not covered by ZnO. The covering is higher for sample Q/ZnO (Fig. 7.2(a)) as compared to that of sample R/ZnO (Fig. 7.2(b)). However, the covering is increased for higher thickness of ZnO on Si

NWs. In case of sample Q/ZnO with ZnO thickness 525 nm, the Si NWs were entirely covered by ZnO layer.

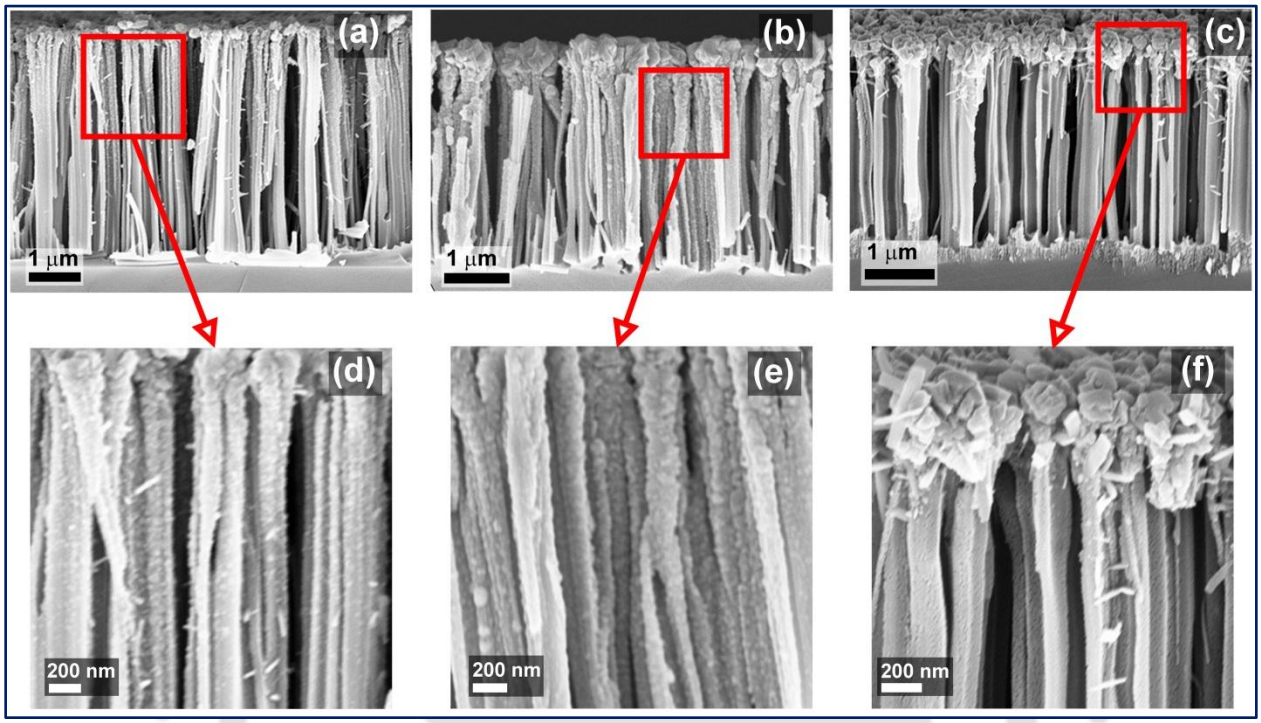

Fig. 7.2. FESEM cross sectional micrographs of samples (a) Q/ZnO (ZnO thickness ~175 nm), (b) Q/ZnO (ZnO thickness ~525 nm) and (c) R/ZnO. (d-f) Corresponding enlarged view of selective portion in (a-c).

7.3.2. TEM Imaging

It is already discussed that the Si NWs grown by both one-step and two-step MACE show rough side walls due to the side wall etching and it shows formation of Si NCs on the surface of the Si NWs.[9, 31-38] The shape and size of the Si NCs depend on the etching conditions and size/density of the Ag metal islands during the MACE process, as discussed in the earlier chapters and our previous report.[9, 31-38] When the ZnO layer is deposited on the mesoporous Si NWs from the top surface, the deposited ZnO goes into the pores between two adjacent Si NWs as well as in between the Si NCs and it bridges the gap (pores) between the Si NCs. The dimensions of majority of the Si NCs as well as the pores are in the quantum size range (Bohr radius of electrons in Si ~4.9 nm) and the Si NCs surrounded by the ZnO layers behave like a quantum well HSs due to the larger bandgap of ZnO as compared to that of Si NCs.[31, 39]

Fig. 7.3(a) represent the TEM image of an individual Si NW of sample Q showing the rough surface due to sidewall etching, while (b) shows the single Si NW coated with ZnO layer.[9] Fig. 7.3(a) confirms that the Si NCs decorated Si NWs are covered by an ultrathin SiO_x layer with a

thickness ~2 nm, while the NW diameter is about 70 nm. Fig. 7.3(b) indicates that the surface roughness of the NWs increased due to the ZnO coating. Fig. 7.3(c) and (d) represent the corresponding EDX spectra. From the composition analysis using EDX spectra, the sample Q shows that the Si NCs/NWs are covered with a thin layer of SiO_x (x ~ 0.5), while the sample Q/ZnO shows oxygen deficiency in the ZnO layer.

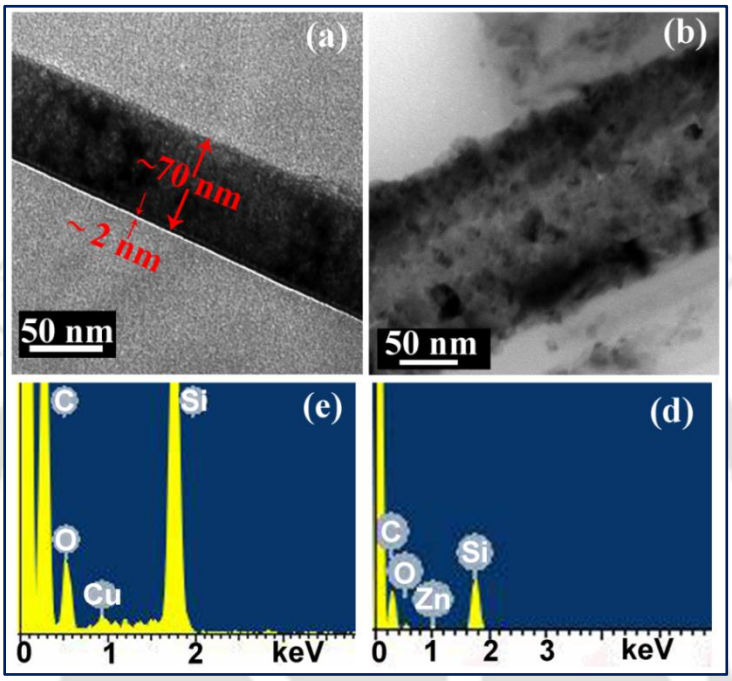

Fig. 7.3. TEM images of (a) a single Si NW in sample Q and (b) rough surface of a ZnO coated Si NW. Diameter of the Si NW is ~70 nm and the thickness of the SiO_x layer is ~2 nm in (a). (c), (d) Corresponding EDX spectra showing Si, O and Zn.

7.4. Structural and Composition Analysis

7.4.1. X-Ray Diffraction (XRD)

For the confirmation of crystalline phase and composition, we performed XRD analysis of the as-grown samples. Fig. 7.4 shows a comparison of the XRD pattern of the sample Q, Q/ZnO and ZnO on Si wafer.[9] The peaks corresponding to crystalline Si are indicated as "∗", while "♦"represent the peaks corresponding to ZnO crystallites. Both the Si NCs/NWs and the ZnO layer are found to be highly crystalline in nature and Q/ZnO sample shows pure hexagonal wurtzite phase of ZnO.[9] However, two additional peaks (indicated as "♠") located at ~2θ = 44.7° and ~2θ = 53° appear in the XRD pattern of sample Q/ZnO, as shown in Fig. 7.4. Based on the JCPDS data, these peaks are tentatively assigned to ZnO_2 phase (JCPDS reference no. 77-2414,

76-1364). This implies that some portion of the ZnO layer that is coated on the Si NWs/ NCs is oxygen rich.[9]

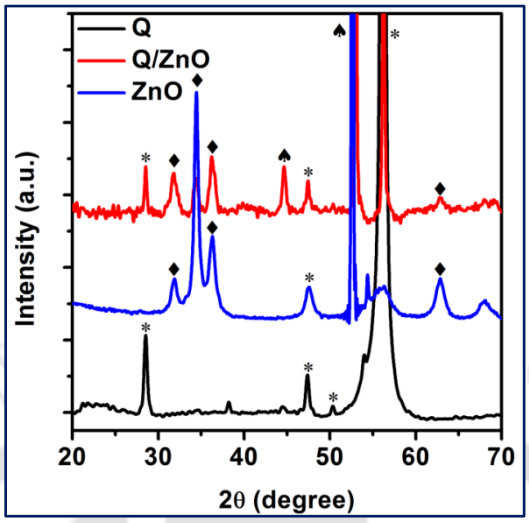

Fig. 7.4. A comparison of the XRD pattern of the samples Q and Q/ZnO and the ZnO film on Si wafer. The "∗" represent the peaks corresponding to Si crystals and "♦"represent the peaks corresponding to ZnO crystallites. "♠" indicates presence of ZnO_2 phases in ZnO coated on Si and on Q/ZnO.

7.4.2. X-Ray Photoelectron Spectroscopy (XPS)

Fig. 7.5(a-c) represents the XPS core level spectra of the sample Q and Q/ZnO.[9] Each spectrum was calibrated using Carbon 1s spectrum keeping the peak at 284.8 eV.[40] Si 2p core level XPS analysis of sample Q confirms that the Si NCs decorated on Si NWs are covered by a native oxide layer of Si i.e. (SiO_x ($0<x<2$)), as shown in Fig. 7.5(a).[9] The Si 2p core-level spectrum of sample Q shows two peaks at ~ 98.9 eV and ~102.5 eV. These two peaks correspond to the neutral Si and its oxidation state; 98.9 eV peak corresponds to Si^{0+} (Si) and 102.5 eV peak corresponds to Si^{3+} (Si_2O_3), respectively.[9, 40, 41] However, deconvoluation of the spectrum (Table 3.3, *Chapter 3*) confirms that different oxidation states of Si are present in the sample (Si^{0+} (Si), Si^{1+} (Si_2O), Si^{2+} (SiO), Si^{3+} (Si_2O_3), and Si^{4+} (SiO_2)). Due to the thick ZnO layer, sample Q/ZnO does not show any Si-related XPS peak in Fig. 7.5(a), though it shows a distinct Zn $2p_{3/2}$ peak at 1021.7 eV, as shown in Fig. 7.5(b) and it is assigned to Zn^{2+} in ZnO.[9] From the O 1s spectrum of the sample Q, the peak at energy ~ 532.3 eV is attributed to O^{2-} ions in the Si-O bonds due to the sub-oxide of Si, i.e., Si_2O_3, which is consistent with the Si 2p core level spectrum.[9] The asymmetric shape of O 1s spectrum for sample Q/ZnO in Fig. 7.5(c) is fitted by one Gaussian and one Lorentz peak by choosing the appropriate XPS baseline (Shirley). A strong Gaussian

peak at 530.3 eV and a relatively weak Lorentz peak at 531.7 eV are seen. The peaks at 530.3 eV and 531.7 eV for sample Q/ZnO are assigned to O^{2-} ions in the Zn-O bonds and O^{2-} ions in the oxygen deficient (i.e., oxygen vacancy, V_O) regions, respectively.[42, 43] This is consistent with the EDX analysis.[9] On the other hand, the composition analysis from the XPS spectra from the

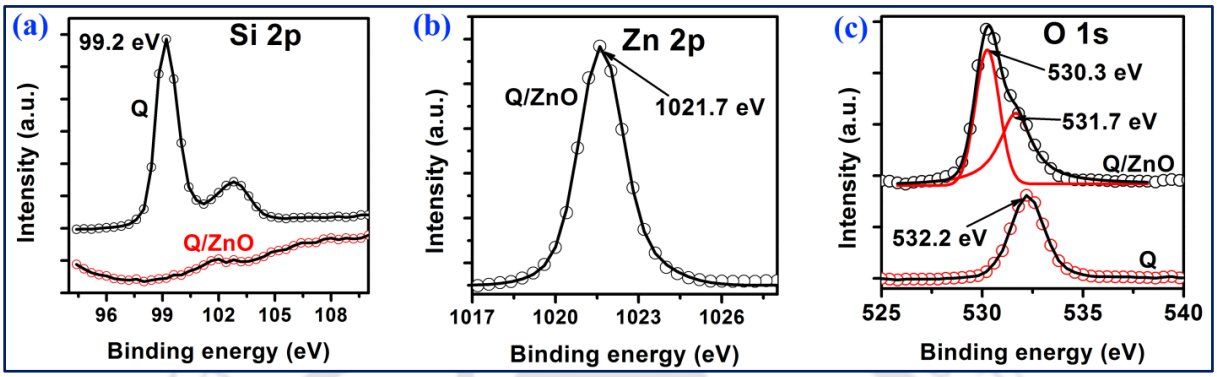

Fig. 7.5. (a) Core level Si 2p XPS spectra of the samples Q and Q/ZnO, (b) core level Zn 2p XPS spectrum, the peak at 1021.7 eV refers to the Zn $2p_{3/2}$ arising from ZnO. (c) Comparison of the O 1s spectra of the sample Q and Q/ZnO. The spectrum of Q/ZnO is fitted with two Gaussian peaks.

surface of Q/ZnO reveals that the atomic percentage of oxygen is higher than that of zinc (i.e., instead of ZnO it is $ZnO_{1.2}$).[9] Note that the XPS probes only a few nm of the surface layer of ZnO and it shows a higher percentage of oxygen than that of zinc near the surface. Whereas EDX spectrum comes from a bigger volume of the Si/ZnO HS due to higher penetration depth of electrons and it shows an overall oxygen deficiency in the ZnO layer.[9] This is consistent with the XPS depth profile analysis in Fig. 3.19(e), *Chapter 3* which showed that the oxygen deficiency increases with the depth. Thus, oxygen content is not uniform across the entire thickness of the ZnO layer, perhaps due to higher deposition temperature.[9] We found that outer layer of ZnO contains excess oxygen, while the inner layers contain less oxygen than the zinc concentration. This is consistent with our XRD analysis.[9] Hence, both oxygen rich regions and oxygen deficient regions are present in the as-deposited ZnO layer.[9]

7.5. Optical Characterization

7.5.1 Absorption Study

The optical absorption of the Si NWs/NCs samples was investigated by measuring the diffuse reflectance spectra (DRS) under oblique incidence. From the reflectance data, optical absorbance can be approximated by the Kubelka-Munk function given by

$$F(R) = (1 - R)^2/2R, \quad \ldots\ldots\ldots\ldots\ldots\ldots (7.1)$$

where R is the diffuse reflectance.[44] Fig. 7.6(a) shows the comparison of the optical reflectivity as a function of wavelength for the bulk Si wafer and different NW samples, while Fig. 7.6(b) shows the corresponding optical absorbance spectrum derived from reflectivity data of these samples.[9] Fig. 7.6(c) shows the Tauc plot i.e. the $[F(R)h\nu]^2$ vs hν plot, considering the direct band-gap for the corresponding absorption spectrum of the samples P/ZnO and Q/ZnO. Both the bare Si NWs ZnO-coated Si NWs show significantly high absorbance at all wavelengths as compared to the bulk Si wafer, as seen in Fig. 7.6(b).[9] Due to multiple reflections at the inner surface of the Si NWs and a broad range of size distribution of the Si NCs, the absorption is significantly high in case of Si NWs/NCs over the entire range of visible-NIR wavelength.[3, 9, 31-33] In case of Si NW/ZnO hybrids, the reflectance spectra arise from the constructive and destructive interference between the light from the air/ZnO (top) interface and ZnO/Si (bottom) interface and their positions depending on Si NCs/NWs' size.[9, 45, 46] It is observed that the absorbance in P/ZnO and Q/ZnO is relatively high as compared to the

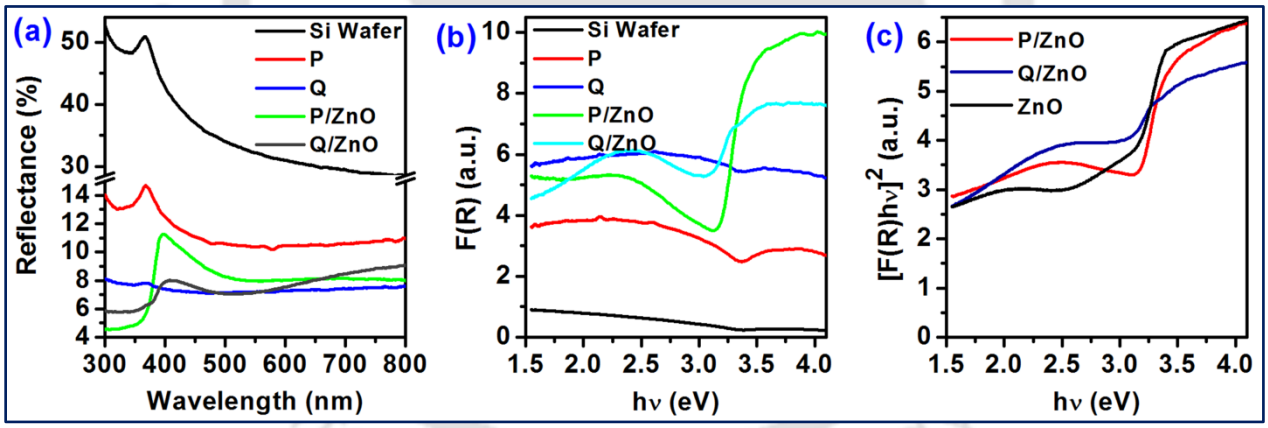

Fig. 7.6. (a) Comparison of the diffused reflectance spectra for samples P, Q, P/ZnO and Q/ZnO with that of the bulk Si wafer. (b) Comparison of the Kubelka-Munk function derived from the reflectivity data of different samples. (c) Tauc plot i.e. the $[F(R)h\nu]^2$ vs hν plot, considering the direct band-gap of the samples P/ZnO and Q/ZnO.

absorbance of P, over the entire visible range and it dramatically increases in the UV range due to the UV absorption by the ZnO layer. Note that, we have observed red shift in absorption edge of all the samples i.e. P/ZnO, Q/ZnO and ZnO film of Si wafer as compared to the as compared pure crystalline ZnO structure (~3.6 eV). The Tauc plot in Fig. 7.6(c) also exhibit a red shift in the absorption edge of Si/ZnO HSs as compared to that of pure ZnO film. Defect-induced red shift of absorption edge of ZnO has been reported in terms of V_O.[9, 43, 47] From XRD and XPS

analyses, it is confirmed that the Q/ZnO HS consists of both the V_O and oxygen interstitial (O_i) defects in the ZnO layer. Due to the red shift, significant absorption of 405 nm (3.06 eV) excitation occurs during the PL measurements and a resulting change in PL spectra of the HSs is expected.

7.5.2. Photoluminescence Study

MACE grown Si NCs decorated Si NWs exhibit strong broadband PL in the visible region at RT.[9, 31-33, 35, 36, 48, 49] Fig. 7.7(a) shows a comparison of the broad visible-NIR PL from the Si NWs/NCs before and after the deposition of the ZnO overlayer, with laser excitation 405 nm.[9] For comparison, the PL spectrum of the as-grown ZnO film on a clean Si wafer is also included in Fig. 7.7(a). Fig. 7.7(b) shows the comparison of the UV-visible PL of the sample P/ZnO and Q/ZnO with a different laser excitation (325 nm).[9] The inset of Fig. 7.7(b) shows the PL spectrum of the ZnO film on Si wafer in the UV-visible region with 355 nm laser excitation. The UV PL peak at ~3.3 eV is due to the near band edge (NBE) emission from ZnO layer and it is a signature of good crystallinity of the ZnO layer.[9] In Fig. 7.7(a) both the samples P and Q show strong broadband visible-NIR PL emission. It was already explained in *Chapter 4* that the

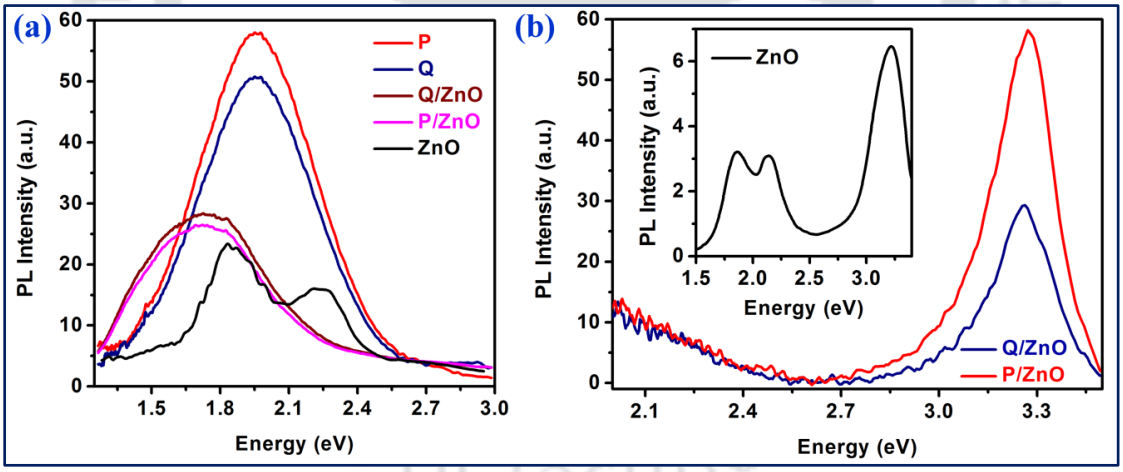

Fig. 7.7. (a) Comparison of the PL spectra with 405 nm laser excitations for samples P and Q before and after ZnO coating; spectrum from ZnO film on Si substrate is shown for comparison. (b) Comparison of the PL spectra for samples P/ZnO, Q/ZnO in the UV-visible region with 325 nm laser excitation. The inset shows the PL spectrum of the ZnO film on Si wafer in the UV-visible region with 355 nm laser excitation.

quantum confinement (QC) in the Si NCs is the most likely source of strong visible PL from sample P and Q, as observed in Fig. 7.7(a). The broad PL peak arises due to the large size distribution of the Si NCs, as argued in the earlier chapters and published reports.[9, 31-33, 35, 36] Any contribution of SiO_x layer to the PL was also assessed and it was found that a higher energy PL

band centered at ~2.6 eV that becomes prominent only at low temperature (<200K) arises due to the SiO_x layer.[31] However, NBOHC defect has also some contribution on the visible PL of sample P and Q.[32, 33]

The as-grown ZnO film on a Si substrate shows two distinct visible bands centered at ~1.86 eV and ~2.25 eV and a UV band peaking at 3.24 eV, as shows in Fig. 7.7(b) (inset). During the photon excitation process, some of the electrons directly recombine with the holes in the valence band. This direct electron-hole recombination features extremely short lifetime, because ZnO is a direct bandgap semiconductor. Actually, the released energy is substantially converted into the NBE emission of ZnO, as manifested in Fig. 7.7(b) by the UV band peaking at 3.24 eV. Besides this, other excited electrons in the conduction band of ZnO fall into the defect-related states and then drop down to the valence band to recombine with holes therein. Such indirect recombination of carriers in the ZnO host gives rise to the visible PL emissions.[9] Based on the literature reports, the most probable identity of the defect giving rise to PL band centered at ~1.86 eV is V_O[19, 20], while that of the band centered at ~2.25 eV is O_i[20] or V_{Zn}[9, 19]. Interestingly, in the Si NW/ZnO HS samples the PL intensity is partly quenched and the center of the PL band is clearly red shifted with a tail in the low energy side for both P/ZnO and Q/ZnO hybrids as compared to that of bare Si NW/NCs (Fig. 7.7(a)). In contrast to the earlier report of PL quenching in Si NW/ZnO grown by atomic layer deposition, we observed efficient visible-NIR emission from Si NWs coated with the ZnO thin film grown by a RF sputtering method.[23] Thus, the deposition method and the nature of the interface at the HS decide the efficiency of the visible-NIR emission from the Si NW/ZnO HSs.[9]

Due to the presence of the intrinsic defects in ZnO layer and the close proximity of the Si NCs with the ZnO layer (separated by a ultrathin oxide layer), part of the excited electrons in the conduction band of ZnO firstly fall into the defect-related states and then drop down to the valence band of Si after resonantly transferring energy to the carriers in the conduction band (size dependent) of Si NCs.[9] Based on the earlier reports and features of Fig. 7.7(a), it is clear that the indirect recombination of carriers in the ZnO host releases the energy covering the visible spectral range and the PL spectra of the Si NCs are also in the same visible range.[9, 17-20] Since the defect related emission energy in ZnO is resonant with the emission energy range of the Si NCs, a Forster type resonant energy transfer (FRET) is highly plausible.[30] Therefore, the aforementioned energy transfer can essentially trigger the excitations of Si in the CB.[9] In case of

the FRET, the NCs excited by the FRET produce emission with energy determined by the size of the Si NCs.[30] Therefore, the excited electrons of Si further go through a radiative transition to the ground level via a visible-NIR emission depending upon the shape and size of the Si NCs. The transfer of the energy released from the defect induced recombination of carriers in ZnO to the Si NCs may be a possible mechanism behind the broad visible-NIR emission from the Si/ZnO HS.[9] The energy released from the CB of ZnO to VB of Si NCs can result in saturation of the trapping sites for the electrons and is likely to prevent the radiative recombination of electrons from the CB to VB of Si NCs. Since ZnO is a direct band gap semiconductor, the probability of such a process is expected to be low.[9] It can be noted that after ZnO deposition, the NBOHC defects in the SiO_x layer (sandwiched in between Si and ZnO) reduces. As a result, the PL contribution of NBOHC defect (~1.9 eV) reduces in the HS samples, which may be partly responsible for the decreased PL intensity, as shown in Fig. 7.7(a). Due to this, the spectra are also red shifted.

Note that the ZnO layer has an absorption tail extended to the visible region due to high density of defects. Thus, reabsorption of PL from Si NC by the ZnO layer cannot be ignored. The reabsorption of photons by the ZnO layer may alter the higher energy side of the PL spectrum yielding a truncated and a red shifted PL spectrum. However, such a mechanism cannot explain the extension of the PL to the lower energy tail of spectrum from the combined system, as shown in Fig. 7.7(a).[9] Note that reabsorption may cause a reduction in the intensity of the PL and this is consistent with some of our PL data. However, the intensity of the resulting PL would also depend on the efficiency of energy transfer process. Thus, an enhancement of PL intensity is possible in some cases, which is contrary to the reduction is intensity expected from reabsorption process. Thus, due to strong resonance in the PL spectrum of bare Si NCs and the defect related PL spectrum of bare ZnO, FRET is expected to be the most dominant process.

In order to gather further evidence in support of the FRET mechanism, we have compared the change in PL spectra for samples with (P1/ZnO) and without (R/ZnO) significant overlap in the PL spectra of ZnO and Si NCs, i.e. resonant and non-resonant PL emission cases.[9] Fig. 7.8(a, b) shows a comparison of the PL spectra with λ_{ex} = 405 nm for samples R and P1 before and after the ZnO coating. The PL spectrum from ZnO film on a Si substrate is also shown for comparison. The PL spectrum of sample R and that of ZnO do not show a strong resonance, as evident from Fig. 7.8(a). As a result, the energy transfer process is expected to be less efficient and no marked redshift is PL is observed in the hybrid system when compared with

the bare Si NW/NCs. If reabsorption process is dominant, one would have expected a clear red shift and reduced intensity of PL peak in all cases, which is inconsistent with the data from sample R/ZnO, as evident from Fig. 7.8(a). On the other hand, the PL spectra of sample P1 and

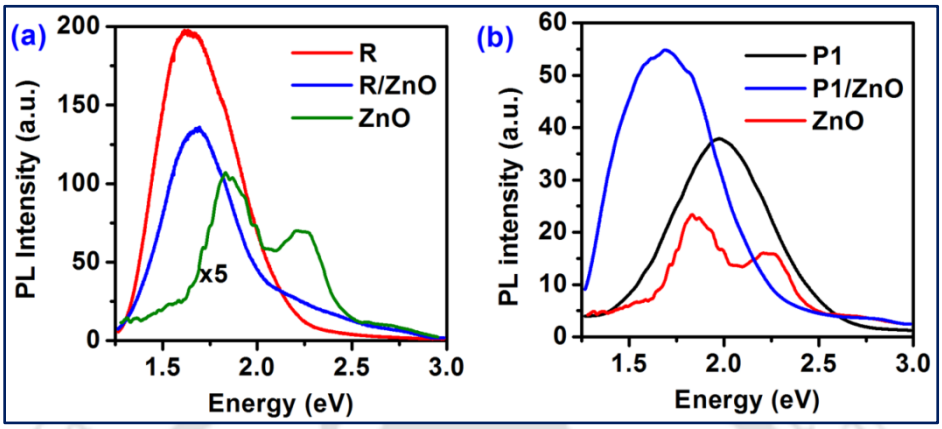

Fig. 7.8. (a), (b) Comparison of the PL spectra with λ_{ex} = 405 nm for samples R and P1 before and after the deposition of ZnO film. Spectrum from ZnO film on Si substrate is shown for comparison. Spectrum from ZnO film on Si substrate in (a) is scaled up 5 times to enable comparison.

ZnO show a strong resonance in emission energies and this promotes strong energy transfer resulting in a strongly red-shifted PL peak due to the excitation of larger Si NCs, as evident from Fig. 7.8(b).[9] Interestingly P1/ZnO shows higher intensity of PL as compared to that of P1 and this may be due to the efficient energy transfer from ZnO to Si NCs. These results provide stronger support to our assertion that the red shift in PL is primarily caused by the resonant energy transfer process and FRET is the most likely mechanism behind the observed changes. It is also noticeable that the defect related visible PL emission of ZnO at ~2.2 eV is completely absent in all the HS samples.[9] In absence of energy transfer, the 2.2 eV peak is expected to be present in the PL spectra of hybrid system. Thus, absence of 2.2 eV peak in all the hybrid samples (ZnO coated on P, Q, R and P1) further supports our assertion that energy transfer is the dominant mechanism for the changes in the PL spectra of Si/ZnO hybrid system.[9] Shimada et al. reported a decrease in the PL intensity of the donor[29] due to the energy transfer process and our results are consistent with this report. However, the resonant PL of ZnO at ~1.86 eV causes red shift in PL in each sample of Si NCs/ZnO due to FRET and this is consistent with the earlier reports.[50, 51]

According to the Forster formalism, FRET efficiency depends on the overlap between the ZnO (donor) emission and Si NCs (acceptor) absorption energy. The ZnO film on Si wafer show

PL band in the visible region with peaks centered at ~1.86 eV and ~2.25 eV (Fig. 7.7(a)). Note that the Si NCs samples (sample P and Q) in Fig. 7.6 shows very high absorption covering the entire visible region. Therefore, the defect associated donor (ZnO) emission energies have significant overlap with the acceptor (Si NCs) absorption energies.[9]

Note that FRET is significant only when the separation between the donor and acceptor is below 10 nm (resonant distance).[27, 52] FRET is a non-radiative process and the non-radiative interaction decreases sharply with increasing the distance between the donor and acceptor, though it also depends upon the conjugate materials of the hybrids.[9] The Si NCs involved in the PL on the surface of the Si NWs consist of wide range of sizes (Table 3.3, *Chapter 3*) and are covered with a thin SiO_x layer (~2 nm from Fig. 7.3(a)). Thus, the average distance between the donor and acceptor is ~2 nm, which very similar to the reported values in organic/inorganic systems.[9, 27] Note that the SiO_x layer thickness may not be uniform along the length of the Si NWs. As FRET occurs from ZnO to adjacent Si NCs by tunneling through SiO_x and tunneling probability of carriers due to FRET decreases inversely with the SiO_x layer thickness following a power law, FRET is thus most effective when the SiO_x thickness is the smallest.[53] However, the self-generated arbitrary shaped Si NCs on the surface of the Si NWs have sizes within quantum size range and the intermediate distance between the two adjacent NCs i.e. the size of the pore is also in the quantum size range. Hence, the ZnO inside the pore behaves as the quantum well due to its higher band gap, while the Si NCs behave as the quantum dots.[9] In our case the typical sizes of the Si NC/ZnO hybrids are comparable to the resonant distance or much less than that (<10 nm). So, FRET process is very likely to take place in the Si NCs/ZnO conjugate.[9]

Table 7.2: *PL peak positions extracted from the fitting of the PL spectra for two different excitation wavelengths (λ_{ex}).*

Sample	PL Peak centers (eV)						
	λ_{ex} = 405 nm				λ_{ex} = 325 nm		
	Peak 1	Peak 2	Peak 3	Peak 4	Peak 1	Peak 2	Peak 3
Q/ZnO	1.46	1.75	1.98	2.64	1.96	3.16	3.27
P/ZnO	1.44	1.73	1.96	2.64	1.91	3.18	3.28
Q	1.59	1.95	2.3	--	1.59	1.90	2.33
ZnO	1.86	2.25	--	--	1.86	2.14	3.24

In Fig. 7.7(a), it is clear that: (i) the PL peak intensity of both P/ZnO and Q/ZnO is nearly half that of the sample P and Q, respectively; (ii) the center of PL peak of the HS is strongly red shifted as compared to that of the bare Si NWs/NCs (both P and Q) and the peaks are asymmetric in nature. These characteristics common to samples P/ZnO and Q/ZnO can be explained by invoking FRET from ZnO to Si NCs.[9] The bare ZnO film shows visible PL with peaks at ~ 1.86 eV and 2.25 eV. The Si NCs has a broad PL emission band in the range 1.6-2.4 eV and this is almost resonant with the 1.86 eV PL emission of ZnO. Since the Si NCs are partly covered with the ZnO shell with an intermediate SiO_x dielectric layer, the Si NCs are excited secondarily by the defect related emission energy of ZnO.[9] In other words, Si NCs depending on their sizes, take away energy from ZnO shell by the FRET process due to their close proximity. Due to this process, PL peak center is red shifted in the hybrid system as compared to the bare Si NCs/NWs.[9]

In order to understand the asymmetry, broadening and contributions of different factors affecting the PL spectrum, each spectrum is deconvoluted. The PL peak positions are tabulated in Table 7.2. The 325 nm excitation is used to probe the crystalline quality of the ZnO layer,

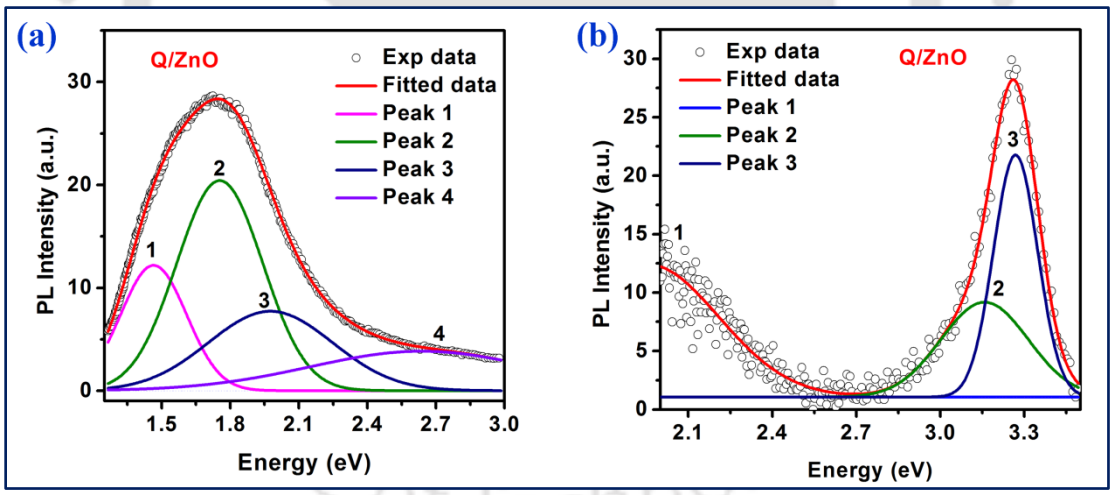

Fig. 7.9. (a) The broad and asymmetric PL spectrum of sample Q/ZnO in the visible-NIR range was fitted by four Gaussian peaks (1, 2, 3 and 4). (b) The PL spectrum of sample Q/ZnO in UV-visible range was fitted with three Gaussian peaks (1, 2 and 3).

while the 405 nm excitation is used to probe mainly the defect related emission in ZnO. Fig. 7.9(a) and 7.9(b) represent the deconvoluted spectra of the sample Q/ZnO measured with 405 nm and 325 nm laser excitations, respectively.[9] In accordance with earlier reports, it is understood that visible PL peaks originate from the Si NCs depending upon the size of Si NCs due to QC

effect,[31-33, 35, 39, 54] while the 2.64 eV PL may originate from SiO_2.[55] Usually, PL spectrum of ZnO is composed of a visible blue-green band related to deep level defect emission and UV peak due to the ZnO excitonic emission.[9, 20, 56] In Fig. 7.9(b), peak 1 at 3.27 eV arises due to the bound excitonic NBE emission of the ZnO, whereas peak 2 at 3.16 eV peak is attributed to the surface capping by the OH group i.e. zinc hydroxide ($Zn(OH)_2$).[9, 20, 21, 23]

In order to understand the effect of thickness of the ZnO shell layer on Si NCs in the energy transfer and PL efficiency, we deposited a thicker ZnO layer of thickness ~525 nm on the Si NWs/NCs.[9] Fig. 7.10(a) shows the comparison of the PL spectra in the visible-NIR range for samples Q/ZnO with two different thicknesses, while 7.10(b) shows the same for ZnO on Si wafer with two different thicknesses. It is observed that the visible-NIR PL intensity of the Q/ZnO with thickness (t) 525 nm was enhanced by a factor of nearly 5 as compared to that of Q/ZnO with t = 175 nm (Fig. 7.10(a)).[9] It is also clear from Fig. 7.10(a) that the PL peak profile is almost unchanged with the change in the thickness of the ZnO layer. With the increase in thickness of the ZnO layer, the defect related PL emission of ZnO also increases, as manifested in Fig. 7.10(b). With the higher thickness of ZnO, higher fractions of the Si NCs/NWs are covered by the ZnO layer as shown in Fig. 7.2(b). As a result, more no. of Si NCs take part as acceptor through the FRET-mediated process. This may be the responsible for the enhancement in the PL intensity for Q/ZnO with ZnO thickness 525 nm as shown in Fig. 7.10(a).[9]

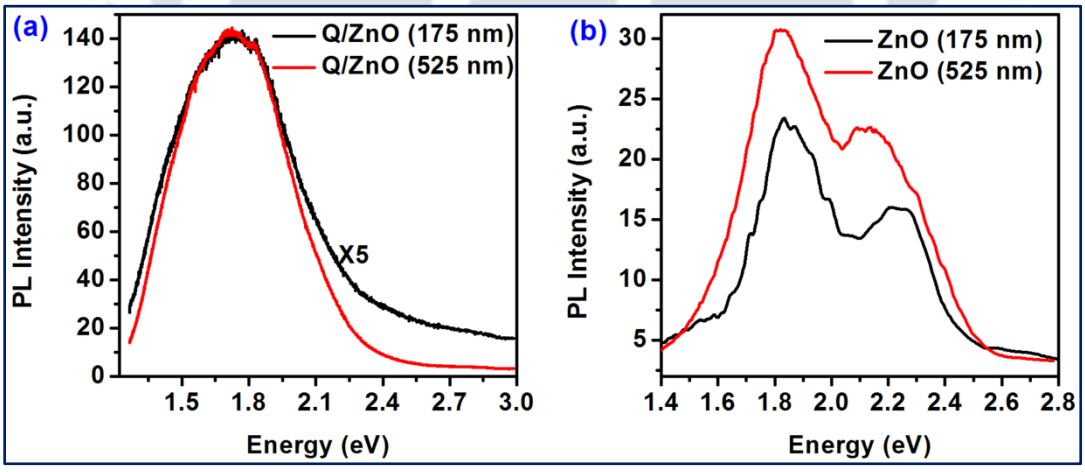

Fig. 7.10. (a) Comparison of the PL spectra for samples Q/ZnO with two different thicknesses (t) of ZnO layer. Note that the PL spectrum of Q/ZnO with t = 175 nm is sealed up by a factor 5 to enable comparison. (b) Comparison of the PL for ZnO on Si wafer with two different thicknesses.

In order to gain further evidence in support of FRET from ZnO to Si NCs, the samples Q/ZnO and ZnO film on Si substrate were annealed under high vacuum (7×10^{-5} mbar) for 30

minutes at 700 °C.[9] The vacuum annealed samples show significant change in PL spectra. Fig. 7.11 represents a comparison of the PL spectra of the as-grown Q/ZnO and annealed Q/ZnO and the ZnO film on Si substrate, using a 405 nm laser excitation. The visible PL intensity of the Q/ZnO is strongly enhanced and the peak is blue shifted after annealing. We notice that the visible PL band is blue shifted in the annealed ZnO film as compared to the as-grown film. Due to the blue shift in PL of ZnO layer, resonant energy is blue shifted and as a result, smaller size Si NCs with higher bandgap are excited and contribute to the PL of the HSs.[9] This results in the overall blue shift of the PL bands of both P/ZnO and Q/ZnO. It is believed that the vacuum annealing causes higher density of V_O in the ZnO shell layer and this enhances the visible PL

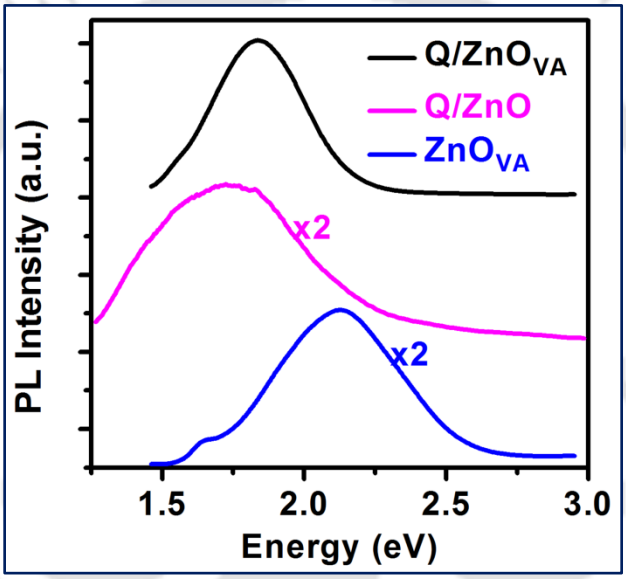

Fig. 7.11. Comparison of the PL spectra of the Q/ZnO after vacuum annealing (VA) at 700 °C. The curves are vertically shifted for better clarity. The visible PL intensities are strongly enhanced and blue shifted after annealing as compared to that of as-grown sample.

originating from various defects in ZnO (V_O or Zn_i). As a result, the probability of FRET is also increased and this leads to the enhancement of the visible PL intensity as well as the blue shift of the PL peak centers for the sample P/ZnO and Q/ZnO.[9] Annealing also improves the interface between the Si/SiO_x and SiO_x/ZnO and this may partly be responsible for higher rate of resonant energy transfer.[9]

7.5.3. Time Resolved Photoluminescence (TRPL)

A more convincing evidence of resonant energy transfer in Si NCs/ZnO HSs comes from TRPL studies. Si NCs in the Si/ZnO HSs showed considerably lower PL lifetimes as compared to the

PL lifetimes of bare Si NCs prior to the deposition of ZnO layer. PL decays of the Si NCs before and after ZnO coating are shown in Fig. 7.12(a), at emission energy 2.03 eV with 405 nm laser excitation and it shows PL decays in the nanosecond time scale.[9] For comparison, the TRPL decay of ZnO film on the Si wafer is also given in Fig. 7.12(a). Since the PL primarily originates from the Si NCs and the sizes of the Si NCs are widely distributed, the shape of the PL transient may be multi-exponential, which is a well-known characteristic of the Si NCs. Due to less interaction among the Si NCs and the highly crystalline core, a small group of Si NCs can emit in a particular energy range.[31] So, the broad PL spectra consist of emission from a large number of small groups of Si NCs. Interestingly, we found that the PL decay of the Si NCs is best fitted with a bi-exponential decay curve, instead of a multi-exponential or a stretched exponential decay curve. This may be due to the fact that two small group of Si NCs in the SiO_x matrix are mainly contributing to the PL in the corresponding PL emission energy. For example, PL decay

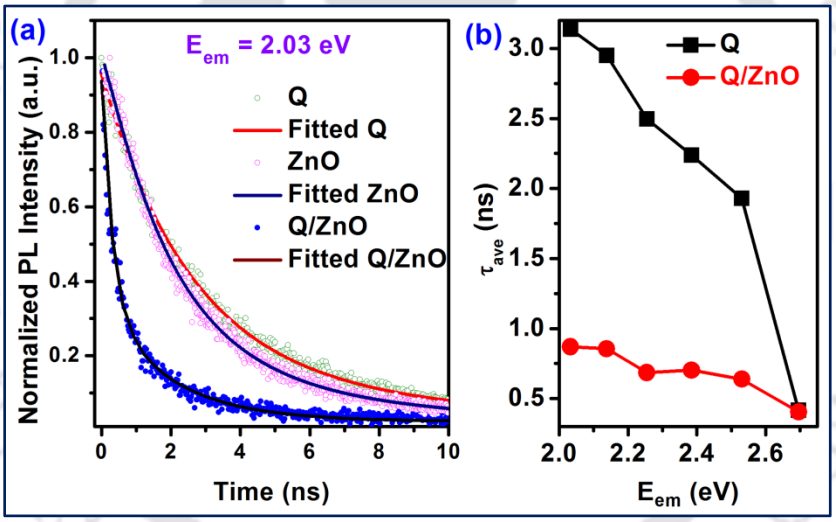

Fig. 7.12. (a) Comparison of the TRPL decay (symbols) of the samples Q, Q/ZnO and ZnO film on Si wafer at emission energy 2.03 eV. Since the decays are bi-exponential in nature, we estimated the average lifetimes (τ_{avg}) by fitting each spectrum by a second-order equation. (b) The variation of τ_{avg} in Q and Q/ZnO at different emission energies.

at 2.03 eV in Q/ZnO is contributed mainly by the PL emissions with center of the peaks at 1.75 eV and 1.98 eV (see Fig. 7.9(a)).[9] Another possible explanation for the bi-exponential decay is that all the Si NCs in each group has identical decay time. Since the decays are bi-exponential in nature, we estimated the average lifetimes (τ_{ave}) of Si NCs (τ_{NC}: τ_1 = 2.5 ns, τ_2 = 9.2 ns), ZnO (τ_{ZnO}: τ_1 = 1.9 ns, τ_2 = 6.6 ns) and that of Si NC/ZnO ($\tau_{NC/ZnO}$: τ_1 = 0.3 ns, τ_2 = 1.9 ns) using the relation[57],

$$\tau_{ave} = \frac{A_1\tau_1 + A_2\tau_2}{A_1 + A_2} \quad \text{..... (7.2)}$$

where A_1 and A_2 are the amplitudes of the decay with lifetime τ_1 and τ_2, respectively. The variation of average lifetime with emission energy is shown in the Fig. 7.12(b).[9] Note that the amplitude of the faster decay component (τ_1) is found to be about one order of magnitude higher than that of the shorter decay component (τ_2). Thus, the faster decay component mainly dictates the effective PL lifetime.[9] A comparison of the TRPL spectra of the samples Q and the Q/ZnO monitored at different emission energies are shown in Fig. 7.13.[9] It is evident from the TRPL data that the τ of Si NCs in presence of the ZnO layer ($\tau_{NC/ZnO}$) is drastically reduced at each emission energy in comparison to that of the Si NC (τ_{NC}) alone i.e. $\tau_{NC/ZnO} < \tau_{NC}$. A decrease of τ_{NC} with emission energy is consistent with our earlier report and the literature reports.[9, 31, 58, 59] The lower energy emission corresponds to the larger size Si NCs and the larger Si NCs have longer lifetime τ.[9] Note that the $\tau_{NC/ZnO}$ is nearly independent of emission energy, as shown in the inset of Fig. 7.12(b). It is also to be noted that $\Delta\tau = \tau_{NC} - \tau_{NC/ZnO}$ is positive at all energies.[9] The shortening of τ for Si NCs/NWs after ZnO deposition may also indicate the influence of non-radiative recombination in the PL of the hybrid system However, if the reduction in lifetime is due to the influence of nonradiative recombination with a shorter lifetime (τ), the energy dependence of lifetime of the Si/ZnO hybrid system would follow the trend opposite to that observed for the hybrid system shown in the Fig. 7.12(b) for Q/ZnO.[9] It is reasonable to assume that the nonradiative lifetime is independent of emission energy and is shorter than the radiative lifetime such that effective lifetime may be shortened due to the influence of nonradiative process. In such a case, $\tau_{NC/ZnO}$ would increase gradually with the emission energy, contrary to our observation of decrease in lifetime with increase in energy.[9] Hence, the observed energy dependence of the reduction in lifetime cannot be explained with the help of nonradiative recombination. This leads us to believe that the FRET is the most likely mechanism for the observed change in lifetime as well as the redshift in the steady state PL spectra. Note that our observation of $\tau_{NC/ZnO} < \tau_{NC}$ and $\tau_{NC/ZnO} < \tau_{ZnO}$ i.e. shortening of the PL lifetime of the donor as well as the hybrid system is fully consistent with the FRET mechanism.[9] This strongly supports the assertion that FRET is responsible for the red shift in PL of the Si/ZnO hybrid nanostructures. The FRET efficiency (η) can be estimated in terms of PL lifetimes of donor with and without the acceptor using the relation:

$$\eta = 1 - \frac{\tau_{NC/ZnO}}{\tau_{ZnO}} \quad \text{..... (7.3)}$$

Based on the above equation, η at emission energy 2.03 eV is estimated to be ~64% for ZnO donor and Si NCs acceptor combination.[9]

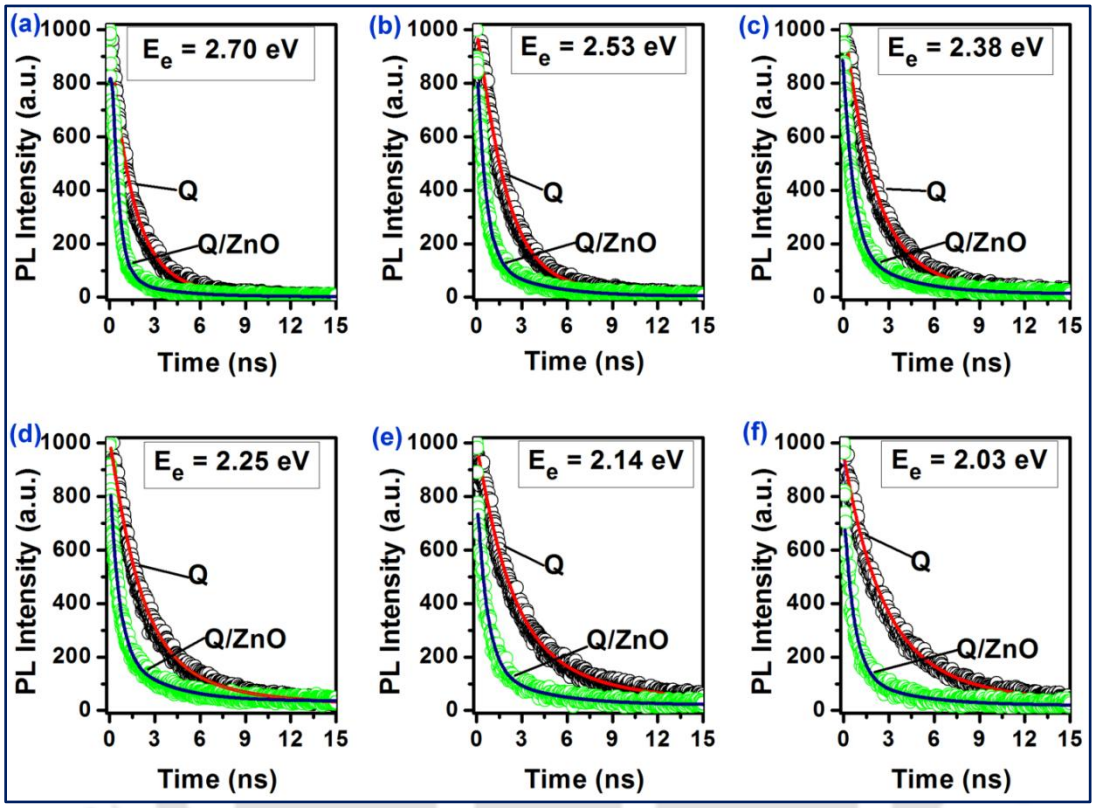

Fig. 7.13. (a-f) A comparison of the TRPL spectra of Si NCs with the ZnO coated Si NCs at different emission energies. In each case, the ZnO coated Si NCs show faster decay compared to the bare Si NCs.

7.6. Illustration of Si NW/ZnO Band Alignment and the FRET Process

Fig. 7.14(a) and (b, c) illustrate a schematic of the HS, the energy band diagram of the Si-SiO_x-ZnO HS and the pathway for the proposed energy transfer from the ZnO to the Si NCs.[9] In Fig. 7.14(b), the energy band of ZnO bends upward at the SiO_x-ZnO interface, while that of Si bends downward. Due to the difference in dielectric constant, the slope near the SiO_x layer is usually steeper than those in the Si or ZnO layers.[9] Since the band bending is extended to μm length scale and the SiO_x layer is of nm width, the energy band for the Si and ZnO in the interface layer is simply a flat line without any visible bending. Fig. 14(c) shows a magnified view of the energy bands of Si NCs and ZnO with short tics and dotted lines, respectively. The Fermi level (EF), the defect or donor level (ED) in ZnO, and the acceptor level (EA) in Si are shown in Fig. 7.14(c).[9] In thermal equilibrium, i.e., in the absence of illumination, EF is flat over

the device and EA is pinned at ED in ZnO due to the presence of the localized surface states. After illumination, e-h pairs will be created in the interface and there may be EF splitting.[9] However, the CB effective mass is much smaller than the VB counterpart, so the discreteness in the CB would be negligible and CB is almost continuous. The discrete levels are confined to nm scale (comparable to excitonic Bohr diameter of Si, i.e. ~9.8 nm), so the discrete levels will not follow CB band bending. However, in the ZnO host after light excitation, some of the electrons in the conduction band directly recombine with the holes in the valence band, generating the UV emission while other electrons in the conduction band of ZnO first transit to the defect-related energy levels and then recombine with holes in the valence band.[9] The defect mediated

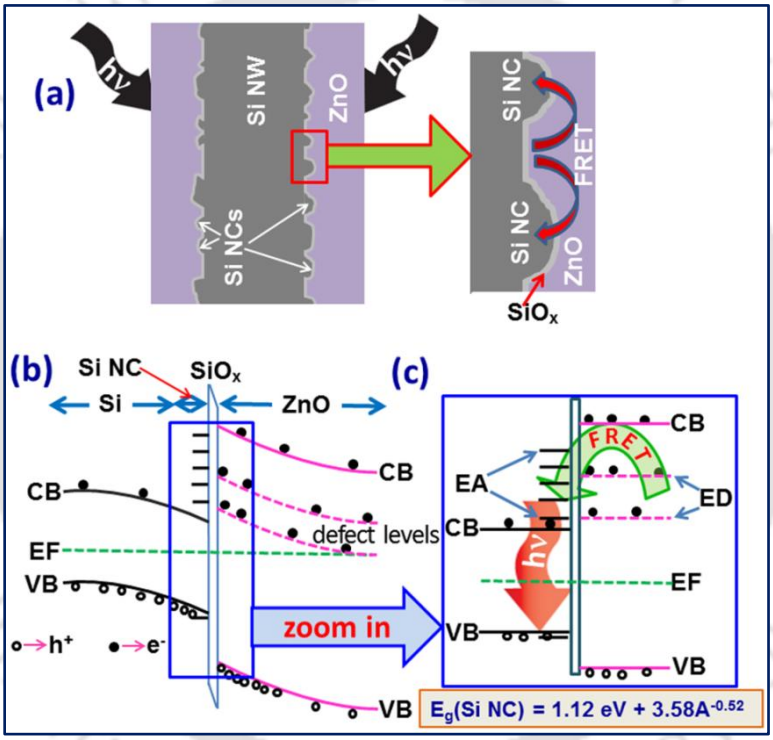

Fig. 14. (a) Schematic of the hybrid Si/ZnO HS. The structure consists of Si NCs decorated Si NW, coated with ZnO. There is a thin layer of SiO_x in the fence of Si. (b) Band diagram of the sample Si/ZnO in the interface of Si NC-SiO_x-ZnO immediately after illumination. (c) The magnified view of a portion of (b). The NCs excited by FRET process emit energy that is determined by the NCs size according to the relation Eg (NC) = Eg (bulk) + $3.58A^{-0.52}$, where A is the cross-sectional areas of the arbitrary shaped Si NCs on the surface of the Si NWs.

recombination of carriers in the ZnO host produces a visible PL and resonantly transfer energy by FRET to the core Si NCs to trigger the excitations of Si NCs with broad range of shape and size.[9] This is followed by the de-excitation process through the band to band radiative transition of excitons, which leads to the modified visible emissions from Si NCs depending upon the size of the Si NCs.[9] As a result, the PL spectrum is red-shifted along with a tail in the low energy

region. Due to the efficient energy transfer, the PL lifetime is reduced in the HS system, as discussed above. Since the influence of the nonradiative channels cannot be fully ruled out in the PL decay, in absence of any nonradiative channels, the energy transfer would be more efficient and that would give rise to enhanced intensity of PL in the HSs. Further optimization of the growth parameters is required for achieving the same.[9]

7.7. Conclusions

In this chapter, we have analyzed the mechanism of red-shift in visible PL emission from arbitrary shaped Si NCs decorated Si NWs after coating of ZnO thin film on it. The Si NC/ZnO HS shows extremely high absorption in the entire UV-visible-NIR range. The red shift and reduced intensity of the visible PL of the Si/ZnO HSs are explained on the basis of resonant energy transfer from ZnO layer to the proximal Si NCs. It is believed that due to the ultrathin intermediate dielectric SiO_x layer, the energy is transferred by the FRET process from the defect assisted recombination of the carries in the ZnO shell that excites the Si NCs core close to the defects and the subsequent de-excitation process gives rise to red shifted visible PL emission via radiative recombination. Both the PL intensity and the PL decay time of the Si NCs are reduced in presence of the ZnO layer due to the formation of heterojunction of Si NCs and ZnO that promote efficient energy transfer. The energy transfer process is explained through an energy band diagram of the Si NC/ZnO HS. This work is important for efficient solar energy harvesting across the entire spectrum of visible-NIR wavelengths based on the concept of hybrid core shell nanocrystals and it also sheds light on the development of Si-based light emitting devices using heterostructured oxide semiconductors, such as, ZnO.

References

1. Tian, B.; Zheng, X.; Kempa, T. J.; Fang, Y.; Yu, N.; Yu, G.; Huang, J.; Lieber, C. M. *Nature,* **2007,** 449, 885.
2. Yan, R.; Gargas, D.; Yang, P. *Nature photonics,* **2009,** 3, 569-576.
3. Peng, K. Q.; Lee, S. T. *Adv. Mater.,* **2011,** 23, 198–215.
4. Duan, L.; Wang, P.; Wei, F.; Yu, X.; Fan, J.; Xia, H.; Zhu, P.; Tian, Y. *Journal of Alloys and Compounds,* **2014,** 602, 290-293.
5. Feng, Z.; Jia, R.; Dou, B.; Li, H.; Jin, Z.; Liu, X.; Li, F.; Zhang, W.; Wu, C. *Appl . Phys. Lett.,* **2015,** 106, 053118.
6. Rakshit, T.; Mondal, S. P.; Manna, I.; Ray, S. K. *ACS applied materials & interfaces,* **2012,** 4, 6085-6095.
7. Dhara, S.; Giri, P. K. *Reviews in Nanoscience and Nanotechnology,* **2013,** 2, 1-24.

8. Chan, Y. F.; Su, W.; Zhang, C. X.; Wu, Z. L.; Tang, Y.; Sun, X. Q.; Xu, H. J. *OPTICS EXPRESS,* **2012,** 20, 24280.
9. Ghosh, R.; Giri, P. K.; Imakita, K.; Fujii, M. *J. Alloy Compd.,* **2015,** 638, 419.
10. Tan, S. T.; Sun, X. W.; Zhao, J. L.; Iwan, S.; Cen, Z. H.; Chen, T. P.; Ye, J. D.; Lo, G. Q.; Kwong, D. L.; Teo, K. L. *Appl. Phys. Lett.,* **2008,** 93, 013506.
11. Yuan-Ming, C.; Sheng-Rui, J.; Hsin-Yi, L.; Chih-Ming, L.; Jenh-Yih, J. *Nanotechnology,* **2010,** 21, 385705.
12. Sun, L.; He, H.; Liu, C.; Lu, Y.; Ye, Z. *CrystEngComm,* **2011,** 13, 2439.
13. Hsieh, Y.-P.; Chen, H.-Y.; Lin, M.-Z.; Shiu, S.-C.; Hofmann, M.; Chern, M.-Y.; Jia, X.; Yang, Y.-J.; Chang, H.-J.; Huang, H.-M.; Tseng, S.-C.; Chen, L.-C.; Chen, K.-H.; Lin, C.-F.; Liang, C.-T.; Chen, Y.-F. *Nano Lett.,* **2009,** 9, 1839.
14. Han, H.-C.; Chong, C.-W.; Wang, S.-B.; Heh, D.; Tseng, C.-A.; Huang, Y.-F.; Chattopadhyay, S.; Chen, K.-H.; Lin, C.-F.; Lee, J.-H.; Chen, L.-C. *Nano Lett.,* **2013,** 13, 1422.
15. Kargar, A.; Sun, K.; Kim, S. J.; Lu, D.; Jing, Y.; Liu, Z.; Pan, X.; Wang, D. *Phys. Status Solidi A,* **2013,** 210, 2561.
16. Liao, J.; Li, Z.; Wang, G.; Chen, C.; Lv, S.; Li, M. *Phys. Chem. Chem. Phys.,* **2016,** 18, 4835.
17. Børseth, T. M.; Svensson, B. G.; Kuznetsov, A. Y.; Klason, P.; Zhao, Q. X.; Willander, M. *Applied Physics Letters,* **2006,** 89, 262112.
18. Vanheusden, K.; Seager, C. H.; Warren, W. L.; Tallant, D. R.; Voigt, J. A. *Applied Physics Letters,* **1996,** 68, 403-405.
19. Kaftelen, H.; Ocakoglu, K.; Thomann, R.; Tu, S.; Weber, S.; Erdem, E. *Physical Review B,* **2012,** 86, 014113.
20. Lin, B.; Fu, Z.; Jia, Y. *Applied Physics Letters,* **2001,** 79, 943-945.
21. Djurišić, A. B.; Leung, Y. H.; Tam, K. H.; Hsu, Y. F.; Ding, L.; Ge, W. K.; Zhong, Y. C.; Wong, K. S.; Chan, W. K.; Tam, H. L.; Cheah, K. W.; Kwok, W. M.; Phillips, D. L. *Nanotechnology,* **2007,** 18, 095702.
22. Grabowska, J.; Meaney, A.; Nanda, K. K.; Mosnier, J. P.; Henry, M. O.; Duclère, J. R.; McGlynn, E. *Physical Review B,* **2005,** 71, 115439.
23. Chang, Y.-M.; Liu, M.-C.; Kao, P.-H.; Lin, C.-M.; Lee, H.-Y.; Juang, J.-Y. *ACS applied materials & interfaces,* **2012,** 4, 1411-1416.
24. Tan, S. T.; Sun, X. W.; Zhao, J. L.; Iwan, S.; Cen, Z. H.; Chen, T. P.; Ye, J. D.; Lo, G. Q.; Kwong, D. L.; Teo, K. L. *Applied Physics Letters,* **2008,** 93, 013506.
25. Yang, Y.; Li, Y.; Xiang, L.; Ma, X.; Yang, D. *Applied Physics Letters,* **2013,** 102, 181111.
26. Yang, Y.; Li, Y.; Jin, L.; Ma, X.; Yang, D. *Applied Physics Letters,* **2013,** 102, 021108.
27. Clapp, A. R.; Medintz, I. L.; Mattoussi, H. *ChemPhysChem,* **2006,** 7, 47-57.
28. Higuchi, S.; Ishizumi, A.; Sawahata, J.; Akimoto, K.; Kanemitsu, Y. *Physical Review B,* **2010,** 81, 035207.
29. Shimada, R.; Urban, B.; Sharma, M.; Singh, A.; Avrutin, V.; Morkoç, H.; Neogi, A. *Opt. Mater. Express,* **2012,** 2, 526-533.
30. Achermann, M.; Petruska, M. A.; Kos, S.; Smith, D. L.; Koleske, D. D.; Klimov, V. I. *Nature,* **2004,** 429, 642-646.
31. Ghosh, R.; Giri, P. K.; Imakita, K.; Fujii, M. *Nanotechnology,* **2014,** 25, 045703.
32. Ghosh, R.; Imakita, K.; Fujii, M.; Giri, P. K. *Phys. Chem. Chem. Phys.,* **2016,** 18, 7715.
33. Ghosh, R.; Giri, P. K. *RSC Adv.,* **2016,** 6, 35365.
34. Pal, A.; Ghosh, R.; Giri, P. K. *Appl. Phys. Lett.,* **2015,** 107, 072104.
35. Ghosh, R.; Pal, A.; Giri, P. K. *J. Raman Spec.,* **2015,** 46, 624.
36. Ghosh, R.; Giri, P. K. *Sci. Adv. Today,* **2016,** 2, 25230.
37. Hochbaum, A. I.; Gargas, D.; Hwang, Y. J.; Yang, P. *Nano Lett.,* **2009,** 9, 3550.
38. Qu, Y.; Zhoua, H.; Duan, X. *Nanoscale,* **2011,** 3, 4060.

39. Valenta, J.; Bruhn, B.; Linnros, J. *Nano Lett.,* **2011,** 11, 3003.
40. Barbagiovanni, E. G.; Goncharova, L. V.; Simpson, P. J. *Physical Review B,* **2011,** 83, 035112.
41. Kim, S.; COKim; Shin, D. H.; Hong, S. H.; Kim, M. C.; JKim; Choi, S.-H.; Kim, T.; Elliman, R. G.; Kim, Y.-M. *Nanotechnology,* **2010,** 21, 205601.
42. Mosquera, A. A.; Horwat, D.; Rashkovskiy, A.; Kovalev, A.; Miska, P.; Wainstein, D.; Albella, J. M.; Endrino, J. L. *Sci. Rep.,* **2013,** 3.
43. Wang, J.; Wang, Z.; Huang, B.; Ma, Y.; Liu, Y.; Qin, X.; Zhang, X.; Dai, Y. *ACS applied materials & interfaces,* **2012,** 4, 4024-4030.
44. Tauc, J.; Grigorovici, R.; Vancu, A. *physica status solidi (b),* **1966,** 15, 627-637.
45. Choudhury, B. D.; Abedin, A.; Dev, A.; Sanatinia, R.; Anand, S. *Opt. Mater. Express,* **2013,** 3, 1039-1048.
46. Lee, Y.-J.; Ruby, D. S.; Peters, D. W.; McKenzie, B. B.; Hsu, J. W. P. *Nano letters,* **2008,** 8, 1501-1505.
47. Ansari, S. A.; Khan, M. M.; Kalathil, S.; Nisar, A.; Lee, J.; Cho, M. H. *Nanoscale,* **2013,** 5, 9238-9246.
48. Kuznetsov, A. S.; Shimizu, T.; Kuznetsov, S. N.; Klekachev, A. V.; Shingubara, S.; Vanacken, J.; Moshchalkov, V. V. *Nanotechnology,* **2012,** 23, 475709.
49. Najar, A.; Slimane, A. B.; Hedhili, M. N.; Anjum, D.; Sougrat, R. *Journal of Applied Physics,* **2012,** 112, 033502.
50. Heliotis, G.; Itskos, G.; Murray, R.; Dawson, M. D.; Watson, I. M.; Bradley, D. D. C. *Advanced Materials,* **2006,** 18, 334-338.
51. Lunz, M.; Bradley, A. L.; Gerard, V. A.; Byrne, S. J.; Gun'ko, Y. K.; Lesnyak, V.; Gaponik, N. *Physical Review B,* **2011,** 83, 115423.
52. Biju, V.; Itoh, T.; Baba, Y.; Ishikawa, M. *The Journal of Physical Chemistry B,* **2006,** 110, 26068-26074.
53. Yamada, T.; Saito, T.; Suzuki, M.; Wilhite, P.; Sun, X.; Akhavantafti, N.; Fabris, D.; Yang, C. Y. *Journal of Applied Physics,* **2010,** 107, 044304.
54. Ledoux, G.; Guillois, O.; Porterat, D.; Reynaud, C.; Huisken, F.; Kohn, B.; Paillard, V. *Physical Review B,* **2000,** 62, 15942-15951.
55. Tsybeskov, L.; Vandyshev, J. V.; Fauchet, P. M. *Physical Review B,* **1994,** 49, 7821-7824.
56. Verma, D.; Kole, A. K.; Kumbhakar, P. *Journal of Alloys and Compounds,* **2015,** 625, 122-130.
57. Galli, S.; Maspero, A.; Giacobbe, C.; Palmisano, G.; Nardo, L.; Comotti, A.; Bassanetti, I.; Sozzani, P.; Masciocchi, N. *Journal of Materials Chemistry A,* **2014,** 2, 12208-12221.
58. Delerue, C.; Allan, G.; Reynaud, C.; Guillois, O.; Ledoux, G.; Huisken, F. *Physical Review B,* **2006,** 73, 235318.
59. Hartel, A. M.; Gutsch, S.; Hiller, D.; Zacharias, M. *Physical Review B,* **2013,** 87, 035428.

Chapter 8

Metal Nanoparticle Decorated Si Nanowire Heterostructures: Fabrication, Properties and Applications

Metallic nanoparticles (NPs) decorated Si nanowires (NWs) have been attracting a great deal of research interest for various applications including bio-chemical, gas sensing, photonics, solar cells and photocatalysis etc. Ag is one of the most effective metals for the growth of HSs and the unique and enhanced properties of the Ag NPs decorated Si NWs open up huge opportunities for a variety of applications in technological and industrial field. In this chapter, we have studied the Ag NPs decorated Si NWs for diverse range of applications in optics, photonics, photocatalysis and sensors.

8.1. Introduction

By incorporating additional complexities and functionalities through the heterostructure (HS) approach, it is possible to modify/improve the selective properties of the Si NWs according to the requirements. The unique and enhanced properties of the Si NWs by forming HSs open up huge opportunities for a variety of applications in technological and industrial field, such as photovoltaics, artificial photosynthesis, sensors, environmental cleaning, and micro to nanoelectronic devices etc. Among different Si NWs based HSs, metal NPs decorated HSs have drawn enormous attention from the application point of view. For example, noble metals have high work function, which can facilitate the effective separation of the photoinduced electron-hole pairs in Si NWs and the noble metal NPs decorated Si NWs show excellent photocatalytic property. Metallic NPs for plasmonics have been investigated for various applications including bio-chemical, gas sensing, photonics, solar cells and photocatalysis. Recent studies demonstrate that metal NPs decorated Si NWs-based nanohybrids exhibit remarkable enhancement in the above mentioned properties as compared to the free metallic NPs or HSs with other semiconductors. In this context, different metals, e.g. Au, Ag, Pt, Cu, Pd, Ni and Al etc. are used and studied in detail.[1-7] In most of the cases, the metal NPs were loaded on Si NWs surface by an electroless deposition technique using chemical solution. A variety of metal NPs, such as Ag,

Au, Pt, Pd, Cu, Co have been decorated on Si NWs by dipping the Si NWs into a solution containing HF and $AgNO_3$, $HAuCl_4$, H_2PtCl_6, $PdAc_2$, $Cu(NO_3)_2$, $Co(NO_3)_2$, respectively.[7] Thermal evaporation techniques have also been utilized to decorate the metal NPs on the Si NWs.[1] Interestingly, bimetal NPs, such as Au-Pd, Pd-Ni are also used to decorate on Si NWs and the HSs exhibited superior properties as compared to the case of single metal NPs decoration. Sometimes the NPs are coated on radial and branched HSs of Si NWs for improving the device performance.[2, 3] Out of different metals, Ag is the most effective material for the fabrication of multifunctional Si NWs HSs. The fabrication of Ag NPs on the surface of the Si NWs by an easy, cost effective and efficient process and its utilization in various areas of nanotechnology is very attractive.

In this chapter, we have studied the Ag NPs decorated Si NWs grown by a chemical method in HF and $AgNO_3$ solution. Au and Au-Pd bimetal thin films/NPs were decorated on Si NWs by the sputtering method. We have studied the PL properties of the metal NPs decorated Si NWs. We have investigated the origin of the enhanced PL (~1.4-3.0 eV) coming from Ag NPs loaded Si NWs. The noble metals with high work function decorated on Si NWs have shown enhanced photocatalytic activity as compared to the bare Si NWs and origin of that phenomenon is also examined. We have also studied the sensing properties of the Ag NPs decorated Si NWs as a surface enhanced Raman scattering (SERS) effective substrate for the selective and sensitive detection of methylene blue (MB). We have also explored the sensing properties of these HSs by fluorescence based detection of MB.

8.2. Fabrication of Metal NP Decorated Si NWs

8.2.1. Fabrication of Si NWs

Si NWs were grown from boron-doped p-type Si (100) wafers with resistivity 0.01 Ω-cm. A typical MACE process was used to grow the aligned Si NWs decorated with arbitrary shaped quantum sized Si NCs on its surface, as discussed in the earlier chapter and our published reports.[8-14] Details of the sample information including type of wafer, type of etching, etching conditions are described in *Chapter 2, Section 2.1* and the corresponding sample codes have been provided in the same *Section.*

8.2.2. Metal NPs Decoration on Si NWs

Ag NPs are decorated on the surface of the Si NWs by immersing the Si NWs in a solution containing 0.015 M $AgNO_3$ and 5.55 M HF for different duration (a few seconds only). A film of Ag NPs on bulk Si wafer was also created by the same process. On the other hand, Au NPs were deposited on Si NWs and Si wafer by a mini sputtering system (C7620, Polaron, UK) with fixed bias of 1 kV. The sputtering was carried out in vacuum at a current of 5 mA for different time using a pure Au target.

AgAu bimetal NPs were decorated on Si NWs by deposition of Au NPs on the Ag NPs loaded Si NWs. AuPd NPs were formed by sputtering using a AuPd target. Sample codes of the metal NPs decorated Si NWs are changed to X_metal, where X stands for the bare Si NWs sample code; for example Ag NPs decorated S1HF5 are termed as S1HF5_Ag.

8.3. Morphology and Structure of Ag NP Decorated Si NWs

8.3.1. FESEM Analysis

Fig. 8.1 shows the FESEM top-view micrographs of the sample S1HF5 (a) before and (b) after Ag NPs decoration, while (c, d) represent the corresponding cross-sectional images. Fig. 8.1(e, f) depicts the enlarged views of the selective portion in (d). The FESEM images confirm the

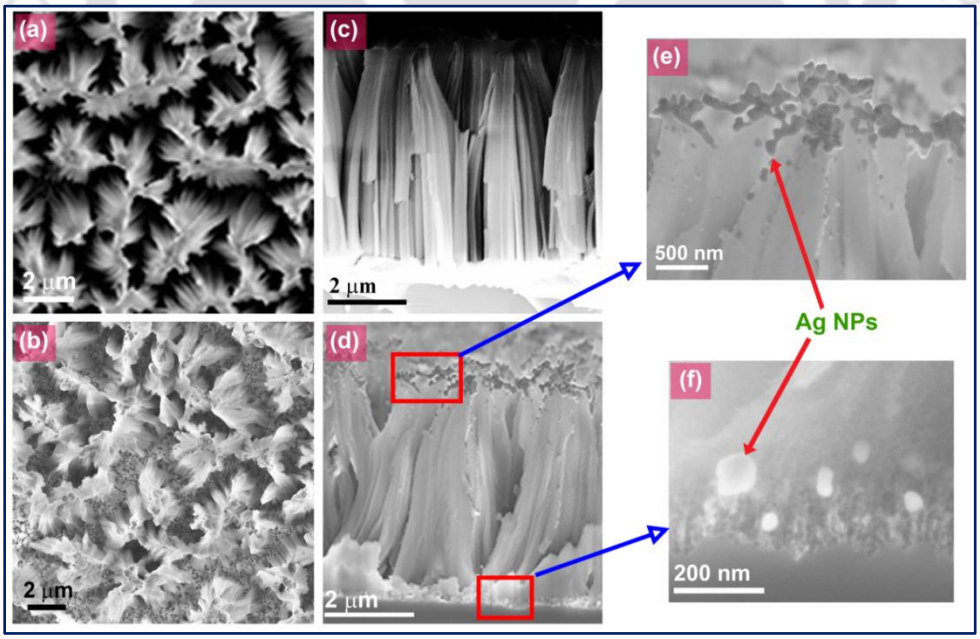

Fig. 8.1. FESEM top-view micrographs of the sample S1HF5 (a) before and (b) after Ag NPs decoration. (c, d) Corresponding cross-sectional images. (e, f) Enlarged view of selective p**o**rtions of (d). The presence of the Ag NPs is indicated in (e, f).

presence of the Ag NPs on the top, sidewall and bottom of the Si NWs. However, most of the Ag NPs are on the top and bottom of the Si NWs. Note that the average dimension of the Ag NPs is of ~30-40 nm with a wide range of diameter distribution (20-100 nm). It is seen that the Ag NPs are agglomerated near the top of the Si NWs and become large and arbitrary shaped.

8.3.2. XPS Analysis

In order to investigate the chemical composition, different oxidation states and defects, XPS studies were carried out on the sample S1HF5 before and after Ag NPs decoration. Fig. 8.2 shows the core level XPS spectra of the samples S1HF5 and S1HF5_Ag, (a) Si 2p, (b) Ag 3d and (c) O 1s, respectively. It is clear from Fig. 8.2(a) that the ~99.4 eV peak corresponding to neutral Si is diminished after Ag NPs decoration, while the other broad peak centered at ~103.0 eV corresponding to different sub-oxides of Si is unaltered. XPS provides the surface property of the

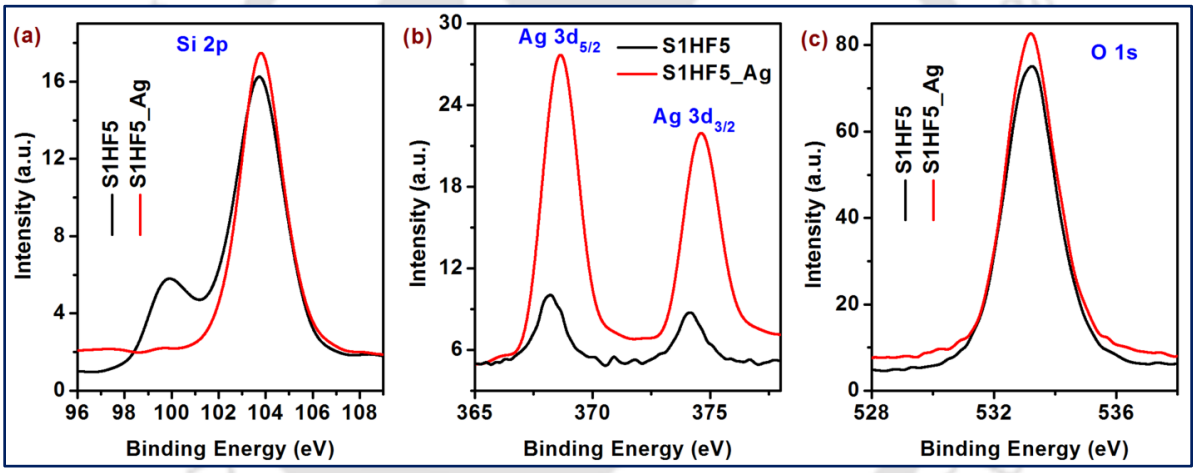

Fig. 8.2. Comparison of the Core level XPS spectra of the samples S1HF5 before & after Ag decoration: (a) Si 2p, (b) Ag 3d and (c) O 1s.

sample and information comes only from the few first nm layers. FESEM images confirm that the Ag NPs are agglomerated on the top of the Si NWs in case of sample S1HF5_Ag and thus the neutral Si peak of the HS sample is diminished in Si 2p core level XPS spectrum. The Ag 3d core level XPS spectra in Fig. 8.2(b) confirm the presence of Ag NPs on the HS sample. The Ag $3d_{5/2}$ and Ag $3d_{3/2}$ peaks are broad and indicate the presence of Ag_2O NPs, which is also confirmed from the O 1s XPS core level spectrum of the HS sample in Fig. 8.2(c).

8.4. Optical Properties of Metal NP Decorated Si NWs

8.4.1. *Reflectance Study*

In order to better understand the PL and photocatalytic properties (discussed later) of the Ag NPs decorated Si NWs, diffused reflectivity was measured for the samples under oblique incidence (P-polarized light). Fig. 8.3 shows the comparison of the diffused reflectance spectra (DRS) for samples S1HF5 and S1HF5_Ag. The diffuse reflectivity of the samples was measured by an ellipsometer (GES5-E, SEMILAB Sopra) for p-polarized light with incident angle 77˚ (Brewster angle of porous Si[15]). It is clear that the sample S1HF5_Ag shows significantly lower reflectivity over the entire visible range as compared to the sample S1HF5. Multiple reflections on the inner surface of the Si NWs, broad range of size distribution of the Si NCs and the surface plasmon resonance (SPR) effect in Ag NPs may be responsible for this ultralow reflectance or significantly high absorption in case of sample S1HF5_Ag.

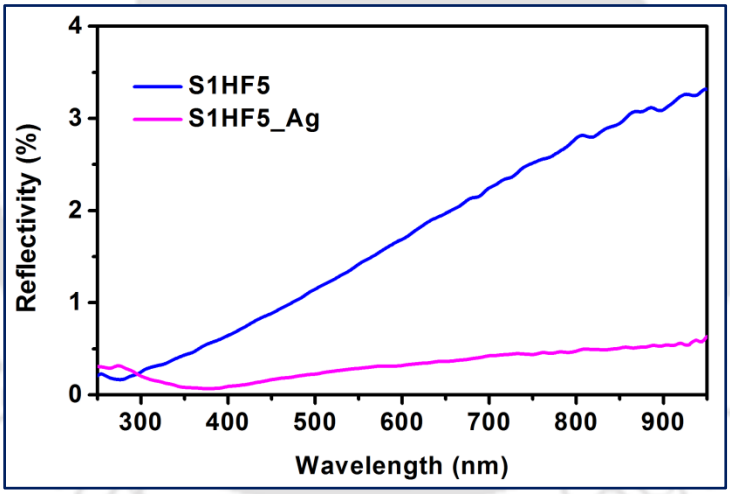

Fig. 8.3. Comparison of the diffused reflectance spectra for samples S1HF5 and S1HF5_Ag. Data was taken for p-polarized light with incident angle 77˚.

8.4.2. *Photoluminescence Study*

The MACE grown Si NWs/NCs (Sample S1HF5) exhibit high intensity, broad visible-NIR PL.[8-10, 12] It is revealed that the PL emission is due to the QC effect in Si NCs and NBOHC defects at the interface of Si-SiO_x (as discussed in *Chapter 4*).[8-10, 12] In order to understand the effect of different noble metal NPs on the PL spectra of MACE grown Si NWs/NCs, we have measured the PL spectra of the metal NPs decorated Si NWs under identical condition. Fig. 8.4 shows the

comparison of the PL spectra of the sample S1HF5 before and after different metal NPs decoration. After metal NPs decoration, the PL intensity of the samples has reduced in each case. Sample S1HF5_Ag shows the highest decrease in the PL intensity as compared to the Au or AuPd NPs decorated samples. Note that, Ag NPs were deposited by a chemical process and during the deposition, Ag NPs may have covered the pore sites of the Si NWs. Due to the covering of Ag NPs, the PL from the Si NWs/NCs may be partly absorbed by the Ag NPs. Since the absorption spectrum of the Ag NPs fall in the same range as that of PL emission energies of

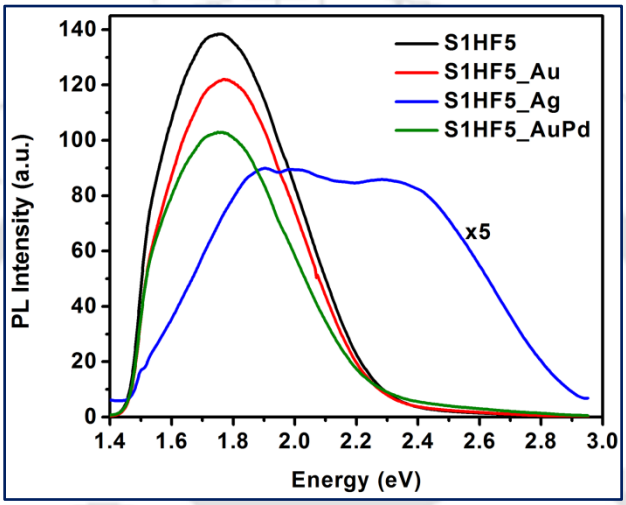

Fig. 8.4. Comparison of the PL spectra of the sample S1HF5 before and after different metal NPs decoration. PL spectrum of the sample S1HF5_Ag is scaled up by a factor 5 to enable comparison. PL measurement was carried out with 405 nm laser excitation at 10 mW power (at source).

the Si NCs, it is quite likely to reduce the PL intensity. Earlier studies suggest the enhancement in PL instead of decrease, due to SPR effect of the NPs. For example, in case of Si NCs in a SiO_2 matrix, the highest reported PL intensity enhancement in the presence of nanoscale Ag island arrays is 7-fold[16], while in case of Si NWs it is only 4-fold.[17] Huh et al.[18], Potrick et al.[19], and Goffard et al.[20] reported an enhancement by a factor of 2, 3.9 and 6 respectively, in light emission efficiency of Si NCs light-emitting diodes via SPR by employing Au NPs. Recently, 8-fold enhanced PL was reported for porous Si NWs after Au NPs decoration.[21] Similar enhancement by a factor of 3 in PL intensity in Si NWs/Au NPs composite was reported by Au-catalyzed chemical etching method.[22] The enhancement in PL efficiency was explained in terms of radiative energy exchange between Si NCs and metal NPs due to enhanced radiative coupling of exciton-plasmon.[19, 22] In the present case we have not seen any kind of enhancement in PL of Si NWs/NCs after metal NPs incorporation, instead we obtained decreased intensity of PL. The

decreased intensity of PL can also be explained by the phenomena at the Schottky junction between Si and the metal NPs. Because of the differences in the Fermi levels (EF) between the metal and the Si band structure, Schottky barrier is introduced in between the metal NPs and Si NWs/NCs. The built-in potential at the Schottky diode junction can facilitate the efficient separation of photogenerated e-h pairs and reduce the radiative recombination which results in the decreased PL. Shao et al. reported that the high work function (Φ) of the noble metals accelerate the electron from conduction band of semiconductor to metal and reduce the radiative recombination rate.[5] This phenomenon can be helpful for the photocatalytic degradation of the organic dye (discussed later).[9, 10] Furthermore, the electronegativity of the noble metal (Au, Ag or AuPd bimetal) is higher than that of Si.[9] Hence, these metal NPs can accelerate the separation of photoinduced e-h pairs better, which can decrease the radiative recombination, hence the PL intensity.

It is clear from Fig. 8.4 that the PL spectrum of the sample S1HF5_Ag is much broader than the S1HF5 and it covers the whole visible range (1.4-3 eV). The density of the Ag NPs can be increased by increasing the deposition time. Fig. 8.5(a) shows a comparison of the PL spectra of the sample S1HF5_Ag for different deposition time of Ag NPs, while (b) shows PL spectrum of the sample bulk Si_Ag. The PL intensity is decreased when the thickness of the Ag NPs becomes high. The spectral shape also changes with increasing the thickness of the Ag NPs. In

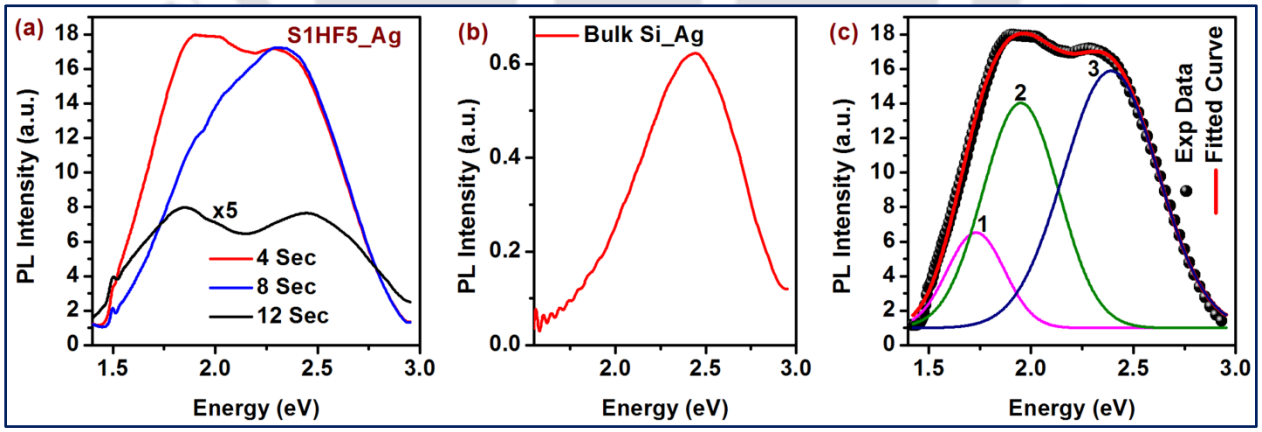

Fig. 8.5. (a) Comparison of the PL spectra of the sample S1HF5_Ag for different deposition time of Ag NPs. PL spectrum of the sample S1HF5_Ag for 12 sec deposition time is scaled up to enable comparison. (b) PL spectrum of the sample Bulk Si_Ag. (c) The fitted PL spectrum of the sample S1HF5_Ag for 4 sec Ag deposition time.

order to understand the origin of the broad PL and the effect of different species, we have fitted the PL spectrum of the sample S1HF5_Ag by 3 Gaussian bands. Fig. 8.5(c) shows the

deconvoluted PL spectrum of the sample S1HF5_Ag (deposition time, 4 sec). Peak 3 centered at ~2.4 eV is generally attributed to electronic transitions between the upper d band and conduction sp band of Ag NPs.[23] Note that the sample Bulk Si_Ag also possesses the same peak due to the Ag NPs. Yeshchenko et al. reported that this PL of Ag NPs is due to the radiative decay of SPR excited in NPs.[24] It was clear from the XPS spectra that the mix states of Ag and Ag_2O were present in the sample S1HF5_Ag. According to Gangopadhyay et al., the 2.4 eV PL is attributed to the band-to-band radiative transition in Ag_2O.[25] Other two peaks i.e. peak 1 and peak 2, centered at ~1.73 eV and ~1.94 eV are due to the QC effect in Si NCs and NBOHC defects in the interface of Si-SiO_x, respectively (as discussed in *Chapter 4*).[8-10, 12] Though the intensity of the PL of Si NWs/NCs is reduced after Ag NPs decoration, the broad PL covering the entire visible range which opens up the possibility of using Ag NPs decorated Si NWs in the fabrication of white light LED.

8.4.3. *Photocatalysis Study*

As discussed in Chapter 6, the excitons generated within the mesoporous Si NWs could be energetic enough to drive photoelectrochemical reactions due to its wide range of optical absorption with high intensity and broad visible emission centered near the red-infrared region. It was revealed that the electron deficient Si-H surface states present in the MACE grown Si NWs/NCs samples serve as electron sink and hence accelerate the separation of photoinduced e-h pairs, which facilitate the photocatalytic activity of the Si NWs/NCs.[9, 10] We have studied the visible light photocatalytic activities of different metal NPs decorated Si NWs/NCs for the degradation of MB. Fig. 8.5(a) shows the comparison of the photodegradation efficiencies of sample S1HF5 decorated with different metal NPs, while (b) shows the corresponding rate constant (k) of the respective samples considering the 1st order degradation rate kinetics (as discussed in Section 6.6, Chapter 6).[9, 10] We observed that after the metal NPs decoration, photodegradation efficiency increases for some of the samples (S1HF5_Ag and S1HF5_AuPd), while it decreases for other samples (S1HF5_Au and S1HF5_AgAu). This type of mixed photocatalytic behavior was also observed in earlier studies.[4, 5] For example, Shao et al. have shown that the photodegradation efficiency (in RhB) of H-Si NWs are higher than the Ag, Au or Pd coated Si NWs.[5] The charge separation capabilities of Si-H bonds are better for some of the noble metals. In the present case, the metal deposition partially removes/covers Si-H bonds in the samples, which are responsible of the decrease in the photocatalytic efficiencies.

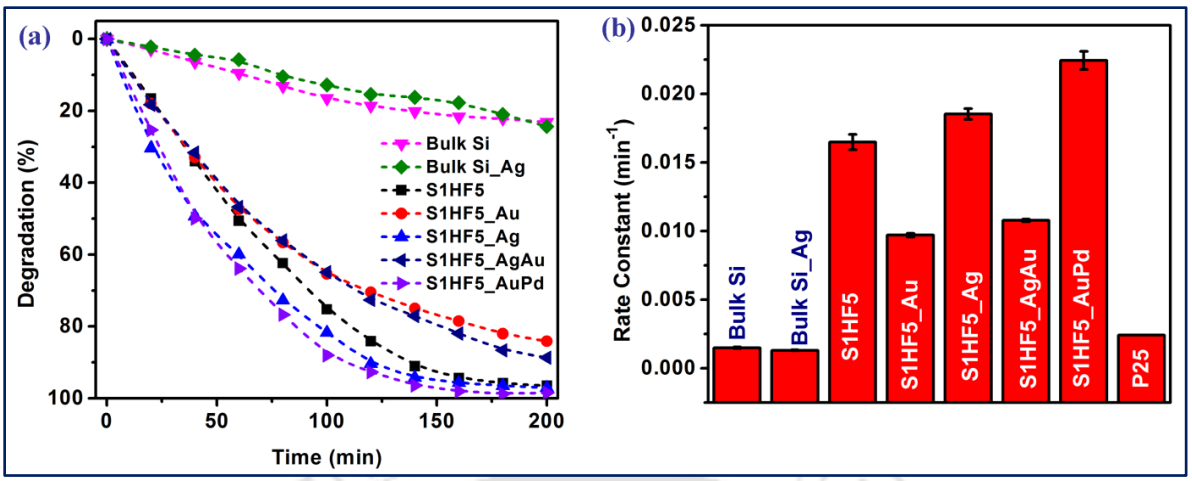

Fig. 8.5. (a) Comparison of the photodegradation efficiencies of sample S1HF5 decorated with different metal NPs. (b) Comparison of the rate constants for different samples.

Note that, we have observed enhanced photodegradation for the samples S1HF5_Ag and S1HF5_AuPd. The enhancement can be explained in the following way. The differences in the Fermi levels can introduce a Schottky barrier between the metal NPs and Si NWs/NCs. The schematic diagram of the MACE grown Si NWs/NCs decorated with metal NPs along with the band alignment is shown in Fig. 8.6. The possible charge separation in presence of Si-H bonds and metal NPs, and the dye degradation mechanism are schematically illustrated in Fig. 8.6. The built-in potential at the Schottky junction can facilitate the efficient separation of photogenerated e-h pairs and influence the degradation of the dye strongly.[9, 10] The charge separation occurs due to the charge transfer from the CB of Si to metal. Note that the additional effect of charge separation (instead of only Si-H) in sample S1HF5_Ag and S1HF5_AuPd is responsible for the enhanced rate constant as shown in Fig. 8.5(b). On the other hand, the electronegativity of the noble metals Au, Ag or Ag/Au bimetal is higher than that of Si.[9] Hence, these metal NPs can accelerate the separation of photoinduced e-h pairs better, which can increase the photocatalytic activity of the HS samples.[4, 5, 9, 10] Shao et al. reported that the photocatalytic activity of metal-semiconductor catalysts depends largely on the electron work function (Φ) of metals, which is a key parameter in the electron transfer process from conduction band of semiconductor to metal.[5] The charge transfer process is enhanced for the metal with higher Φ.[5] Pd has a higher value of Φ (5.12 eV) as compared to the other metals we have used in the present study. Thus, the rate constant is maximum when Pd is incorporated as bimetal in AuPd coated Si NWs/NCs. Liao et al. reported that AuPd bimetal decoration on Si NWs results

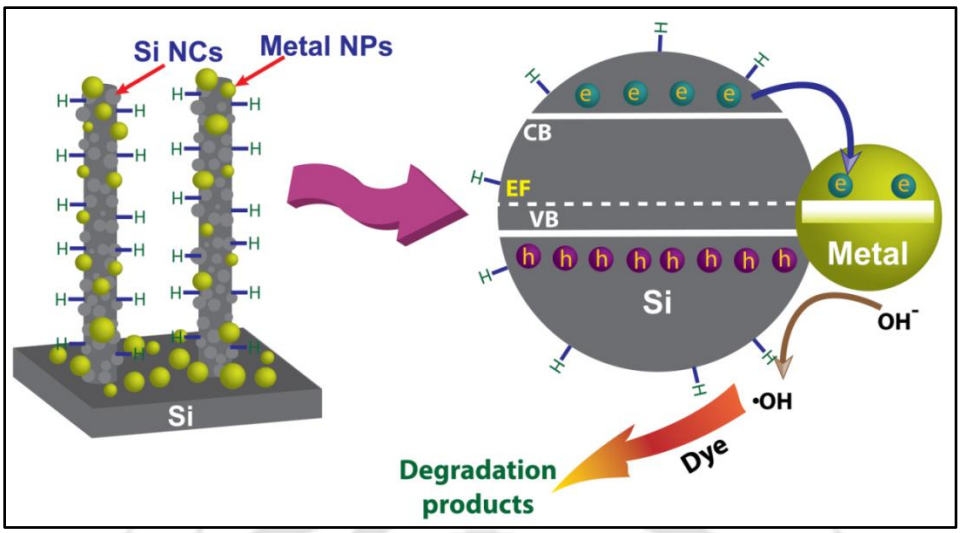

Fig. 8.6. Illustration of photocatalysis mechanism by metal NPs decorated Si NWs/NCs describing the e-h pair production, effective charge separation and dye degradation.

in the higher degradation rate of p-nitroaniline as compared to the single metal decorated Si NWs.[26] However, SPR related broad visible absorption due to these metal NPs can also function as the catalysts to facilitate certain redox reactions to degrade MB dye.[9, 10, 27] Note that after Ag decoration, the PL intensity decreases and photodegradation efficiency increases which confirm the effective charge separation in the sample S1HF5_Ag.

8.4.4. *Optical Sensing and SERS Detection Using Mesoporous Si NWs*

Metal NPs decorated Si NWs provide excellent charge transport properties, biocompatibility and environment friendly nature and are demonstrated as excellent candidate for sensing of chemical and biological molecules.[28-35] Different sensitive methods, including optical-based detection (surface enhanced Raman scattering (SERS) or fluorescence), mechanical based detection (cantilevers), and electrical-based detection (FET) are attractive in a number of sensing applications. Out of these different sensing methods, optical-based detection process is most interesting and non-destructive method for the selective, sensitive and quantitative detection of bio-chemical species. Here, we have studied the optical sensor based on Ag NPs decorated Si NWs.

8.4.4.1. *Fluorescence Detection of Methylene Blue*

Optical sensor based on PL spectroscopy is one of the well-known sensing techniques for the detection of biological species. Metal NPs decorated Si NWs have been used as a fluorescence

sensor for the selective detection of bio-chemical species, gas molecules and heavy metal ions.[34, 36, 37] We have used Ag NPs decorated Si NWs/NCs for the detection of the organic molecule MB by the PL sensing technique. We have examined the PL spectra of the sample S1HF5_Ag in presence of MB at different concentrations. For doing so, we have kept the pieces of sample S1HF5_Ag in aqueous solution of MB with different concentrations. We performed the same experiment for the bulk Si as well. The samples are kept in dark for 12 hours, to adsorb the MB fully. The sample code after MB adsorption is S1HF5_Ag_MB and Bulk Si _MB, respectively. Fig. 8.7(a) shows a comparison of the PL spectra of the sample S1HF5_Ag in presence of MB at different concentrations. Fig. 8.7(b) shows the change in PL peak intensity of sample S1HF5_Ag (red) and Bulk Si (black) as a function of MB concentration in nanomolar level. The PL intensity of S1HF5_Ag and bulk Si are shown by the dashed lines. It is clear that the PL peak intensity of MB is strongly enhanced in case of sample S1HF5_Ag as compared to the bulk Si for different

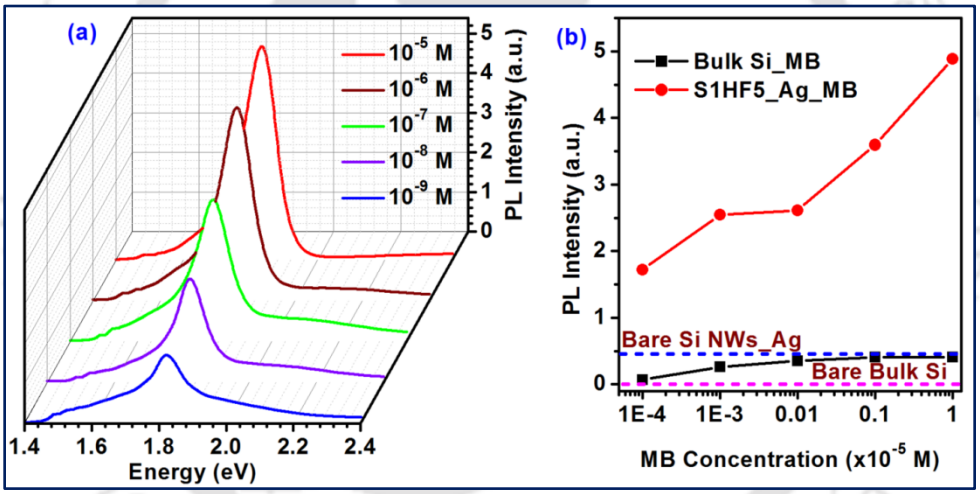

Fig. 8.7. (a) Comparison of the PL spectra of the sample S1HF5_Ag in presence of MB at different concentrations. (b) PL peak intensity of sample S1HF5_Ag (red) and Bulk Si (black) as a function of MB concentration. The PL intensity of S1HF5_Ag and Bulk Si are shown by the horizontal dashed lines.

concentration of MB. This enhancement can be explained by the following way: (a) enhanced surface area of Si NWs/NCs; (b) density of pores on the Si NWs surface, which are active sites for the attachment of MB molecules, and (c) the SPR enhanced PL due to the presence of Ag NPs. Ag NPs decorated Si NWs can detect MB ~25 times more efficiently as compared to bulk Si even at extremely low concentration (10^{-9} M). So, the Ag NPs decorated Si NWs can be used as fluorescence based sensor for the selective detection of organic species. Note that the detection limit of the sensor can be increased by tuning the (a) length of the Si NWs, (b) porosity

of the Si NWs, (c) size, density and thickness of the Ag NPs, (e) the optical excitation intensity and (f) detector sensitivity of the spectrometer.

8.4.4.2. *SERS Detection of Methylene Blue*

Optical based SERS detection by metal NPs decorated Si NWs HSs is another efficient way of sensing chemical and biological molecules with surface-seeking groups, since only molecules on or near the metal surface experience the large near-field enhancements upon resonant plasmon excitation. Si NWs coated with metal NPs, mainly Ag, Au, Pd, Cu, and Pt have been used as SERS effective substrates for sensing a variety of inorganic and organic molecules. In order to understand the SERS effect in Ag NPs decorated Si NWs, we have carried out Raman measurement of MB with extremely low concentration (10^{-6} M) on the sample S1HF5_Ag. We have kept one piece of sample S1HF5_Ag and bulk Si in MB solution (10^{-6} M) in dark for 12 hours to adsorb it fully. Raman measurement of the samples was carried out with 514 nm laser

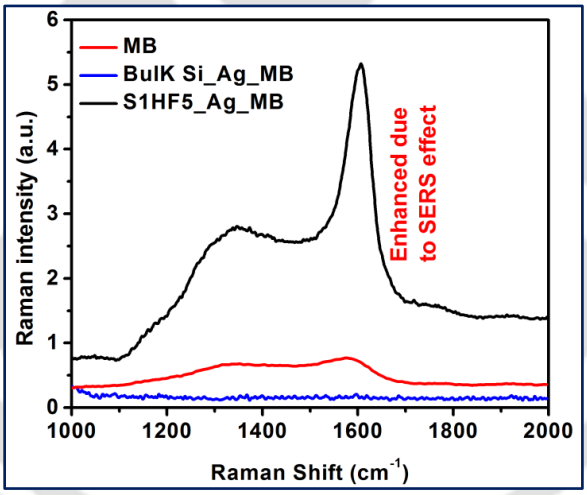

Fig. 8.8. Comparison of the Raman spectra of the samples S1HF5_Ag_MB (black line), Bulk Si_Ag_MB (blue line) and the bulk MB powder (red line).

excitation with 1.2 mW laser power. Raman spectrum of the bulk MB powder was also taken under identical condition. Fig. 8.8 shows a comparison of the Raman spectra of 10^{-6} M concentrated MB for samples S1HF5_Ag_MB (black line), Bulk Si_Ag_MB (blue line) and the bulk MB powder (red line). We have observed high intensity peaks centered at ~1606 cm^{-1} and ~1344 cm^{-1} for the MB solution. The ~1606 cm^{-1} peak is attributed to aromatic ring vibrations, while ~1344 cm^{-1} peak is due to C-N symmetrical and asymmetrical vibration in MB structure.[38] We did not observe any peak corresponding to MB in case of sample Bulk Si_Ag_MB at this

concentration. However, the peak at ~1606 cm^{-1} of sample S1HF5_Ag_MB is enhanced by ~7 times as compared to the bulk MB powder due to the SERS effect of Ag NPs on the Si NWs. These results are very promising for the high sensitive SERS detection of organic and bio-molecules with Si NWs

8.5. Conclusion

In this chapter, we have fabricated Ag NPs decorated mesoporous Si NWs by a very simple and easy chemical process. The broad band white light PL emission from the HS samples was explained in light of emission from Ag NPs, QC effect in Si NCs and the NBOHC defects in the Si-SiO_x interface. The reduced intensity in PL emission is attributed to the reduced radiative recombination due to the efficient electron transfer from Si conduction band to the metal at the Schottky junction. High work function of the noble metal NPs facilitate the effective separation of the photoinduced electron-hole pairs in Si NWs and the Au-Pd bimetal NPs decorated Si NWs show highest photocatalytic efficiency. The Ag NPs decorated Si NWs exhibited high potential and sensitivity for the selective and quantitative detection of MB even with extremely low concentration (10^{-9} M) by both SERS effective Raman analysis and fluorescence detection. These versatile properties of the Ag NPs decorated Si NWs open up huge opportunities for a variety of energy and environmental applications, such as white LED, solar cell, artificial photosynthesis, disposal of organic pollutant and bio-chemical sensors.

References

1. Convertino, A.; Cuscunà, M.; Martelli, F.; Manera, M. G.; Rella, R. *J. Phys. Chem. C,* **2014,** 118, 685.
2. Wang, X.; Peng, K.-Q.; Pan, X.-J.; Chen, X.; Yang, Y.; Li, L.; Meng, X.-M.; Zhang, W.-J.; Lee, S.-T. *Angew. Chem. Int. Ed.,* **2011,** 50, 9861.
3. Yenchalwar, S. G.; Azhagan, V. K.; Shelke, M. V. *Phys. Chem. Chem. Phys.,* **2014,** 16, 17786.
4. Megouda, N.; Cofininier, Y.; Szunerits, S.; Hadjersi, T.; ElKechai, O.; Boukherroub, R. *Chem. Comm.,* **2011,** 47, 991.
5. Shao, M.; Cheng, L.; Zhang, X.; Ma, D. D. D.; Lee, S. T. *J. Am. Chem. Soc.,* **2009,** 131, 17738.
6. Brahiti, N.; Hadjersi, T.; Menari, H.; Amirouche, S.; El Kechai, O. *Mater. Res. Bul.,* **2015,** 62, 30.
7. Fang, C.; Agarwal, A.; Widjaja, E.; Garland, M. V.; Wong, S. M.; Linn, L.; Khalid, N. M.; Salim, S. M.; Balasubramanian, N. *Chem. Mater.,* **2009,** 21, 3542.
8. Ghosh, R.; Giri, P. K.; Imakita, K.; Fujii, M. *Nanotechnology,* **2014,** 25, 045703.
9. Ghosh, R.; Imakita, K.; Fujii, M.; Giri, P. K. *Phys. Chem. Chem. Phys.,* **2016,** 18, 7715.
10. Ghosh, R.; Giri, P. K. *RSC Adv.,* **2016,** 6, 35365.
11. Pal, A.; Ghosh, R.; Giri, P. K. *Appl. Phys. Lett.,* **2015,** 107, 072104.

12. Ghosh, R.; Pal, A.; Giri, P. K. *J. Raman Spec.,* **2015,** 46, 624.
13. Ghosh, R.; Giri, P. K. *Sci. Adv. Today,* **2016,** 2, 25230.
14. Ghosh, R.; Giri, P. K.; Imakita, K.; Fujii, M. *J. Alloy Compd.,* **2015,** 638, 419.
15. Lublow, M.; Kubala, S.; Veyan, J.-F.; Chabal, Y. J. *J. Appl. Phys.,* **2012,** 111, 084302.
16. Biteen, J. S.; Lewis, N. S.; Atwater, H. A.; Mertens, H.; Polman, A. *Appl. Phys. Lett.,* **2006,** 88, 131109.
17. Chern, W.; Hsu, K.; Chun, I. S.; Azeredo, B. P. d.; Ahmed, N.; Kim, K. H.; Zuo, J.-m.; Fang, N.; Ferreira, P.; Li, X. *Nano Lett.,* **2010,** 10, 1582.
18. Huh, C.; Choi, C.-J.; Kim, W.; Kyu Kim, B.; Park, B.-J.; Jang, E. H.; Kim, S.-H.; Yong Sung, G. *Appl. Phys. Lett.,* **2012,** 100, 181108.
19. Potrick, K.; Huisken, F. *Phys. Rev. B,* **2015,** 91, 125306.
20. Goffard, J.; Gérard, D.; Miska, P.; Baudrion, A.-L.; Deturche, R.; Plain, J. *Sci. Rep.,* **2013,** 3, 2672.
21. Tang, H.; Liu, C.; He, H. *RSC Adv.,* **2016,** 6, 59395.
22. Bassu, M.; Strambini, M. L.; Barillaro, G.; Fuso, F. *Appl. Phys. Lett.,* **2010,** 97, 143113.
23. Mooradian, A. *Phys. Rev. Lett.,* **1969,** 22, 185.
24. Yeshchenko, O. A.; Dmitruk, I. M.; Alexeenko, A. A.; Losytskyy, M. Y.; Kotko, A. V.; Pinchuk, A. O. *Phys. Rev. B,* **2009,** 79, 235438.
25. Gangopadhyay, P.; Kesavamoorthy, R.; Bera, S.; Magudapathy, P.; Nair, K. G. M.; Panigrahi, B. K.; Narasimhan, S. V. *Phys. Rev. Lett.,* **2005,** 94, 047403.
26. Liao, F.; Wang, T.; Shao, M. *J. Mater. Sci: Mater. Electron.,* **2015,** 26, 4722.
27. Qu, Y.; Zhong, X.; Li, Y.; Liao, L.; Huangbc, Y.; Duan, X. *J. Mater. Chem.,* **2010,** 20, 3590.
28. Luo, L.; Jie, J.; Zhang, W.; He, Z.; Wang, J.; Yuan, G.; Zhang, W.; Wu, L. C. M.; Lee, S.-T. *Appl. Phys. Lett.,* **2009,** 94, 193101.
29. Huang, Y.; Ferhan, A. R.; Cho, S.-J.; Lee, H.; Kim, D.-H. *ACS Appl. Mater. Int.,* **2015,** 7, 17582.
30. Wipf, M.; Stoop, R. L.; Tarasov, A.; Bedner, K.; Fu, W.; Wright, I. A.; Martin, C. J.; Constable, E. C.; Calame, M.; Schönenberger, C. *ACS Nano,* **2013,** 7, 5978.
31. Zhang, C. X.; Liu, L.; Yin, H. J.; Fang, H.; Zhao, Y. M.; Bi, C. J.; Xu, H. J. *Appl. Phys. Lett.,* **2014,** 105, 011905.
32. Shao, M.-W.; Zhang, M.-L.; Wong, N.-B.; Ma, D. D.-d.; Wang, H.; Chen, W.; Lee, S.-T. *Appl. Phys. Lett.,* **2008,** 93, 233118.
33. Xu, T.-T.; Huang, J.-A.; He, L.-F.; He, Y.; Su, S.; Lee, S.-T. *Appl . Phys. Lett.,* **2011,** 99, 153116.
34. Su, S.; Wei, X.; Zhong, Y.; Guo, Y.; Su, Y.; Huang, Q.; Lee, S.-T.; Fan, C.; He, Y. *ACS Nano,* **2012,** 6, 2582.
35. Han, S. W.; Lee, S.; Hong, J.; Jang, E.; Lee, T.; Koh, W.-G. *Biosensors and Bioelectronics,* **2013,** 45, 129.
36. Zhuo, S.; Shao, M.; Cheng, L.; Que, R.; Zhuo, S.; Duo Ma, D. D.; Lee, S.-T. *Appl. Phys. Lett.,* **2010,** 96, 103108.
37. Wang, H.; Mu, L.; She, G.; Shi, W. *RSC Adv.,* **2015,** 5, 65905.
38. He, Y.; Han, X.; Chen, D.; Kang, L.; Jin, W.; Qiang, R.; Xu, P.; Du, Y. *RSC Adv.,* **2014,** 4, 7202.

Chapter 9

Summary and Outlooks

The highlights of the major contributions of the thesis and important conclusions of the work are presented in this chapter. New findings on the controlled growth and formation mechanism of Si nanostructures; identification of defects in surface of the nanostructures; the origin and tunability of photoluminescence properties and its quantitative analysis based on quantum confinement effect; quantitative analysis of the phonon confinement effect in arbitrary shaped Si NCs decorated Si NWs are summarized. New findings on the Si-ZnO heterostructure and its optical properties are also concluded. The usefulness and versatility of the Ag nanoparticles decorated Si nanowires are summarized. Open questions and scope for future work are also presented at the end.

9.1. Summary

In this dissertation, we have presented the controlled growth of 1D mesoporous Si nanowires array by an easy and inexpensive MACE method and elucidated the formation mechanism of 1D Si nanowires (NWs) by a novel scaling approach. We have controlled the morphologies of the as-synthesized Si NWs decorated with arbitrary shaped ultra-small Si NCs by controlling various etching parameters (Chapter 3). We have investigated the effects of different growth conditions and the measurement parameters on the strong visible-NIR photoluminescence (PL) of the Si NWs/NCs for understanding the origin of the strong PL as well as the its tunability (Chapter 4). We quantitatively analyzed the PL and Raman spectra of mesoporous Si NWs based on the electron and phonon confinement models, respectively, and demonstrated its applicability even for arbitrary shaped Si NCs that are self-grown on the mesoporous Si NWs (Chapter 5). We observed highly efficient visible light photocatalysis by the Si NWs/NCs for the photodegradation of methylene blue (MB). We have tuned the etching conditions for understanding the origin of the strong photocatalytic nature of Si NWs/NCs and explained the occurrence of the two contrasting phenomena, PL and photocatalysis from the same MACE grown Si NWs/NCs (Chapter 6). We have observed red shift and reduced intensity in the visible PL of the Si NWs/NCs after forming Si-ZnO core-shell heterostructures (HSs), which is

elucidated on the basis of resonant energy transfer from defect site of ZnO layer to the proximal Si NCs (Chapter 7). We have observed white light emission, enhanced photocatalytic efficiency, exciting SERS effect and fluorescence based ultrasensitive detection of MB with Ag nanoparticles (NPs) decorated Si NWs. We have elucidated these versatile properties of the Ag NPs decorated Si NWs in the light of SPR effect in Ag NPs and Schottky effect in the metal-Si interface (Chapter 8).

The major contributions and new findings of the present thesis are summarized below.

9.2. Highlight of the Thesis Contributions

9.2.1. Critical Growth Parameters for the Morphology Controlled Growth of Si NC Decorated Si NWs

We have fabricated large area, highly oriented and controlled array of Si NWs by a very simple, easy, fast and cost effective MACE process. The etching mechanism of Si by MACE is elucidated by systematic studies on Ag assisted chemical etching of Si and for the first time, we have demonstrated that the early stages of growth of NWs resembled the shadowing instability model explaining columnar growth of Si NWs during MACE. The Si NWs are highly crystalline and decorated with arbitrary shaped quantum size Si NCs due to the sidewall etching during Si NWs formation. We have systematically investigated the impact of etching parameters on the morphologies and structure of the as-synthesized Si nanostructures. A wide variation in morphology in terms of length, diameter and porosity of the Si NWs and structures were observed. The possible reason for the formation of wide varieties of morphologies may be due to the oxidation ability of different etching solutions and their relative concentration; the nature of the noble metal catalysts as well as their shape, size and interspacing; doping nature and orientation of the initial Si wafer; and the etching duration. These parameters have a strong effect on the structure and surface defects of the as-grown Si NWs, thus ultimately influencing their photophysical properties. Ag/Au bimetal assisted etching of Si provides improved morphology over conventional single Ag or Au metal layer as a catalyst for the MACE growth of Si NWs/NCs. MACE grown Si NWs/NCs are covered by a layer of amorphous Si-H and SiO_x and NBOHC defects are present within the SiO_x layer, which are very significant to explain the coexistence of excellent photoluminescence and efficient photocatalytic properties of MACE grown Si. The density of the Si NCs, defect centers and Si-H terminated sites are tunable and can

be controlled by the etching parameters. Thus, the Si NWs/NCs with tunable morphology and optical properties are extremely important for device applications. Due to the ease of control over the morphology and structure of the as-synthesized Si NWs, the solution based MACE can be used as an inexpensive but significant tool for the rapid fabrication of high quality, large area, aligned and well controlled Si NWs as compared to the other conventional Si NWs fabrication methods.

9.2.2. Elucidating the Origin of Visible and NIR Photoluminescence from the Mesoporous Si Nanowires

We have observed tunable visible-NIR PL at room temperature (RT) from the MACE grown Si NWs/NCs. Through quantitative analysis, it is revealed that the broad band and tunable PL emission originates from the combined effect of QC in self-grown Si NCs on Si NWs and the NBOHC defects in SiO_x layer. We have identified the mechanism of the enhancement and broadening of the PL from the mesoporous Si NWs by the systematic investigation of the following parameters: (a) nature of the noble metal catalyst, (b) the nature of etching solution and its concentration, (c) the doping type, resistivity and the orientation of the Si wafer, (d) etching duration, (e) post HF treatment on the samples, (f) laser excitation power and the laser exposure time and (g) low temperature PL measurement. Interestingly, one-step etched Si NWs in $AgNO_3$/HF solution, which is covered with thick layer of Si sub-oxide shows additional sharp NIR PL at ~1.1 eV at RT, which is distinctly different from the size dependent and NBOHC defect mediated visible-NIR PL from mesoporous Si NWs. For the first time, the NIR PL emission is observed in Si NWs at RT and it is attributed to phonon assisted radiative recombination of EHP inside the core of the Si NWs. Our observations and conclusions are strongly supported by the TRPL, Raman, XPS, FTIR, DRS and HRTEM analysis. This MACE grown Si NWs/NCs are beneficial for the low-cost production of solar cells, photodiode, LED and other optoelectronic applications in the field of nanotechnology.

9.2.3. Quantitative Analysis of the Phonon & Electron Confinement Effect in the Arbitrary Shaped Si NCs based on Raman and PL Studies

We have observed a considerable red shift and lower energy asymmetry in 1^{st} order Raman peak of Si for the mesoporous Si NWs. Despite of the effect of compressive strain in Raman spectra, it is revealed that the QC of phonons in the Si NCs is responsible for the red shift and asymmetric

broadening of the Raman spectra. We have quantitatively analyzed the Raman spectra of the Si NWs/NCs and calculated the size distributions of Si NCs in terms of their mean diameter and skewness of the distribution. The size distribution of the Si NCs follows the typical skew-symmetric Gaussian nature with positive skewness and is fairly consistent with the size calculation based on the QC of electron through the PL analysis. The calculated size distribution of Si NCs from the PL and Raman spectra is comparable with the size distribution obtained from the HRTEM analysis. Such a correlation between Raman and PL spectra allows non-destructive and spectroscopic evaluation of the accurate size distribution of the Si NCs on the surface of the Si NWs even for arbitrary shaped Si NCs.

9.2.4. Efficient Photocatalytic Degradation of Organic Dyes by Mesoporous Si Nanowires

We observed high efficiency visible light photocatalysis of MB by the mesoporous Si NWs. Our systematic studies confirm that the electron deficient Si-H surface states present in the Si NWs/NCs samples serve as an electron sink and accelerate the separation of photoinduced e-h pairs, which facilitate the photocatalytic activity of the Si NWs/NCs. The unaltered metal NPs during etching also accelerate the separation of photogenerated e-h pairs through the Schottky junction between Si-metal and influence the degradation of the dye strongly. We are able to enhance the photocatalytic efficiency and stability of the Si NWs/NCs by tuning the following parameters: (a) nature of the noble metal catalyst, (b) the nature of etching solution and its concentration, (c) the doping type, resistivity and the orientation of the Si wafer, (d) etching duration, (e) post HF treatment on the samples and (f) the ionic nature of the organic dyes. XPS, FTIR and Raman spectra support our conclusions. We have achieved the specific etching condition for which the MACE grown mesoporous Si NWs are able to utilize the entire visible spectrum of light for the degradation of MB and its degradation efficiency is higher than the commercial photocatalyst P25. For the first time, we have observed and explained the mechanism behind the coexistence of two contrasting phenomena, PL and photocatalysis in the same Si NWs/NCs. Thus, the MACE grown Si NWs/NCs are highly beneficial for the replacement of P25 in visible light photocatalytic applications, such as artificial photosynthesis and environmental cleaning.

9.2.5. Multifunctional Si NW Heterostructures: Tunable Photoluminescence, Efficient Photocatalytic Performance and SERS Detection

We have fabricated Si-ZnO core-shell NW HSs by sputter deposited ZnO thin film on MACE grown Si NWs. We have analyzed the mechanism of red-shift and partial quenching in visible PL emission from arbitrary shaped Si NCs decorated on the Si NWs after coating of ZnO thin film on it. In order to explain the observation, for the first time we have invoked the Forster resonant energy transfer (FRET) from the defect affected ZnO layer to the proximal Si NCs. It is believed that due to the ultrathin intermediate dielectric SiO_x layer, the energy is transferred by the FRET process from the defect induced recombination of the carries in the ZnO shell that excites the Si NCs core close to the defects and the subsequent de-excitation process gives rise to red shifted visible PL emission via radiative recombination. Both the PL intensity and the PL decay time of the Si NCs are reduced in presence of the ZnO layer due to the formation of heterojunctions of Si NCs and ZnO that promote efficient energy transfer. This work is important for the development of Si-based LEDs using HS approach. The hybrid nanostructures exhibit extremely high absorption in the entire UV-visible-NIR range, which is important for efficient solar energy harvesting across the entire UV-visible-NIR solar spectrum based on the concept of core-shell Si-ZnO NW heterostructures.

In order to utilize the MACE grown mesoporous Si NWs in multiple areas of nanotechnology and to improve the photophysical properties of the Si NWs/NCs, we have fabricated different metal (Ag, Au, AgAu, and AuPd) NP decorated on Si NWs/NCs. We have observed enhanced/modified optoelectronic properties of the Si NWs/NCs after the metal NP decoration. A broad (1.4-3.0 eV) white light emission was observed for the Ag NPs decorated Si NWs/NCs, which was explained in the light of Ag NP emission, QC effect in the Si NCs and the NBOHC defects in the Si-SiO_x interface. The reduced intensity of PL after metal NPs decoration of the Si NWs/NCs is attributed to the reduced radiative recombination due to the efficient electron transfer from Si conduction band to the metal at the Schottky junction. High work function of the noble metal NPs simply enable the effective separation of the photoinduced electron-hole pairs in Si NWs/NCs and the Au-Pd bimetal NPs decorated Si NWs/NCs show highest visible light photocatalytic efficiency (much higher than commercial P25). The Ag NPs decorated Si NWs have shown substantial potential and sensitivity for the selective and quantitative detection of MB even with extremely low concentration (10^{-9} M) by both SERS

effective Raman analysis and fluorescence based detection. These versatile properties of the metal NPs decorated mesoporous Si NWs open up huge opportunities for a variety of energy and environmental applications of the HSs in daily life, such as white LED, solar cell, artificial photosynthesis, disposal of organic pollutant and bio-chemical sensors etc.

9.3. Future Scope

Herein, we have demonstrated the fabrication of well-controlled high quality Si NWs/NCs using an inexpensive and easy MACE process by controlling the suitable etching conditions and the growth mechanism of Si NWs is explained by an appropriate model. Since the photophysical properties of the Si NWs/NCs strongly depends on the morphology, structure and the surface/interface properties of the Si NWs/NCs, we are able to control the emissive nature and photocatalytic nature of the Si NWs/NCs by controlling the growth parameters. For further improvement/modification of the photophysical properties of the MACE grown Si NWs, we have fabricated high quality Si-ZnO and different metal NPS decorated Si NWs. These Si NWs and the metal NPs decorated Si NWs have shown enough potential for different energy and environmental applications. We are quite affirmative about the real life applications of the Si NWs and its HSs with superior performances, since the properties are being improved continuously through the newer findings. However, there are several problems and challenges open to us for utilizing the Si NWs and its HSs. Thus, there is enormous scope to extend the present work for developing high performance devices to fulfill the ever rising energy demands and environmental issues, as discussed bellow:

1. The etching of crystalline Si wafer is highly anisotropic. Instead of Si wafer, the MACE could be implemented on bulk Si powder to form highly porous Si nanoflower or hierarchical nanostructure. These nanostructures may have high aspect ratio and high porosity, which could be useful for the photodegradation of organic pollutants.
2. Si NWs/NCs have shown ultralow reflectance in the entire visible range. Doping of the Si NWs can be performed ex situ to form core-shell p-n homojunction solar cell, which are very promising to meet the future energy demands.
3. The Si NW/ZnO HSs exhibited extremely high absorption in the entire UV-visible-NIR range. Al doped ZnO (AZO) can be used to fabricate core-shell Si/AZO p-n junction for solar light harvesting devices.

4. In the present work, Ag NPs decorated Si NWs/NCs exhibited extremely broad (1.4-3.0 eV) emissive property. Details study of Ag NPs decorated Si NWs is necessary and these HSs could be attempted for the fabrication of white light LED.

5. H-terminated Si NWs and Ag NPs as well as AuPd NPs decorated Si NWs have shown excellent visible light photocatalytic nature as compared to the commercial photocatalyst P25. These H-terminated Si NWs and metal NPs decorated Si NWs can be explored for the organic waste treatment and hydrogen production by photocatalytic water spitting at the industry scale.

6. In the present work, we have observed that the Ag NP decorated Si NWs are very much sensitive to detect methylene blue even for extremely low concentration by using both SERS effective Raman analysis and fluorescence based detection. These hybrids could be utilized for the fabrication of ultrasensitive bio-chemical sensors based on fluorescence detection or SERS effect.

7. The surface of the Si NWs is highly rough due to the sidewall etching, which makes the Si surface hydrophilic. MACE grown Si NWs could be used as platform to create complex HSs, such as branched/hierarchical HSs. The Si NWs/ZnO and Si NWs/TiO_2 branched HSs could be attempted for energy and environmental applications.

8. The mesoporous Si NW heterostructures could be utilized for the energy storage device, such as Li ion battery and supercapacitor.